Title	Structural condensed matter physics study of strongly correlated LaMO3(M = Mn, Ni) interfaces
Author(s)	穴田, 壮人
Citation	大阪大学, 2020, 博士論文
Version Type	VoR
URL	https://doi.org/10.18910/76599
rights	
Note	

Structural condensed matter physics study of strongly correlated LaMO$_3$ (M = Mn, Ni) interfaces

MASATO ANADA

MARCH 2020

Structural condensed matter physics study of strongly correlated LaMO$_3$ (M = Mn, Ni) interfaces

A dissertation submitted to
THE GRADUATE SCHOOL OF ENGINEERING SCIENCE
OSAKA UNIVERSITY
in partial fulfillment of the requirements for the DOCTOR OF PHILOSOPHY IN SCIENCE

BY

MASATO ANADA

March 2020

Abstract

From the late 20 th century, the development of the nanofabrication technology of ultrathin films promotes surface/interface science and the study of dimensionality. Researches and applications of various interfaces such as metal magnetic materials and oxides have been attempted since the discovering of superconducting in copper oxides. Quantum well state of optical devices, 2 dimensional electron gas in high electron mobility transistor, quantum Hall effect and solar cells are popular applications of phenomena emerging at 2 dimensional clean interface. In recent years, functional oxide interface of strongly correlated oxide materials have been studied as new alternative candidates to Si-based integrated devices. The interface of them is very interesting subject of discussion from the viewpoint of quantum mechanics because of the interaction of strongly correlated electrons with different neighbors. The structural modulation of the crystal structure across the interface and strong correlation with degrees of freedom of electrons such as valence, spin, and orbital can manipulate their emerging physical properties from rich electronic phase.

One of the problems of surface/interface science is the lack of experimental methods to observe the structure of surface/interface. The lack of structural information prevent the understanding of the behavior of the electrons in the spatially inhomogeneous potential near the surface/interface region. Especially in strongly correlated oxides, sub Å spatial resolution is required because the scale of structural modulation as a result of correlation with d electron state is sub Å.

In this dissertation, we focus on the two subject of discussion. One is the development of a new analysis technology based on crystal truncation rods(CTR) scattering method, a kind of surface X-ray diffraction technique. Second is the structural condensed matter physics study of the strongly correlated oxides interface. This dissertation is organized in 6 chapters.

Chapter 1 presents the background of my study. Some previous important reports about interfacial phenomena in strongly correlated materi-

als and previous technique of surface/interface structural observation techniques are introduced. These are candidates of the study of interface for the activity of developing application tools utilizing the behavior of electrons in 2 dimensional surroundings. Then, the utility and difficulties of CTR scattering method are presented. The principle and experimental method used through this dissertation are also presented in this chapter.

In chapter 2, our developed analysis technique for CTR scattering data based on the Bayesian inference theory is described. Bayesian inference extracts the structural parameters as probability distribution. This makes it possible to quantitatively evaluate the validity of structural models. Monte-Carlo optimization actualize semi-auto refinement of 60 to 100 parameters of complex structural model of the interface in few days. To reveal the utility of the techniques, our developed software is applied to the virtual and experimental CTR data from $LaAlO_3$ ultrathin film on $SrTiO_3$ substrate. The 0.01 Å of precision of atomic position is expected by our developed method.

The structures of $LaNiO_3$ thin films whose conductivity depend on a film thickness and two different substrates, $SrTiO_3(001)$ and $LaAlO_3(001)$ are investigated by CTR scattering experiment in chapter 3. The different mechanisms of metal-insulator transition of $LaNiO_3$ thin films depending on the substrates are suggested by the depth dependence of the value of structural parameters.

Chapter 4 presents the structural study of $LaMnO_3$ thin films on $SrTiO_3(001)$ substrate whose magnetism depends on a film thickness. In addition, the analysis method and results of Mn valence distribution in $LaMnO_3$ film by resonance CTR scattering data are presented. As a results, we found the value of c-lattice spacing corresponding to $LaMnO_3$ antiferromagnetic phase only at the top of a $LaMnO_3$ layer, while that of middle layers of the $LaMnO_3$ is the same as ferromagnetic phase. In addition, in the 10 unit-cell thick film, localized Mn^{2+} at the interface was observed, suggesting the existence of charge transfer effect in the $LaMnO_3/SrTiO_3$ interface.

The structural information and Mn valence distribution of the $LaMnO_3/LaNiO_3$ multilayer and exchanged one $LaNiO_3/LaMnO_3$ are investigated in chapter 5. Our analysis results show the stacking order dependent Mn^{4+} distribution in LMO region, which implies the different mechanism of emergent ferromagnetism in multilayer. In particular, the measurement of spatial distribution of valences state by non-destructive methods provides complementary information to spectroscopic methods.

Finally, chapter 6 is devoted to summary of this dissertation.

Contents

Chapter 1

Introduction

1.1 Surface/interface related phenomena in strongly correlated oxide study

Strongly correlated oxides often have large electron-lattice coupling. Using this coupling, new electronic states have been pursued in the metal oxide films and interfaces. Basic research and physical property design have been conducted for various combinations of strongly correlated material interfaces[1, 2]. A large response with a small external field controlling is expected due to the phase competition state of different energetically antagonistic electronic phases.

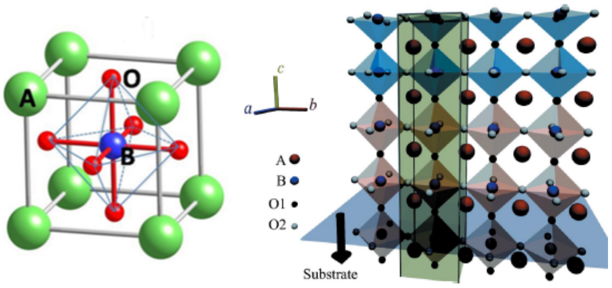

Figure 1.1: Schematic picture of the perovskite structure and its expitaxial interface

1.1.1 Electronic state engineering through the epitaxial strain

Perovskite oxides display a wide variety of their physical properties such as magnetism, electronic transport, superconductivity, and so on[3, 4]. The various electronic phase is derived from the strong coupling among degrees of freedom of *d*-electrons, such as orbital, valence and spin as well as the degree of lattice. Their chemical stability and variety of physical properties make them not only ideal for the study of electronic correlation but also useful for explorations of functional material design for application as electronic devices. In recent years, there has been a lot of approaches to manipulate their property as well as create new functionalities in heterostructures. One can make a clean epitaxial interface due to structural similarity of perovskites. Such coherent interfaces of perovskite oxides provide us with an opportunity to study the effect of low dimensionality on strongly correlated electron systems. Because electrons are affected by surrounding electrons, their behavior must be different at surfaces [5] or interfaces [6, 7, 8]. The broken time reversal symmetry, space inversion symmetry, and gauge symmetry across the interface can tune peculiar phenomena not found in the bulk constituents[1]. New electronic phases due to the symmetry breaking are accompanied with the structural modulation of epitaxial interface and vice versa. The epitaxial modulation, atomic interdiffusion, and BO_6 connectivity modulation across the interface change the atomic coordination, affecting the magnetic and electronic properties.

The study of thin film properties in the early 2000s was mainly to investigate the influence of epitaxial strain from the substrate. For example, Ref.[9] indicated that lattice deformation caused by applying epitaxial strain to $BaTiO_3$ could manipulate the Curie temperature(T_C). T_C of epitaxially strained $BaTiO_3$ film on $DyScO_3$ is enhanced from 400K to 900K. This enhancement and residual polarization are originated from Ti^{4+} displacement by compressive strain from $DyScO_3$. Another example is the correlation between lattice and orbital, that is, the manipulation of the Jahn-Teller(JT) effect. Fig. 1.2 shows the magnetization and electrical resistivity of strained manganese oxides. Under compressive($c/a > 1$) or tensile($c/a < 1$) strain, the stabilization of outermost $d_{x^2-y^2}$ and $d_{3z^2-r^2}$ is selected and they exhibits the different type of antiferromagnetic or ferromagnetic order state[10]. The epitaxial strain effect to convert the magnetic state has been studied for various heterointerfaces including the notable three component[11, 12, 13].

1.1.2 Electronic reconstruction of the interfaces

Recent research has expanded to charge, orbital and spin reconstruction due to electron correlation at the interface in addition to the effect of strain. The most studied two-dimensional electron systems at the oxide heterointerface is the formation of a two-dimensional electron gas at the $LaAlO_3$

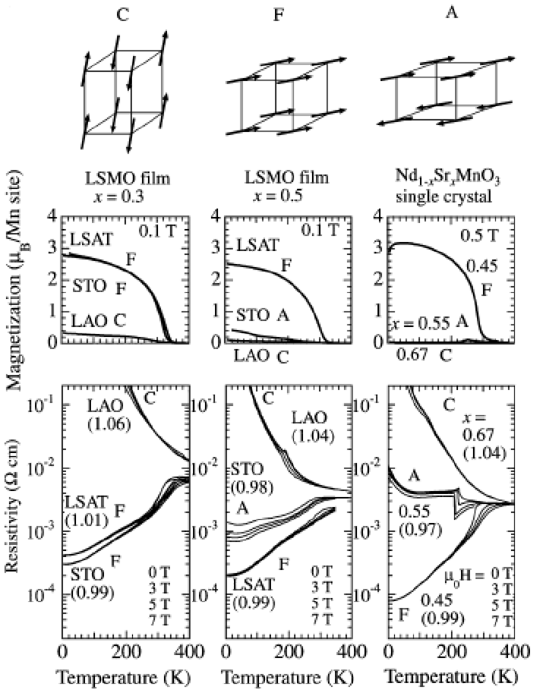

Figure 1.2: Temperature dependence of magnetization(upper panel) and resistivity(bottom panel) of Mn oxides fabricated on LaAlO$_3$, SrTiO$_3$ and La$_{1-x}$Sr$_x$Al$_{1-y}$Ta$_y$O$_3$[10]. The number attached below the substrate in upper panel is the ration of lattice constant c/a. Compressive(LAO) and tensile(STO) strain to La$_{1-x}$Sr$_x$MnO$_3$ each stabilize the d$_{3z^2-r^2}$ and d$_{x^2-y^2}$, resulting in C, F, and A type antiferromagnetic spin order.

and $SrTiO_3$(LAO/STO) interface [14]. The conductivity data shown in Fig. 1.3 exhibits the films thicker than 4 u.c. of $LaAlO_3$ layer is metallic. This thickness dependence of conductivity is discussed by polar discontinuity at the interface[15]. When electrically polarized LAO is stacked on a non-polar STO substrate, the electrostatic potential increases toward the surface. As a result, the electrons near the surface move to the interface to avoid an increase in potential energy, resulting in a two-dimensional electron gas.

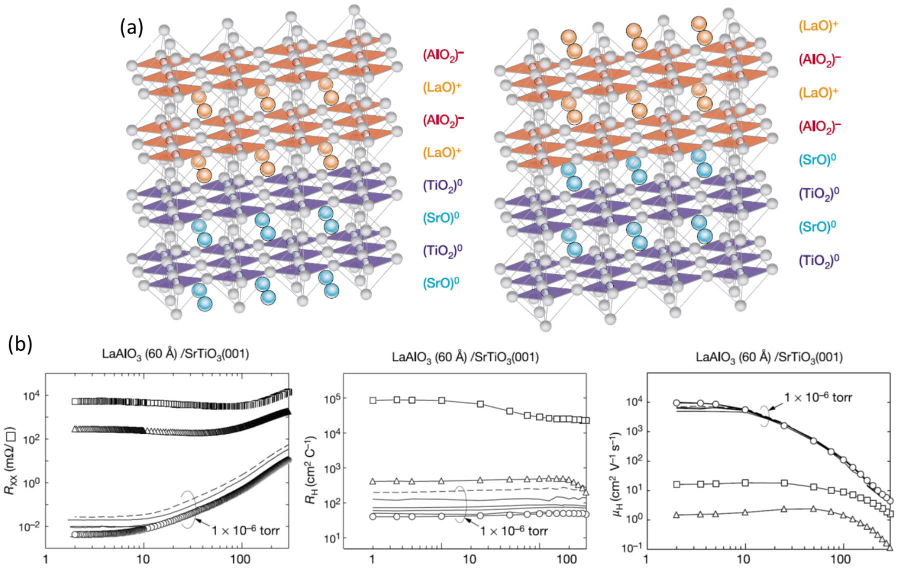

Figure 1.3: (a)Schematic LAO/STO interface, (b)resistivity[14]

One can design the band structure of the strongly correlated substance interface from the idea of polarity discontinuity[16]. They successfully tuned the Schottky barrier heights between metallic $SrRuO_3$ and n-type semiconductor of Nb doped $SrTiO_3$ by inserting the positive charged LaO layer or negative charged AlO_2 layer. The inserted layer and screening charges make a dipole at the interface and generate the local electric field which bend the interfacial band. The remarkably large tunable energy range of 1.7 eV of Schottky barrier and its flexibility of combination of materials exhibit high potential of versatile application for nano-scale material design.

Rotation modes of the BO_6 octahedron contained in the perovskite structure affects the hybridization of $3d$ and O_{2p} orbitals, resulting in changes in the behavior of $3d$ electrons. Such a rotation mode can also be controlled by forming epitaxial interface[17, 18]. Fig. 1.4 shows the formation interval dependence of B-O-B bond angles and B-O bond length in superlattice of cubic $SrMnO_3$ and rhombohedral $LaNiO_3$. For superlattices with formation periods $m = 1$, the rotations are strongly suppressed in both MnO_6 and NiO_6, while large rotations are induced in the $SrMnO_3$ layers for the case of $m = 4$. This is one of the manipulation methods of interfacial properties utilizing the structural modulation and electronic reconstruction across the interface[19].

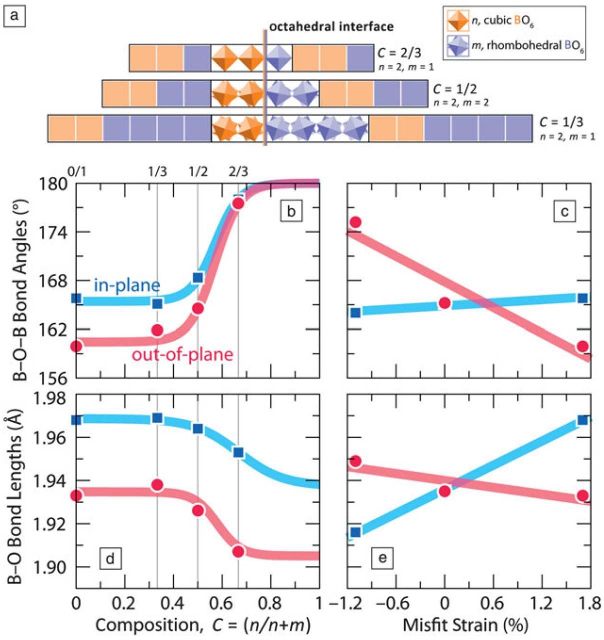

Figure 1.4: Propagation of octahedral rotation in $(SrMnO_3)_n/(LaNiO_3)_m$ super lattice[17].(a)Schematic picture of super lattice with different periods of cubic and rhombohedral BO_6 octahedra. (b)B-O-B bond angles and (d) bond length as a function of composition, $C{=}(n/n + m)$ and (c), (e) are those as a function of misfit strain

The effect of charge transfer (described in chapter 4 and 5) and the exchange interaction between spins across the interface also lead reconstruction of their electronic phase and create new properties. Thus, many studies have been conducted on the interface of strongly correlated materials as a target for the interfacial engineering.

1.2 Experimental techniques for surface/interface structure

Total understanding of mechanism of functionality of the strongly correlated materials requires not only macroscopic physical properties but also microscopic structural information. There are several reasons. For one thing, we need to confirm whether the fabricated sample is constructed as designed. The structure inside the thin film like perovskites is spatially inhomogeneous from one layer to layer in the depth direction. Theoretical studies are based on ideal interface without assumption of effects of structural disorder and surface termination. Characterization of chemical and structural order is also a critical issue because intermixing of cation atoms can alter the chemical potential at the interface and promotes charge transfer[20, 21]. The structural observations can exclude such assumptions of the structure and provide accurate physical properties of the interface[22, 23]. Second, the sub AA spatial resolution of atomic position is required to understand the behavior of electrons, especially in perovskites oxides. The Thomas-Fermi screen length of strongly correlated careers is expected to be much shorter(1-2 nm) than the semiconductor junctions($\sim$10 nm), so the details of the structure of interface is more important than that in conventional semiconductors. The charge transfer effect alter the atomic valence and cause structural modulation due to Coulomb interaction. Jahn-Teller active materials like $R\mathrm{MnO}_3$ have different Metal-Oxygen bonds. The scale of these structural alternation is 0.1 Å.

The interfacial structures are often examined by using scanning transmission electron microscopy, which is sometimes combined with electron energy loss spectroscopy [24, 25]. This requires slicing the sample, which sometimes causes damage to the newly exposed surface. The beam damage to sample sometimes alter the electronic state. In addition, the sample environment is hardly controlled. The resolution of the atomic displacement is typically 0.5 Å. However, when we want to study the electric polarization, which is an essential for the physical properties of oxides, the resolution is still insufficient.

1.2.1 Surface X-ray diffraction

A technique for examining the structure of a material surface using X-rays is called surface X-ray diffraction. The greatest feature of surface X-ray diffraction is that the structure in the depth direction from a material surface can be obtained without any physical contacts. Surface X-ray diffraction has high versatility that can be simply applied to any materials regardless of the their physical properties because of its weak interaction with matters. Surface X-ray diffraction is classified into X-ray reflectivity(XRR) method, Crystal truncation rod (CTR) scattering method, and grazing-incidence small-angle X-ray scattering (GISAX) method. These are roughly distinguished by the difference in the incident angle of X-rays. GISAX measures the scattering from small incident angle comparable with the total reflection critical angle. The scattering in GISAX region reflects the spatial distribution of particles aggregated on a larger scale than interatomic distance, such as nanoparticles. XRR is a method for determining film structure parameters such as film thickness, density, and surface and interface roughness by examining the incident angle dependence of X-ray reflectivity.

The CTR scattering method has been proposed since the 1980s[26, 27, 28, 29]. It is the scattering signal from the truncated periodic structures having atomically flat surfaces. The advantage of CTR method is to observe the depth dependence of structural information and the spatial resolution of sub Å scale. The high transmission of x-ray reveals the atomic position of tens nm region in the depth direction from the surface. CTR scattering method measures the scattering intensity at high incident angle from crystal without large structural disorder.

Atomic structure with high spatial resolution by CTR method provides us various insights of the mechanism of emerging physical property around the surface/interface. Ref.[23] reports the atomic arrangement of a five monolayer film of $\mathrm{LaAlO_3}$ on $\mathrm{SrTiO_3}$. The formation of a quasi-two-dimensional electron gas is explained as that the atomically intermixed region($\mathrm{La_{1-x}Sr_xTiO_3}$) form tetragonal structure and increase hopping integral via O_{2p}, enhancing the conductivity. The band structure calculated by density functional theory calculation based on the obtained structure also exhibits the metallic band. Thus, synergy of structural information with first-principles calculation is also a great advantage of CTR scattering method.

Thus, CTR method has many advantages for examining transition metal oxide interface that requires strict evaluation of atomic coordinates. However, CTR method has not been used as a general surface observation technique. Ordinary X-ray generators do not provide sufficient flux to obtain CTR scattering intensity necessary for analysis. In addition, since systematic software for the phase retrieval of CTR data has not been established, great deal of works and cost are required to extract the structural information from CTR data.

1.2.2 Principles of Crystal truncation rods scattering method

The CTR scattering method is described by the kinematical diffraction theory. In addition to Bragg reflections in the reciprocal space, rod-like scattering is obtained in the surface normal direction if the electron density distribution is truncated at the surface. This rod like scattering is called CTR scattering. Fig. 1.5 shows the structure of the interface of $LaAlO_3$ and $SrTiO_3$ observed by STEM(left) and CTR method. While the electron microscope can directly observe the electron density in real space with a resolution of about 0.5 Å, the CTR scattering method enables structural observation with a resolution of about 0.1 Å by analyzing the diffraction data.

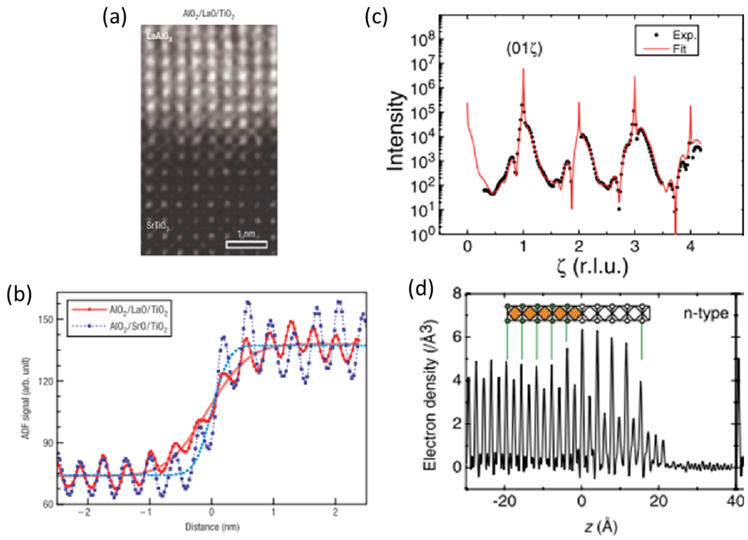

Figure 1.5: (a)The observed interfacial structure of LAO/STO by STEM. (b)Depth dependence of electron density of LAO/STO interface by STEM[15]. (c)The CTR data and (d)analyzed electron density distribution as a function of depth[30].

Calculation of the CTR scattering

Here, the scattering amplitude of CTR scattering from a sample having a atomically flat surface without any effects of surface reconstruction and adsorption is derived. We assume the crystal has a surface parallel to the c planes, that is, surface normal direction is z axis, and x, y axis is located within the c plane. The wave vectors of incident and scattered X-ray are $\boldsymbol{k}$ and $\boldsymbol{k}'$, and $\boldsymbol{Q} = \boldsymbol{k}' - \boldsymbol{k}$ is the scattering vector. The scattering amplitude $F(\boldsymbol{Q})$ is proportional to the Fourier transform of electron density. The $F(\boldsymbol{Q})$ from single crystal with a finite size is calculated by Fourier transform of the product of the electron density of a crystal with infinitely spread periodicity $\rho_\infty(\boldsymbol{r})$ and the function of the crystal shape $\mathrm{BOX}(\boldsymbol{r})$. The value of $\mathrm{BOX}(\boldsymbol{r})$ is 1 and 0 for in and out of the crystal region. Then, $F(\boldsymbol{Q})$ is written as

$$F_B(\boldsymbol{Q}) = \int \rho_\infty(\boldsymbol{r})\mathrm{BOX}(\boldsymbol{r}) \exp[-\mu t(\boldsymbol{r})] \exp[i\boldsymbol{Q}\cdot\boldsymbol{r}] d\boldsymbol{r}, \tag{1.1}$$

the term $\exp[-\mu t(\boldsymbol{r})]$ gives the decay of incident X-ray as a function of the depth from the surface $t(\boldsymbol{r})$. In case of a wide plate shape sample whose periodicity parallel to the surface is unchanged from the interior region of the crystal, $F_B(\boldsymbol{Q})$ written by discrete Fourier transform is,

$$\begin{aligned} F_B(\boldsymbol{Q}) &= \sum_{n_1=-\infty}^{\infty}\sum_{n_2=-\infty}^{\infty}\sum_{n_3=-\infty}^{0}\sum_{\mathrm{j}}^{\mathrm{cell}} f_\mathrm{j} \exp\left[i\boldsymbol{Q}\cdot(\boldsymbol{r}_\mathrm{j} + n_1\boldsymbol{a} + n_2\boldsymbol{b} + n_3\boldsymbol{c})\right] \exp(\mu n_3 c) \\ &= L_F(\xi)L_F(\eta)\sum_{\mathrm{j}}^{\mathrm{cell}} f_\mathrm{j}\exp(i\boldsymbol{Q}\cdot\boldsymbol{r}_\mathrm{j}) \sum_{\bar{n_3}=\infty}^{0} \exp(2\pi i\bar{n_3}\zeta)\exp(-\mu\bar{n_3}c) \\ &= \frac{L_F(\xi)L_F(\eta)}{1-\exp(2\pi i\zeta)\exp(-\mu c)} F_\mathrm{cell}(\boldsymbol{Q}), \end{aligned} \tag{1.2}$$

where $\boldsymbol{a}$, $\boldsymbol{b}$ and $\boldsymbol{c}$ are the unit translational vectors, L_F is the Laue function and $F_\mathrm{cell}(\boldsymbol{Q})$ is the structure factor of the unit cell. The summation for n_3 is rewritten by $\bar{n_3} = -n_3$. f_j is the atomic scattering factor for j-th atom written as

$$f_\mathrm{j}(\boldsymbol{Q}) = \int \rho_\mathrm{j}(\boldsymbol{r})\exp(i\boldsymbol{Q}\cdot\boldsymbol{r})\exp[-B_\mathrm{j}Q^2]d\boldsymbol{r}, \tag{1.3}$$

where ρ_j is the electron density. $B_\mathrm{j}(\text{Å})$ is the atomic displacement factor of j-th atom defined as $B_\mathrm{j}(\text{Å}^2) = 8\pi^2\langle u_\mathrm{j}^2\rangle$, where u_j is the atomic displacement from averaged position $\boldsymbol{r}_\mathrm{j}$. We have the limit of the absorption coefficient to zero ($\mu \to 0$) because the μ tends to be the small value(typically 10^{-6} to 10^{-5} for 5 keV to 20 keV) in case of hard X-ray beam. The scattering intensity $I(\boldsymbol{Q})$ is given by the square value of the amplitude. The scattering amplitude from truncated crystal at certain plane is calculated by Eq. 1.2. The scattering amplitude $F_S(\boldsymbol{Q})$ from the different structure in film or interface region is calculated as follows.

$$\begin{aligned} F_S(\boldsymbol{Q}) &= \sum_{n_1=-\infty}^{\infty}\sum_{n_2=-\infty}^{\infty}\sum_{\mathrm{j}}^{\mathrm{cell}} f_{\mathrm{j}} \exp\left[i\boldsymbol{Q}\cdot(\boldsymbol{r}_{\mathrm{j}}+n_1\boldsymbol{a}+n_2\boldsymbol{b}+z_{\mathrm{j}}\boldsymbol{c})\right]\exp(-\mu z_{\mathrm{j}}) \\ &= L_F(\xi)L_F(\eta)\sum_{\mathrm{j}}^{\mathrm{cell}} f_{\mathrm{j}}\exp(i\boldsymbol{Q}\cdot\boldsymbol{r}_{\mathrm{j}})\exp(-\mu z_{\mathrm{j}}). \end{aligned} \tag{1.4}$$

Here, z_{j} is the atomic position in depth direction of j-th atom. The scattering amplitude $F(\boldsymbol{Q})$ is given by $F_B(\boldsymbol{Q}) + F_S(\boldsymbol{Q})$. Fig. 1.6 shows the effect of structural modulation in the surface to the CTR profile. The CTR profiles were calculated by the 4 models of 4 u.c. thick LAO film on $\mathrm{SrTiO_3}$(001) flat surface(A to D). The number of bumps between the substrate Bragg peaks increased with the thickness, as expected from a simple calculation of interference. However, unlike the bulk structure determination, the lattice spacing of the film could not be derived from the peak positions. This is because the lattice spacing for the j th layer from the surface is not necessarily the same as that of the (j + 1) th layer. In addition, the Bragg reflections for ultrathin films are ill defined; one cannot find clear Bragg peak positions for the films. Therefore, one has to perform a structure refinement using the CTR profiles even to derive the lattice spacing as a function of the depth. The roughness of the surface(Model B) decreases the intensity in the intermediate points of Bragg peaks. The structural disorder enlarge the Debye-Waller factorexp$(-BQ^2)$, resulting in the exponential decay to high angle region(Model C). Analytical calculation of the roughness and disorder effects on CTR intensity was studied elsewhere[26]. Comparing the results of model A and D in Fig. 1.6, the only 1.02 times larger *c*-lattice spacing(about 0.08 Å) make a clear difference in CTR profile appears. Thus, CTR scattering strongly reflects the structure in the depth direction of the material near the surface. The surface structure can be determined with sub Å resolution by analyzing the CTR scattering data.

Experiment of CTR method

Fig. 1.7 shows (a)four-circle diffractometer we used for CTR scattering experiment in Photon factory BL-3A. The yellow arrows shows the incident and scattered X-ray. The sample was set to the center of four axis and kept in a vacuum chamber at 10^{-5} torr covered with the Beryllium window to prevent the radiation damage. The scattered X-ray is detected by a two dimensional pixel array detector XPAD(imXpad)(Fig. 1.7(b)) or an ordinary point detector. Fig. 1.8 shows the schematic picture of experiment

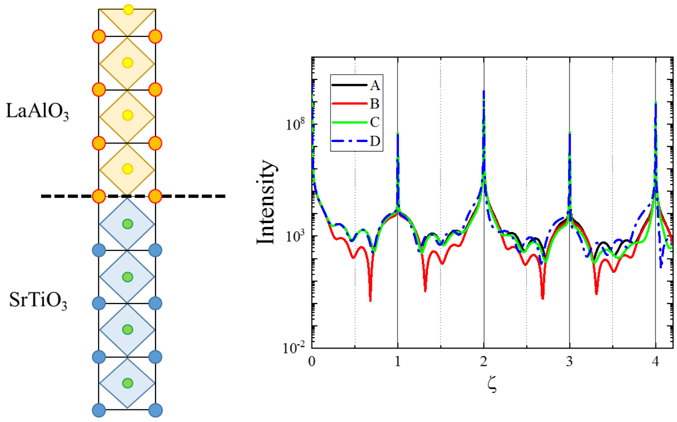

Figure 1.6: CTR scattering calculated by 4 u.c. thick $LaAlO_3$ film models on $SrTiO_3$. A: All atoms is placed at $SrTiO_3$ lattice points. Their atomic occupancy is 1, and atomic displacement parameters B is 0.5. B: The occupancy of top layer is 0.5. C: Atomic displacement parameters B is 2. D: The value of c-lattice constant of all $LaAlO_3$ layers is 1.02 times as large as model A.

arrangements in the reciprocal space. The detector acceptance with XPAD extends across CTR scattering(a part of red solid curve of Ewald's sphere). The CTR scattering is detected by moving the 4 axis of diffractometer so that the detector acceptance moves along $c^\star$ direction. After subtracting the background noise, illumination area and Lorentz factor corrections were applied to the integrated intensity following Ref.[31]. To avoid count loss of intensity due to geometric factors, oscillation photograph method was used for low-ζ measurements. The definition of oscillation photograph is the image data recording integrated scattering intensity during exposure time of X-ray with rotating sample around the origin of the reciprocal space. The integrated intensity is stored in one piece of photograph data. In case of the measurements of four circle diffractometer, the θ angle is rotated to make the detectable region crossing CTR scattering(Fig. 1.7). The velocity at which the Ewald's sphere passes through the rod differs depending on $\boldsymbol{Q}$, so the Lorentz correction factor for oscillation photograph is also necessary. One example of single shot of CTR scattering is shown in Fig. 1.9.

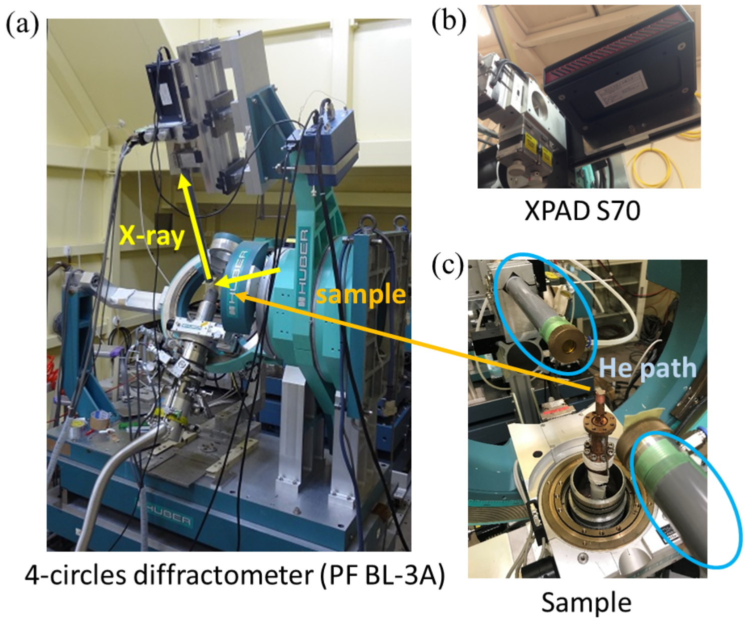

Figure 1.7: (a) 4-circle diffractometer installed at KEK-PF BL-3A, (b)2 dimensional detector ‘XPAD(imXpad S70)’ (c)A plate shape sample of perovskite oxide thin film(10 mm × 5 mm)

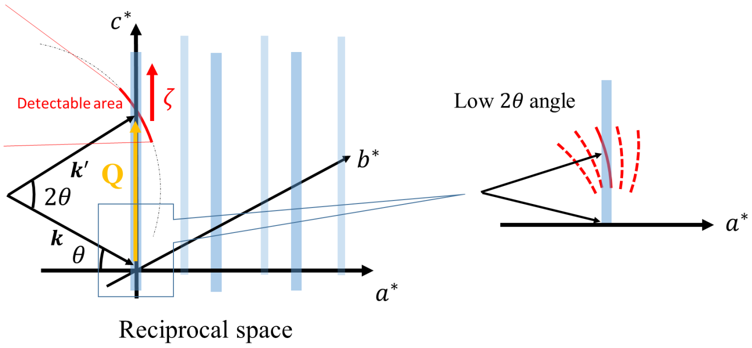

Figure 1.8: Schematic CTR scattering in reciprocal space is presented. The blue bars elongating to ζ direction express the CTR scattering. The red curve, a part of Ewald sphere, is detector acceptance by single shot of 2D detector. CTR scattering can be observed at the crossed point of red curve and blue rod. ζ dependence of CTR scattering is detected by ζ scanning. The CTR scattering of low angle region of 2θ is observed by oscillation photograph method.

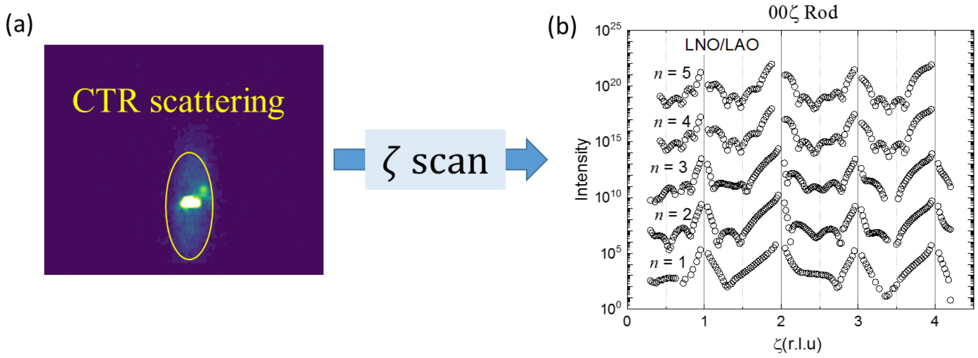

Figure 1.9: (a) Single shot photograph of CTR scattering by XPAD. (b) The CTR scattering intensity profiles from 1 to 5 unit-cell thick $LaNiO_3$ thin films on $LaAlO_3$ substrate.

1.2.3 Previous technique for analysis method of CTR scattering

In the kinematical diffraction theory, the structure could be determined easily by calculating the inverse Fourier transform, if it were possible to directly measure the complex amplitude. Actually, the experiments observe only the intensity, the squared value of amplitude, and lost the phase information of the scattered wave. This problem is known as ‘phase problem’. In the case of single crystal structures, the real space structure can be derived by ’direct method’ software to solve the phase problem. An initial structural model is constructed to reproduce the experimental results well, then the least square method is applied. Likewise, the phase problem must be also solved for CTR data. However, high freedom of the structural arrangement makes it difficult to produce the correct structure because the breaking of the lattice translational symmetry in the depth direction causes the increase of the number of independent structural parameters. The large number of parameters makes it easy to fall into a local minima. The acceptance for the initial model to achieve the global minimum is often narrow. Here, we consider the case of ten unit-cell-thick perovskite-type strongly correlated oxide epitaxial thin films as an example. Assuming Each layer has 6 structural parameters, the total number of parameters is 60 to 100. Grid search is a distant idea in this case. A grid search with 60 structural parameters and 10 calculations per parameter require 10^{60} times calculations. In other words, some analytical method is required to extract information on the electron density distribution. The previous techniques to obtain the appropriate first model are classified into following three methods, (1) iterative phase recovery,(2) holograph method, and (3)direct space method.

(1)Iterative phase recovery

Iterative phase recovery is utilized for not only the X-ray diffraction but also the general diffraction experiments[32]. In this method, iterative calculation cycle of the Fourier and inverse Fourier transform are executed repeatedly until the electron density distribution that satisfies the constraints in real and reciprocal space is obtained. The basic process is written as follows.

1. The provisional electron density distribution $\rho_1(\boldsymbol{r})$ is calculated by the inverse Fourier transform of the product of the experimental scale of amplitude with the first random phase $\phi(\boldsymbol{Q})$ like $\rho_1(\boldsymbol{r}) = FT^{-}[\sqrt{I_{\mathrm{exp}}(\boldsymbol{Q})}\exp[\phi(\boldsymbol{Q})]]$.
2. The constraint condition in the real space is applied to $\rho_1(\boldsymbol{r})$ and next generation $\rho_2(\boldsymbol{r})$ is generated. For example, the $\rho(\boldsymbol{r})$ is corrected by the characteristic distribution of electron density like atomicity, non-negativity, the zero values outside of the crystal(generally called support region S), the similarity of the bulk structure and so on.
3. The amplitude $F(\boldsymbol{Q})$ is obtained by the Fourier transform of $\rho_2(\boldsymbol{r})$. Then the constraint condition in the reciprocal space is applied to the $F(\boldsymbol{Q})$. The amplitude is replaced with the root of the scattering intensity obtained in the experiment with the phase unchanged.
4. The inverse Fourier transform is applied to the new $F(\boldsymbol{Q})$ again to derive the improved $\rho(\boldsymbol{r})$.
5. After repeating n cycles($n \sim 10^3$) of the process 2 to 5, the $\rho_n(\boldsymbol{r})$ satisfied with both real and reciprocal constraint is recovered.

There are some expanded technique of iterative phase recovery method called Hybrid input-output (HIO)[33], difference-map method[34], etc., depending on the type of constraints in real and reciprocal space. The advantage of this method is the flexibility of initial electron density distribution. However, there are two fatal problems. One is the difficulty in model converging into a physically appropriate solution without strong constraints in the real space. In a technique called DCAF[35], the electron density distribution of the $LaAlO_3/SrTiO_3$ heterostructure can be obtained stably by incorporating unique constraints in the iterative method.(shown in Fig.

1.10) Another problem is the low density of the real space information due to the limitation of the measurable region of the reciprocal space. In order to obtain a sufficient density, the scattering intensity data are needed to be extrapolated. Such a problem of the degree of freedom of the structure, and the operation of the data insertion cause a convergence to arbitrary answers.

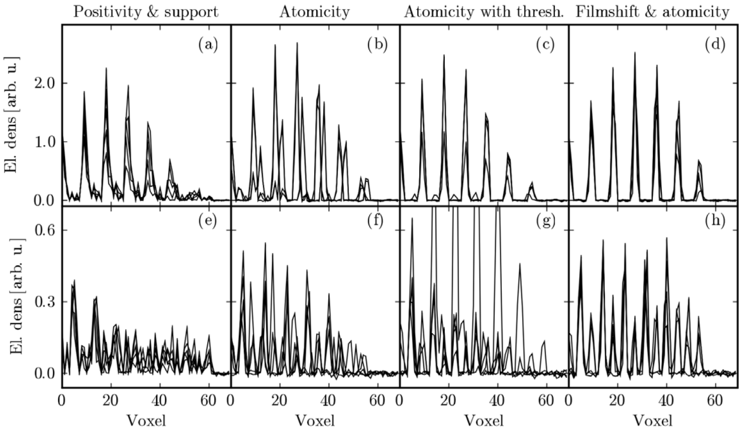

Figure 1.10: The results of electron density of LAO/STO by DCAF[35]. The more and more right side of these figures are the results more constrained in real space, such as positivity, atomicity, and translational similarity of electron dencity. The strong constraint is required to obtain stable results of electron density.

(2)Holography method

In the Holography method, the phase of the scattered amplitude is directly recovered from the absolute value of the scattering amplitude obtained in the experiment and the structure of the the bulk as known information. The concept of Holography method given by Takahashi in 2001 and several similar methods have been proposed so far[36]. Here, the basic theory of holography is introduced following the treatment of Takahashi's method to determine the phase of the amplitude F_S from unknown surface structure. Fig. 1.11 shows the conceptual scheme of this method. As mentioned in previous section, the scattering amplitude $F(\boldsymbol{Q})$ at a certain scattering vector $\boldsymbol{Q}$ is decomposed into a contribution $F_B(\boldsymbol{Q})$ from the bulk and that $F_S(\boldsymbol{Q})$ from the region having unknown structure. The scattered intensity $I(\boldsymbol{Q})$ can be written as

$$I(\boldsymbol{Q}) = [F_B(\boldsymbol{Q}) + F_S(\boldsymbol{Q})]^\star [F_B(\boldsymbol{Q}) + F_S(\boldsymbol{Q})]. \tag{1.5}$$

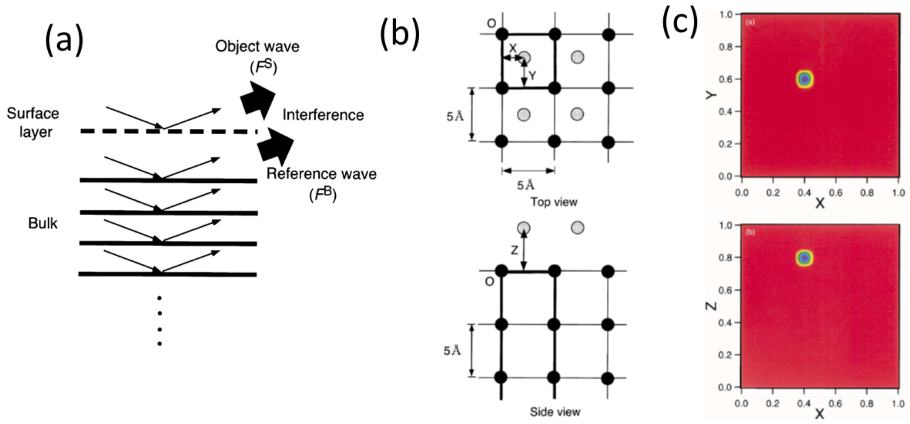

Figure 1.11: (a)The concept of holograph method[36]. F_S and F_B are the scattered amplitude from unknown structure near the surface. (b) Answer model for simulation. (c)Recovered images of electron density from CTR intensity profile calculated by model(b)

This equation can be rewritten as

$$\begin{aligned} I &= F_B F_B^\star + F_B F_S^\star + F_S F_B^\star + F_S F_S^\star \qquad (1.6)\\ &= I_0 + F_B F_S^\star + F_S F_B^\star, \qquad (1.7)\end{aligned}$$

where $I_0 = |F_B|^2$ is the squared absolute value of the scattering amplitude. ($\boldsymbol{Q}$) is omitted for clarity. The last term in Eq.(1.6) is ignored due to the square of the small number. When we define the Hologram function χ as

$$\chi(\boldsymbol{Q}) = \frac{I - I_0}{F_B^\star} = F_S + F_S^\star \frac{F_B}{F_B^\star}. \qquad (1.8)$$

The Fourier transform of χ gives the structural change together with the ghosts derived from the second term. One famous method based on holography, ‘Coherent Bragg rods analysis’ (COBRA) given by Sowwan and Yacoby[37, 38] is also utilized for the analysis of oxides interface, the organic semiconductor[39](shown in 1.12), quantum dots[40], and so on.

The problem with holography methods including COBRA, which is same as the iterative method, is that structural parameters may not be obtained with low density of points in real space because of the limit of the measurable Q space. The lack of the data at low scattering angle and near the Bragg points is also serious. In order to perform Fourier transform, continuous data in reciprocal space is required. Hence, we need to interpolate and extrapolate

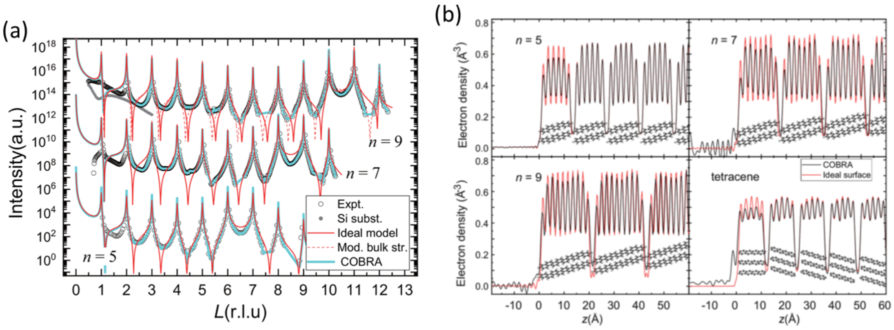

Figure 1.12: (a)Experimental and calculated CTR scattering profile of organic semiconductors. (b)Surface structure of analyzed by COBRA[39].

the calculated values from the calculated values to lacked points, which may affect the analysis results by added artificial data.

(3)Direct space method

When we have a structure, the intensity can be easily calculated. The meanings of ‘direct space method’ is defined as the computational method to search the appropriate structural model to reproduce the intensity profiles. In the direct space methods, the best combination of the structural parameters to reproduce the experimental results by some kind of sampling methods. The advantages of this methods are (1)the strict constraint can be introduced by known information to exclude the physically incorrect models preliminary, (2)the atomicity and positivity of electron density are kept and (3) the possible application to the CTR data from inhomogeneous domain structure.

The disadvantage of direct space method is the difficulty in search for the optimal solution. The enormous number of structure parameters could generate the countless local minimum optima in the parameter space. Therefore, a efficient searching algorithm is essential. In addition, accurate model selection is required because a model can produce the intensity within only the range of its expression. The assumption of appropriate model is difficult for samples with a surface/interface structure different from the expected in fabrication like a unknown surface reconstruction, multi domain structure.

Currently, there are several software programs and algorithms for the surface structure analysis. ROD[41] and its successor[42] are classical examples, whose main purpose is the refinement of the surface atomic arrangement using χ^2 minimization by numerial optimization method like steepest decent, Powell's linear optimization, simulated annealing [43] and genetic algorithm[44]. An analysis software GenX[45] utilizes the genetic algorithm called different evolution. The next generation of the parameter is calculated by adding parameter vector $\boldsymbol{p}$ generated by the randomly selected parents to another selected parameter(See.[46] and Fig. 1.13) per calculation cycle. In addition, to avoid the local optima, the random parameter vector is also added to the parameter vector if the figure of merits(FOM) (For example, χ^2 factor for χ^2 minimization analysis) increased. These programs provides us the speedy convergence of the structural parameters when the model and FOM can be correctly tuned. However, some questions about the reliability of the refined model still remain. In χ^2 minimization for arbitrary function $y(\boldsymbol{x})$, estimated value of the error of parameter x_i which gives the global minimum of $y(\boldsymbol{x})$ is defined as the $\delta x_{\pm}$ so that the value of χ^2 increase by 1(Called 68 % confidence level). In this method, the correlation between parameters cannot be reflected in the error estimation and results in tendency to evaluate error smaller than physical expectation.

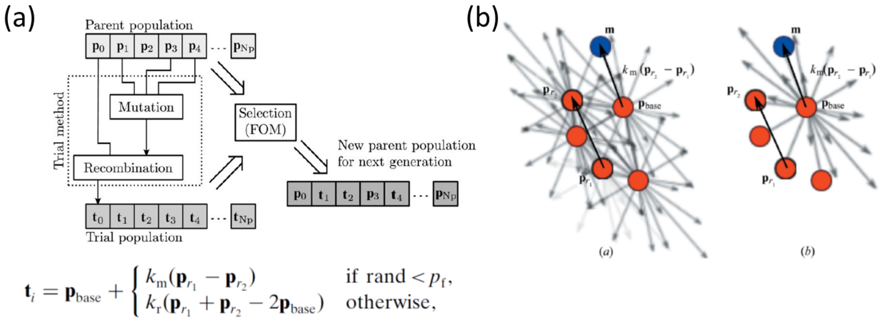

$$\mathbf{t}_i = \mathbf{p}_{\mathrm{base}} + \begin{cases} k_{\mathrm{m}}(\mathbf{p}_{r_1} - \mathbf{p}_{r_2}) & \text{if rand} < p_{\mathrm{f}}, \\ k_{\mathrm{r}}(\mathbf{p}_{r_1} + \mathbf{p}_{r_2} - 2\mathbf{p}_{\mathrm{base}}) & \text{otherwise,} \end{cases}$$

Figure 1.13: GenX[45] (a)Algorithm of genetic algorithm called different evolution. (b)schematic picture of evolution process for the next generation $\mathrm{t_i}$ from randomly selected parents $\mathrm{p_j}$.

1.2.4 Purpose of this dissertation

As mentioned in the previous sections, for the material design and development of new devices in the future, establishment of the new system clarifying the interfacial structure in sub Å resolution is indispensable to accurately understand the characteristics of electrons located in surface and interface region. In particular, magnetic and electronic properties of metal oxides are affected by a sub Å difference of interatomic distance. The surface X-ray diffraction method has a high potential to determine atomic arrangement in sub Å scale without any contact to alter or break the electronic state.

The purpose of this dissertation is following two subjects:

1. Construction of an efficient system to obtain the structural information of surface/interface region from the CTR data.
2. Exploration of the origin of properties in the interface between various perovskite type oxides, especially strongly correlated $3d$ electron systems of nickel and manganese oxides thin films.

To achieve these aims, we have developed a new software to construct the most probable structure model and its accuracy. After a performance test of the software, we applied this system to experimental CTR data from $LaAlO_3/SrTiO_3$ sample(chapter 2).

Chapter 2

Development of Bayesian inference software for CTR data

2.1 Introduction

In this chapter, we describe the developed analysis method based on the Direct space method. Direct space method can exclude physically inappropriate structures in advance because the refinement of atomic position corresponds to the strict condition of constraint for electron density distribution. In addition, highly accurate analysis results are expected because this method is not affected by lowering the density of the real space information when performing the Fourier transform of the CTR data. Considering these advantages, Direct space method is most effective one among 3 methods introduced in previous chapter. In particular, strongly correlated oxide interfaces that require analysis of atomic arrangement with high accuracy of sub Å. On the other hand, the problem with the Direct space method is that the time-scale to search for a global minimum becomes more and more enormous as the structural parameters increase. Also, once a certain answer model is obtained, some kind of evaluation index is necessary for quantitative evaluation of accuracy and precision of parameters. Accuracy and precision of structural parameters directly relate to the validity of physical property discussion.

Therefore, what are required for direct space method are

· Lowering the requirement for the initial values of parameters to refine them.
· To devise a method to quantitatively evaluate the accuracy and precision of a refined structural model.

In response to these problems, we have developed analysis software that introduces the Bayesian inference combined with the Monte-Carlo method. Bayesian inference is a information science technique based on Bayes' theorem to estimate the unknown information we want to know[47, 48]. From observed data and prior information such as empirical or other experimental facts, the unknown information can be estimated as probability distribution which reflects the experimental noise of the data. The advantages of the Bayesian inference is its practical feasibility of estimation even with a small amount of data. The estimation becomes more and more accurate with increasing the observed data. In addition, flexible update of estimation is realized by adding the prior distribution one after another from other experimental or theoretical facts. From these aspects, Bayesian inference is widely utilized for the analysis of big data. In terms of application, it is also utilized for various medical care, machinery, machine learning, artificial intelligence and so on.

As mentioned above, the searching for maximum value is not straightforward due to the large number of parameters as mentioned above. One of the an effective way for optimization problems of large scale, especially ones where a desired global minimum(or maximum) hidden among many local minima is the Markov chain Monte Carlo method[49]. The method we adopt is similar to the reverse Monte Carlo method used for liquids or amorphous bodies [50, 51, 52].

2.1.1 Fundamentals of Bayesian inference

Here, we let the unknown value we want to know be written as $\boldsymbol{\theta} = (\theta_1, \theta_2, \ldots, \theta_m)$, and the observed values be written as $\boldsymbol{y} = (y_1, y_2, \ldots, y_n)$[$m$ and n are the number of parameters and that of independent data]. $p(\boldsymbol{\theta}|\boldsymbol{y}) = \frac{p(\boldsymbol{\theta},\boldsymbol{y})}{p(\boldsymbol{y})}$ denotes a conditional probability density which means the probability distribution of $\boldsymbol{\theta}$ after we have information of $\boldsymbol{y}$, where $p(\boldsymbol{y}, \boldsymbol{\theta})$ is the simultaneous probability. The Bayes' theorem gives the relationship between the conditional probability density led by the rules of probability theory[47, 48]. This formula is written as

$$p(\boldsymbol{\theta}|\boldsymbol{y}) = \frac{p(\boldsymbol{\theta})p(\boldsymbol{y}|\boldsymbol{\theta})}{p(\boldsymbol{y})} \propto p(\boldsymbol{y}|\boldsymbol{\theta})p(\boldsymbol{\theta}). \tag{2.1}$$

The left term $p(\boldsymbol{\theta}|\boldsymbol{y})$ is called the posterior probability distribution which reflects the uncertainty of the estimation of the unknown $\boldsymbol{\theta}$. The $p(\boldsymbol{y}|\boldsymbol{\theta})$ is called the likelihood function. It expresses the probability distribution of observed value $\boldsymbol{y}$ from the unknown object $\boldsymbol{\theta}$, in other words, the probability distribution of experimental data from samples. The value of $\boldsymbol{\theta}$ for maximizing $p(\boldsymbol{y}|\boldsymbol{\theta})$ is the most reliable estimation to reproduce the observed $\boldsymbol{y}$. To pursuit such a value of $\boldsymbol{y}$ is called maximum likelihood estimation(MLE). χ^2 minimization analysis is based on MLE in case that $\boldsymbol{\theta}$ dependence of $p(\boldsymbol{y}|\boldsymbol{\theta})$ is Gaussian distribution. If the number of independent data is large enough to determine the parameters, the parameters can be estimated with high accuracy by MLE.

However, sufficient information for data analysis cannot always be obtained easily. Even when a lot of samples of data are available, the selection of conditions of samples and the measurement conditions for efficiently obtaining high-precise results of analysis sometimes need to be determined by intuition and experience of skilled researchers. The introduction of prior probabilities has a strong effect on these case. Using Bayes' rule with a chosen probability model means that the data $\boldsymbol{y}$ affect the posterior inference only through the function $p(\boldsymbol{y}|\boldsymbol{\theta})$ regarded as a function of $\boldsymbol{\theta}$ for fixed $\boldsymbol{y}$. To estimate the posterior distribution using Bayes' theorem is called posterior probability estimation. Bayes' theorem can be interpreted as a formula that converts the probability distribution of $\boldsymbol{\theta}$ into a probability that $\boldsymbol{\theta}$ occurs under $p(\boldsymbol{y})$ condition. (in other words, updates the maximum likelihood function with prior information before and after new data acquisition). MLE is the one case of Bayesian inference using the prior distribution as uniform distribution($p(\boldsymbol{y}) = 1$) which means the estimation of the distribution of parameters only derived from the given data without prior information of $\boldsymbol{\theta}$.

An example of applying Bayesian inference for X-ray diffraction data is the electron density analysis of a single protein molecule called 'sparse phase retrieval(SPR)'[53]. According to SPR method, by setting the prior information of the electron density as the prior distribution which reflects the external form. The prior distribution is set to the parabolic function to express the spatial concentration of electron density. Fig. 2.1 shows the results of the electron density derived by SPR method and ordinary HIO method. The electron densities are reconstructed with a reasonable computational cost, and errors of the results are smaller than the HIO method. Bayesian inference is also utilized for single crystal structure analysis. The quality of single crystal structure analysis results obtained from selected samples and the data obtained under specified measurement conditions can be preevaluated. By replacing intuition and experience with statistical analysis, even researchers with little experience can easily determine the measurement conditions necessary to obtain accurate analysis results[54].

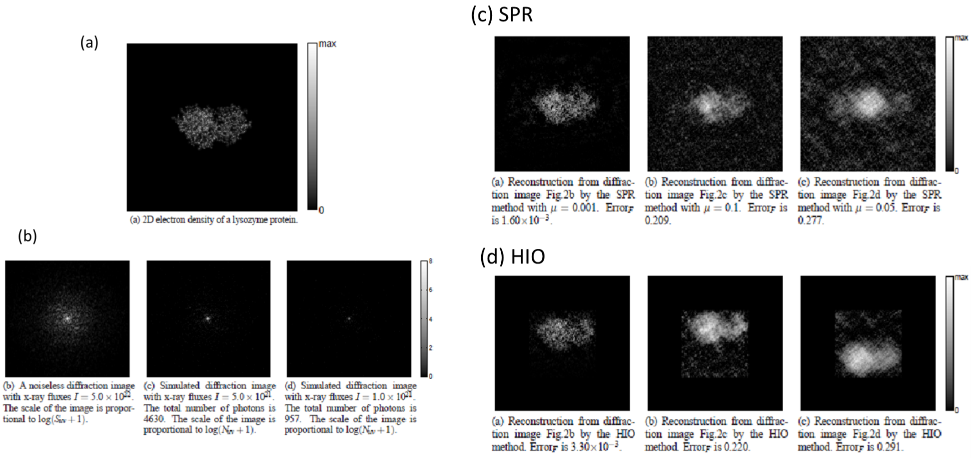

(a) 2D electron density of a lysozyme protein.

(b) A noiseless diffraction image with x-ray fluxes $I = 5.0 \times 10^{22}$. The scale of the image is proportional to $\log(S_{kv}+1)$.

(c) Simulated diffraction image with x-ray fluxes $I = 5.0 \times 10^{21}$. The total number of photons is 4630. The scale of the image is proportional to $\log(N_{kv}+1)$.

(d) Simulated diffraction image with x-ray fluxes $I = 1.0 \times 10^{21}$. The total number of photons is 957. The scale of the image is proportional to $\log(N_{kv}+1)$.

(a) Reconstruction from diffraction image Fig.2b by the SPR method with $\mu = 0.001$. $\mathrm{Error}_{\mathcal{F}}$ is 1.60×10^{-3}.

(b) Reconstruction from diffraction image Fig.2c by the SPR method with $\mu = 0.1$. $\mathrm{Error}_{\mathcal{F}}$ is 0.209.

(c) Reconstruction from diffraction image Fig.2d by the SPR method with $\mu = 0.05$. $\mathrm{Error}_{\mathcal{F}}$ is 0.277.

(a) Reconstruction from diffraction image Fig.2b by the HIO method. $\mathrm{Error}_{\mathcal{F}}$ is 3.30×10^{-3}.

(b) Reconstruction from diffraction image Fig.2c by the HIO method. $\mathrm{Error}_{\mathcal{F}}$ is 0.220.

(c) Reconstruction from diffraction image Fig.2d by the HIO method. $\mathrm{Error}_{\mathcal{F}}$ is 0.291.

Figure 2.1: SPR method[53] (a)Electron density of single protein molecule (b)simulated data. Results of recovered electron density from (b) by (c)SPR method and (d) HIO method

2.1.2 Analysis technique for efficient sampling of models

Markov chain Monte-Carlo sampling

This section describes Markov chain Monte-Carlo Sampling taking Metropolis method as an example[55]. Metropolis method is one of the sampling method with simulated annealing. At the central concept of simulated annealing is an analogy with the thermodynamics, specially with the way that liquids freeze, metals anneal and so on. For example, at high temperatures, the molecules of a liquid move freely with respect to one another while the smooth thermal mobility is lost step by step in cooling. The so-called Boltzmann probability distribution ($P(E,T){\sim}\exp(-E/kT)$) express the idea that a system in thermal equilibrium at temperature T has its energy probabilistically distributed among all different states $E(T)$. Here, we consider the situation that the transition process between different state $A, B, \ldots$ dependent on variable $\boldsymbol{x}$ whose energy are written as $E_A(\boldsymbol{x}), E_B(\boldsymbol{x}), \ldots$. The existence probability π of state A in the equilibrium state is expressed as $\pi_A = \frac{\exp(-E_A/T)}{\exp(-E_A/T)+\exp(-E_B/T)\ldots}$. The frequency of any transition process is equal to the that of the inverse process in thermal equilibrium condition. Using the transition probability from the state A to B as $P(A|B)$, equilibrium condition between A and B is written as $\pi_A P(A \to B) = \pi_B P(B \to A)$. The transition probability depends only on the state A B and is independent of the state through which the system has passed during the procedure. If one of the variable $x \in \boldsymbol{x}$ is moved with this condition kept, we can extract one of the states from the Boltzmann distribution $P(E, T)$. This process is called Markov chain sampling. The meanings of Monte-Carlo here is the change of $x \in \boldsymbol{x}$ with random step δx. By repeating this process, a set of variables $\boldsymbol{x}$ having a large Boltzmann weight can be extracted efficiently. Typical examples of the definition of P that satisfies the equilibrium condition include a heat bath method, a Gibbs sampling method, and a Metropolis method and so on. The Metropolis method is one that maximizes the acceptance P if energy decreases by changing the variable $x \in \boldsymbol{x}$, that is, $P = 1$. Then, the acceptance P from state $E(x)$ to $E(x + \delta x)$ is written as

$$P(x \to x + \delta x) = \min[1, \exp(E_{x+\delta x} - E_x)/kT]. \tag{2.2}$$

If $E_{x+\delta x} < E_x$, the P is always 1 while the other is accepted with the probability $\exp(E_B - E_A)/kT$. This means if a change in $x \in \boldsymbol{x}$ causes an increase in E, the probability of accepting the transition can be given. The acceptance $\exp(E_B - E_A)/kT$ fluctuates according to the temperature parameter. It approaches random walk at high temperature limit $T \to \infty$ and steepest descent at low temperature limit $T \to 0$. In the simulated annealing process, T is set to a high value at the beginning of sampling, and gradually decreased as the calculation cycle number.

Replica exchange Monte-Carlo sampling

The expanded sampling method of Markov chain Monte-Carlo is replica exchange MC method. The definition of replica is the copies of n number of variable $\boldsymbol{x}_\mathrm{i}$ under the different annealing temperature $T_i = T_1, T_2, \ldots, T_n$ distributed for each replica. The high T implement the searching in wide a parameter space while low T can make the $\boldsymbol{x}$ converged to the nearest minima quickly. In replica exchange MC method, the T exchange event is executed per certain cycles of MC sampling to utilize the advantage of character of low and high T. This exchange manipulation help replicas to jump from one minima to another minima easily, that is, the search in wide parameter space is possible. In the replica exchange MC method, multiple MC calculations per $\boldsymbol{x}$ with different values of T are performed in parallel. During the calculation, each replica $\boldsymbol{x}_\mathrm{i}$ is being annealed following the acceptance procedure of Metropolis sampling under the corresponding T_{i}. Then, for each appropriate number of steps, the states $\boldsymbol{x}_{\mathrm{i}}$ and $\boldsymbol{x}_{\mathrm{i+1}}$ are exchanged(or alternatively exchanging the two temperatures). According to the Metropolis method, the acceptance probability p_{i} of exchange event for i and i + 1 th replica having the energy value E_{i} is given by

$$p_i = \min[1, \exp{(E_{\mathrm{i+1}} - E_{\mathrm{i}})}(\frac{1}{kT_{\mathrm{i+1}}} - \frac{1}{kT_{\mathrm{i}}})]. \tag{2.3}$$

Since the exchanging replicas follows the idea of the Metropolis method, the Markov chain is designed so that the distribution of a whole replicas $P(\boldsymbol{x}_1, \ldots, \boldsymbol{x}_{\mathrm{i}}, \ldots)$ satisfies the condition of detailed balance with a careful choice of temperatures for each replicas.

Bootstrap analysis

The bootstrap method is a statistical method for estimating the properties of a population estimator (such as average, variance) by random sampling from approximate distribution[56]. Standard use of an approximate distribution is empirical distribution obtained from measured values. More specifically, observed data $\boldsymbol{X} = (\mathrm{X}_1,\ \mathrm{X}_2,\ \mathrm{X}_3,\ldots)$ is assumed to be the population of statistical quantity $\boldsymbol{\theta} = (\theta_1,\ \theta_2,\ \theta_3,\ \ldots)$. Bootstrap without assuming a probability distribution function based on a specific parameter is so-called a nonparametric method for statistical inference. It is used instead of estimation based on parametric assumptions when the assumed distribution is unreliable or when parametric assumptions are impossible or require complex calculations.

The bootstrap method also includes parametric parameter estimation based on data generation simulation. To execute parametric bootstrap, statistical model(probability distribution with certain parameters) is assumed by the distribution of original data, like an assumption of likelihood function in previous subsection. Then, the variance of the statistical quantity is estimated by the pseudo data distribution generated from the assumed statistical model. the bootstrap has come to be known to have a tendency of providing the narrower width of err bars because the rare events of the true distribution of data is hardly included in the statistics of experimental data. The error of obtained electron density by COBRA analysis is estimated by bootstrap[57].

2.1.3 Observation of polarization structure by differential X-ray diffraction data

At the LAO/STO interface mentioned in chapter 1, the control of conductivity by applying external gate voltage has been reported. The worth noting properties of external voltage effect in LAO/STO metallic interface is metal-insulator switching and superconductivity[58] by career tuning[59]. In addition, the voltage dependence of carrier mobility and carrier density has been reported, suggesting the possibility that not only the effect of simple carrier injection but also some structural change has occurred[59]. Information of quantitative polarized structure around the interface can clarify various remarks as to whether polarization occurred at LAO side or the STO side[60].

To detect a tiny structural modulation around surface caused by an external field, the change ratio of the intensity induced by the switching external is useful[61]. The change ratio of the difference of observable quantity S is defined as

$$S_{\text{ratio}} = \frac{S(+) - S(-)}{S(+) + S(-)}, \tag{2.4}$$

where $S(\pm)$ is the signal under the positive and negative external fields. The advantage of differential measurement is that common experimental environment-dependent errors, i.e. systematic errors, are canceled out. Highly sensitive measurements that capture even small changes buried in systematic errors can be performed with S_{ratio}.

By the differential measurement data of CTR scattering, it is possible to capture minute signal changes by external fields in X-ray diffraction data. R. V. Wang demonstrated the reversible switching of the ratio of polarized domain at the surface of $\mathrm{PbTiO_3}$ thin films by controlling the chemical environment extracted from the X-ray scattering measurements[62]. Although they succeeded in observing the external field effect on structure change from the Bragg intensity, the internal detailed polarization structure have not yet been observed. In order to analyze the details of changes in the polarization of the surface structure, similar experiments and analyzes on the CTR scattering intensity needs to be conducted. For that purpose, accurate observation of the signal change of the CTR scattering intensity reflecting the change of the polarization structure and to conversion method of the CTR signal change into a structural change are required.

2.2 Development of analysis software

This section describes the concept of our developed software based on the Bayesian inference combined with Monte-Carlo simulation. We describe the algorithms used in the software and demonstrate the performance of the software.

2.2.1 Bayesian Inference for CTR data

Let us adopt the Bayes' theory to extract the probability distribution of structural parameters from CTR data. The experimentally observed diffraction intensity from a unit area of the sample surface at scattering vector $\boldsymbol{Q}$ is expressed by $I_{\mathrm{exp}}(\boldsymbol{Q})$. A set of CTR data is composed of the diffraction intensities at different $\boldsymbol{Q}$, $\boldsymbol{I}_{\mathrm{exp}}(\boldsymbol{Q}) = [I_{\mathrm{exp}}(\boldsymbol{Q}_1), I_{\mathrm{exp}}(\boldsymbol{Q}_2), \ldots, I_{\mathrm{exp}}(\boldsymbol{Q}_N)]$, where N denotes the total number of measured $\boldsymbol{Q}$ positions. The posterior probability $P(\boldsymbol{\Theta}|\boldsymbol{I}_{\mathrm{exp}})$, that is, a probability distribution of structural parameters under the likelihood function of the measured CTR data is given by

$$P(\boldsymbol{\Theta}|\boldsymbol{I}_{\mathrm{exp}}) \propto P(\boldsymbol{I}_{\mathrm{exp}}|\boldsymbol{\Theta})P(\boldsymbol{\Theta}), \tag{2.5}$$

where $P(\boldsymbol{I}_{\mathrm{exp}}|\boldsymbol{\Theta})$ is the likelihood function, which represents the statistical property of the measurement noise,and $P(\boldsymbol{\Theta})$ is the prior probability, which represents prior information on the structure provided by other experimental facts or theories. Here, $P(\boldsymbol{\Theta})$ is set to a uniform distribution, which means that no prior information is assumed for $\boldsymbol{\Theta}$. As a result, $P(\boldsymbol{\Theta}|\boldsymbol{I}_{\mathrm{exp}})$ isproportional to $P(\boldsymbol{I}_{\mathrm{exp}}|\boldsymbol{\Theta})$. Under the assumption that the variation of the measured value from the model point can be approximated by a Gauss distribution, the conditional probability is given by Gaussian distribution with a standard deviation of $\sigma(\boldsymbol{Q}_{\mathrm{i}})$:

$$P(\boldsymbol{I}_{\mathrm{exp}}|\boldsymbol{\Theta}) = \frac{1}{(2\pi)^{\frac{1}{2}}}\frac{1}{\sigma(\boldsymbol{Q}_{\mathrm{i}})} \times \exp\left\{-\frac{[I_{\mathrm{exp}}(\boldsymbol{Q}_{\mathrm{i}}) - I_{\mathrm{calc}}(\boldsymbol{Q}_{\mathrm{i}};\boldsymbol{\Theta})]^2}{2[\sigma(\boldsymbol{Q}_{\mathrm{i}})]^2}\right\} \tag{2.6}$$

The calculated intensity for structure $\boldsymbol{\Theta}$ at $\boldsymbol{Q}_{\mathrm{i}}$ is expressed as $I_{\mathrm{calc}}(\boldsymbol{Q}_{\mathrm{i}};\boldsymbol{\Theta}) = S|F(\boldsymbol{Q}_{\mathrm{i}};\boldsymbol{\Theta})|^2$, where $F(\boldsymbol{Q}_{\mathrm{i}};\boldsymbol{\Theta})$ denotes thescattering amplitude for structure $\boldsymbol{\Theta}$ at $\boldsymbol{Q}_{\mathrm{i}}$ and S is a scale factor. Let $\sigma(\boldsymbol{Q}_{\mathrm{i}})$ be given by $\sqrt{(\{\gamma\,[I_{\mathrm{calc}} + I_{\mathrm{bg}}(\boldsymbol{Q}_{\mathrm{i}})]\}^2 + [\gamma I_{\mathrm{bg}}(\boldsymbol{Q}_{\mathrm{i}})]^2)}$ to express the Gaussian noise whose standard deviation is proportional to the intensity, which imitates the error arising from the optical misalignment. Here, $I_{\mathrm{bg}}(\boldsymbol{Q}_{\mathrm{i}})$ is the background intensity at $\boldsymbol{Q}_{\mathrm{i}}$. More general formula of $\sigma(\boldsymbol{Q}_{\mathrm{i}})$ is given by $\sqrt{(\{\gamma[I_{\mathrm{calc}}]\}^2 + [\gamma \mathrm{N_V} + I_{\mathrm{stat}}]^2)}$, where I_{stat} is the statistical noise of counting photons and $\mathrm{N_V}$ short for 'Noise-Value' is the value of other experimental noise. From the typical standard deviation of our CTR data at equivalent positions in the reciprocal space, we estimate the value of the structural parameter $\boldsymbol{\Theta}$ that gives the maximum value of $P(\boldsymbol{I}_{\mathrm{exp}}|\boldsymbol{\Theta})$ is the most likely one to reproduce the experimental data. For convenience, we introduce a cost function $E(\boldsymbol{\Theta}) = (\frac{-1}{N})\ln P(\boldsymbol{\Theta}|I_{\mathrm{exp}})$, whose minimization is equivalent to maximizing a posterior distribution. Substituting equation 2.6 into $E(\boldsymbol{\Theta})$, one obtains

$$E(\boldsymbol{\Theta}) = \frac{1}{N}\sum_{\mathrm{i}=1}^{N}\left\{\frac{[I_{\mathrm{exp}}(\boldsymbol{Q}_{\mathrm{i}}) - I_{\mathrm{calc}}(\boldsymbol{Q}_{\mathrm{i}};\boldsymbol{\Theta})]}{2[\sigma(\boldsymbol{Q}_{\mathrm{i}})]^2} - \ln\frac{1}{(2\pi)^{\frac{1}{2}}}\frac{1}{\sigma(\boldsymbol{Q}_{\mathrm{i}})}\right\} \tag{2.7}$$

up to a constant that is independent of $\boldsymbol{\Theta}$. The reason why the division of data points N is to keep the same scale of the cost function for any data with different number of N.

2.2.2 Monte-Carlo sampling procedure for CTR data

According to the Bayesian inference, we need to search the most reliable model by achieving the maximum value of the posterior distribution function, that is the minimum value of cost function $E(\boldsymbol{\Theta})$. If the cost function is regarded as the energy of the system, a kind of sampling method can be utilized for searching the global minimum of the cost function, that is, the most reliable structure.

Simulated annealing method

The procedure of Metropolis method in The CTR analysis is as follows.

1. One component of $\theta \in \boldsymbol{\Theta}$ is randomly selected to be modified. The parameter is modified by a small step $\delta\theta$ defined by a Gaussian random number with a standard deviation. (0.004 Å for atomic position and 0.01 for atomic occupancy)

2. The change in $E(\boldsymbol{\Theta})$ with the parameter modification is evaluated. Then, the change of cost function is calculated as $\Delta E(\boldsymbol{\Theta})$=$E(\boldsymbol{\Theta}_{\mathrm{new}})$-$E(\boldsymbol{\Theta}_{\mathrm{old}})$, where $\boldsymbol{\Theta}_{\mathrm{new}}$ and $\boldsymbol{\Theta}_{\mathrm{old}}$ are the structure models before and after the modification. The probability r that the modification is accepted or not is given by,

$$r = \begin{cases} \exp[-\Delta E(\boldsymbol{\Theta})/T_{\mathrm{MC}}] & [\Delta E(\boldsymbol{\Theta}) > 0] \\ 1 & (\text{otherwise}). \end{cases} \tag{2.8}$$

Here, T_{MC} is a temperature parameter to adjust how often modifications are accepted in MC sampling. If the modification is not accepted, $\boldsymbol{\Theta}_{\mathrm{new}}$ is restored to $\boldsymbol{\Theta}_{\mathrm{old}}$.

3. The process (1) and (2) are iterated until the value of cost function converge to the small value with the value of T_{MC} decreased according to an exponential annealing schedule.

The ratio of probabilities of two states is known as the Boltzmann factor. The Boltzmann factor characteristically depends on only the states energy difference. The annealing schedule of T_{MC} parameter controls the transition probability of $\boldsymbol{\theta}$. This software employs a method of exponentially decaying T, which is empirically effective for practical searching.

Replica exchange Monte-Carlo method

The more improved searching algorithm 'exchange MC method' is introduced to our program [63] mainly by Mr. Nagai. The acceptance ratio W of exchanging T_{MC} between two replicas with adjacent T_{MC} is given by

$$W(\boldsymbol{\Theta}_{\mathrm{i}}, T_{\mathrm{i}}^{\mathrm{MC}} | \boldsymbol{\Theta}_{\mathrm{i+1}}, T_{\mathrm{i+1}}^{\mathrm{MC}}) \tag{2.9}$$

$$= \begin{cases} \exp\{(\frac{1}{T_{\mathrm{i}}^{\mathrm{MC}}} - \frac{1}{T_{\mathrm{i+1}}^{\mathrm{MC}}})[E(\boldsymbol{\Theta}_{\mathrm{i}}) - E(\boldsymbol{\Theta}_{\mathrm{i+1}})]\} & (E(\boldsymbol{\Theta}_{\mathrm{i}}) < E(\boldsymbol{\Theta}_{\mathrm{i+1}})) \\ 1 & (\text{otherwise}). \end{cases} \tag{2.10}$$

where $T_{\mathrm{i}}^{\mathrm{MC}}$ denotes the T_{MC} for i th replica. The first temperature T_{1}^{MC} is set to be $1/N$, the inverse of the number of the data points. The probability distribution of $\boldsymbol{\Theta}$ can be determined by the statistic of sampling from the first replica which reproduces the posterior probability. This exchange MC enables us to spare times for analysis because we can abbreviate the arrangement of first structure for convergence and reduce the probability of trapped into other local minima. When this updated software is executed, we need to set the number of replicas and temperature distribution for each replica instead of the annealing schedule. We used exchange replica sampling method for the experimental data in the chapter 3, 4 and 5 of this dissertation.

2.2.3 Error evaluation method

After we have constructed a structural model that gives a satisfactory small value of $E(\boldsymbol{\Theta})$ is recorded during the MC calculation with a constant temperature $T_{\mathrm{MC}} = \frac{1}{N}$, the inverse of the number of data points for normalization of the effect of N. This procedure generates samples from the posterior probability $P(\boldsymbol{\Theta}|\boldsymbol{I}_{\mathrm{exp}})$ because the equilibrium condition is satisfied with the Metropolis method. If each component-wise posterior probability has a peak, the peak position and standard deviation are interpreted as theresulting structural parameter θ_{i} and its uncertainty. Since it evaluates the precision of structural parameters by directly sampling from their posterior probabilities, the MC technique can be applied to general cases where a strong correlation exists between the structural parameters.

The correlation between the data points is affected by the systematic error of the experimental condition such as the error of mounting position of the sample. The parameter uncertainty is underestimated because of the assumption of independent measurements we introduced in Eq .2.7. In the present method of error estimation, the T value we use for sampling is the same as N, the number of $\boldsymbol{Q}$ positions in the experimental data. Smaller T_{MC} gives smaller MC fluctuation. Thus, if the assumption of independent measurement is not assessed, one can use an arbitrarily small T value by measuring many points in a narrow $\boldsymbol{Q}$ range to increase N. One has to make some assessment of the assumption of independent measurement. While the distance between successive points in the present data is wider than the instrumental resolution, the number of effective data points may be overestimated. To estimate the effective number of data points, we calculated the error autocorrelation $C_E(\mathrm{j})$:

$$\Delta(\boldsymbol{Q}_{\mathrm{i}}) = \frac{I_{\mathrm{exp}}(\boldsymbol{Q}_{\mathrm{i}}) - I_{\mathrm{calc}}(\boldsymbol{Q}_{\mathrm{i}};\boldsymbol{\Theta})}{\sigma(\boldsymbol{Q}_{\mathrm{i}})} \tag{2.11}$$

$$C_E(\mathrm{j}) = \sum_{\mathrm{i}} \frac{\Delta(\boldsymbol{Q}_{\mathrm{i}})\Delta(\boldsymbol{Q}_{\mathrm{i+j}})}{\Delta(\boldsymbol{Q}_{\mathrm{i}})^2} \tag{2.12}$$

The effective number of observations for such correlated data, N_{eff} , is defined by $N/[1+\sum_{\mathrm{j}}(N-\mathrm{j})C_E(\mathrm{j})/N]$. The precision of parameters are correctly estimated, considering the N_{eff}.

2.2.4 Software coding

The coding of our developed software is designed by c++ language. Some input text files are needed for analysis as follows.

(a)Bulk structure file
(b)Initial structural parameters file
(c)Intensity profile data file
(d)Atomic scattering factor file
(e)Anomalous scattering factor file

File (a) includes the lattice constants $(a, b, c, \alpha, \beta, \gamma)$ and atomic position (x, y, z) of atoms in bulk. This file assumes the bulk having (001) flat surface. The structural model of film structure is defined in file (b). The atom number and initial value of structural parameters $\boldsymbol{\Theta}$ (atomic position, atomic occupancy and atomic displacement parameter) for each atoms are listed in this file. The movement range of $\boldsymbol{\Theta}$ can be introduced in this file. The intensity scale factor, the σ value for cost function are also managed in this file. The file (c) has the information of the experimental CTR profile and its statistic error for each $\boldsymbol{Q}$. The values of atomic scattering factor are listed in file (d). Besides, the value of anomalous factor is written in file (e). Since the value of anomalous factor varies with energy of X-ray used for experiments and samples, it should be determined experimentally or referred to Ref.[64]. The details of the format of these files are instructed in Appendix chapter.

The flow chart of this software is shown in Fig. 2.2. To execute the software, we need to specify the input file names, annealing schedule(The value of T_{MC}), a number of MC cycle, and output filename in a command line. When sampling by replica exchange, we need to specify the number of replicas and the T_{MC} to be distribute for each replicas. The number of Monte Carlo steps is typically 10^6 to 10^7. A 10^6 cycle iteration takes half an hour using a 4 GHz core i7 CPU with single-core calculation. After finishing the MC cycles, some output files will be generated as follows.

(f)Final structural parameters file
(g)Final intensity profile data file
(h)The process of the value of cost function file
(i)The records of parameters file

The value of refined parameters are listed in file (f). The final results of intensity is also output in file (g). The format of (f) and (g) is the same as (b) and (c) respectively. File (h) records the all process of the value of cost function. We need to confirm complete convergence of parameters by that of cost function. File (i) is the records of all refined parameters $\boldsymbol{\Theta}$ during MC calculations. These values are used for extracting posterior probability distribution.

2.3 Performance of the software

To check the performance of the developed software, we applied it for virtual measurement data. Virtual measurement data is defined as simulated

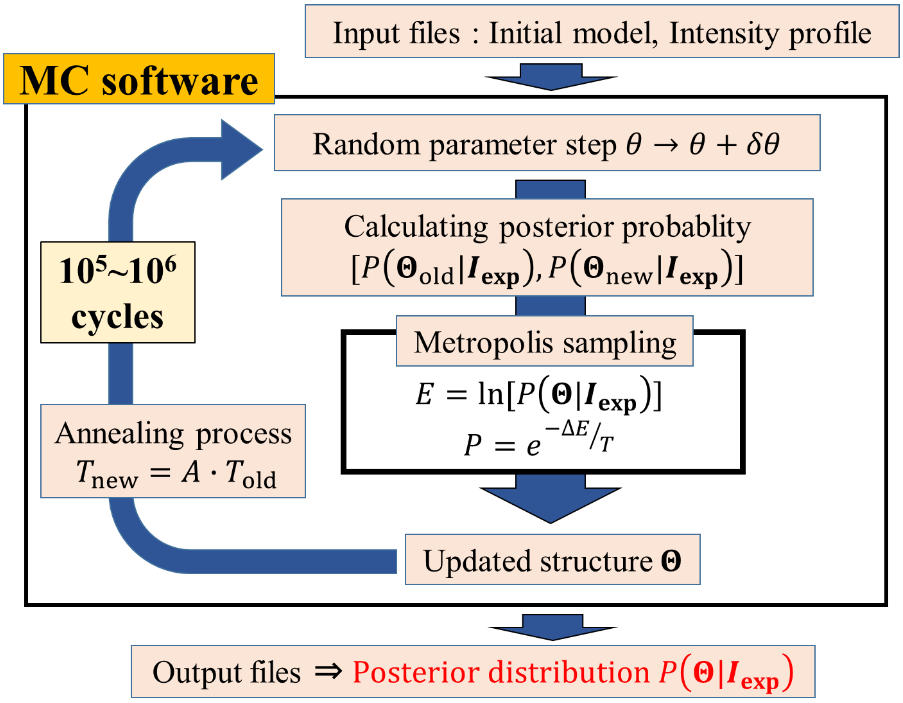

Figure 2.2: Analysis procedure of MC software

intensity profile calculated from a known structure. The simulation to the intensity from the known structure verify whether the known structure can be restored, then the performance of the software is expected to be verified.

Here, we consider (001)-oriented perovskite-type ultra-thin films represented in Fig. 1.1. The structural model is regarded as an alternating stack of AO and BO2 planes; the oxygen site in the AO plane is called the O1 site, and those in the BO2 plane are called O2 sites. In the present study, we refined the structure of a ten-unit-cell-thick region from the surface. Here, the structural model as follows. The in-plane structure is assumed to have no superstructure, and the a in-plane lattice parameter to be the same as that of substrate. Now we have only two parameters per site, that is, the atomic displacements along the surface normal direction from the ideal substrate lattice $\delta z(\alpha, n)$ and the occupancy $\mathrm{occ}(\beta, n)$, where α denotes A, B, O1 or O2, β denotes the element of each site (La and Sr occupy the A site, and Al and Ti occupy the B site in case of $\mathrm{LaAlO_3/SrTiO_3}$ thin film) and n denotes the layer index starting from the ideal substrate. Constraint conditions of $\sum_{\beta,n} \mathrm{occ}(\beta, n) = 1$ are assumed, except for n values close to the surface which suppose no defects and express the surface roughness. The isotropic atomic displacement parameter $B(\text{Å}^2)$ was defined as being common to all atoms within the film. The total number of independent parameters m depends on the constraints we use, and the typical value of m for the present study was 60. The structural parameters of the model are expressed as $\boldsymbol{\Theta} = (\theta_1, \theta_2, \ldots, \theta_m) = [\delta z(\mathrm{A}, 1), \delta z(\mathrm{B}, 1), \delta z(\mathrm{O1}, 1)$, $\delta z(\mathrm{O2}, 1), \ldots, \mathrm{occ}(\mathrm{A}, 1),\ \mathrm{occ}(\mathrm{B}, 1), \mathrm{occ}(\mathrm{O1}, 1), \mathrm{occ}(\mathrm{O2}, 1), \ldots]$. The software developed was applied to artificial CTR intensity profiles calculated from the reported structure parameters of a five-unit-cell-thick $\mathrm{LaAlO_3}$ film on a $\mathrm{TiO_2}$-terminated $\mathrm{SrTiO_3(001)}$ substrate [30]; we will refer to this structure as $E(\boldsymbol{\Theta})^{\mathrm{VM}}$. We define $I_{\mathrm{exp}}^{\mathrm{VM}}(\boldsymbol{Q}_{\mathrm{i}}) = |F(\boldsymbol{Q}_{\mathrm{i}}; \boldsymbol{\Theta}^{\mathrm{VM}})|^2 + I_{\mathrm{noise}}(\boldsymbol{Q}_{\mathrm{i}})$. Artificial noise $I_{\mathrm{noise}}(\boldsymbol{Q}_{\mathrm{i}})$ was introduced with a Gaussian distribution having a standard deviation of $\gamma^{\mathrm{VM}}|F(\boldsymbol{Q}_{\mathrm{i}}; \boldsymbol{\Theta}^{\mathrm{VM}})|^2$, where γ^{VM} was chosen to be 0.2. Hereafter, we call $I_{\mathrm{exp}}^{\mathrm{VM}}(\boldsymbol{Q}_{\mathrm{i}})$ the virtual measurement (VM) data. $I_{\mathrm{exp}}^{\mathrm{VM}}(\boldsymbol{Q}_{\mathrm{i}})$ are plotted in Fig. 2.3. The prepared VM data were 00, 01 and 11 rods. The total number of data points N was 575. Here, the correlation of data points was ignored, that is, the error autocorrelation $C_E(\mathrm{j})$ to i-th data is 0 for all data points.

The minimum value of the cost function $E(\boldsymbol{\Theta}^{\mathrm{VM}})$ was 6.84. The initial model made with a grid search provided $E(\boldsymbol{\Theta}) = 29.38$, which corresponds to $R = \sum |(|F_{\mathrm{exp}}| - |F_{\mathrm{calc}}|)| / \sum |F_{\mathrm{exp}}| = 0.354$, using the initial value of $\gamma = 0.15$. The initial values of the structural parameters are modeled by using the error functions $\mathrm{Erf}(x - x_c, s)$, where x_c and s are the peak position and the width of the corresponding Gaussian function. For example, the initial values of the c-lattice spacing $c+\delta z(\mathrm{A}, n+1)-\delta z(\mathrm{A}, n)$ are expressed as $c+\Delta c\ \mathrm{Erf}(n-n_{\mathrm{int}}, s_z)$, where c is the bulk substrate lattice parameter, Δc denotes the difference in the c-lattice spacing between the film and substrate, n_{int} denotes the nominal interface position, and s_z gives the sharpness of the interface. The depth profile of the initial distance $c+\delta z(\mathrm{A}, n+1)-\delta z(\mathrm{A}, n)$ is presented in Fig. 2.4(a), and the corresponding initial $\delta z(\mathrm{A}, n)$ profile is shown in panel (b) by the blue triangles. After that, all variable parameters $\mathbf{\Theta}$ were relaxed by the MC software. The MC calculation was divided into two stages by different temperature sequences. In the first temperature sequence, $\delta z(\mathrm{O1},\ n)$, $\mathrm{occ}(\mathrm{O1},\ n)$, $\delta z(\mathrm{O2},\ n)$ and $\mathrm{occ}(\mathrm{O2},\ n)$ were constrained to the corresponding values of metal ions on the same layer. The initial temperature was set to 0.5 to sample a wide parameter space. The second MC calculation with a different temperature sequence was applied to the model resulting from the first sequence by removing the constraints on $\delta z(\mathrm{O1},\ n)$ and $\delta z(\mathrm{O2},\ n)$, while the constraints on the occupancy for oxygen sites were maintained. The initial T_{MC} was set to 0.1 and decreased by 1 percent per 2000 steps. In total 2×10^6 calculation steps were performed for both stages of MC calculation.

The intensity profiles calculated from the resulting structure are shown in Fig. 2.3 as red curves. The structure model was improved to $E(\mathbf{\Theta}) = 7.25$ ($R = 0.04$), and the resulting γ was $0.215\pm\ 0.002$. The refined values of the structural parameters of the A site are presented in Fig. 2.4. Fig. 2.4(b) shows the depth dependence of $\delta z(\mathrm{A}, n)$. A positive displacement represents atomic movement towards the surface. Fig. 2.4(c) shows the depth dependence of $\mathrm{occ}(\beta, n)$. The average value of the standard deviation of $\delta z(\alpha, n)$ for each site (σ_z) is listed in Table 2.1. Here, the average is taken over the sites whose occupancy is larger than 0.5. A typical value of (σ_z) for metal sites is 0.01 Å and that for the oxygen sites is 0.04 Å. Standard deviations for the occupancy parameters at the interface ($\sigma_{\mathrm{occ}}^{\mathrm{int}}$) and at the surface ($\sigma_{\mathrm{occ}}^{\mathrm{surf}}$) are also listed in the same table. The typical precision of the metal occupancy is 3 %. The accuracy of the structure parameters is estimated from the differences between the resulting $\mathbf{\Theta}$ and $\mathbf{\Theta}^{\mathrm{VM}}$, which are plotted in Fig. 2.4(b) and 2.4(c). The difference for $\delta z(\alpha, n)$ was approximately the same as the magnitude of the error bar, and the typical difference for $\mathrm{occ}(\beta, n)$ was three times larger than the standard deviation estimated by this procedure. The quantitative similarity between the accuracy and the precision suggests that the amount of information provided by the CTR profiles is well estimated by the number of data points N in present case.

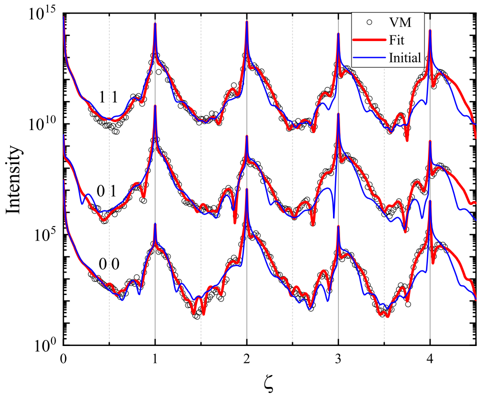

Figure 2.3: CTR scattering profile of Virtual measurement data(White plot), the calculation from initial model(blue solid curve) and Fitting(red solid curve).

2.4 Application on experimental data

2.4.1 n-type interface of $LaAlO_3$ thin films on $SrTiO_3$ substrate

The experimental data of $LaAlO_3/SrTiO_3$ along the 00, 01 and 11 rods with $N = 575$[30] were analyzed with our MC software. The initial value of S was determined in advance of the MC calculation by the steepest descent method using only the data near the Bragg peaks, where the CTR intensity is rather insensitive to the detail of the surface structure model. The initial values of the other structural parameters were the same as those used for the analysis made on the VM data. The initial systematic noise scale was chosen to be 0.15. The initial model made with the grid search provides the value of $E(\mathbf{\Theta}) = 42.54$ ($R = 0.391$). The analysis process for the MC sampling was the same as in the previous section of performance check for virtual measurement data, except for the refinement of the atomic displacement parameter B for the whole film.

Fig. 2.6 shows the experimentally observed CTR intensity profiles together with the calculated profiles from the resulting structure. The value of $E(\mathbf{\Theta})$ was reduced to 7.66 ($R = 0.110$). The MC refinement is proven to be robust enough for practical use of perovskite interfacial structure determination. Fig. 2.6(a) shows the depth dependence of $\delta z(\alpha, n)$. The main structural features reported in Ref. [30], namely the shift of the O atoms in

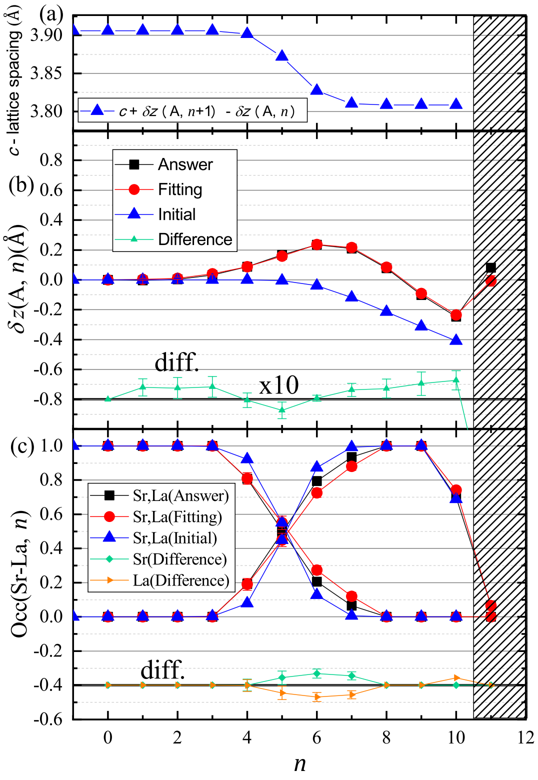

Figure 2.4: Depth dependence of structural parameters. (a)The initial values of c-lattice spacing. (b)Atomic displacement $\delta z(\mathrm{A}, n)$ and (c) occ(Sr-La, n) of answer, initial and refined(Fitting) structure of LAO/STO. The difference between answer and refined structure is also presented as green plots. The scale of difference is enhanced by ×10 for presentation.

$SrTiO_3$ towards the surface and the lattice expansion around the interface, are reproduced in this analysis. Fig. 2.6(b) shows the depth dependence of $\mathrm{occ}(\beta, n)$. Some amount of atomic interdiffusion at the interface is visible. The average values of the standard deviation of the structural parameters are listed in Table 2.1, where the average was taken over the sites where the occupancy was larger than 0.5. The precision of the parameters was similar to that in the VM analysis. The B value for the film region was found to be $1.16 \pm 0.08\text{Å}^2$, which is about three times larger than that of the substrate atoms. We also tried to refine the B parameters for each atom, and found that the B parameters were scattered from site to site discontinuously in depth direction, while the other parameters were nearly unchanged. This is because the effect of each B parameter on the cost function is too small to refine with the present data set. Lastly, we present the effect of the prior probability $P(\boldsymbol{\Theta})$. The thickness of the film in the refined structure can be defined as the total values of $\mathrm{occ}(\mathrm{La}, n)$ or $\mathrm{occ}(\mathrm{Al}, n)$, which are 4.91 ± 0.08 and 4.46 ± 0.12 in the results of the refinement presented in Fig. 2.6. By applying a Gaussian prior probability with an average value of 5.0 and a standard deviation of 0.1, we obtained thicknesses of 4.92 ± 0.07 and 4.74 ± 0.13 for the La and Ti sites with the cost of a slight increase in R value. The R values before and after the application of the prior probability were 0.110 and 0.111, respectively. One can define an arbitrary $P(\boldsymbol{\Theta})$, which will help us to find a physically reasonable model in a short time.

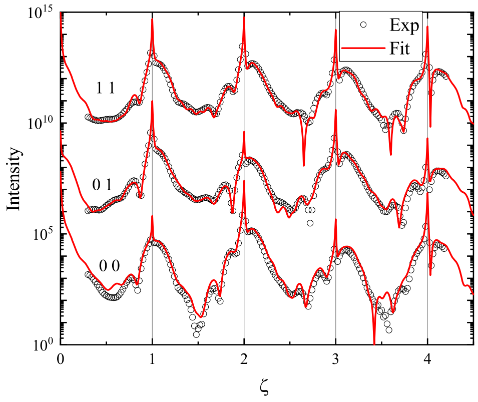

Figure 2.5: CTR scattering profiles of Experimental(white plots) and calculated(red solid curves) of LAO/STO.

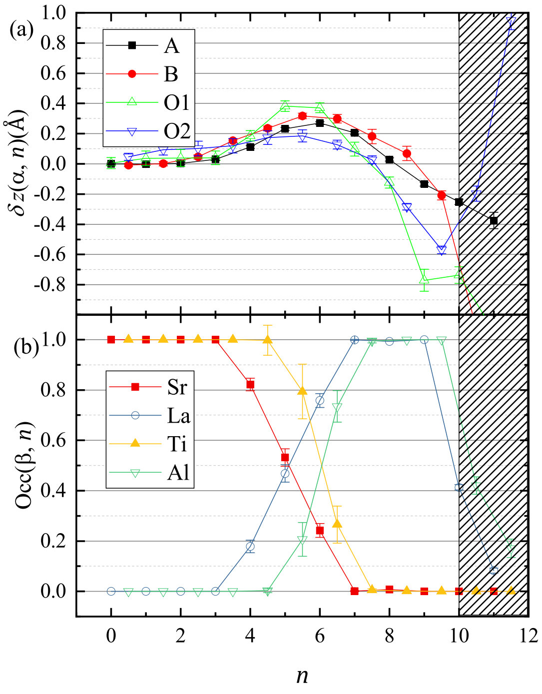

Figure 2.6: Refined structural parameters of LAO/STO. The refined value and uncertainty of (a)Atomic displacement $\delta z(\mathrm{A}, n)$ and (b) occ(Sr-La, n) are presented.

Table 2.1: The average value of the standard deviation of the structural parameters derived from VM and experimental data.

	VM			Experimental data		
Atom	σ_z(Å)	$\sigma_{\mathrm{occ}}^{\mathrm{int}}$	$\sigma_{\mathrm{occ}}^{\mathrm{surf}}$	σ_z(Å)	$\sigma_{\mathrm{occ}}^{\mathrm{int}}$	$\sigma_{\mathrm{occ}}^{\mathrm{surf}}$
A	0.006	0.031	0.005	0.009	0.023	0.010
B	0.016	0.071	0.031	0.022	0.036	0.026
O1	0.043			0.044		
O2	0.036			0.033		

2.4.2 Differential measurement analysis combined with Monte-Carlo and bootstrap method

The purpose of this section is to develop an expanded practical use of Bayesian inference technique to the 'differential measurement data'. In this study, we aimed to detect the structural change of the LAO/STO interface by using the difference data when an external electric field was applied to the interface.

2.4.3 Application for differential measurement data

The CTR measurement of used differential measurement data was performed by 4 circle X-ray diffractometer installed at Photon factory BL-4C by Mr. Fujii. The observed sample and schematic experimental condition in which V_{g} was applied is presented in Fig. 2.7. The value of positive and negative V_{g} is ±50V. The results of CTR measurement profiles under the voltage are shown in the middle panel.

To extract the significant dependence of the external voltage and exclude the systematic noise from data, the change ratio of the deference of CTR intensity (I^{ratio}) was calculated. I^{ratio} is given by

$$I^{\mathrm{ratio}}(\boldsymbol{Q}) = \frac{I^{+} - I^{-}}{I^{+} + I^{-}}, \tag{2.13}$$

where $I^{\pm}$ is the intensity under $V_{\mathrm{g}} = \pm 50\mathrm{V}$. I_{ratio} along 00ζ is also presented in Fig. 2.7. There are some points with significant signal change, for instance, those around $\zeta = 2.6$ and 4.2. Based on I^{ratio}, we aimed to extract the atomic displacement in the depth direction caused by electric field switching. The problem is how to define the '0V structure' ($\boldsymbol{\Theta}^{0}$) and intensity (I^{0}), the case without applying the electric field. Here, an important experimental result on the electric field dependence of CTR intensity is presented. Fig. 2.8 shows the V_{g} dependence of scattered intensity at $\boldsymbol{Q}$ = (0 0 4.15).

This result suggests that the scattering intensity changes symmetrically with respect to V_{g}, and that has hysteresis behavior. From this result, we determined to obtain the displacement $\boldsymbol{\Theta}^{0}$ under the following two assumptions:(1)The amount of change in intensity δI changes symmetrically with V_{g} ,(2)The atomic displacement δZ changes symmetrically with V_{g}. From

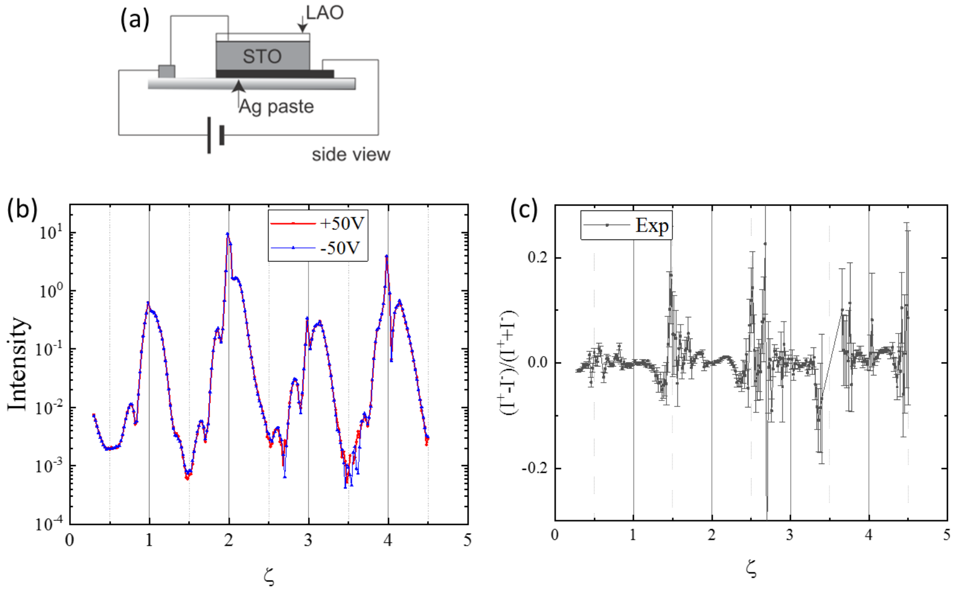

Figure 2.7: (a)LAO/STO sample on Au electrode connected with Al wire. ζ dependence of (b) CTR profile of 00L rods under ±50V and (c) I^{ratio}.

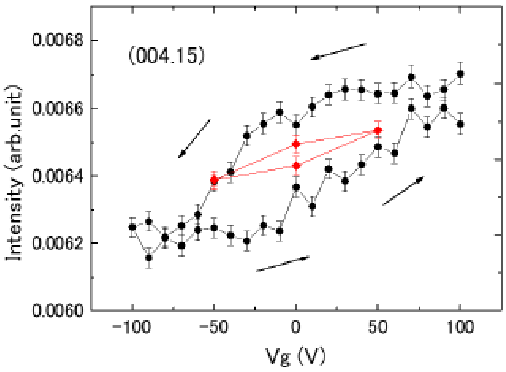

Figure 2.8: Hysteresis curve of scattering intensity at $\boldsymbol{Q}$ = (0 0 4.15)

these two assumptions, the following two equations hold:

$$\begin{aligned} I^{\pm} &= I_0 \pm \delta I, && (2.14) \\ Z^{\pm} &= Z_0 \pm \delta Z, && (2.15) \end{aligned}$$

where I_0 is calculated intensity obtained from 0V structure($V_{\mathrm{g}} = 0$) written as $\boldsymbol{Z}_0 \in \boldsymbol{\Theta}_0$. The δ represents the amount of change when assuming a symmetric change. The calculated value of change ratio $I^{\mathrm{ratio}}_{\mathrm{calc}}(\boldsymbol{Q})$ can be written as

$$\begin{aligned} I^{\mathrm{ratio}}_{\mathrm{calc}}(\boldsymbol{Q}, \boldsymbol{\Theta}) &= \frac{\delta I}{I_0} && (2.16) \\ &= \frac{I_0 - I^{-}_{\mathrm{calc}}}{I_0}. && (2.17) \end{aligned}$$

Then, $Z^{\pm}$ can be extracted from I^{-}_{calc} which reproduce the experimental value of $I^{\mathrm{ratio}}(I^{\mathrm{ratio}}_{\mathrm{exp}})$. Structural model of LAO/STO constructed in sec. 2.4 was utilized as the structure before applying V_{g}, that is, $\boldsymbol{Z}_0$ and intensity I_0. The posterior distribution $P(\boldsymbol{\Theta}|I^{\mathrm{ratio}}_{\mathrm{exp}})$ is assumed to be Gaussian distribution with the deviation σ written as

$$P(\boldsymbol{\Theta}|I^{\mathrm{ratio}}_{\mathrm{exp}}) = \frac{1}{(2\pi)^{\frac{1}{2}}} \frac{1}{\sigma(\boldsymbol{Q}_{\mathrm{i}})} \times \exp\left\{ -\frac{[I^{\mathrm{ratio}}_{\mathrm{exp}}(\boldsymbol{Q}_{\mathrm{i}}) - I^{\mathrm{ratio}}_{\mathrm{calc}}(\boldsymbol{Q}_{\mathrm{i}}; \boldsymbol{\Theta})]^2}{2[\sigma(\boldsymbol{Q}_{\mathrm{i}})]^2} \right\} \quad (2.18)$$

The standard deviation $\sigma(\boldsymbol{Q}_{\mathrm{i}})$ was determined by the law of propagation of statistical error $\sigma^{\pm}$ of $I^{\pm}$. Based on Bayes' theorem, the atomic displacement δZ from one sample of $\boldsymbol{Z}_0$ using an equation (2.18). However, one extracted $\boldsymbol{Z}_0$ also has a distribution that reflects the errors of the surface x-ray diffraction experiment. As a result of Bayesian inference method, the accuracy of atomic arrangement extracted from CTR data is $\sim 10^{-2}$Å. This distribution of Z_0 was extracted from the experimental data with approximately 20 % systematic error. Obtained $P(\boldsymbol{\delta} Z|\boldsymbol{I}^{\mathrm{ratio}}_{\mathrm{exp}})$ from one sample of $P(\boldsymbol{\Theta}|\boldsymbol{I}_{\mathrm{exp}})$ does not reflect the error of $\boldsymbol{Z}_0$. More realistic $P(\boldsymbol{\delta} Z|\boldsymbol{I}^{\mathrm{ratio}}_{\mathrm{exp}})$ can be inferred from a lot of experimental data set of I_0. However, since it takes several days to acquire a series of CTR data of one sample, to accumulate statistics of experimental data is not realistic way.

Here, we demonstrated the nonparametric bootstrap from artificial $\boldsymbol{I}_0$ data distribution. First, artificial $\boldsymbol{I}_0$ data distribution, that is, 128 samples of $\boldsymbol{I}_0$ were extracted from random sampling of $P(I_0^{\mathrm{exp}}|Z_0)$. Then, MC calculations for 128 of extracted I_0^{exp} based on Bayesian inference were performed with posterior distribution given by Eq. 2.18. The atomic displacement

$\delta Z(M,N)$ was calculated by $|Z_0^M - Z^{-(M,N)}|$, where M (0 to 127) is the index of 128 of Z_0^M models and N is that of refined models(here, $N = 128$) inferred by Eq. 2.18.

Results

Fig. 2.9 shows the fitting results of $I^{\mathrm{ratio}}(\boldsymbol{Q})$ of 00ζ and 01ζ for $Z_0^{M=0}$. Results of refinement for other 127 Z_0^M were obtained with approximately same quality.

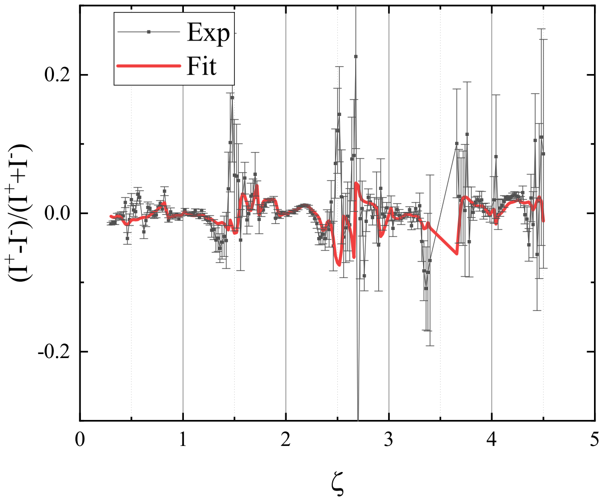

Figure 2.9: An example of one sample of fitting result of intensity ratio of 00ζ and 01ζ rod for one 0V model.

The depth dependence of $\delta Z^{(M,N)}(\alpha,n)$ when the electric field is switched from 50 V to -50 V are presented in Fig. 2.4.3. 1000 answers are randomly selected from $M \times N$ samples for plots. The averaged standard deviation of $\delta Z^{(M,N)}(\mathrm{Sr/La},n)$ and $\delta Z^{(M,N)}(\mathrm{Ti/Al},n)$ is 5.7×10^{-4}Å and 2.9×10^{-3}Å. The accuracy of $z(\alpha,n)$ was improved by 10 to 100 times by differential measurement analysis compared to the analysis for general CTR data in sec. 2.4. Only La atoms were found to displace, which suggests that the polarization caused by the negative V_g induces internal electric field mainly in LAO. This result is surprising because the electric field was applied between the LAO/STO interface and the back gate. The induced electric field in only LAO region suggests the screening effect of V_g by metallic interface in STO side. Vacancies at the interface or adsorbed matter on the surface may be one reason to modulate the polarization between interface and top of LAO. The direction of La displacement is also surprising. This maybe corresponds to the difference of potential between the vacuum level at the surface and increased potential at the LAO/STO interface under the negative gate voltage. For elements with small atomic numbers such as Al and oxygen, the polarization could not be large enough to be detected due to the analytical uncertainty. Hence, local electric field in each layer cannot be evaluated from the data under the experimental condition at PF BL-4C.

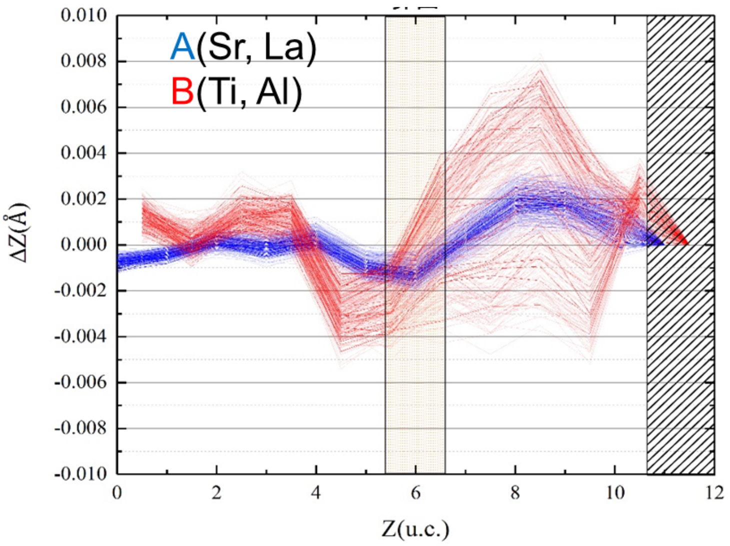

Figure 2.10: Depth dependence of atomic displacement δZ of 1000 models of $M \times N$ when the gate voltage is switched from +50 to -50 V. δZ is drawn by blue(Sr, La) and red(Ti, Al) solid curves. Z = 6 is the interface position.

We can demonstrate a quantitative observation method of surface displacement with higher precision by applying the combined analysis technique of Bayes inference and bootstrap idea to differential measurement of surface X-ray diffraction data. The precision of the atomic displacement was 10^{-3}Å, indicating the possibility of more precise quantitative observation of microscopic displacement at the surface/interface. Local electric field in each layer of LAO/STO cannot be evaluated from the data under the experimental condition in PF BL-4C. By using a strong light source superior in statistical accuracy, even more detailed analysis of polarization structures is expected.

2.5 Summary of this chapter

CTR scattering method has not be generally utilized for the analysis of interface although its versatility for the sample, non-contact measurement and high spatial resolution because of absence of the user-friendly analysis technique. We have developed MC analysis software for the CTR scattering based on Bayes' theorem. Our developed software searches the global minimum value of the cost function by simulated annealing or replica MC sampling method. The performance of the software was demonstrated by using a five-unit-cell-thick $LaAlO_3$ ultrathin film on an $SrTiO_3$ substrate as an example. The precision of the structural parameters estimated from the VM data analysis was ±0.01 and ±0.04 Å for the displacement of metal and O atoms, and that for the occupancy was ±0.03. The accuracy of the structural parameters was also examined, and it was found that the accuracy was similar to the precision. Experimental data were successfully analyzed by the same procedure. Excluding the data handling and appropriate model construction, the analysis time was reduced to just within a few days although it took more than one year so far. The Bayesian inference method can be applied if the experimental data or figure of merits can be formulated as a probability distribution. Final section of this chapter shows that it can also be applied to differential measurement CTR data. The expected precision of atomic position is improved by 10 times in case of the experimental condition at PF BL-4C.

Chapter 3

Structural study of thickness driven metal-insulator films of $LaNiO_3$

3.1 Introduction

Complex electronic phases are expected at the interface of transition metal oxides because of the correlation of the spin, charge, and orbital degree of freedom as mentioned in chapter 1. Among them, Ni perovskite oxide has been investigated as one of the candidates for superconductivity analogous to cuprate oxide with 2 dimensional $S = 1/2$ antiferromagnetic correlation by epitaxial strain of superlattice[65]. However, superconductivity originating from tensile strain was missing, and instead the two-dimensional electronic state exhibited a metal-insulator transition(MIT) in metallic $LaNiO_3$(LNO) experimentally. According to the behavior of electrical conductivity, the different mechanism of MIT from the charge disproportionation with the first order transition developed in $R\mathrm{NiO}_3$.

Here, we focus on the 2 dimensional LNO thin films on two different substrates, both of which reveal the thickness dependence of MIT. We examined the thickness dependence of the structure of LNO by using CTR data. Then the origin of reported thickness induced MIT transition in $LaNiO_3$ thin film under the compressive and tensile strain from $LaAlO_3$(LAO) and $SrTiO_3$(STO) substrate are discussed from the structural point of view.

3.1.1 Known properties of LaNiO$_3$ in the bulk form

The RNiO$_3$ (R: rare-earth ion) is an archetypal strongly correlated d-electron system in the charge transfer regime [65, 66]. The 3d spin configuration of ionic limit of Ni in RNiO$_3$ (Ni^{3+}) is $t_{2g}^6 e_g^2$. As a model incorporating the electron-electron interaction, Mott-Hubbard model is widely used for localized materials even in a system with partially occupied levels. The Hamiltonian is given by $H = \sum_{\langle i,j \rangle,\sigma} t_{ij} c_{i\sigma}^{\dagger} c_{j\sigma} + U \sum_i n_{i\uparrow} n_{i\downarrow}$, where $\langle i,j \rangle$ the index of a site, σ is spin. t_{ij} is the transfer integral between $i - j$ sites and $c^{\dagger}, c$ are the creation-annihilation operator. The d band splits by the on-site Coulomb interaction strength and give rise to the Mott type gap with valence band (= LHB:abbreviation for lower Hubbard band) and a conduction band (= UHB:upper Hubbard band). According to the model, RNiO$_3$ materials are charge transfer type insulator due to the competition between the bandwidth (W), on-site electron-electron correlations (U), crystal structure and charge transfer energy between oxygen and transition metal sites (Δ) as shown in Fig. 3.1 [67].

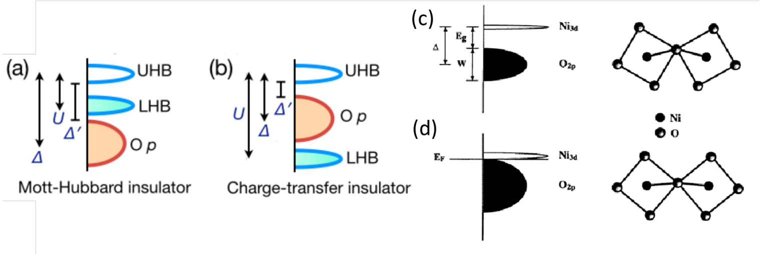

Figure 3.1: Schematic band diagram of Mott-Hubbard model for (a)Mott-Hubbard insulator, (b)Charge-transfer insulator [67], (c)RNiO$_3$ and (d) LaNiO$_3$[68]

The transfer of e_g itinerant electrons between the B-site atom through the ligand oxygen is responsible for conductivity. Therefore, the conductivity of RNiO$_3$ mainly depends on the degree of hybridization of Ni$_{3d}$ and O$_{2p}$ band. Fig. 3.2 shows the Zaanen-Sawatzky-Allen diagram. They calculated the ground state of RNiO$_3$ as a function of the energy gap between UHB and O$_{2p}$ band Δ' ($=U - \Delta$). Such a phase transition of conductivity is correlated with the structural phase and bonding nature of Ni-O. Fig. 3.3 shows the structural, magnetic, and electronic properties of RNiO$_3$ perovskites organized in [68]. Almost all member whose radius is smaller than La(in other words, the tolerance factor become smaller than LaNiO$_3$) show a first order MIT. MIT is accompanied with structural transition from $Pbnm$ orthorom-

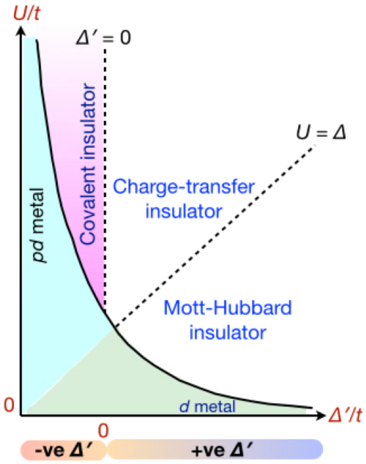

Figure 3.2: Zaanen Sawatzky-Allen diagram of $R\mathrm{NiO}_3$. U, Δ and Δ' are Coulomb interaction, charge transfer energy, and energy gap between Upper Habbard band and O_{2p} band. [67]

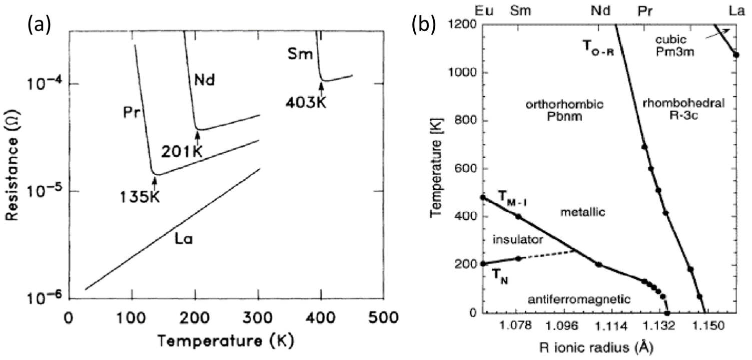

Figure 3.3: (a)Resistivity and (b)phase diagram of $R\mathrm{NiO}_3$ [68]

bic to $P2_1/n$ monoclinic structure confirmed by X-ray diffraction results shown in Fig. 3.4. When one or two of the number of holes contained in the ligand oxygen of Ni ion is expressed as $\underline{L}, \underline{L}^2, \ldots$, the electronic state of Ni ion is separated to two crystallography independent Ni sites. The change of valence state can be written as $2\mathrm{Ni}^{2+}\underline{L} \to \mathrm{Ni}^{2+} + \mathrm{Ni}^{2+}\underline{L}^2$ below the phase transition temperature. This phenomenon is called charge disproportionation[69] which derives Ni magnetic moment coupling via anti-ferromagnetic interaction property. The bulk LNO belongs to a different space group as rhombohedral $R\bar{3}c$ structure. The pseudo cubic lattice parameter a_{pc} is 3.84 Å, and its Glazer notation is $a^-a^-a^-$ pattern($\alpha = \beta = \gamma = 5.2°$). The smaller rotation angle and shorter bond length than other RNiO$_3$ materials bring the wider bandwidth. This is the source of the hybridization of very closed energy level of Ni$_{3d}$ and O$_{2p}$ band. As a result, LNO remains metallic down to the low temperature without any structural transition. The metallic state corresponds to a increase in the bandwidth due to the increase in hybrid of Ni$_{3d}$-O$_{2p}$ with a change in the Ni-O-Ni bond angle from 144° for LuNiO$_3$ to 164° for LaNiO$_3$[68]. In the Zaanen Sawatzky-Allen diagram, LaNiO$_3$ is located in the pd metal region because such a large hybridization enhance the transfer t and minimize the effective charge transfer Δ' to zero.

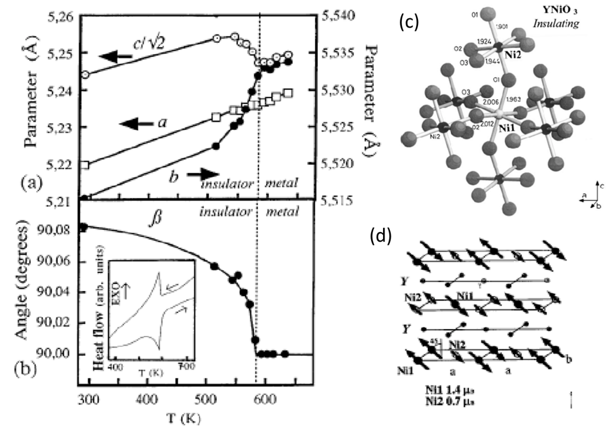

Figure 3.4: Temperature dependence of structural parameters of RNiO$_3$. The sudden change of (a)bond length, (b)Ni sites, (c) Schematic structure of insulating phase of YNiO$_3$ and (d) magnetic structure by charge disproportionation($2\mathrm{Ni}^{3+} \to \mathrm{Ni}^{2+} + \mathrm{Ni}^{4+}$) [69].

Zaanen-Sawatzky-Allen diagram for Ni oxides also argued another possibility of MIT in charge transfer type materials with negative Δ' value, called Covalent insulator. The strong electron negativity of Ni often dominant strong contribution of covalency state of $3d^8\underline{L}$ ($\mathrm{Ni^{2+}O^{-}}$) with shorter Ni-O bonds. This bonds can be regarded as the covalent bonding which splits to the bonding and anti bonding level and open the gap in case of increased t enhanced the mixture between d bands and O_{2p} bands. The phase diagram of bond length and M-O-M angle vs its chemical bonding nature is reported by J-S. Zhou and J.B. Goodenough[70]. Thus, a more realistic ground state, which includes the NiO hybridization of these nickelates can be described as a mixture of the Mott limit $3d^7 2p^6$ ($\mathrm{Ni^{3+}O^{2-}}$) and the covalent limit $3d^8\underline{L}$ ($\mathrm{Ni^{2+}O^{-}}$) configurations.

3.1.2 Metal-Insurator transition of $\mathrm{LaNiO_3}$ urtrathin films

Increasing U or Δ are obviously important for conductivity of LNO. The ground state can be altered with structural manipulation through the size effect, dimensionality, strain from the substrate, and ochtahedral rotation by the forming an epitaxial film. Under the compressive(LAO substrate, $a_{pc} = 3.79$ Å) and tensile(STO substrate, $a_{pc} = 3.905$ Å) strain, the energy split of degenerate e_g band(d_{x-y^2} and $3z^2-r^2$) by Jahn-Teller(JT) effect is expected. The conventional quantification of strain $\epsilon = (a_{\mathrm{film}} - a_{\mathrm{sub}})/a_{\mathrm{film}}$, where the a_{film} and a_{sub} are the lattice constants of film and substrate materials, is negative(positive) for LAO(STO) case. The orbital polarization for both case was observed by some X-ray linear dichroism experiments(XLD). The results indicate the 5 to 7%(0%) higher occupation of $d_{3z^2-r^2}(d_{x^2-y^2})$ in case of LAO(STO) substrate[66, 71, 72, 73], suggesting the asymmetric JT active characterization to epitaxial strain of $R\mathrm{NiO_3}$ system. Indeed many studies have shown that $\mathrm{LaNiO_3}$ (LNO) films behave as a paramagnetic metal like their bulk counterpart when they are thick enough more than 4 u.c thick of LNO. However, it experiences the thickness driven MIT when the thickness is less than 3 u.c under both epitaxial strain type. Let us refer some previous reports about thickness dependence of MIT in LNO films. Fig. 3.5(a) and (b) shows the thickness dependence of resistivity under tensile(STO) and compressive(LAO) strain[74, 75]. The conductivity gradually cease with the decreasing the thickness. The thickness dependence of Angle-resolved photoemission spectroscopy(ARPES) shown in Fig. 3.6 also suggest the insulating behavior in thin LNO from the results in lack of the DOS at E_F[76]. The photoemission spectra of LNO grown on Nb-doped STO and LAO [74, 75] are presented in Fig. 3.5(b) and (c), respectively. As expected from the conductivity of these samples, the density of states around the Fermi energy E_F disappear when the thickness of LNO film is less than 3 u.c.. The notable difference of both substrate was the thickness dependence

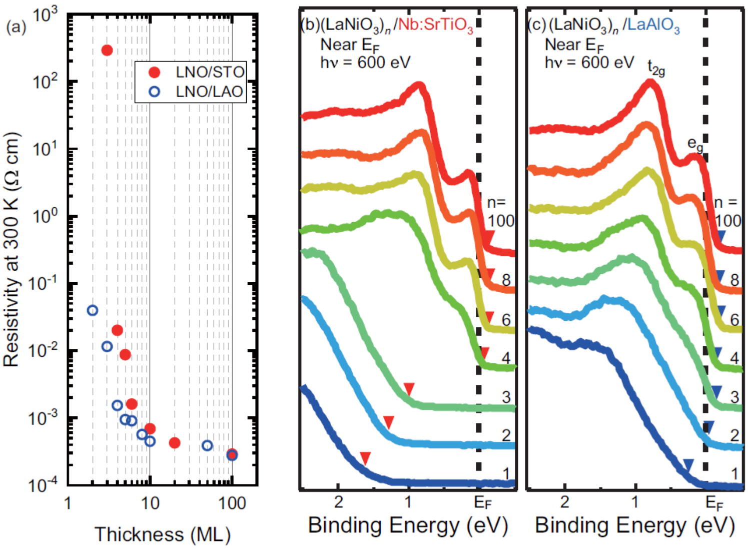

Figure 3.5: Thickness dependence of (a)LNO/STO and LNO/LAO resistivity at 300K, (b)DOS of LNO/STO and(c) DOS of LNO/LAO [74, 75]

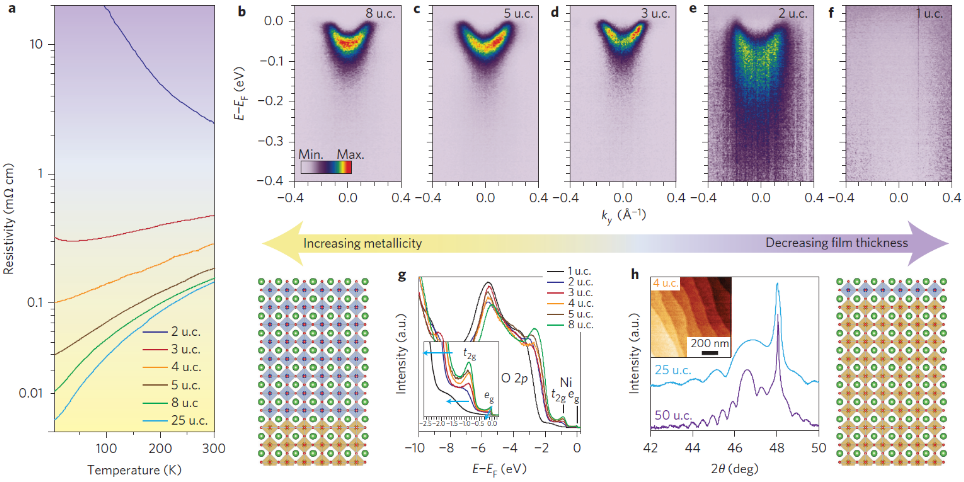

Figure 3.6: Thickness dependence of (a)Temperature vs Resistivity and (b-f) ARPES for LNO/LAO. (g)DOS and energy shift of t$_{2g}$ level(inset) observed by PES. (h)X-ray diffraction and AFM(inset) data of LNO/LAO[76].

of the leading edge of the valence-band spectra of LNO grown on STO and LAO. The sample grown on STO shows a large jump in its density of states when the fourth LNO layer is grown, while the change in the density of states of the LNO films on LAO appears to be much more gradual.

Many possible mechanisms for the thickness-dependent MIT of LNO thin films have been proposed for both epitaxial type. Here we show some previous research proposing the insulation mechanism for LNO film on two different substrates.

3.1.3 Previous studies of MIT for LNO/STO

In case of LNO(4 u.c)/STO(3 u.c) superlattice sample, the insulating layer of LNO is located in only $\sim$ 2 u.c from STO according to the depth resolved studies of electronic structure[77]. In Ref.[77], the valence band measured by X-ray photoemission spectra(XPS) confirms the existence of the gap and another unexpected DOS peak observed just below the Ferml level. Incident angle dependence of XPS from the La 4d core level suggests that the another peak is not originated from the entire LNO but from LNO/STO interface. This results infer the existence of the insulating 'dead layer' located in narrow region in LNO from LNO/STO interface.

The increase of binding energy for Ni e_g and t_{2g} [77] is consistent with the idea of polarity-driven oxygen vacancy [78]. A notable feature of LNO/STO is the discontinuity of polarity as discussed in LAO/STO interface[15]. Fig. 3.7 shows the schematic illustration of LNO layers on STO. The polarity sequence from STO of $(SrO)^0$-$(TiO_2)^0$-$(LaO)^{+1}$-$(NiO_2)^{-1}$-$(LaO)^{+1}$-$(NiO_2)^{-1}$-,$\cdots$, develops the electrostatic potential to the surface, and redistribute the charge to avoid strong potential. The observed depth dependence of c-lattice spacing and thickness dependence of formation energy of deoxidised $LaNiO_{2.5}$ suggests oxygen defects are formed in early stage of LNO fabrication below 3 u.c[78]. It suppress the electrostatic potential developed by polar discontinuity. When the film thickness reaches 4 u.c. thick, the metallic layer of $LaNiO_3$ is recovered as proceeding the film growth because of the increase in formation energy of $LaNiO_{2.5}$. The Ni^{3+}/Ni^{2+} ratio dependence of conductivity of $LaNiO_{3-\delta}$ films was investigated by ARPES[79]. The (a)binding energy, (b)electric resistivity, and (c)Ni^{3+}/Ni^{2+} ratio dependence of schematic diagram of Ni-d and O-2p bands are shown in Fig. 3.8. The underdeoxides LNO-1 with the strong Ni^{2+} nature exhibits the much stronger "A" peak assigned to Ni^{2+} in XPS data and insulating behavior. The oxygen vacancy dependent transport mechanism can be explained by the narrowed band widths because the larger Ni^{2+} enlarges the Ni-O bond

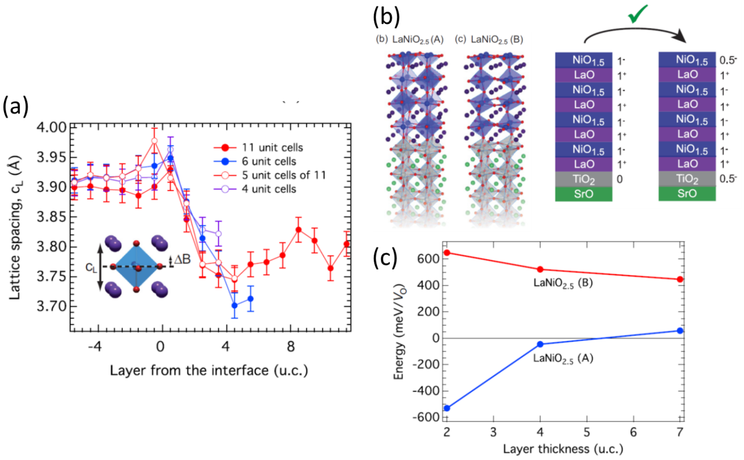

Figure 3.7: (a) Depth dependence of c-lattice spacing of LNO/STO observed by CTR method. (b)polar discontinuity at LNO/STO interface (c)Formation energy for $LaNiO_{2.5}$ relative to $LaNiO_3$ on STO substrate[78].

length and weaken the hybridization of Ni-3d and O-2p bands.

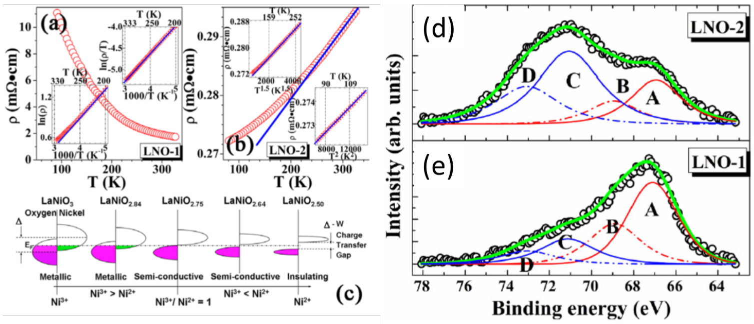

Figure 3.8: (a-b)resistivity, (c)schematic band diagram (d-e) XPS data for O defected $LaNiO_{3-\delta}$ [79]. The value of δ is 0.36 for LNO-1 and 0.16 for LNO-2

3.1.4 Previous studies of MIT for LNO/LAO

LAO and LNO are both polar materials and the polarity at the interface is continuous. Therefore, polar catastrophe is not expected for LNO/LAO. The tilt angle γ of NiO_6 along c is very close to 180°[80] so that the sheet resistance is not affected by the tilt angle in compressive strained LNO.

The MIT of LNO/LAO has been rationalized based on the dimensionality of carrier conduction. The qualitative explanation of dimension crossover given in [81] is as follows. Al on the substrate does not have *d*-electrons and its electronegativity is smaller than that of Ni. Therefore, the electronic state becomes two-dimensional at the interface. Also, on the surface, the number of Ni is small due to the effects of atomic defects and the reconstruction of the polar LNO surface. Therefore, the electronic state of the surface of LNO becomes two-dimensional like the LNO/LAO interface. By reducing the film thickness, the influence of the surface/interface increases, the electronic state changes from three-dimensional to two-dimensional. This picture of carrier localization is regarded as the quantum confinement. From the simple kinematic conductivity theory, when the value of the products of Fermi wave number k_F and the mean free path l become close to unity, MIT is expected in the system. In the two dimensional system, the sheet resistance(R_{sheet}) is in inverse proportion to $k_F l$ and finally approaches to the $h/e^2 \sim 25\text{k}\Omega$ upon the limit of the reduction of LNO thickness according to the kinematic theory of 2D electron gas[82]. R. Scherwitzl points out the temperature dependence of sheet resistance follow the Variable range hopping (VRH) type of conduction[83] written as $\sigma = C\exp[-(T_0/T)^{\alpha}]$, where T_0 is the factor determined on the DOS near the Fermi level[84] and the $\alpha = \frac{1}{d+1}$ is the dimension factor. The temperature dependence of various thickness of LNO films on LAO is presented in Fig. 3.9[75, 83]. The resistivity over 100 layers is proportional to T^2 at low temperatures, similar to the Fermi-liquid behavior of electron-electron scattering confirmed in bulk LNO. The temperature dependence of logarithm of conductance changes gradually to $T^{-1/4}$(VRH model) with decreasing the thickness. This gradual change from the metal state to the insulating state corresponds to the gradual gap opening confirmed by photoelectron spectroscopy shown in Fig. 3.5. In this way, LNO/LAO insulation does not occur abruptly with a certain film thickness as a threshold value. This phenomenon is different from charge disproportionation, which causes rapid temperature driven MIT.

3.1.5 Known structural information of $LaNiO_3$ films

Here we summarize the known structural information of LNO thick films. For the LNO films on STO, the NiO_6 octahedra tilt from the c direction (the surface normal direction), whereas octahedral rotation within the *c* plane was observed for the LNO films on LAO [80]. The *c*-lattice parameter of LNO on STO is 3.801 ± 0.006Å [80, 85] and that on LAO is 3.901 ± 0.006 Å [75, 80]. The *c*-lattice parameter of LNO on STO was increased by 0.05 Å

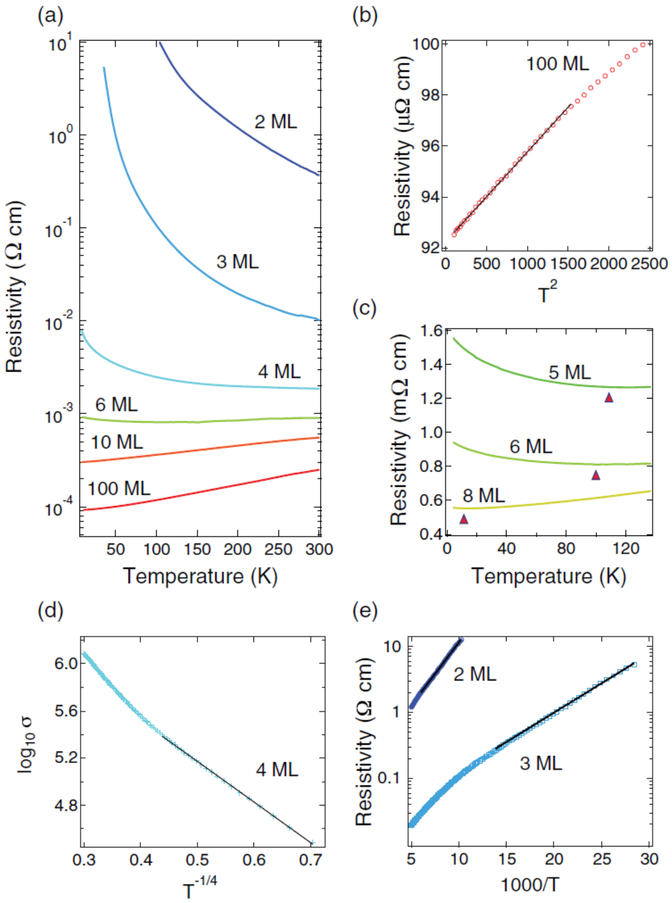

Figure 3.9: Temperature dependence of (a)resistivity various thickness of LNO/LAO. VRH type conductivity. The high temperature region of resistivity is proportional to T^2. (c) The temperature of transition from T^2 to VRH type hopping is shifted to high value with decreasing the thickness. (d)Conductivity of 4 ML sample clearly shows VRH type tendency as $\log(\sigma) \propto T^{-1/4}$. (e)2 and 3 ML sample shows Arrhenius-type temperature dependence of resistivity.[75]

when the oxygen partial pressure during film growth was decreased from 0.2 to 0.02 mbar [80], which is a result of the introduction of oxygen vacancies. As for the known structural information of LNO ultrathin films, there have been several reports on samples grown by molecular beam epitaxy (MBE) [73, 86, 87]. Local polarization estimated by relative displacement of oxygen and metal sites was reported for an LNO film with a thickness of 4 u.c. [73]. Cation displacement from the oxygen layer by ~0.1 Å was found to occur only a few u.c. from the surface, in accordance with their theoretical calculation.

The BO_6 octahedral connectivity and rotation modes also affect the physical property of LNO thin films. The stable rotation modes are mainly controlled by the structural coupling with the substrate.

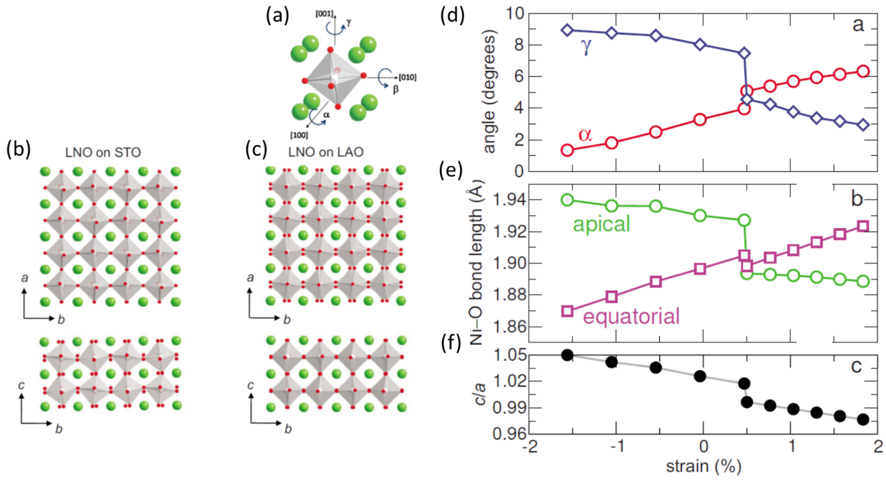

Figure 3.10: NiO_6 octahedral rotation α, β and tilt γ angle observed by X-ray diffraction under epitaxial strain. (a)Definition of α, β, γ angle. (b-c)Schematic pictures of NiO_6 rotation mode of LNO/STO and LNO/LAO. (d)The values of α, β, γ, (e)Ni-O bond length, and (f)the value of c/a ratio as a function of strain. The positive value of strain corresponds to the tensile strain.[80]

The reduced out-of-plane Ni-O-Ni angle θ from 180° narrows the bandwidth. The transfer integral is proportional to the product of square of Slater-Coster parameter($pd\sigma$) and $\cos(\theta)$. The inverse of the sheet resistance ($1/R_S$) of superlattice as a function of the periods of the LNO and STO layer was reported in Ref.[88]. The samples with shorter period presents strong localization character. The out-of-plane θ angle is reduced to 162° for individual single layered LNO for $n = 1$, while that in the inner layer of thick LNO has increased to 172°. Such enhanced rotation by tensile strain give a possibility of insulating character of Ni-O bonds disproportionation state in $R\mathrm{NiO}_3$. DFT calculations for LNO/STO with the experimentally determined lattice constants predicts the existence of the NiO_6 octahedral rotations accommodated by breathing mode distortions that causes the two different short and long Ni-O bonds[71].

The bulk LAO surface maintains charge integrity by reconstruction of the surface structure instead of causing polar catastrophe[89]. When a polar LNO film is fabricated on an LAO substrate having such reconstructed surface, the LAO structure returns to bulk and the LNO surface structure is reconstructed. Thus, surface structure of LNO is easily changed by the influence of the local electric field. The termination effect of local electric field in LNO is studied for LaO-terminated 3 and 4 u.c. LNO films and an NiO_2-terminated 3.5 u.c. LNO film deposited on top of an LAO (001) surface Ref[86]. Fig. 3.11 shows the temperature dependence of sheet resistance for the NiO_2 and LaO terminated LNO sample. The sample with LaO termination surface has low resistivity, whereas the sample with NiO_2 termination surface has high resistivity which showed local polarization as deep as 10 Å from the surface. This difference is considered to be caused by the influence of the local electric field generated by polar LNO. The schematic surface structure and relative distance of oxygen to A site and B site determined by X-ray diffraction and of different terminated sample are shown in Fig. 3.11.

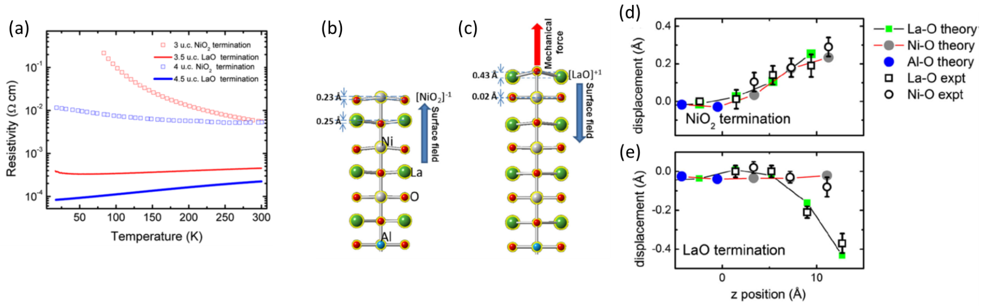

Figure 3.11: (a)Resistivity of different terminated LNO/LAO samples. Surface mechanical force of (b)NiO_2 and (c)LaO -terminated LNO/LAO. Atomic displacement in (d)NiO_2 and (e)LAO -terminated sample[86]. Positive displacement indicates the cation movement towards the surface compared to the oxygen in the same layer.

In case of NiO_2 terminated one, the oxygen has a displacement in the depth direction to the bulk side while that of LaO terminated one is displaced to the surface side affected by the local electric field. In the absence of apical oxygen, LNO cannot negate the effect of the local electric field which enhances polarization to reduce the Ni-O-Ni bond angle remains in the LNO region. D. P. Kumah also reported that this surface polar distortion effect can be restrained by LAO capping layer to supply apical oxygen[87]. The insulating 3 u.c thick LNO on LAO is turned out to be metallic by introducing the apical oxygen onto the top of NiO_2 from capping LAO. The Ni-O-Ni bond angle, which is related to the transfer integral, was strongly affected by the cap layer.

3.2 Motivation

As described above, the view on the insulation mechanism of the LNO film is not unified. To obtain a better understanding of this difference, experimental observation from a different viewpoint is needed. For example, the large amount of oxygen vacancies could enlarge the cation distance due to Coulomb repulsion. The enhancement of BO_6 tilt angle could shorten the c-lattice spacing. In this section, the detailed structures of LNO films on STO and LAO substrate are studied as a function of thickness(1 to 5 u.c. thick), then two different mechanism of MIT is studied from structural information of thickness and substrate dependence of LNO thin films. Structural information provides direct knowledge of the chemical perturbation or spatial coherency of electronic states.

3.3 Experiments and analysis

3.3.1 Experimental conditions

LNO thin films with a thickness of n u.c. were prepared by prof. H. Kumigashira(Tohoku Univ. and KEK), Dr. M. Kitamura(KEK) and Dr. E. Sakai(The Univ. of Tokyo, KEK). LNO thin films were grown on atomically flat (001) surfaces of Nb:STO(n = 2 to 5) and LAO (n = 1 to 5) by pulsed laser deposition (PLD); we denote these samples as $(LNO)_n/STO$ and $(LNO)_n/LAO$, respectively. During deposition, the substrate temperature was maintained at 450 °C under an oxygen pressure of 10^{-3} torr. The film thickness was precisely controlled on the atomic scale by monitoring the intensity oscillation of reflection high-energy electron diffraction. The films were subsequently annealed at 400 °C for 45 min under oxygen at atmospheric pressure to fill the residual oxygen vacancies. The LNO/STO samples were prepared just before the synchrotron measurements because storage at room temperature induces oxygen-vacancy formation [90]. No such sample degradation was found for the LNO/LAO samples.

The transport properties of the LNO films presented in Fig. 3.5 were also measured by our collaborators using the four-probe technique. Non-doped STO substrates were used for these measurements. Temperature dependence of the resistivity of $(\mathrm{LNO})_n/\mathrm{STO}$ for $n < 4$ is similar to the reported ones [78]. That for $(\mathrm{LNO})_n/\mathrm{LAO}$ has already been reported in Ref.[75]. The photo emission spectra presented in Fig. 3.22 were measured in-situ at BL-2C of the Photon Factory, KEK, Japan[75].

The CTR scattering measurements were performed with the four-circle diffractometers installed at BL-3A and BL-4C at the Photon Factory, KEK, Japan and BL15XU of SPring-8, Japan. The X-ray energy was 12.0 or 12.4 keV, which are both nonresonant conditions. The typical beam size was 0.5 × 0.5 mm. The scattering intensity from LNO/LAO samples was detected by a two-dimensional pixel array detector XPAD-S70 (imXpad), and that from LNO/STO samples was detected by an ordinary point detector by Mr. Maeda, an old member of Kimura laboratory. During the measurements, the samples were kept in a vacuum chamber at 10^{-5} torr or Kapton dome filled with He gas to avoid possible radiation damage. Illumination area and Lorentz factor corrections were applied following the formula provided in Ref.[31]. For all samples except for $(\mathrm{LNO})_4/\mathrm{STO}$, the 00, 01, 02, 11, and 12 rods were measured up to at least $\zeta = 4.0$. The data for the 11 and 12 rods were missing for $(\mathrm{LNO})_4/\mathrm{STO}$. Structure refinement and estimation of the standard deviations of parameters were performed using the Bayesian inference technique described in chapter 2. The prior probability of atomic occupancy for all n u.c. sample was introduced by infinite square well potential as the variance range to prevent them from falling into physically inappropriate value. In this study, in-plane atomic displacement was neglected; i.e., only the occupancy parameters and out-of-plane atomic positions were refined. Atomic displacement parameters B were also refined here. B parameters of each layers are common for all elements of eazh layers.

3.3.2 Analysis and results

LNO/STO

CTR scattering data along the $hk\zeta$ rod measured for the LNO films on STO substrates are presented in Fig. 3.12. The solid curves in Fig. 3.12 show the calculated intensity derived from the refined structure. The typical value of $R = \sum |(|F_{\mathrm{exp}}| - |F_{\mathrm{calc}}|)| / \sum |F_{\mathrm{exp}}|$ is 0.2.

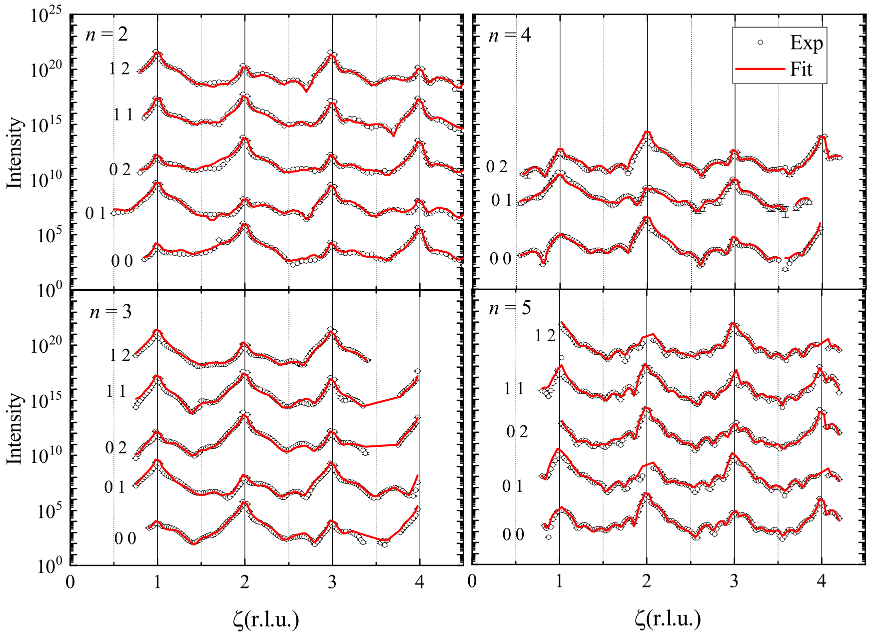

Figure 3.12: CTR scattering profiles and fitting results for n = 2, 3, 4 and 5 LNO/STO samples. White plots are experimental data. Red solid curves are calculated value. The attached number on the left side of intensity profiles is the value of hk.

Fig. 3.13 and 3.14 show the depth profiles of A and B site atomic displacement δz and atomic occupancy with respect to the substrate lattice for insulating and metallic LNO/STO. Atomic position of A site atoms were obtained stably while B site atoms and oxygen of LNO/STO are not stable in this analysis. This is because of the large experimental error of ordinary point detector as the large R value shows.

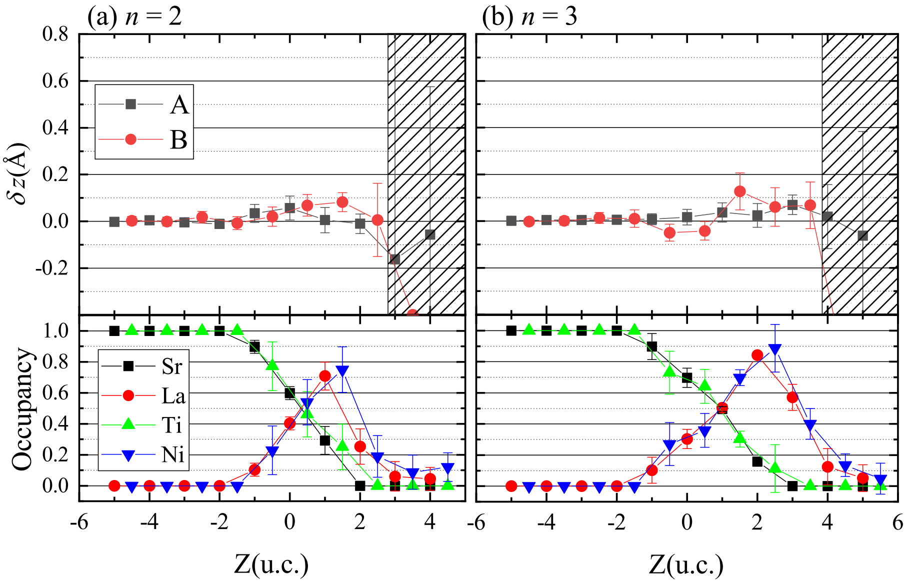

Figure 3.13: (a)Atomic displacement δz from STO lattice and (b)atomic occupancy as a function of depth for LNO/STO($n = 2$ and 3)

The thickness dependence of atomic displacement δz(Å) is shown in Fig. 3.3.2. The lattice spacing is defined by the slope of the curve of δz. Deep inside the substrate, the slope is zero by definition. The thick solid gray line is the slope for the lattice parameter of thick films on STO[80, 85]. The slopes for the thick films coincide with the slopes determined for (LNO)$_5$/STO. LNO film [80, 85] with $c \sim 3.80$ Å only in the layers furthest away from the LNO/STO interface. Therefore, the lattice spacing of the LNO films is strongly affected by the substrate within the range of ~3 u.c. from the interface. The change in the lattice spacing of the LNO film from that of the substrate around their interface is small. The change starts around the third layer from the nominal interface (For example, Z = 0 position in Fig. 3.13). The inner layers around Z = 0 have almost the same or larger c-lattice spacing as that of STO. The following surface layers

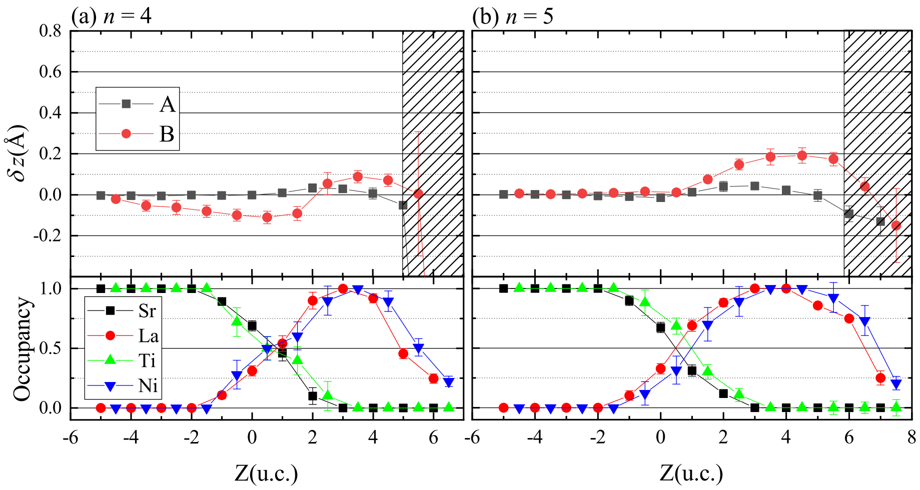

Figure 3.14: (a)Atomic displacement from STO lattice and (b)atomic occupancy as a function of depth for LNO/STO($n = 4$ and 5)

in thicker films have smaller lattice spacing.

LNO/LAO

CTR scattering data along the $hk\zeta$ rod measured for the LNO films on LAO substrates are presented in Fig. 3.16. The typical value of R is 0.1.

The depth dependence of structural parameters for LNO/LAO are presented in Fig. 3.17 and 3.18. Although the structure parameters of oxygen are rather unreliable, those determined for heavy elements stably converged regardless of the details of the fitting procedure and constraints applied.

Thickness dependence of La occupancy, atomic displacement δz(Å) and atomic displacement parameters B(Å^2) is also shown in Fig. 3.19. The same trends of the depth profiles of A-site atomic displacements for all thickness are visible except for $n = 1$ sample. The lattice spacing is the same as that of an $n = 100$ sample, i.e., 3.90 Å, that displays metallic conductivity [75]. The different trend between metallic and insulating samples is the atomic displacement parameters B. $n = 4$ and 5 samples have the middle layers with small value of B, while outermost layer and interface layer have larger value of them. The expanded 'dead layer', whose c-lattice spacing is larger by 0.1 Å than metallic layer seen at LNO/STO interfaces is absent in LNO/LAO interfaces.

LAO and LNO is $R\bar{3}c$ symmetry with NiO$_6$ rotation and tilting. Bragg

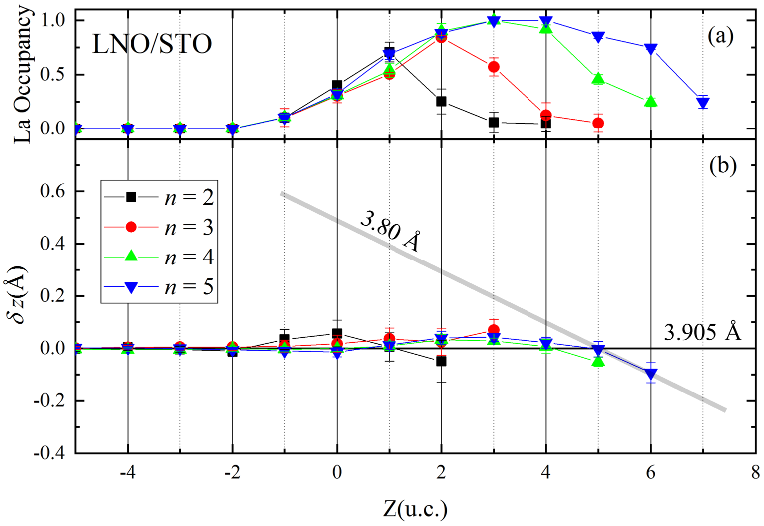

Figure 3.15: (a)La occupancy and (b)atomic displacement δz of La as a function of depth.

reflections from the substrate LAO also appear at points where H, K, and L are half integers except for H = K = L. If a structure with a twofold periodic structure appears in the LNO film, the scattering amplitude from it interferes with the half-integer Rods from substrate, so that some bumps from the film also appears along half integer rods. Fig. 3.20 shows the HK map of observed HKζ rods. If one of the (H, K) is integer and half integer, the intensity was not observed while HKζ rods both of (H, K) is half integer could be observed.

The observed half-integer rods are presented in Fig. 3.21. These rods were not used for MC calculation because of difficulty in separation of intensity from 4 domains of $R\bar{3}c$ structure. Our used LAO substrate have multi domain structure and the ration of contained domains is not clear. Thus half-integer rods obtained from these domain are not equivalent. Besides, the ratio of eliminated area of each domain is not clear. It changes with ζ value. Therefore, we decided not to use this data for Bayesian inference.

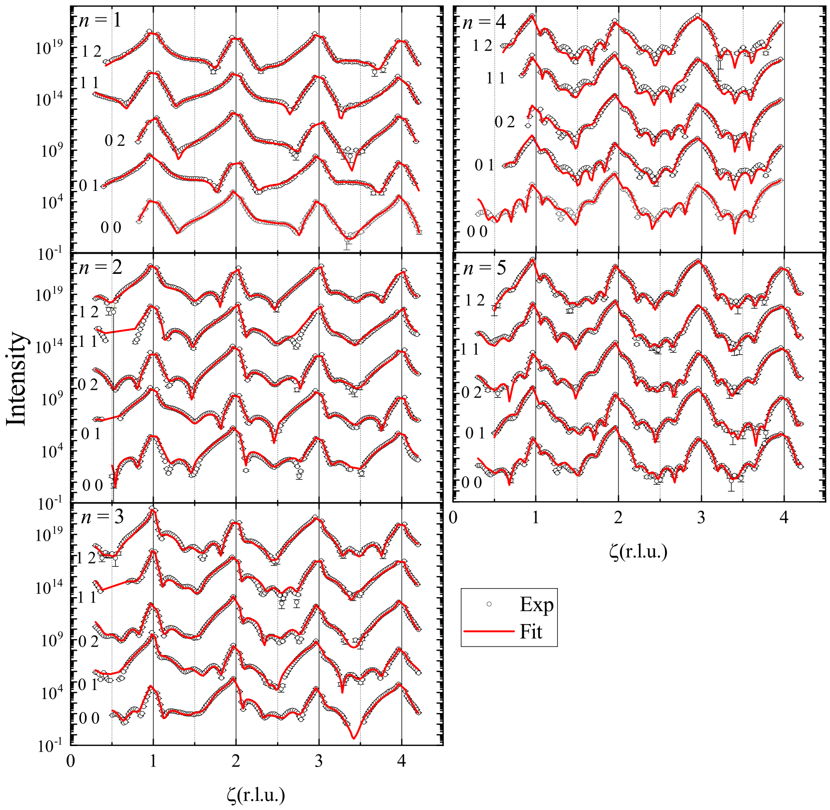

Figure 3.16: CTR scattering profiles and fitting results for LNO/LAO

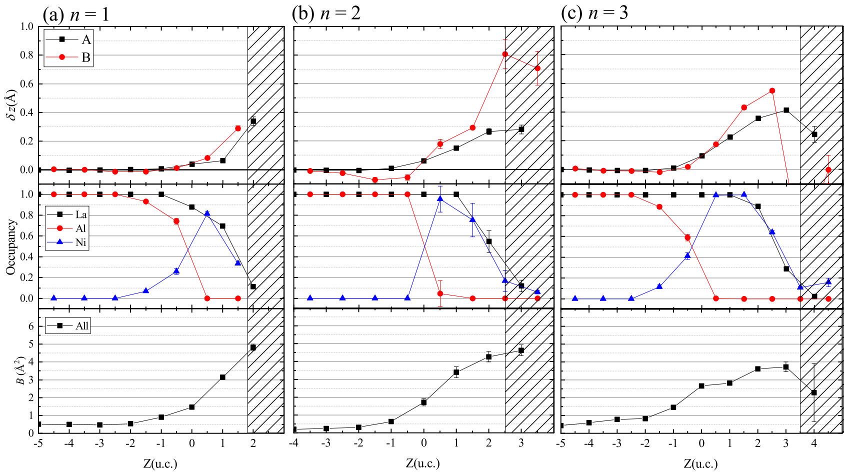

Figure 3.17: (a)Atomic displacement from LAO lattice and (b)atomic occupancy as a function of depth for LNO/LAO(n =1, 2 and 3)

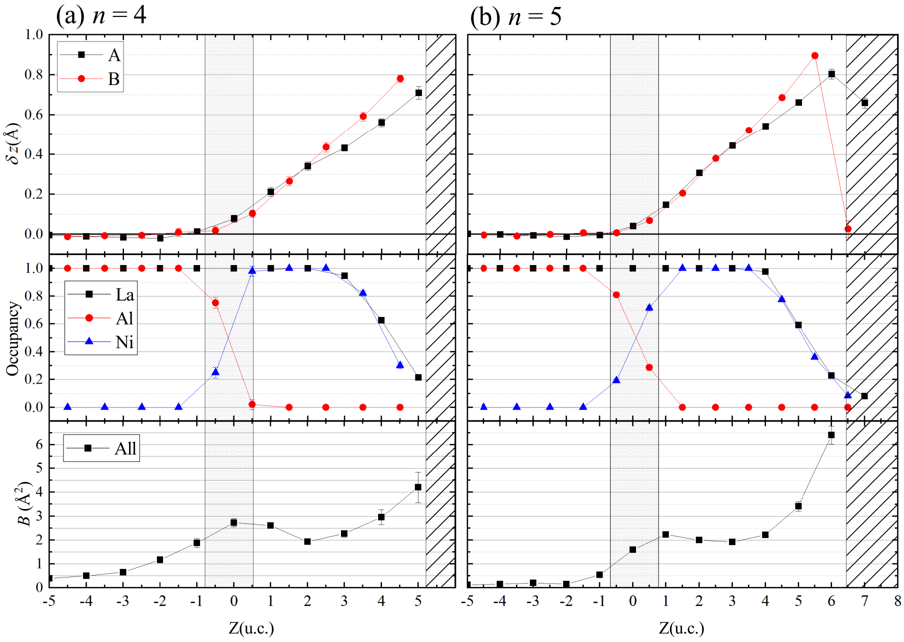

Figure 3.18: (a)Atomic displacement from LAO lattice and (b)atomic occupancy as a function of depth for LNO/LAO(n = 4 and 5)

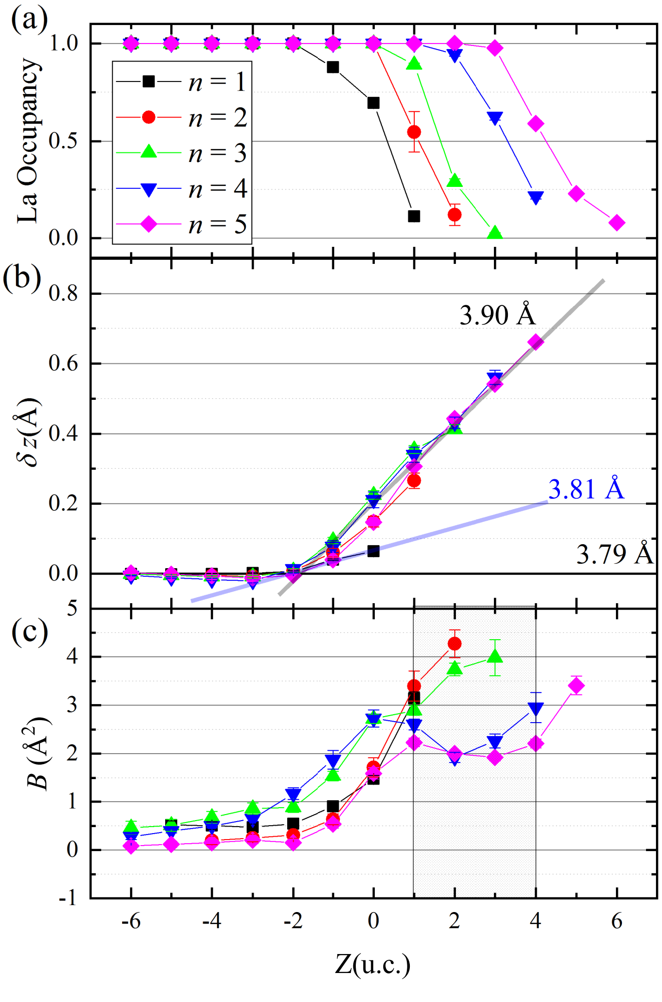

Figure 3.19: Thickness dependence of (a)La Occupancy, (b)δz and (c)B

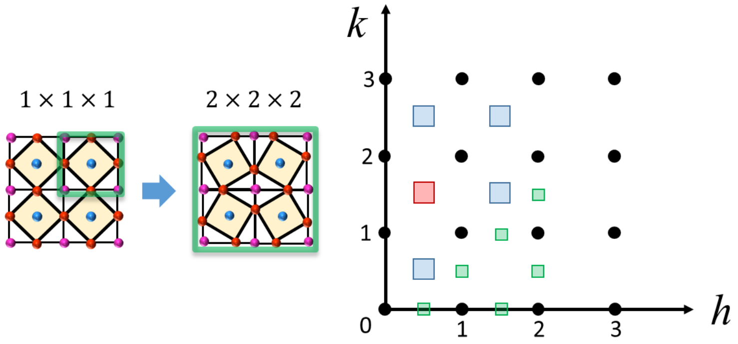

Figure 3.20: 2×2×2 structure and HK plane in reciprocal map. The squared points are measured half integer-rods. We could observe the intensity at the blue and red points while green points could not, which suggests the no orthorombic ordered structure exists in LNO/LAO. Especially, the strong bumps from interference of CTR from LAO and scattering from LNO film were observed along 1/2 3/2 ζ rod(red point).

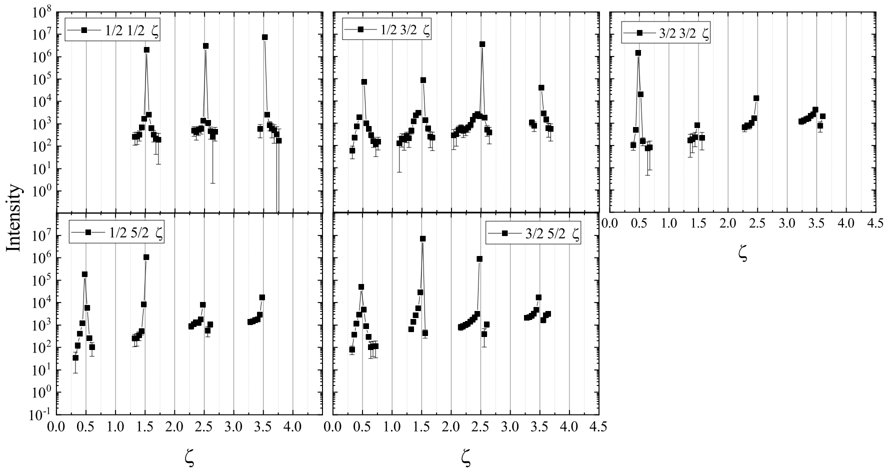

Figure 3.21: Intensity profiles of half order rods of $(LNO)_5/LAO$.

3.4 Discussion

The atomic arrangement of LNO is greatly affected by the valence of Ni. The information on the valence of Ni combined with the analysis results the CTR data is essential. Therefore, we obtained the information on the Ni valence of LNO/STO and LNO/LAO by an experiment on Ni-2p XAS, which was performed by collaborators, H. Kumigashira, M. Kitamura and E. Sakai.

Ni-2p XAS spectra for LNO/STO and LNO/LAO are presented in Fig. 3.22. Here, we focus on the Ni-2p XAS spectra at the Ni-L_2 edge because the (Ni-L_3)-edge structure partially overlaps with the very strong La-$M4$ absorption edge owing to the close proximity of the two energy levels [91]. In order to examine the valence of Ni ions in the thin films, the energy of Ni^{3+} (871.9 eV) and Ni^{2+} (870.3 eV) signals in perovskite nickelates [92] are indicated by solid lines. As can be seen in Fig. 3.22, the Ni^{2+} signal is seen only in $(LNO)_n$/STO with small n values; $(LNO)_2$/STO exhibits a prominent doublet structure, which is characteristic of an Ni^{2+} state [92]. With increasing n, the doublet structure of the Ni-L_2 edge around 871 eV gradually smears and eventually changes into a broad single-peak structure of Ni^{3+} states. In contrast, $(LNO)_n$/LAO do not show an obvious indication of Ni^{2+} states. Although the precise spatial distribution of the Ni^{2+} states in the LNO films was unclear from this measurement, these results strongly suggest that the Ni^{2+} states are generated at the initial stage of LNO film growth on STO.

Based on the information on the Ni valence and the interfacial structure, the origin of MIT of LNO/STO and LNO/LAO will be discussed respectively.

3.4.1 LNO/STO interface

Let us examine the LNO/STO interface first. While the LNO/STO interface involves La-Sr atomic interdiffusion, which is exhibited in Fig. 3.3.2, it should not play an important role in the metal-insulator transition. The reason is that the transition is reported in the samples having a different degree of interfacial mixing, i.e., the samples made by MBE [78], magnetron sputtering [83], and PLD (this work). In particular, Ref.[78] reports the depth profile of the electron density, showing smaller atomic interdiffusion at the interface than our sample. The $n = 2$ and 3 samples have a lattice spacing of 3.905 Å, which is 0.1 Å longer than that of the thick films. Such elongation can be caused by (i) valence modulation of Ni by electrostatic

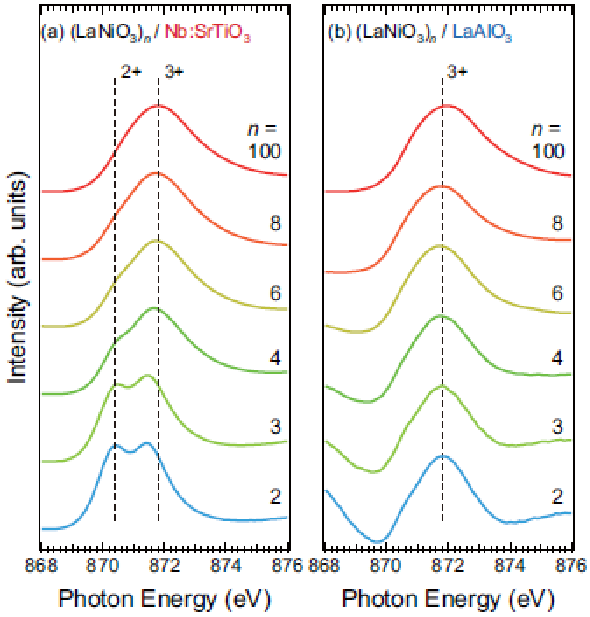

Figure 3.22: Ni *L*-edge absorption spectra for (a)LNO/STO and (b)LNO/LAO

doping, (ii) change in the NiO$_6$ octahedral tilting, or (iii) introduction of oxygen vacancies.

The effect of valence modulation and NiO$_6$ octahedral tilting

Since a Ni^{2+} ion is larger than a Ni^{3+} one, introducing Ni^{2+} expands the lattice spacing of LNO. According to the bond valence sum method, the expected Ni^{2+}-O distance is 4% longer than the Ni^{3+}-O distance. The interfacial expansion of the LNO lattice spacing for 2 and 3 u.c. thick samples is 3%. Therefore, to account for the lattice expansion caused by introducing Ni^{2+}, 70% to 80% of Ni sites should be occupied by Ni^{2+}. The amount of carrier modulation induced by the electrostatic doping mechanism estimated based on the Thomas-Fermi screening length and dielectric constant is less than 10% [93]. Therefore, electrostatic doping cannot account for the observed lattice expansion.

The octahedral tilting is affected by the connectivity to the substrate, and the octahedral tilt angle changes gradually from the value of the substrate to that of the film within 5 u.c. of the epitaxial interface [88]. For the LNO/STO samples, STO has no octahedral tilting in its bulk form. If the first 2 to 3 u.c. of LNO keeps the small octahedral tilting, we should expect larger lattice spacing than that of ordinary LNO. The expected maximum lattice spacing is twice the apical Ni-O distance. However, the lattice spacing of 3.905 Å found for the $n = 2$ and 3 samples is longer than twice the reported Ni-O distance (3.866 Å [80]).

Oxygen vacancy formation

Another way to expand the lattice spacing is oxygen vacancies. A LNO film on an STO substrate suffers from the thermal escape of oxygen atoms even at room temperature [90], which suggests that oxygen has a very low binding energy around the LNO/STO interface. Recent *ab* initio calculation also predicts the oxygen-vacancy formation at the LNO/STO interface [78]. Oxygen vacancies introduce Ni^{2+}, which makes the lattice expand, in addition to the expansion caused by the Coulomb repulsion between cations. The above-mentioned 70% to 80% of Ni^{2+} is achieved when the interfacial composition is $LaNiO_{2.6}$ to $LaNiO_{2.65}$. Such an amount of Ni^{2+} localized at the interface well explains the XAS result presented in Fig. 3.22. Reference [78], which reports a result of 00ζ-CTR measurement on MBE-made LNO/STO interface, also reached the interfacial oxygen-vacancy formation. Oxygen vacancies also alter the local potential distribution and give rise to a wide band gap at E_F [78, 79, 94]. Therefore, we conclude that there is a large amount of oxygen vacancies at the interface, and the oxygen deficiency causes the insulating nature of $(LNO)_n/STO$ for $n \leq 3$. This interpretation is in accordance with the photoemission spectroscopy results indicating the formation of insulating LNO layers at the interface with Nb:STO, although the insulating layers attributed to the formation of a Schottky barrier in that study[93].

3.4.2 LNO/LAO interface

The LNO/LAO samples show no clear change in the structure of the entire film when the fourth layer is deposited. Here, we examine other possibilities of MIT of LNO film, such as the surface termination, Jahn-Teller (JT) effect, covalent bondionic bond crossover, charge disproportionation and structural disorder.

Surface termination

Surface termination is known to affect conductivity in LNO/LAO[87]. However, no clear difference in surface termination was found for the metallic and insulating LNO films in our analysis. The common feature of surface structure is the polarization. The atomic position of B site is displaced to the surface relative to A site position. This trend is explained by the effect on surface by polar nature of LNO/LAO. The LaO and (Al, Ni)O2 layer are charged positive and negative. The atomic displacement of Ni to the surface screen the electronic potential in surface if the termination of LNO is NiO2 plane. This polarized surface structure of LNO/LAO was also reported in Ref.[95].

Confirmation of JT effect in LNO and idea of covalent bond insulator

One of the common origins of octahedral distortion in perovskite oxides is the JT effect. Ni^{3+} in the ionic limit has the e_g^1 configuration, which is JT active. Therefore, an orbital order-driven insulating state appears to be a natural consequence. However, the distortion of the lattice parameter measured by the c/a value does not depends on the thickness of LNO, which contradicts the formation of a JT-driven insulating state.

Nickelates have close Ni $3d$ and oxygen $2p$ energy levels, leading to the idea of a covalent insulator [67, 96], which is a charge transfer insulator with a negative effective energy gap between the upper Hubbard band and oxygen p-band Δ. To make LNO an insulator, a sizable amount of hybridization to form covalent bonds is needed. The metallic and covalent bond lengths of Ni-O bonds are 1.938 ± 0.004 and 1.918 ± 0.006 Å, respectively [70]. The difference of them is 0.02 Å, however, such a large variance of bond lengths are not observed between metallic and insulating samples. Therefore, the idea of covalent bond of Ni-O is irrelevant to this case.

Charge disproportionation and structural disorder

The tendency of large atomic displacement parameter B is not consistent in $R\bar{3}c$ perovskites because La and Ni site atoms located in special site of pseudo cubic lattice points. Two possibility of large B is discussed here. One is the La $2\times2\times2$ ordered structure due to the change of structural symmetry from $R\bar{3}c$ to $Pbnm$ type. $Pbnm$ type structure of $R\mathrm{NiO}_3$ experience the MIT through charge disproportionation between two Ni cite[69, 97, 98].

Another possibility of MIT is structural disordered LNO layer. Indeed, the temperature dependence of conductivity suggests the VRH type of conductivity in LaNiO_3[75, 81, 83]. This MIT mechanism originates from the idea of Anderson localization in Mott materials. The product of mean free path and Fermi wave number of e_g career $k_F l$ of LNO bulk is not more than

5[99]. This is close to the insulating limit $k_F l = 1$. The value of $l = 3.5$Å at 4.2 K is smaller than that of c-lattice spacing of LNO layer, hence such a disordered layer easily results in formation of pseudo gap[100].

Here, we compared the calculated intensity of half-rods data from structural models of La 2×2×2 ordered and various $a^-b^-c^-$ type NiO$_6$ rotation with the experimental value shown in Fig. 3.21. We constructed the models of LNO 2×2×2 film comparable to 6 u.c. thick of 1×1×1 LNO on LAO. The c-lattice spacing was set to 1.03 times larger than LAO and was homogeneous through LNO. Atomic interdiffusion of Al and Ni at the interface and surface roughness is not considered here. We introduced in-plane and out-of-plane La displacement or NiO$_6$ octahedral tilt and rotation to this film as shown in Fig. 3.23. The displacement of A site atoms is written as (A_δx, A_δy, A_δz). Octahedral tilt and rotation are expressed as the displacement of oxygen (O_δx, O_δy, O_δz), which is fractional coordinates of 2×2×2 cubic lattice. The oxygen position of LAO bulk is displaced by 0.044 Å from cubic perovskite lattice points, which corresponds to the value of O_δx = O_δy = O_δz = 0.006. The AlO$_6$ tilt and rotation for 2×2×2 LAO substrate were introduced as (O_δx, O_δy, O_δz) = (0.01, 0.01, 0.01), which are the same values as those in $R3\bar{c}$ structure of LaAlO$_3$ bulk.

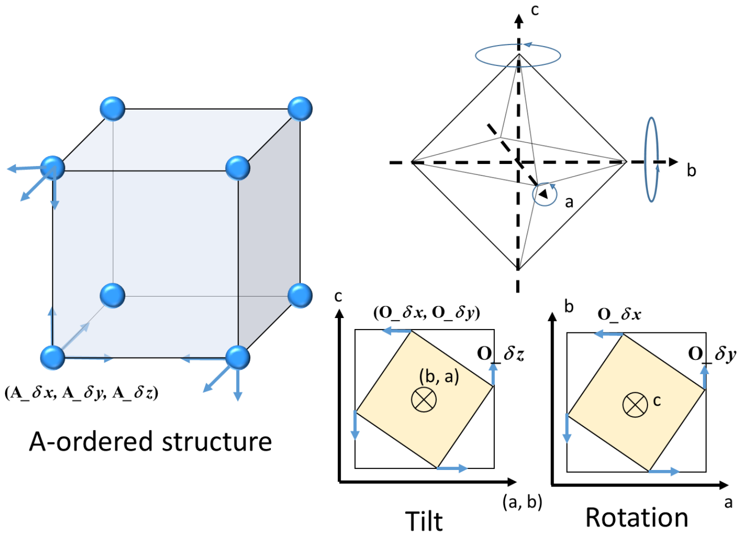

Figure 3.23: The definition of A site(A_δx, A_δy, A_δz) and Oxygen(O_δx, O_δy, O_δz) displacement in 2×2×2 ordered structure are presented.

Then, we have 3 models of 2×2×2 structure of LNO film. One is the NiO$_6$ rotation model which mimic the in-plane Ni-O-Ni angle of LNO/LAO[80, 101]. The values of (O_δx, O_δy, O_δz) were (0.02, 0.02, 0). The second and third model were the La-ordered model. The values of (A_δx, A_δy, A_δz) = (0.02, 0.02, 0) and (0, 0, 0.02) were introduced in second and third La-ordered model. The values of (A_δx, A_δy, A_δz) in second model were the approximately same as the in-plane displacement of Nd in $NdNiO_3$, which exhibits localization character of charge disproportionation[102].

The calculated intensity of (a)11ζ and (b)1/2 3/2 ζ rods from NiO_6 rotation model are presented with solid curves, and those for La-site displacement model of (A_δx, A_δy, A_δz) = (0.02, 0.02, 0) and (0, 0, 0.02) are presented with dashed curves in Fig. 3.24. The intensity bumps along 1/2 2/3 ζ rod around the Bragg peaks at ζ = 0.5, 1.5, 2.5 are 10 to 100 times larger than experimental intensity, while those of NiO_6 rotation model has a same scale as experimental value. These result indicate that no remarkable La order exists in LNO/LAO samples, excluding the possibility of first-order transition of localization character by charge disproportionation effect. The larger B parameters near the surface region are originated from structural disorder of LNO.

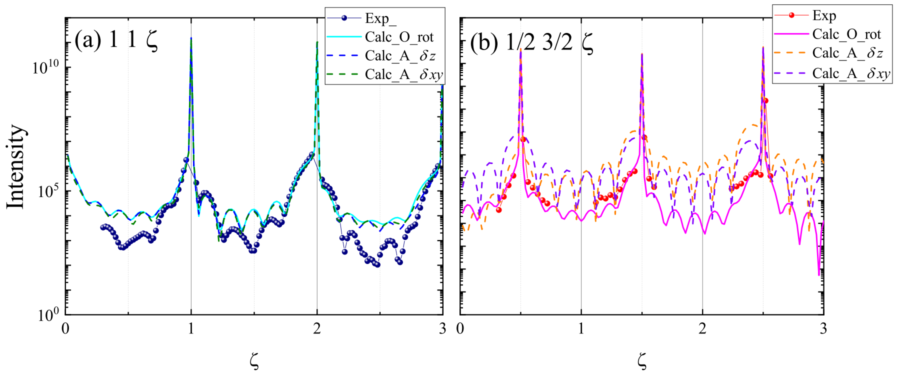

Figure 3.24: CTR scattering profiles of (a)11ζ and (b)1/2 3/2ζ rods. Black and red plots represents the experimental value. The blue solid and light blue dot curves are calculated value of 11ζ rods from NiO_6 octahedral rotation and a 2×2×2 ordered structure of 6 u.c. LNO model. The pink solid and orange dot curves are those for 1/2 3/2 ζ rods.

From analysis results and simulation of half order rods, we concluded that the insulating behavior of LNO/LAO was caused by structural disorder. The disordered structure is prominent on the surface of LNO. n = 1, 2 and 3 samples are composed of only structural disordered surface layers, therefore, they exhibit variable range hopping type insulating behavior.

3.5 Summary of this chapter

The quasi-two-dimensional nature of $LaNiO_3$ (LNO) thin films on $SrTiO_3$(001) (STO) and $LaAlO_3$(001) (LAO) substrates was examined. Although both samples undergo a metal-insulator transition with decreasing thickness,the spatial distributions of the insulating phase within the films differ from each other. The c-lattice spacings of LNO thin films on STO and LAOsubstrates were examined as a function of LNO film thickness using surface X-ray diffraction.The insulating phase in LNO/STO was caused by oxygen deficiency and stayed at the interface even when the film was thicker than 4 u.c. In contrast, large structural disorder was observed in the surface of LNO for LNO/LAO samples. The LNO/LAO samples thinner than 3 u.c. are composed of only structurally disordered layers near the surface region. This disordered structure could shorten the mean free path of LNO and exhibits the variable range hopping type conductivity. This structural study revealed the importance ofthe systematic examination of interfacial structure to conceive a relevant effective model of interfacial electronic structure. Interfacial electronic structure can be modulated by phenomena such as atomic intermixing and unintentional vacancy introduction, as well as by often discussed purely electronic interactions.

Chapter 4

Valence distribution in $LaMnO_3/SrTiO_3$ interface

4.1 Introduction

$LaMnO_3$(LMO) film on STO substrate is known to have thickness-dependent magnetism[103]. Although several mechanisms have been suggested so far, the driving force of ferromagnetism is under discussion. According to the previous studies of LMO/STO, the magnetic property is strongly related to charge transfer(CT) effect[103, 104, 105, 106, 107]. If we can observe the LMO/STO interface structure and the spatial distribution of Mn ions, we will give new insights into changes in LMO properties attributed to the effect.

In this chapter, in addition to the CTR measurement to determine the atomic arrangement of thin film, resonant CTR spectra were measured to obtain the depth dependence of valence state of Mn in individual layer. Attempts to obtain spatial distribution of valence state using resonant CTR spectra are challenging study because the accurate atomic arrangement is required to reproduce Q dependence of CTR the scattering intensity without remarkable error before analyzing energy spectra of CTR scattering.

4.1.1 Spontaneous charge transfer across the interface between $LaMnO_3$ and $SrTiO_3$

The bulk $LaMnO_3$ is categorized in charge-transfer type Mott insulator. The Mn *d*-spin configuration is high-spin d^4 with half-filled fully spin polarized t_{2g} orbitals and of a potentially mobile s = 1/2 carrier in e_g orbital. The ground state of Mn is an A-type antiferromagnetic(AFM) insu-

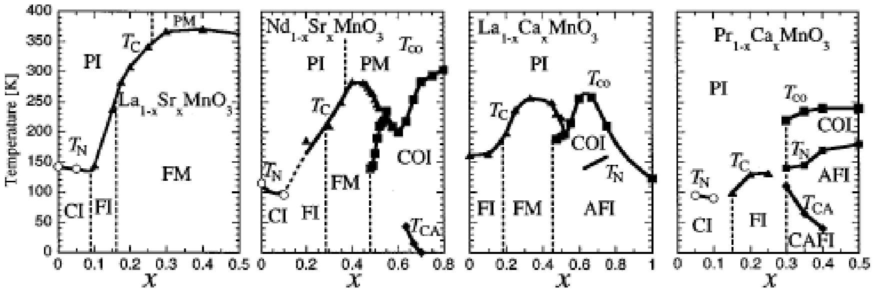

Figure 4.1: Phase diagram of magnetization of Mn oxides under substitution effect into A site atom [111]

lator, where the spin align parallel in-plane and anti-parallel out-of plane, explained by the Mn-O-Mn superexchange interaction and strong Hund's coupling. A lot of hole doped manganese oxides has been studied since the discovery of the negative colossal magnetoresistance(CMR) effect by hole doping[108, 109, 110]. The CMR effect is explained by Double-exchange mechanism qualitatively. Fig. 4.1 shows the phase diagram of Mn oxides the substitution of RE site. In case of bulk $La_{1-x}Sr_xMnO_3$ [111], hole concentration of 10 to 15% gives ferromagnetic(FM) insulator phase, and that of 0 to 10% gives canted magnetic insulator phase, which typically induces 1/10 of magnetization of FM phase.

LMO films grown on STO (001) terminated substrate and their superlattices often show the ferromagnetism not only by excess oxygen or cation vacancies but strain effects and electron-electron interaction between LMO and STO[104, 105]. Such a induced magnetism in heterostructures can be modulated with the different periods of LMO/STO superlattice. Experimental results of STEM combined with electron energy loss spectroscopy observed the induced another oxidation state of $Ti^{4+} \rightarrow Ti^{3+}$, indicating that the change of SE by CT from Mn to Ti is a possible origin of ferromagnetism[106]. X-ray linear dichroism measurements indicates the possibility of manipulating Mn orbital occupation[107]. Different processes of SE for AFM $3z^2 - r^2$ occupied (LMO 17/STO 2) and DE for FM $x^2 - y^2$ occupied (LMO 3/STO 2) between Ti and Mn are suggested as shown in Fig. 4.2.

Another aspect of charge leakage effect is the existence of 'self doped' LMO layer probably due to the polar catastrophe between polar LMO and non-polar STO[103]. The 'self dope' means that CT effect of e_g electron in LMO occurs within LMO film from surface to interface. Fig. 4.3 shows the

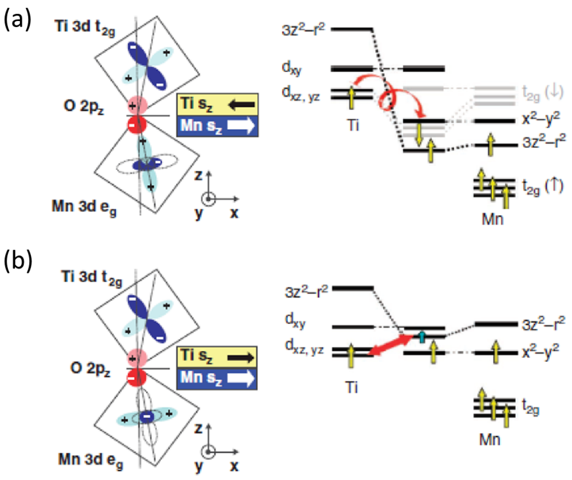

Figure 4.2: Superexchange and double exchange between Ti and Mn ion in LMO/STO superlattice.[107] (a) AFM interaction(LMO 17/STO 2) and (b)FM interaction(LMO 3/STO 2) are expected for different occupation of *d* orbital.

thickness dependence of in-plane image of magnetic field of the LMO films on (001) STO substrate measured by scanning SQUID. When the thickness of LMO is larger than 5 u.c., ferromagnetism over detection limit is confirmed. The critical thickness of emerging FM state suggests the electronic reconstruction mechanism similar to the LAO/STO 2 dimensional electron gas[15].

Additional experimental results of thickness dependence of XAS spectra from LMO films suggests that Mn^{2+} state is located in very thin limited area from the interface[112]. The calculated built in potential from the band gap of LMO and STO predicts electron accumulation region spread only 2 u.c. from interface, which is consistent with the shift of the main peak of Mn *L*-edge spectra by adding the LMO layer. The absence of another peak of Ti *L*-edge spectra also supports the CT effect is limited in LMO region and there is no transferred charge from Mn to Ti via the interface. The magnetic but insulating character is derived from the competitive SE of Mn^{3+}-Mn^{2+} and DE among Mn^{3+}-Mn^{4+}. Accumulated excess charge into the polar film side near the interface inferring self-doping effect was also observed in Sr doped La$_x$Sr$_{1-x}$MnO$_3$ films by scanning transmission electron microscopy[113]. The assumption of the excess charge spread over 2 u.c. is comparative to the the screen length($\sim$0.2 nm) of LSMO[114].

As the debate in chapter 3, tilt and rotation angle BO$_6$ ochtahedron

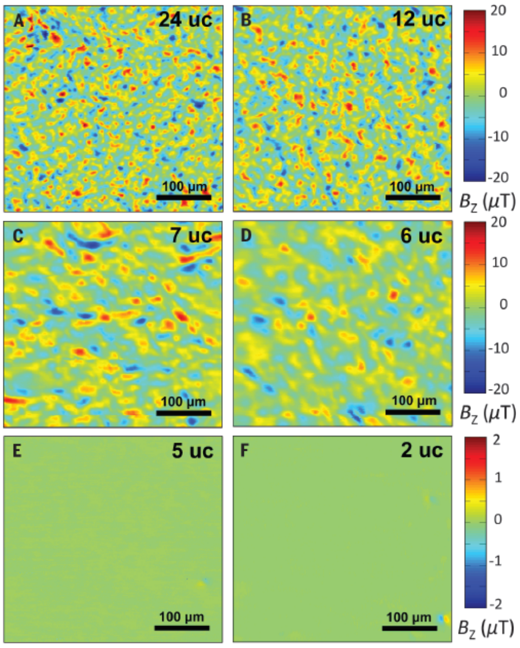

Figure 4.3: The magnetization map of various thickness of LMO on STO by SCAN SQUID.[103]

strongly affects the transfer integral of Mn-O-Mn bonds[115]. The X-ray diffraction measurement for $(LMO/STO)_N$ superlattice where N is the periodicity of deposition suggests the rotation angle can be manipulated by changing periodicity N. The enhanced the rotation angle along c-axis and weakened magnetism observed for smaller N samples suggests that the reduction of transfer integral combined with Mn-O-Mn angle prefer A-type AFM phase.

For LMO films grown on Nb doped STO substrate, the V-I curve and photoelectric effect were observed as in typical *p*-*n* junction semiconductor[116, 117]. This is simply explained by the band bending across the *p*-type $LaMnO_{3+\delta}$ and *n*-type Nb doped $SrTiO_3$. The band diagram of LMO/Nb:STO *p*-*n* junction was determined by XPS measurements[118]. The rich Nb doped STO reaches degenerates semiconductor. The potential difference at the interface is screened by the depletion layer charge. *p*-type semiconducting state of LMO is so-called hole doped FM state from instability of contained amount of oxygen.

4.1.2 Known structural information of LMO thick film on STO

Here we summarize the known structural information of LMO thick films. The differences from LNO is strong JT activity and the instability of amount of oxygen in the LMO during film formation[119]. For the latter reason, there is a lot of variation of *c*-lattice spacing and magnetic properties in film reported, depending on conditions such as annealing schedule and oxygen pressure when forming the LMO film. Here, reported values of the LMO film thickness on STO substrate made by Pulsed laser deposition is summarized in table 4.1.

Table 4.1: Reported *c*-lattice spacing and physical properties of LMO/STO under different process of fabrication.

Ref	thickness	c(Å)	Properties	Annealing condition
[120]	30 nm	3.939	FM/Semiconductor	As grown
[120]	30 nm	3.974	AFM/Insulator	4% H + 96% Ar gas
[112]	55 u.c.	3.94	FM/Insulator	7.5 mTorr of O_2 at 750°C
[121]	-	3.985	AFM/Insulator	5×10^{-3}mTorr of O_2 at 700 to 900°C
[121]	-	3.92	FM/Insulator	200 mTorr of O_2 at 700 to 900°C
[122]	4 to 40 nm	3.864	FM/metallic	-
[123]	30 nm	3.972	AFM/Insulator	4 % H + 96% Ar gas at at 500 to 900°C
[123]	30 nm	3.912	canted AFM	As grown

A number of studies have addressed that smaller *c*-lattice spacing of

LMO tends to be FM insulator. In particular, Ref.[123] investigated the annealing effect of LMO fabrication and its magnetic property. Oxygen reduced annealing promotes to prevent over introducing of O to LMO and keep the LMO canted AF insulator as bulk state of LMO. As grown FM sample have smaller *c*-lattice spacing as shown in Fig. 4.4. We refer these results as the typical thickness of AFM and FM phase of LMO/STO.

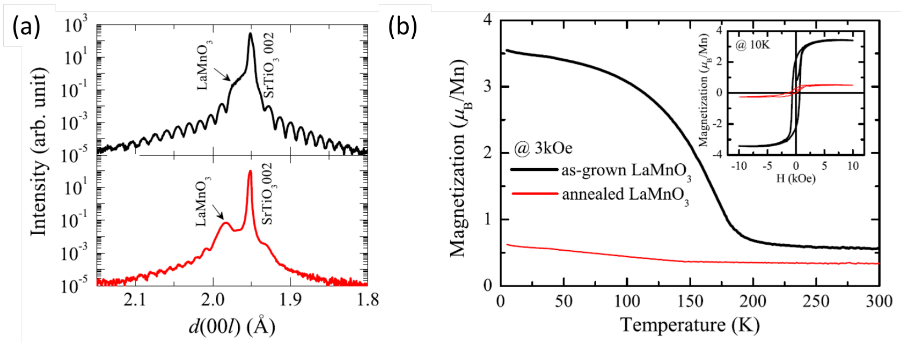

Figure 4.4: (a)X-ray diffraction and (b)magnetization data of $LaMnO_3$ on STO substrate[123]. Black and red solid curve present the data of as-grown and post annealed samples respectively.

4.1.3 Resonant CTR scattering method

In a strongly correlated electron system, not only to examine the atomic arrangement but also to elucidate the electronic state of charge, orbital, and spin is essential. However, we have generally difficulties to capture changes in the electronic state only by diffraction experiments. Resonant X-ray diffraction(RXRD) is a method for extracting electronic state as well as atomic arrangement using the absorption effect of target atoms. It utilizes the response of an atom to X-rays, that is, the atom scattering factor changing greatly near the absorption edge of the atom.

Here is a brief description of the principle of resonant CTR scattering to extract the information of atomic occupancy and valence state of target atom. The atomic scattering factor f described in chapter 2 is expressed as the summation of a Thomson scattering term with $\boldsymbol{Q}$ dependence and an energy dependent term. The formula of f is written as

$$f(\boldsymbol{Q}, E) = f_0(\boldsymbol{Q}) + f'(E) + if''(E), \tag{4.1}$$

where $f_0(\boldsymbol{Q})$ is Thomson scattering term and $f'(E)$, $if''(E)$ are the real and imaginary parts of anomalous scattering factor. Anomalous scattering factor represents the process of excitation of core electrons by X-ray. The energy dependence of the imaginary part is given by

$$f''(E) = (m_e cE/2e^2 h)\mu(E), \tag{4.2}$$

where m_e is the electron mass, c is the velocity of the light, e is the electron charge, and h is Planck's constant. Thus, $f''(E)$ is linear to the products of absorption coefficient $\mu(E)$ and E. Therefore, $f''(E)$ is calculated from $\mu(E)$ by the XANES or X-ray fluorescence spectra experimentally. The real part is calculated by the Kramers-Krönig transformation of $f''(E)$ written as

$$f'(E) = \frac{2}{\pi}\int_0^\infty \frac{E' f''(E')}{E^2 - E'^2} dE'. \tag{4.3}$$

The absorption edge is shifted by the change of valence state of target ion because of the screening effect of the charge in the nucleus of an atom. This energy shift by different surroundings including valence sensitivity is called chemical shifts. Fig. 4.5(a) and (b) show the energy dependence of anomalous scattering factor of Mn^{3+}($LaMnO_3$) and Mn^{4+}($SrMnO_3$)[124] near the K-absorption edge of Mn. At points of $\boldsymbol{Q}$ where the non-resonant scattering amplitude from Mn having different valence interferes as a difference, a specific sharp peak is observed near the absorption edge in the energy spectrum as shown in Fig. 4.5(c). The reference[125] clarified the charge order state of $Nd_{0.5}Sr_{0.5}MnO_3$ from the $\boldsymbol{Q}$ dependence of energy spectra of Bragg peaks and superlattice peaks. Ref.[126] successfully determined the spatial distribution of valence state of Mn in $(LaMnO_3)_n/(SrMnO_3)_n$ superlattice from the energy dependence of intensity at some Bragg points.

In principle, by measuring the energy dependence of CTR scattering for all $\boldsymbol{Q}$ points, the atomic occupancy and valence state are obtained with high accuracy. The problem of resonant CTR is the complexity of the structural model. To recover the energy spectra of scattering intensity at $\boldsymbol{Q}$ points, the accurate atomic arrangement whose structure factor $F(\boldsymbol{Q})$ is consistent with the experimental value is required. The $\boldsymbol{Q}$ dependence of energy sensitivity of CTR scattering was discussed in Ref. [127, 128]. The scattering amplitude from bulk F_B is much larger than that from surface F_S close to the Bragg peaks. The scattering intensity $I = |F_B|^2 + F_B^\star F_S + F_S^\star F_B + |F_S|^2$ would have to be measured with high precision because the second and third term including the contribution of F_S is relatively small. To detect the clear effect of the change of $f'(E)$ and $f''(E)$ from resonant CTR scattering, the intermediate $\boldsymbol{Q}$ points between Bragg peaks is best where F_S is as large as

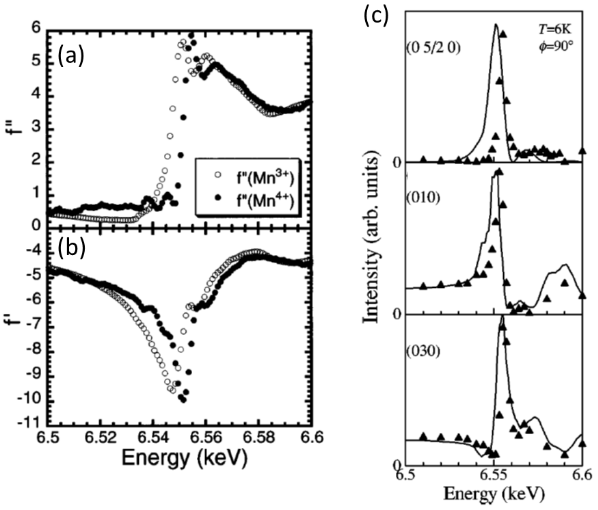

Figure 4.5: Anomalous factor of Mn in $LaMnO_3$ and $SrMnO_3$ near Mn K-edge[124]. (a) The difference between the values of chemical shift indicated by $f''(E)$ (b) $f'(\mathrm{Mn}^{3+}) - f'(\mathrm{Mn}^{4+})$ (c) Energy spectra of Bragg peaks and superlattice peaks of $\mathrm{Nd}_{1-x}\mathrm{Sr}_x\mathrm{MnO}_3$[125].

possible. The higher flux of incident wave is required then to detect the sufficient signal exceeding the background noise.

In Ref.[126], the structural model was simplified to have only five parameters such as the lattice constants of La and Sr region, the relaxation factor of lattice constants near the interface, and the periodicity of superlattice. On the other hands, for the CTR data obtained from complex surface structure like LAO and LNO thin films discussed in chapter 2 and 3, more complicated structural models composed of structurally different layers are required to reproduce the experimental scattering amplitude correctly. The successful example of the analysis of spatial distribution of the valence state from resonant CTR data is limited to the oxidation state at the surface of simple metal[129]. Hence, the general application of resonant CTR has usually been used to distinguish the atoms whose scattering power are close, for example, the determination of atomic occupancy in Cu/Si(111) epitaxial interface[130], ultrathin layers of GaAs grown on InGaAs buffers[131].

4.2 Motivation

Some theoretical works[132, 133] predicts that the epitaxial strain from STO modulate the structure LMO film, resulting in the emergent FM order state. However, calculations assuming a clean interface and a stable oxygen supply do not reproduce the experimental results. As described in section, several mechanisms of the Mn valence modulation have been proposed as the origin of ferromagnetism in the LMO film.

To confirm whether such self-doping actually occurs, the observation of interface structure and valence distribution of Mn are straightforward. In this study, we investigated the thickness dependence of the structure and Mn valence distribution of LMO thin films on Nb:STO(001) substrate by resonant CTR scattering data. The spatial distribution of the electronic state of Mn gives an accurate interpretation of the ferromagnetism with CT effect in LMO. When Mn^{2+} by self-doping[103] is concentrated at the interface, a large lattice should be realized according to the ionic radii of Mn. Such accumulated valence state exhibits specific peak of energy spectra of CTR scattering as shown in Fig. 4.8(d). We aim to understand the mechanism of induced magnetism from the observed spontaneous CT effect from the $\boldsymbol{Q}$ and E dependence of CTR scattering data.

4.3 Experiments and analysis

4.3.1 Experimental conditions

LMO/STO samples were provided by Prof. H. Kumigashira, Prof. K. Horiba and Dr. M. Kitamura. Epitaxial LMO films with various thicknesses were fabricated onto atomically flat TiO_2-terminated Nb:$SrTiO_3$ (STO) (001) substrates in a laser molecular-beam epitaxy chamber connected to a photoelectron spectroscopic system at beamline BL-2A MUSASHI of the Photon Factory, KEK. A Nd-doped yttrium-aluminum-garnet laser in the frequency-triplet mode ($\lambda = 355$ nm) at a repetition rate of 1 Hz was used for ablation. A sintered LMO pellet was used as the target. Before the film growth, the Nb:STO substrates were annealed at 1050°C under an oxygen pressure of 1×10^{-7} Torr to obtain atomically flat and chemically clean surfaces. During LMO deposition, the substrate was kept at the temperature of 600°C and the oxygen pressure was maintained at 1×10^{-7} Torr. The thickness of LMO layers was precisely controlled by monitoring the intensity oscillation of the specular spot with reflection high-energy electron diffraction during the growth. The LMO films were subsequently annealed at 400°C for 45 min under an atmospheric pressure of oxygen to fill residual oxygen vacancies. There 4 LMO samples prepared with a various thickness n, as the thicker FM samples ($n = 7$ and 10) and the thin suppressed magnetized ($n = 2$ and 4) samples. We denote these samples as $(\mathrm{LMO})_n$/STO in this chapter.

The CTR scattering measurements were performed at the Photon Factory, KEK. In off resonant condition, the procedure of measurements was almost the same as that for the LNO film(Chapter 3). The X-ray energy was set to 12 keV for non-resonant condition. The typical beam size was 1 × 1 mm. At least 5 $hk\zeta$ rods[(h, k) = (0, 0), (0, 1), (0, 2), (1, 1), (1, 2) and (1, 3)] were measured for all samples up to $\zeta = 4.1$. The data intervals $\Delta\zeta$ is 0.02 for (LMO)$_2$/STO and (LMO)$_4$/STO and 0.015 for (LMO)$_7$/STO and (LMO)$_{10}$/STO. The path of X-ray was filled with He gas to prevent the attenuation of X-ray.

The resonant CTR scattering near the Mn K-absorption edge experiments was also performed to determine the atomic occupancy of Ti and Mn whose scattering power is close. That for (LMO)$_2$/STO was not observed due to the insufficient measurement time. First, the 00ζ scan was performed up to $\zeta = 2.3$ along the rods. The energy of incident beam for resonant rods was set to 6.3, 6.4, 6.5, 6.6 and 6.7 keV. Since the used 2D detector does not have energy resolution, we excluded some harmonics peaks from resonant rods at $\zeta = 0.5$ and 1.5.

We also measured the energy spectra of CTR scattering at several ζ along the rods to determine the spatial distribution of the different valence state of Mn. Two types of energy scans were performed per selected ζ with the wide and narrow range of energy scan. The typical range and interval of the observed points for the wide scan was 6.5 to 6.7 keV per 10 eV while those for the narrow scan was 6.545 to 6.565 keV per 1 eV. For (LMO)$_2$/STO and (LMO)$_4$/STO, the narrow scan was performed as 6.54 to 6.56 keV per 1 eV. The selected ζ points were picked up from $\zeta = 0.7$, 0.8, 0.9, 1.1, 1.2, 1.4, 1.52, 1.6 and 1.8 along 00ζ rod.

In addition, CTR measurement at low temperature(10 K) in addition to measurement at room temperature (300 K) was also performed for 10 u.c samples. The smaller thermal expansion coefficient $\beta = \frac{1}{V}\frac{dV}{dT}$ of LaMnO$_3$(1.6×10^{-5}K^{-1}) than SrTiO$_3$(2.6×10^{-5}K^{-1}) could lead more strongly compressive strain into LMO, which stabilize the $3z^2 - r^2$ orbital. We investigated the effect of this difference in volume expansion on the crystal structure. We aimed to demonstrate the systematic observation of external field dependence of interface structure by CTR measurement and analysis. There has been almost no report on the temperature dependence of the structure of such a strongly correlated interface.

All CTR data were collected by using the 2 dimensional pixel array detector(imXPAD). After the measurements, illumination area correction and Lorentz factor correction were multiplied to all off and on resonant data.

4.3.2 Data processing in resonant condition

The data correction of the energy dependence of absorption coefficient must be performed to the resonant scattering data. For general resonant diffraction experiments, the absorption coefficient $\mu(E)$ is determined by the normalization of the intensity of Bragg peak. The incident beam and scattered beam travels in the long He/Air path and penetrates the beryllium dome and several different thickness of Al plates as attenuators, hence the absorption correction cannot be obtained only from the absorption coefficient of the sample. Here, we determined the absorption correction '$C_\mu(E)'$ approximately by the fraction of the ζ average of scattering intensity of five 00ζ rods with different energy, written as $\frac{\overline{I_{\text{exp}}(E)_\zeta}}{\overline{I_{\text{exp}}(E{=}6.5\text{keV})_\zeta}}$, where $\overline{I_{\text{exp}}(E)_\zeta}$ is the ζ average of experimental intensity $I(E) = D(E)I_{\text{exp}}(E)$. The absorption correction $D(E)$ for energy spectra was calculated by the fitting linear function of E dependence of 5 $C_\mu(E)$ points as $D(E) = \text{A}'E + \text{B}'$, where A' and B' is a fitting parameter of $D(E)$. Finally, we obtained the corrected intensity by $I(E) = D(E)I_{\text{exp}}(E)$.

4.3.3 Analysis procedure

The model construction of all LMO/STO samples were performed by replica exchange MC software. The number of replicas was set to 64 for all calculations. The analysis procedure was separated to 4 stage as follows.

In the first calculation, the atomic position (z), atomic displacement parameters (B), and atomic occupancy (occ) were refined. The in-plane lattice constant was $a = b = 3.905$Å at 300K and 3.895 Å at 10K determined by the Bragg peak position of the substrate. We also refined B parameters for AO1 plane and BO2 plane for each atomic layer. At that time, the parameters of $\text{occ}(\beta, n)(\beta = \text{Ti or Mn})$ around the interface were fixed to the assumed value whose depth dependence were smoothly connected.

In the second calculation, we added the 00ζ rods under the resonant condition to the off resonant data set. All $\text{occ}(\beta, n)$ parameters were refined with other $\boldsymbol{\Theta}$. As described in previous section, the anomalous term of the atomic scattering factor should be determined by calculating the absorption coefficient from the energy dependence of the fluorescent X-ray. However, Mn fluorescent X-rays of LMO films were too weak to be detected. Therefore, the calculated anomalous factor of Mn was used for analysis. We calculated it by FDMNES[134], a the simulation software for resonant X-ray diffraction. The absorption coefficient $\mu(E)$ near the K absorption edge (from 6450 to 6700 eV) of Mn calculated from the bulk structure of LMO was used as pseudo experimental data. Then, we calculated the energy dependence of imaginary part $f''(E)$ as

$$f''(E) = \mathrm{A}''\mu(E)E + \mathrm{B}''. \tag{4.4}$$

The constant number A" and B" were determined by the smooth connection to the theoretical value at 6450 and 6700 eV of $f''(E)$ calculated from Mn monoatom listed in Ref.[64]. The energy correction of the incident beam at BL-3A was determined by the comparison of the absorption edge by fluorescent X-rays measurement from Mn foil and that of reported value[135]. $f'(E)$ was calculated from $f''(E)$ by equation 4.3. The anomalous factor of [Mn^{2+}, Mn^{4+}] was generated by the $f'(E - E_{\mathrm{chem}})$ where the E_{chem} is the chemical shift between Mn^{3+} and [Mn^{2+}, Mn^{4+}]. The reported values of chemical shift of Mn^{2+} and Mn^{4+} from XANES data were varied as ± 3 to 5 eV for different substitution of A site cation to Mn oxides as $\mathrm{SrMnO_3}$, $\mathrm{CaMnO_3}$[126, 136]. Here we used chemical shift $E_{\mathrm{chem}} = 4$ eV for Mn^{4+} and -3 eV for Mn^{2+} ion. The value of $f'(E)$ and $f''(E)$ are presented in Fig. 4.6.

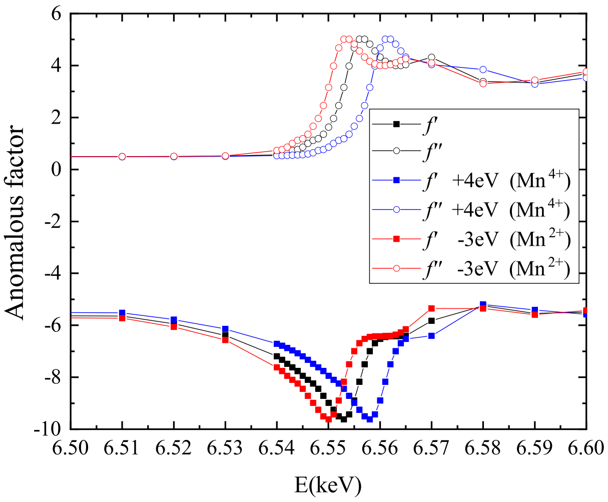

Figure 4.6: Energy dependence of anomalous scattering factor of Mn near Mn K-edge. f' and f'' of Mn^{2+} and Mn^{4+} are calculated by shifting that of the simulation value of Mn^{3+} in $\mathrm{LaMnO_3}$.

In the third calculation, we added the energy spectra data of CTR scattering measured at several ζ along 00ζ rod to $\boldsymbol{I}_{\mathrm{exp}}(\boldsymbol{Q})$. The refined $\boldsymbol{\Theta}$ in the third calculation were the same as in the second calculation. When analyzing the data for $(LMO)_{10}/STO$ at 10K, the $\mathrm{occ}(\beta, n)$ parameters around the interface were fixed to the refined value of 300K.

In the fourth calculation, the spatial distribution of Mn^{4+} was refined by using the energy spectra measured at several ζ along 00ζ rods. Although the non-resonant amplitude was calculated based on the result of third calculation, it inevitably contains some error. This error was corrected by adding a small complex value '$C(\boldsymbol{Q})$' to the non-resonant scattering amplitude. An example of the deviation of spectra between experimental and calculated value before and after adding $C(\boldsymbol{Q})$ to scattering amplitude $F(\boldsymbol{Q})$ is presented in Fig. 4.7.

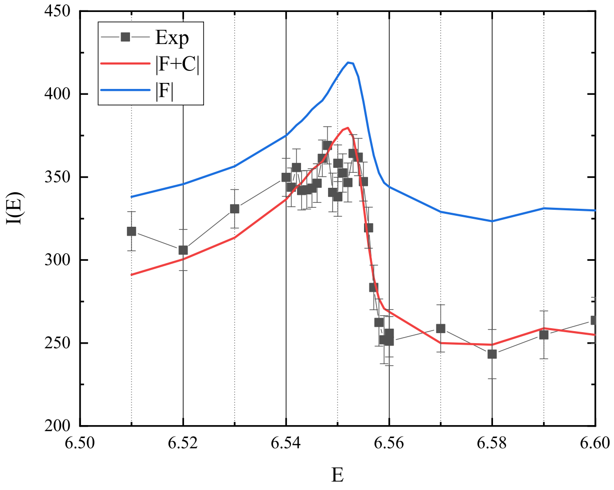

Figure 4.7: Energy spectra of CTR scattering at $00\zeta = 0.9$ for $(LMO)_4/STO$ before and after adding C

For the analysis of the energy spectra, we introduced an the additional structural parameter to express the mixture rate of different valence state of Mn ion in the same site. Here, we call this parameter fractional occupancy $\mathrm{focc}(\gamma, n)$, where γ is the notation of the different valence state of element β (In this case, $\beta = \mathrm{Mn}$, $\gamma = Mn^{2+}$, Mn^{3+}, Mn^{4+}). The atomic occupancy is expressed as $\mathrm{occ}(\beta, n) \times$ $\mathrm{focc}(\gamma, n)$. The analysis was also performed by the Bayesian inference assuming the systematic noise to be 10 % of the intensity.Only $\mathrm{focc}(\gamma, n)$ parameters in LMO region were refined in the fourth calculation.

The simulated CTR spectra from the models of LMO films on STO(001) with different spatial distribution of Mn^{4+} and Mn^{3+} are presented in Fig. 4.8. The anomalous factor f' and f'' in a layer composed of mixed valences state of Mn with the ratio of Mn^{3+}:Mn^{4+} $= \alpha : 1-\alpha$ are given by the difference as $f' = \alpha f'_{3+} - (1-\alpha f'_{4+})$ and $f'' = \alpha f''_{3+} - (1-\alpha f''_{4+})$. A model No.1 having a homogeneous Mn valence($Mn^{3.1+}$) throughout LMO region shows no significant change in spectral intensity. On the other hand, if the valence are inhomogeneously distributed, the signal change is noticeable. Since the change in the spectrum shows a clear $\boldsymbol{Q}$ dependence, spatial distribution of valences can be determined from the spectral intensities at multiple $\boldsymbol{Q}$ points.

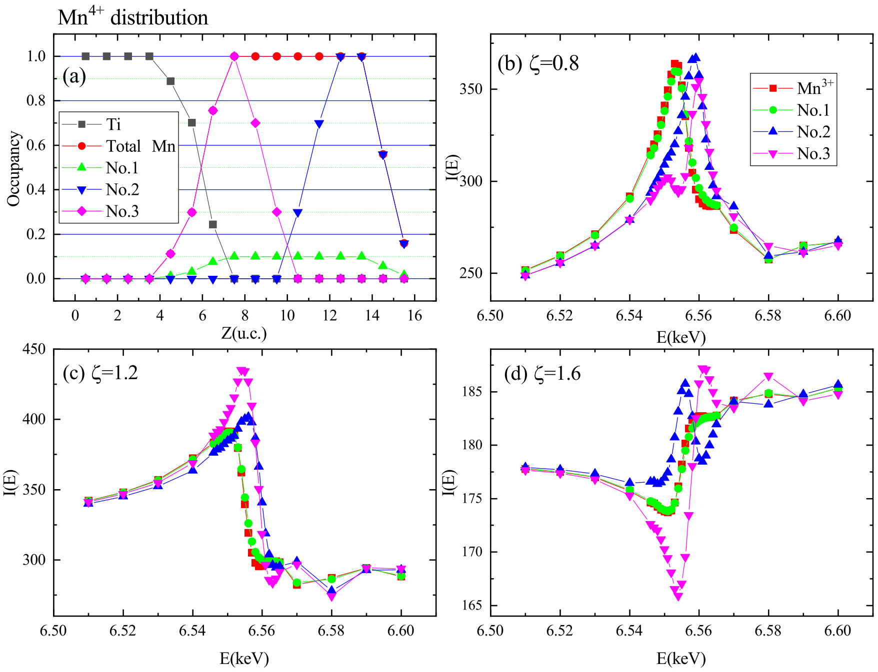

Figure 4.8: (a)Depth dependence of Ti/Mn atomic occupancy of LMO/STO model. The plots in panel (a) labeled as No.1-3 have different spatial distribution of Mn^{4+}(green, blue and pink plots)/Mn(red plots) ratio. Panels (b-d) show energy spectra of CTR scattering at $\zeta = 0.8$, 1.2, 1.6 along 00ζ rod.

4.3.4 Analysis and results

Fitting results of Q dependence of CTR data

CTR scattering data along the $hk\zeta$ rods measured for $n = 2$ and $n = 4$ and 7 samples are presented in Fig. 4.9 and Fig. 4.10. The solid curves show the calculated intensity derived from the refined structures. CTR scattering data measured at 10K and 300K for $n = 10$ sample are shown in Fig. 4.11. CTR scattering data along the $hk\zeta$ rod for non-resonant condition and 00ζ resonant rods measured for the $n = 4$, 7 and 10 samples are also presented in Fig. 4.10 and Fig. 4.11. The typical value of $R = \sum |(|F_{\mathrm{exp}}| - |F_{\mathrm{calc}}|)| / \sum |F_{\mathrm{exp}}|$ is 0.11 to 0.13.

The reduction of one bump between the substrate Bragg peaks(for example, only 6 bumps per L were observed for $(LMO)_7/STO$) suggests the thinner thickness by 1 u.c than designed thickness of LMO films or rough interface. Appropriate models were determined by the validity from the physical point of view of the structure. For example, the models whose depth dependence of the structural parameter is not spatially continuous were rejected.

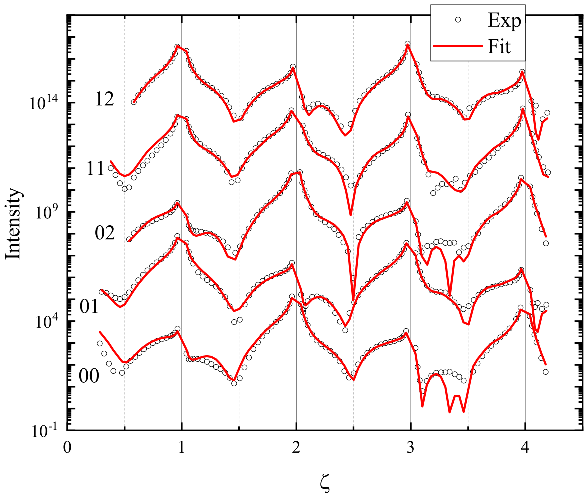

Figure 4.9: CTR intensity profile and fitting result for $(LMO)_2/STO$. White plots are experimental data. Red solid curves are calculated value. The attached number on the left side of intensity profile is the value of hk.

The refined $\mathbf{\Theta}$ for all samples as a function of depth are presented in

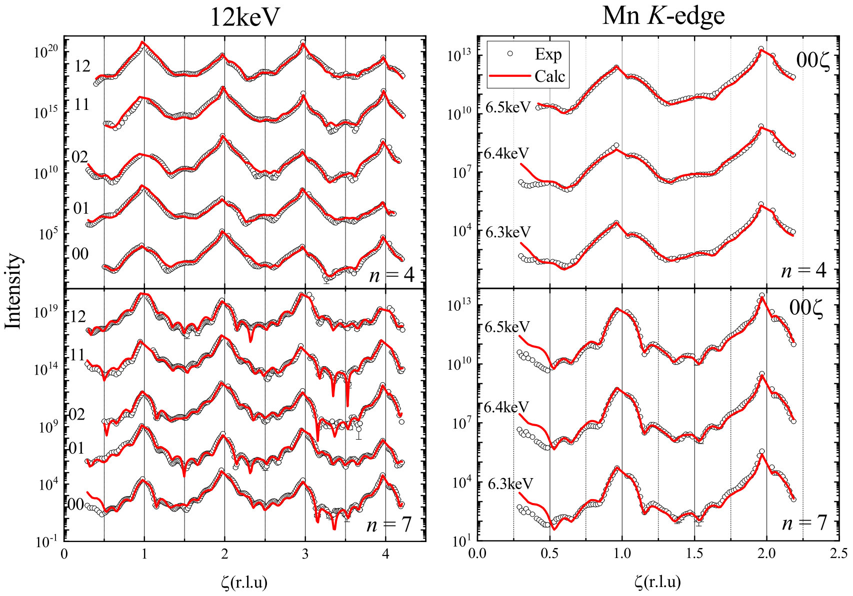

Figure 4.10: Non resonant and resonant CTR intensity profile and fitting result for $(LMO)_4/STO$ and $(LMO)_7/STO$

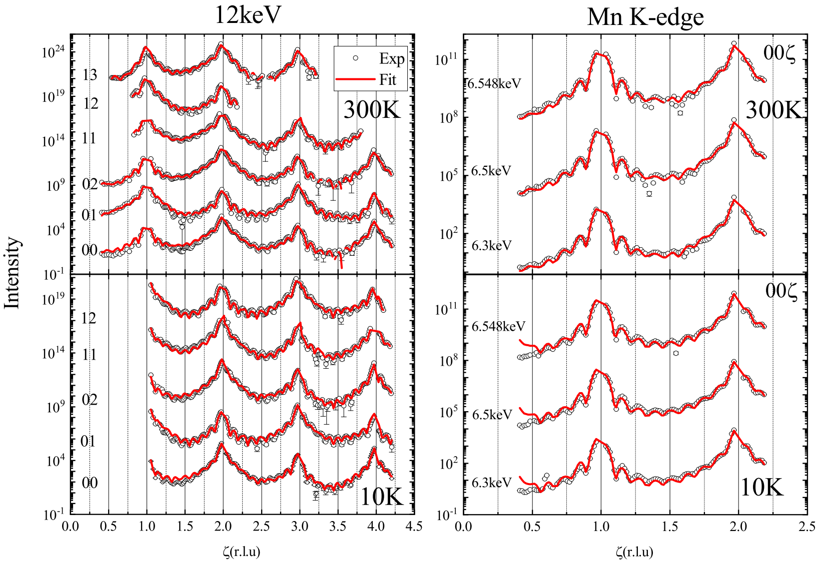

Figure 4.11: non resonant and resonant CTR intensity profile and fitting result for $(LMO)_{10}/STO$ at 300K and 10K

Fig. 4.12, Fig. 4.13 and Fig. 4.14. Atomic displacement δz from the substrate lattice points, the atomic occupancy, and atomic displacement parameters $B(\text{Å}^2)$ are plotted in panel(a), (b) and (c). The values of c-lattice spacing calculated by the difference of atomic position of A site atoms ($c_{\text{sub}} + z(\text{A}, n+1) - z(\text{A}, n)$), where c_{sub} is the value of c-lattice spacing of STO substrate, are also presented in Fig. 4.15. The dotted line represents the reported value of LMO thick film fabricated under the condition of as grown(FM state) and annealing with oxygen reduced gas(AFM state)[123]. The value of c-lattice spacing = 3.94Å is the expected boundary of FM and AFM phase from Table.4.1. The error bars of $\boldsymbol{\Theta}$ were determined in consideration of the effective number of the data points.

As shown in Panels(a) in Fig. 4.12, 4.13 and 4.14, all samples have a positive slope of atomic displacement δz corresponding to the compressive strain from STO substrate. Typical c-lattice spacing of inner LMO region of $(\text{LMO})_7$/STO and $(\text{LMO})_{10}$/STO are 3.91 to 3.92 Å comparable to the FM phase of LMO films, while that of LMO layers around surface region is comparable to 3.94 Å, which suggests AFM phase. The separation of the slope between the A site and B site in surface LMO region means the polarization structure exists in surface region of LMO. This tendency is lost in the center of LMO between interface and surface region for $(\text{LMO})_7$/STO and $(\text{LMO})_{10}$/STO. Focusing on the temperature dependence of $(\text{LMO})_{10}$/STO, the smaller c-lattice spacing at 10K is observed in STO region, while almost the same value of that is recognized in LMO region.

Panels (b) and (e) in Fig. 4.12, 4.13 and 4.14 show the depth dependence of atomic occupancy. The atomic interdiffusion of the LMO/STO interface spreads 2 to 3 layers. The tendency of Ti diffusion into LMO side becomes more remarkable for thicker LMO sample.

Panels (c) and (f) in Fig. 4.12, 4.13 and 4.14 show depth dependence of atomic displacement parameters B. B parameters of all samples increase as Z increases. The larger B values for La than that for Mn was observed in case of GdFeO_3-type octahedral buckling, which is the same structure of bulk LMO. Therefore the in-plane displacement of A-site is expected to remain in LMO region. The larger B value of $(\text{LMO})_{10}$/STO at 10K than 300K is caused by tetragonal $I4/mcm$ distortion of STO from cubic $Pm\bar{3}m$.

Analysis results of energy spectra data of CTR scattering

The ζ dependence of absolute value of C and $F(E = 6.51\text{ keV})$ are presented in Fig. 4.16. We confirmed that the absolute values of C were smaller than that of amplitude F at all ζ points, which means correction C

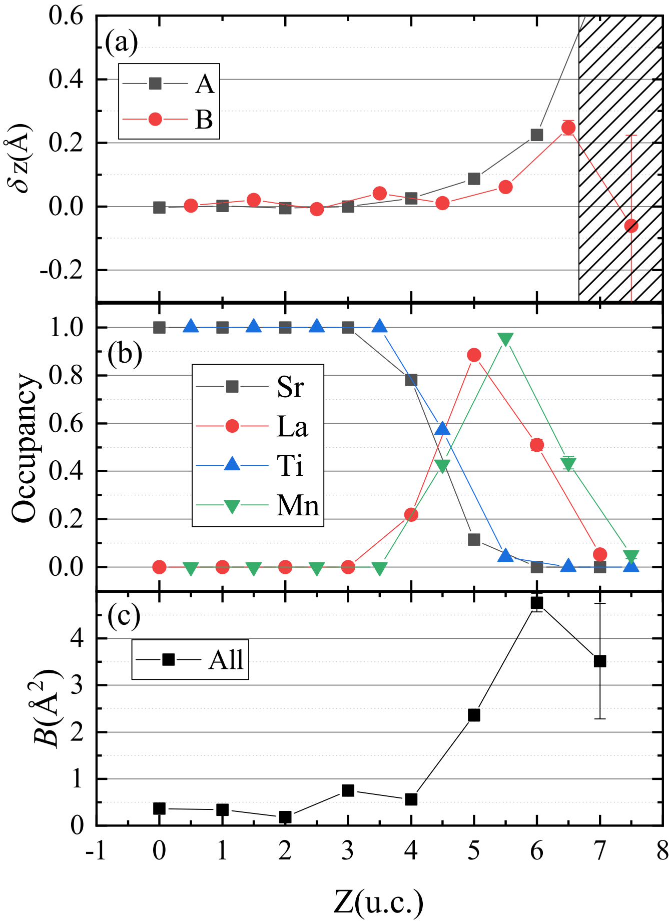

Figure 4.12: Depth dependence of the value of (a)δz, (b)atomic occupancy and (c)B for $(LMO)_2$/STO

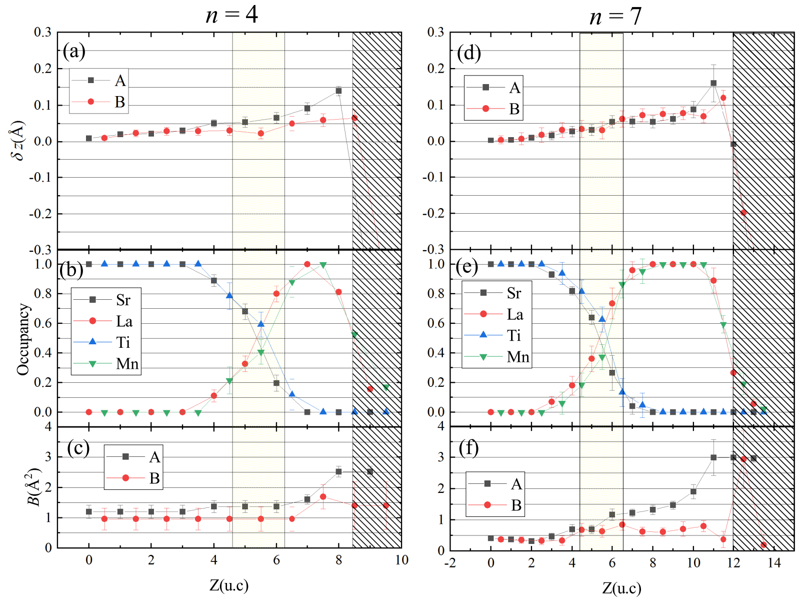

Figure 4.13: Depth dependence of the value of (a, d)δz, (b, e)atomic occupancy and (c, f)B for $(LMO)_4/STO$ and $(LMO)_7/STO$ samples

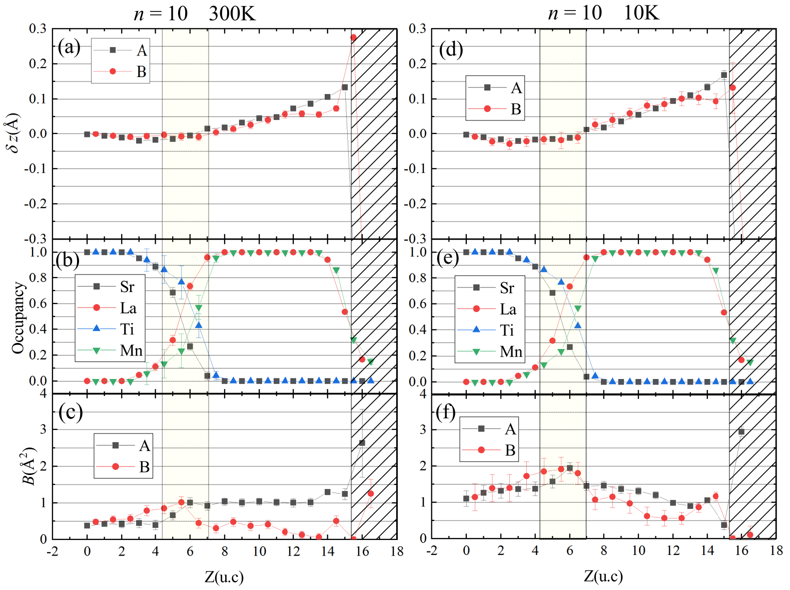

Figure 4.14: Depth dependence of the value of (a)δz, (b)atomic occupancy and (c)B for $(LMO)_{10}/STO$ sample at 300K and 10K

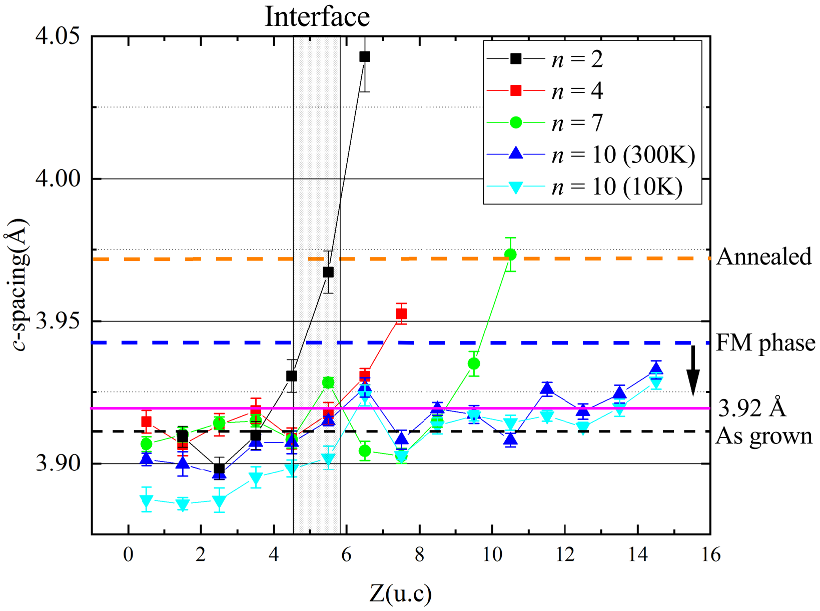

Figure 4.15: Depth dependence of c-lattice spacing defined as the difference of A site position

for non-resonant scattering amplitude F is certainly small and F is generally obtained correctly. All energy spectra of n=4, 7 and 10 sample after adding C are shown in Fig. 4.17, 4.18 and 4.19.

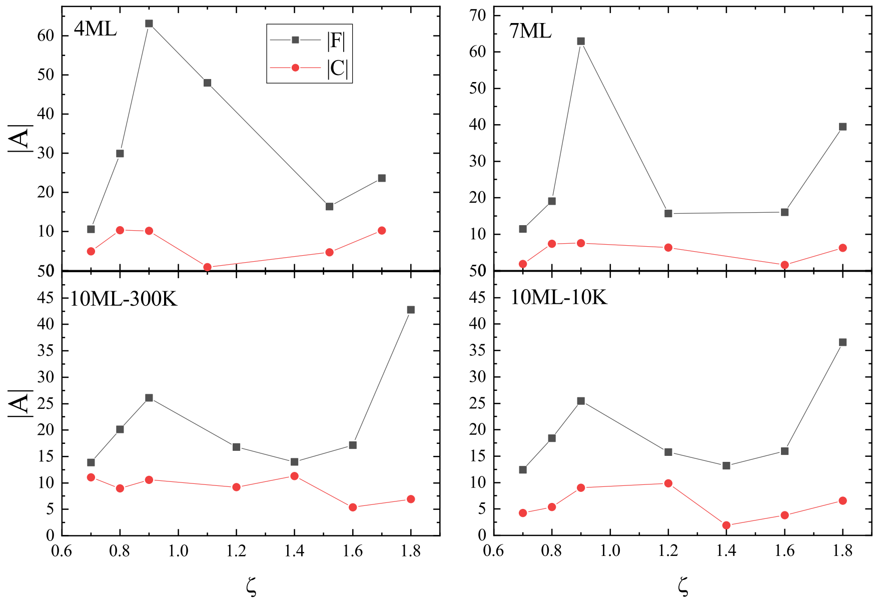

Figure 4.16: ζ dependence of absolute value of scattering amplitude F and added complex number C

We had a difficulty in refining the Mn valence distribution that reproduce the all of CTR spectra well by Bayesian inference. Therefore, we constructed several models with different Mn valence distribution and compared the calculated value with experimental spectra. Then, we selected the best one. The constructed models as a function of depth and calculation from them are shown in Fig. 4.20 to 4.36. From 6 to 7 models with different Mn valence distribution were assumed here. For example, the red solid curve labeled 'Model-2P' assume the accumulated Mn^{2+} around LMO/STO interface indicated in Ref. [103].

The best answer models of Mn valence distribution for (LMO)$_7$/STO and (LMO)$_{10}$/STO are shown in Fig. 4.39. For (LMO)$_4$/STO, the energy spectra calculated from 6 assumed models were not improved from no valence modulation model shown in Fig. 4.17. Therefore, we could not pick up the best answer of Mn valence distribution. For (LMO)$_7$/STO, Model-2P/4P is the best. The models 'Model-2P' and 'Model-2P/4P' reproduce

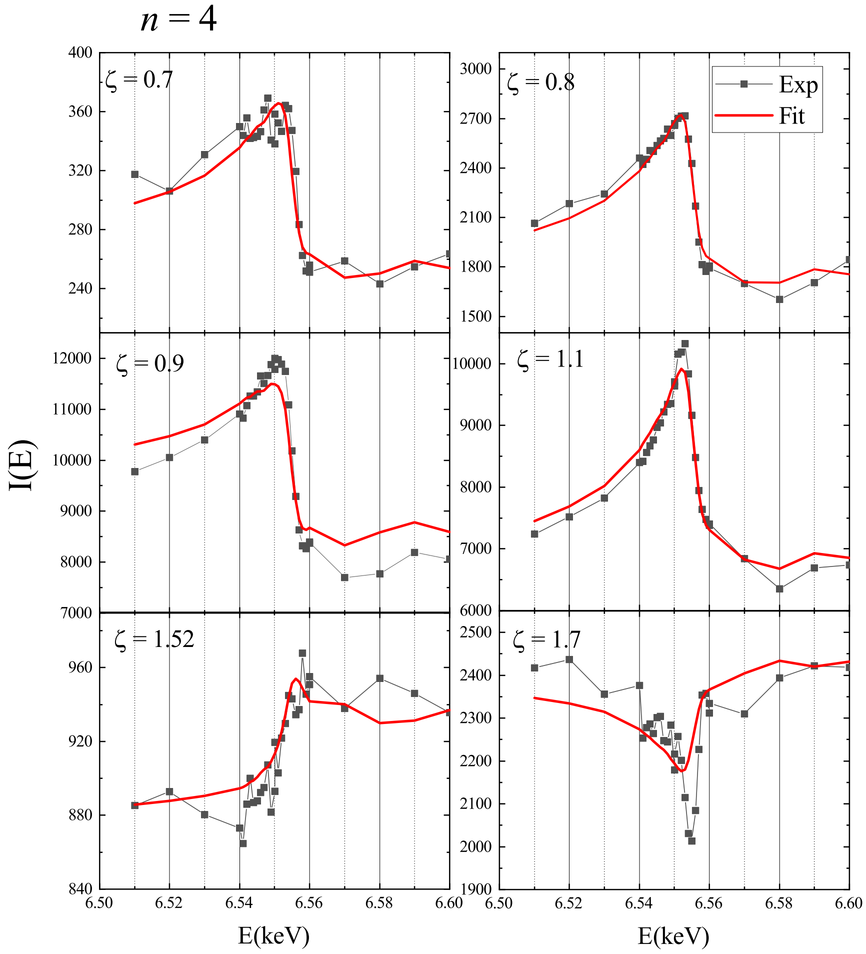

Figure 4.17: Energy spectra of CTR scattering at 00ζ for $(\mathrm{LMO})_4/\mathrm{STO}$. Black plots are experimental value. The red solid curve is calculated value after adding C.

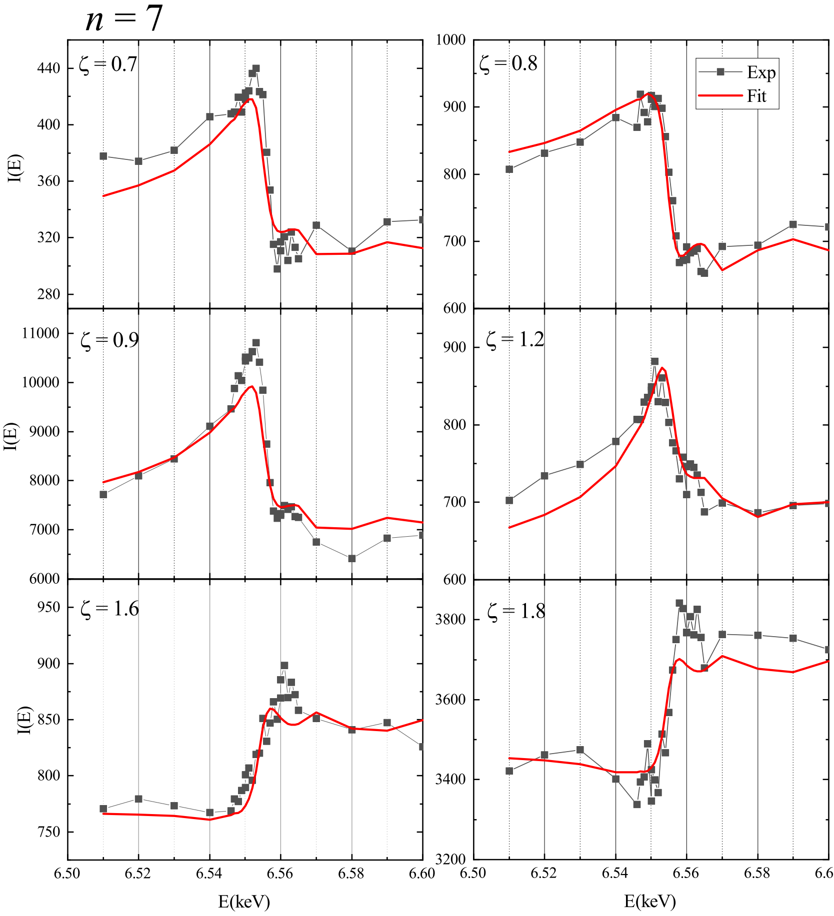

Figure 4.18: Energy spectra of CTR scattering at 00ζ for $(LMO)_7/STO$.

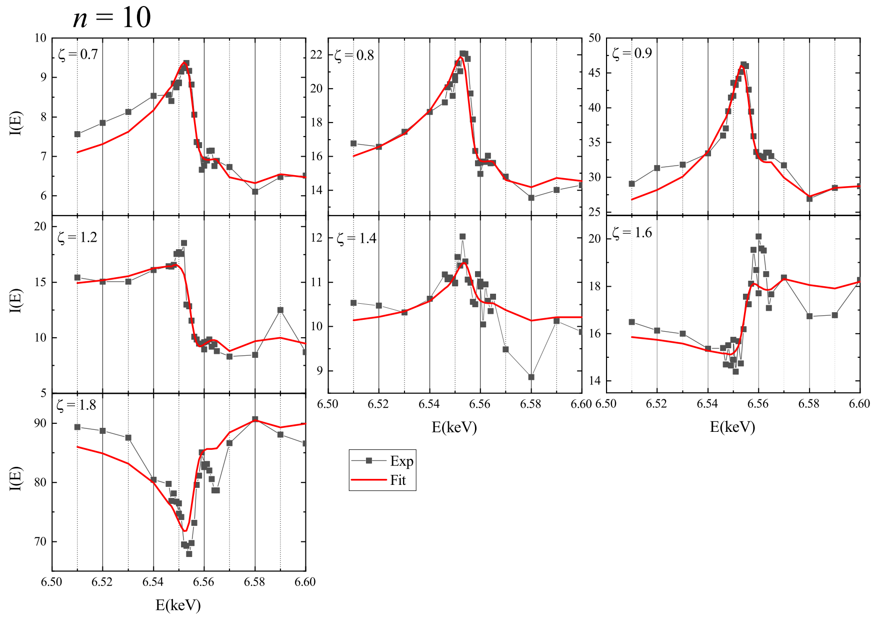

Figure 4.19: Energy spectra of CTR scattering at 00ζ for $(\mathrm{LMO})_{10}/\mathrm{STO}$.

the sharp peaks around $E = 6.54$ to 6.56 keV at $\zeta = 0.9$, 1.6 and 1.8 derived from the localization of Mn^{2+} around the LMO/STO interface. At $\zeta = 1.2$, the energy spectrum is reproduced by 'Model-2P/4P' better than 'Model-2P'. The Mn^{4+} state is located not in interface but in the middle of LMO region. The same tendency of Mn valence distribution was observed for $(\mathrm{LMO})_{10}/\mathrm{STO}$. The models having Mn^{2+} at the interface captured the tendency of the sharp peaks around 6.54 to 6.56 keV of spectra at $\zeta = 1.2$, 1.4 and 1.6.

The models of 'Model-2P-2' for $(\mathrm{LMO})_4/\mathrm{STO}$, 'Model-2P-3' for $(\mathrm{LMO})_7/\mathrm{STO}$ and 'Model-2P-2' for $(\mathrm{LMO})_{10}/\mathrm{STO}$ assume the electron accumulation of Mn at the surface. However, these models were rejected. The lattice expansion at the surface region should not be caused by the Coulomb repulsion of increasing Mn^{2+}.

The models of 'Model-2P/4P-2' for $n = 4$, 7 and 10 samples are also rejected. These results indicate that accumulation of Mn^{2+} at the interface is not described by a simple self-dope model assuming homogeneous structure and homogeneous internal electronic field of LMO reported in Ref.[103, 112].

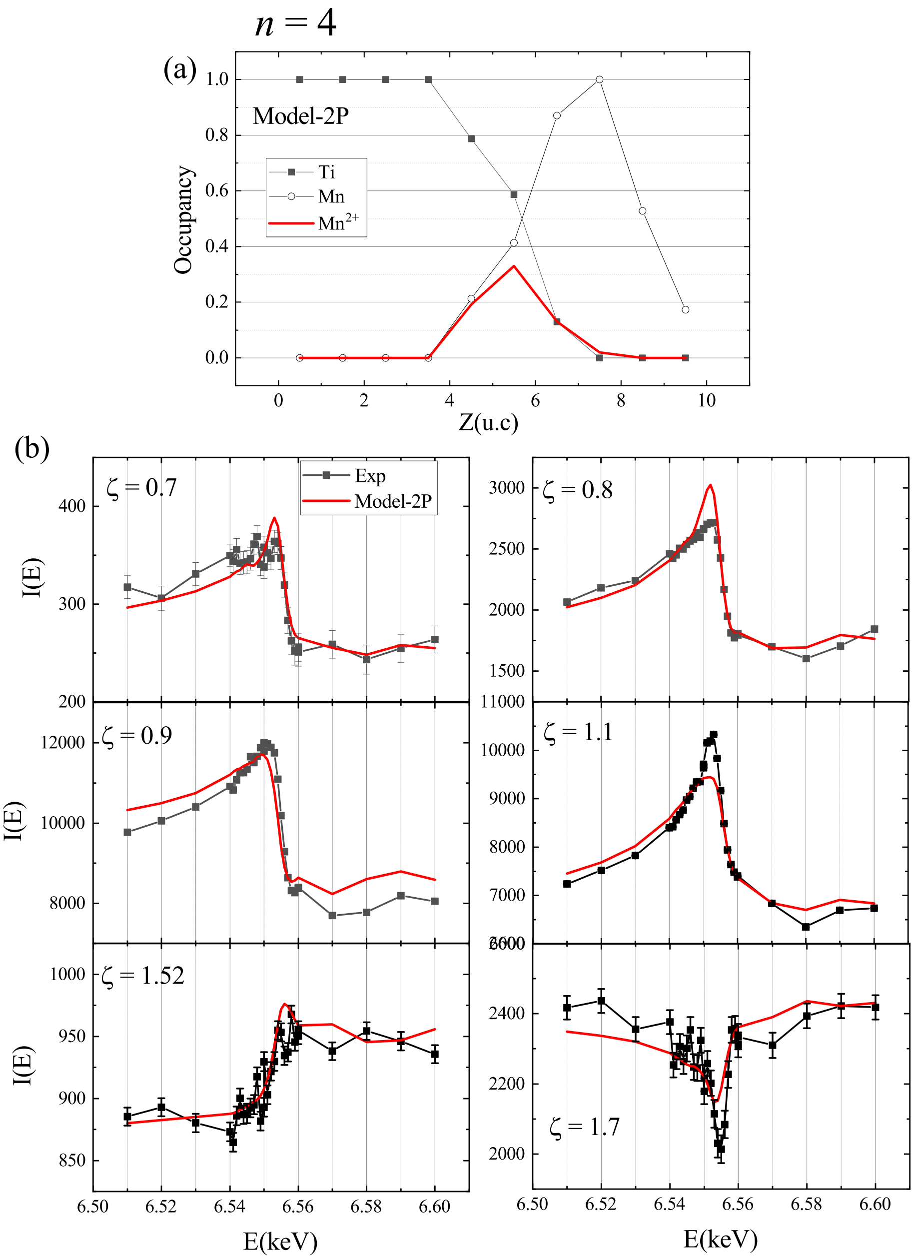

Figure 4.20: (a)The depth dependence of B site atomic occupancy of 'Model-2P' for $(LMO)_4/STO$ was plotted. 'Ti' and 'Mn' represents the total atomic occupancy. The Mn^{2+} distribution are drawn by red solid line. (b)The intensity profiles of energy spectra. The black plots are experimental values. Solid curves are calculated value from Model-2P model.

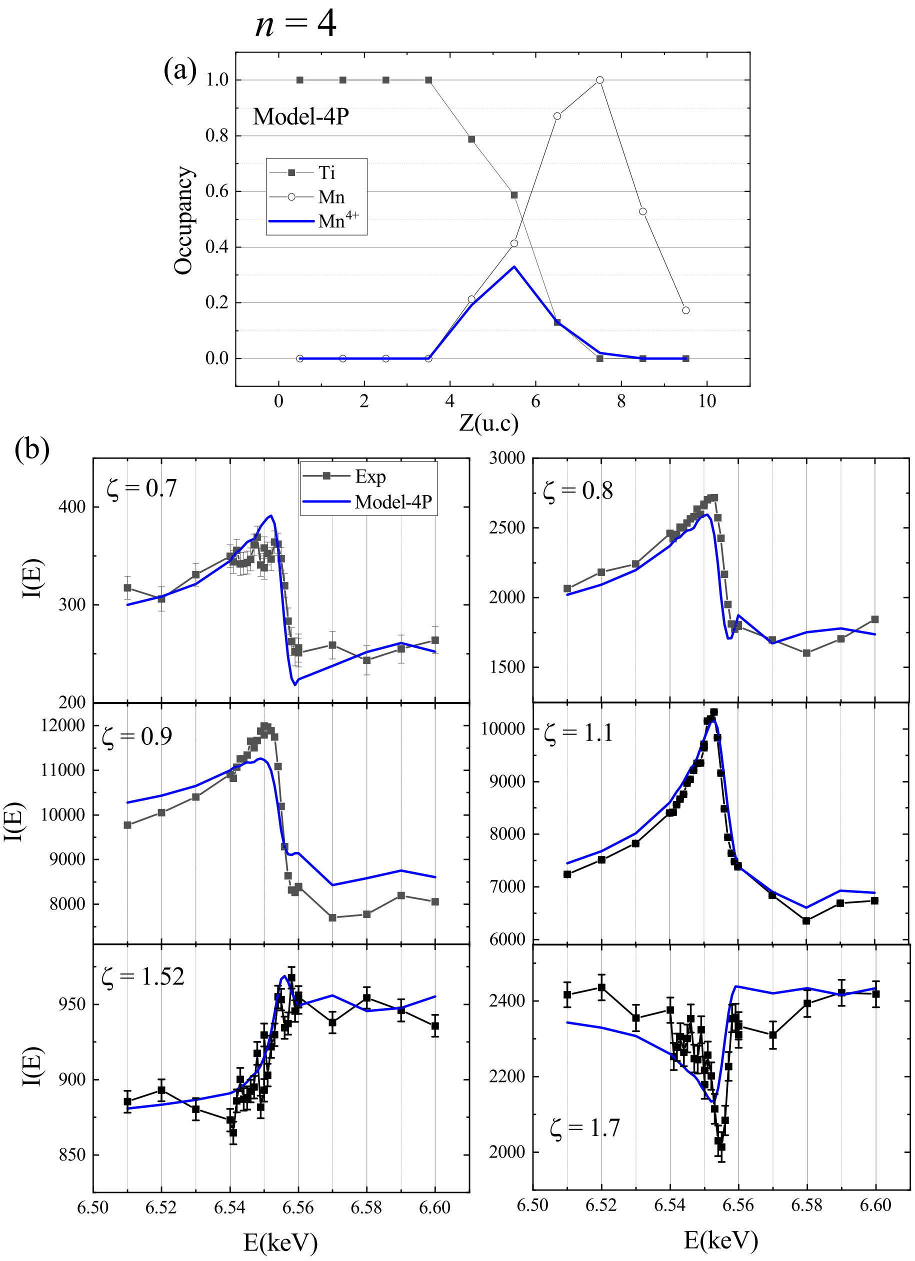

Figure 4.21: (a)The depth dependence of B site atomic occupancy of 'Model-4P' for $(LMO)_4/STO$. The Mn^{4+} distribution are drawn by blue solid line. (b)The intensity profiles of energy spectra.

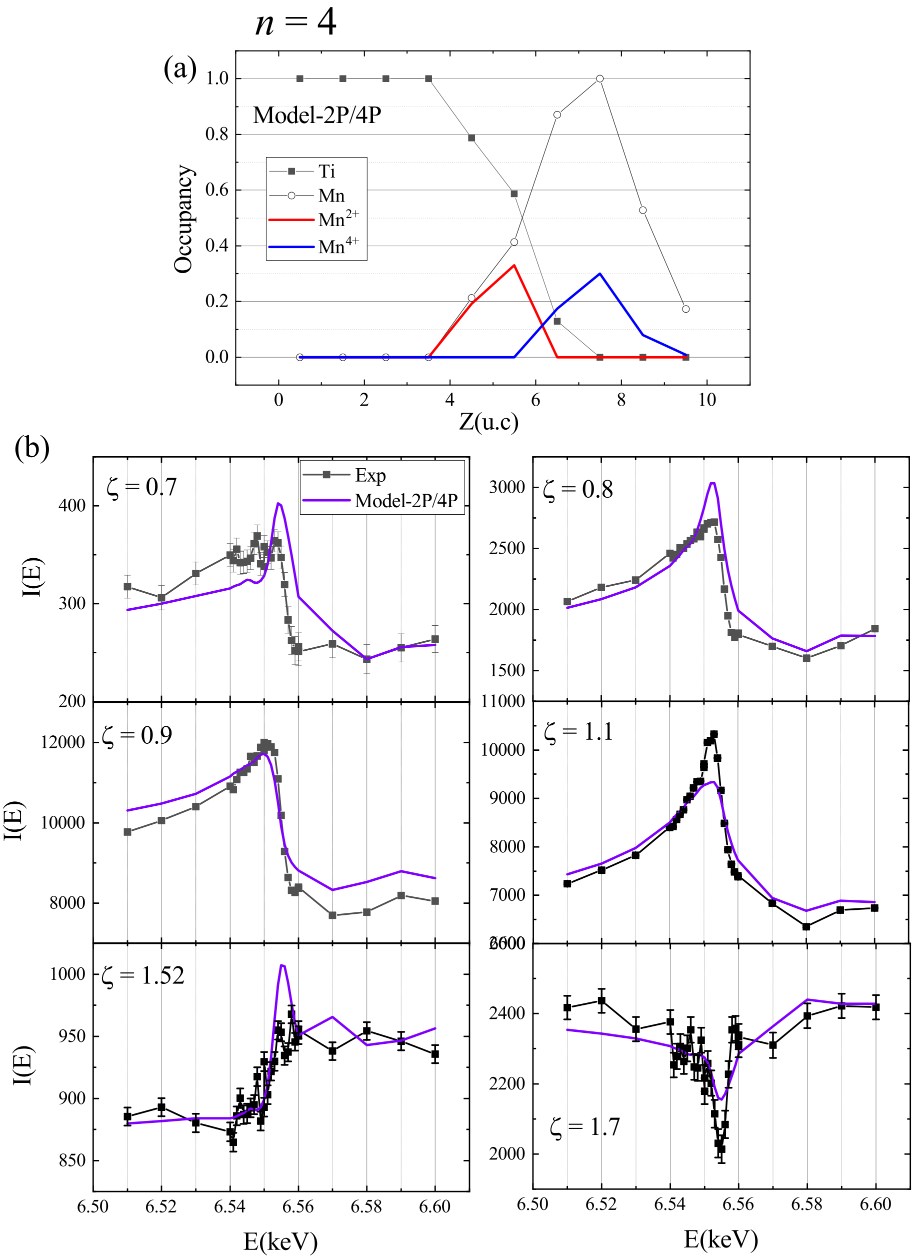

Figure 4.22: (a)The depth dependence of B site atomic occupancy of 'Model-2P/4P' for $(LMO)_4/STO$. (b)The intensity profiles of energy spectra.

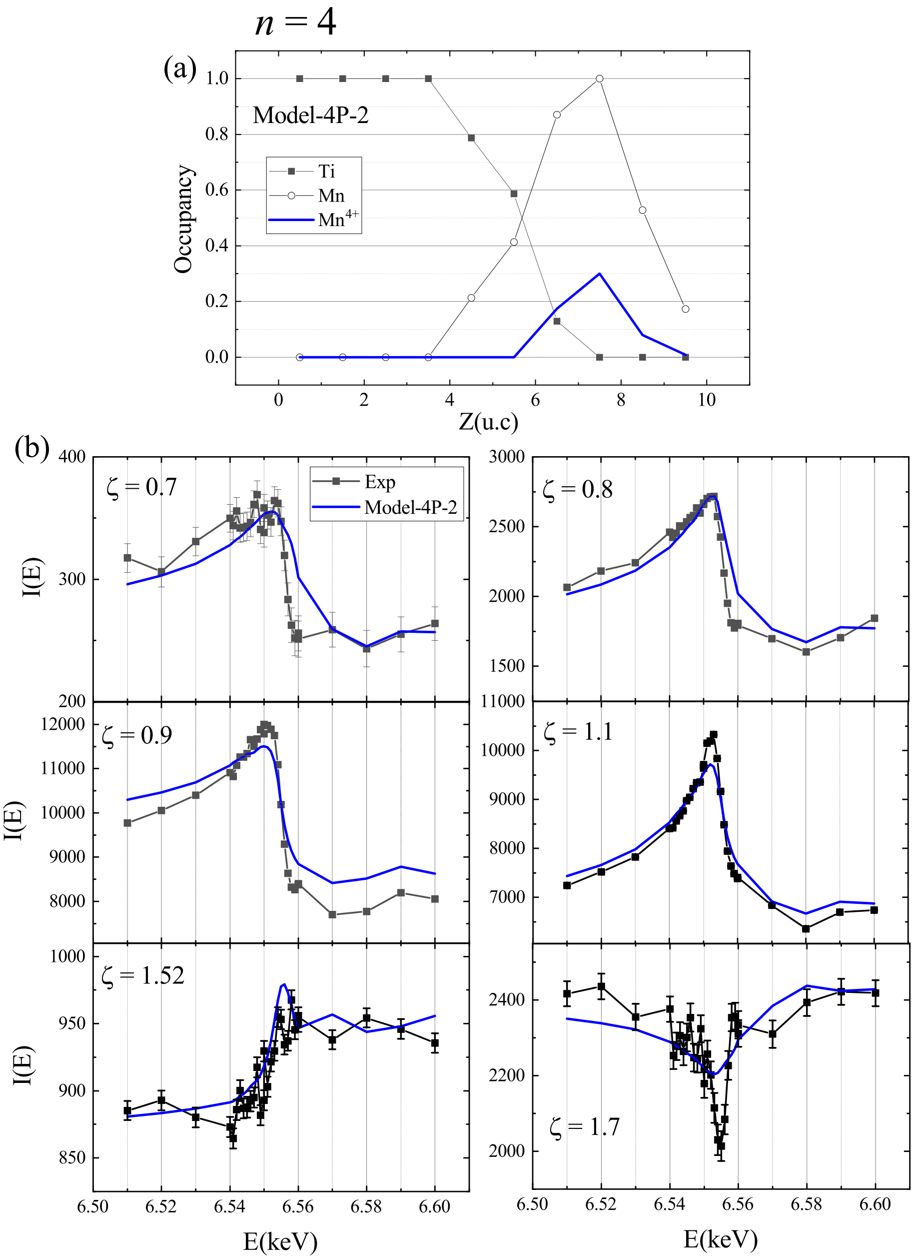

Figure 4.23: (a)The depth dependence of B site atomic occupancy of 'Model-4P-2' for $(LMO)_4/STO$. (b)The intensity profiles of energy spectra.

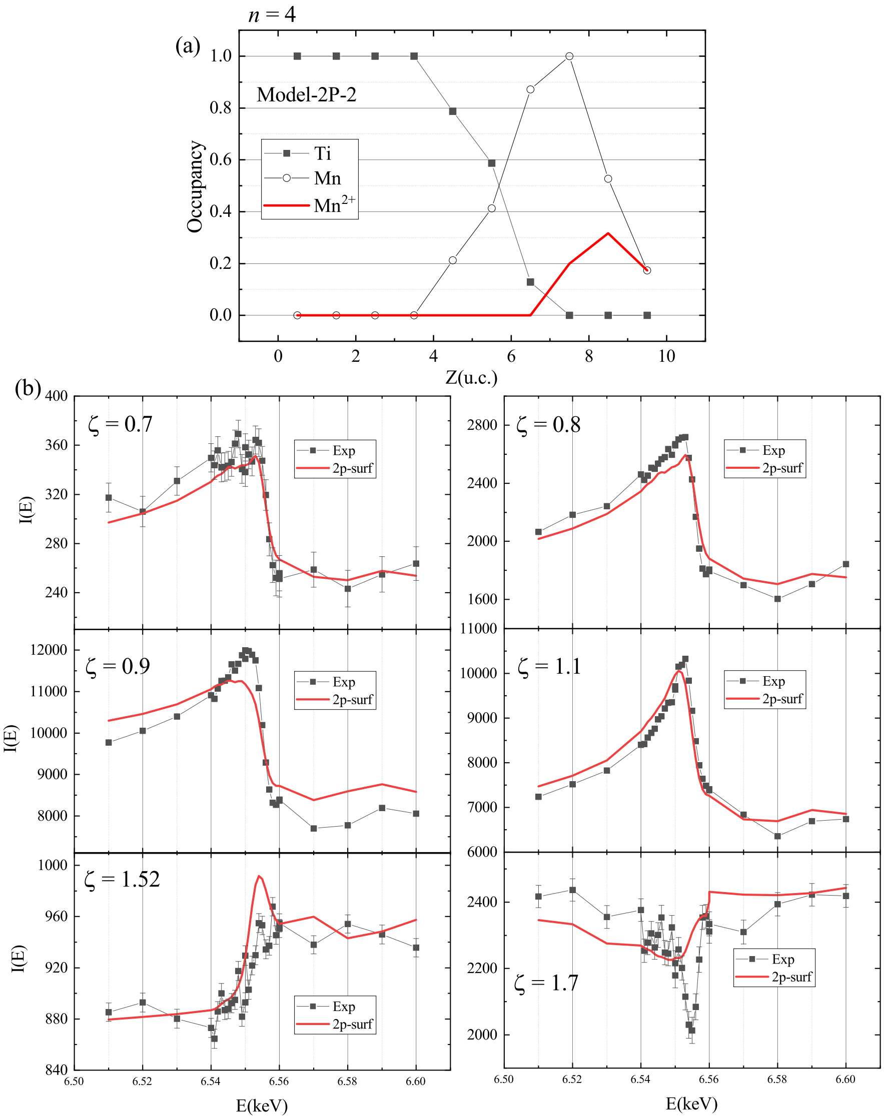

Figure 4.24: (a)The depth dependence of B site atomic occupancy of 'Model-2P-2' for $(LMO)_4/STO$. (b)The intensity profiles of energy spectra.

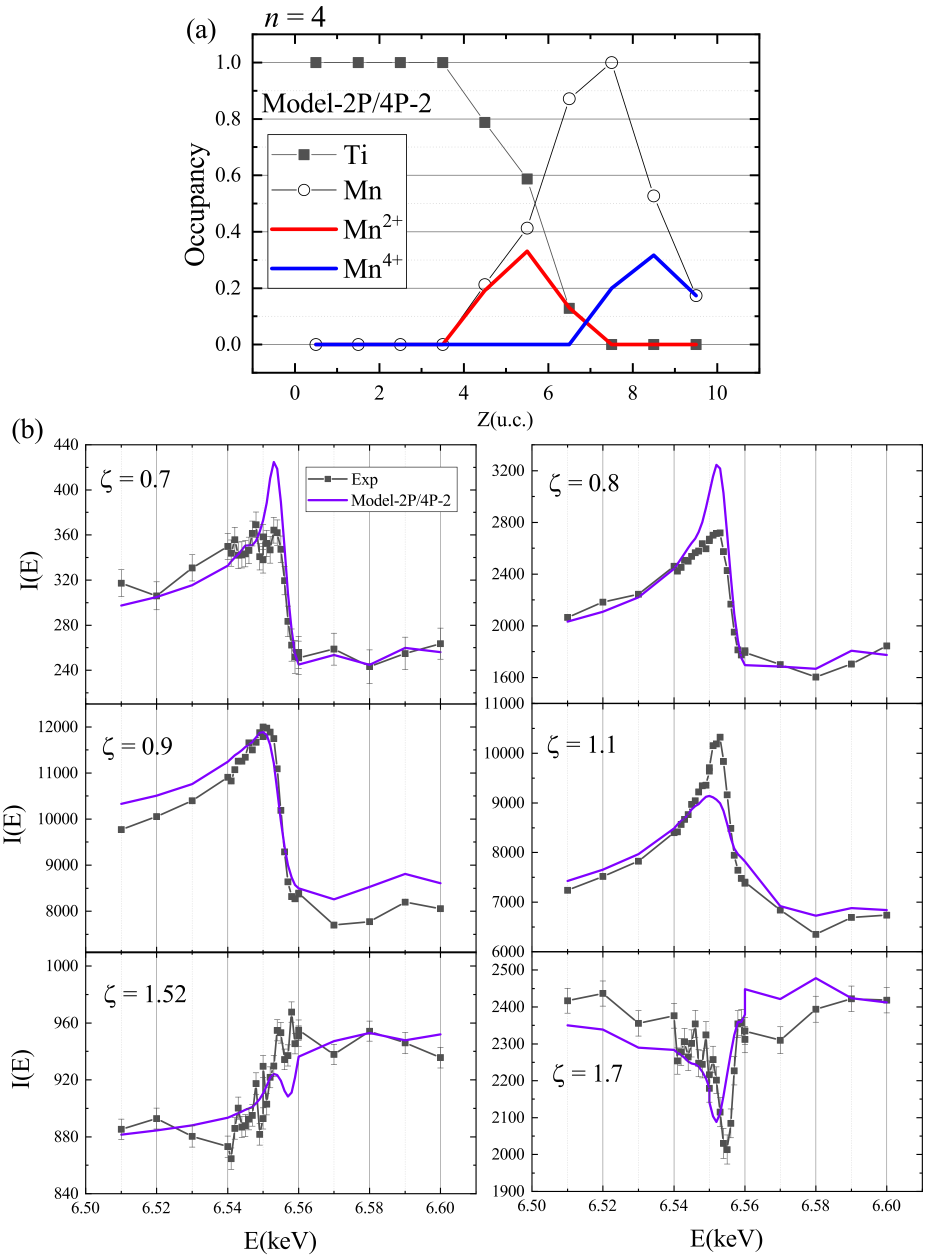

Figure 4.25: (a)The depth dependence of B site atomic occupancy of 'Model-2P/4P-2' for $(LMO)_4/STO$. (b)The intensity profiles of energy spectra.

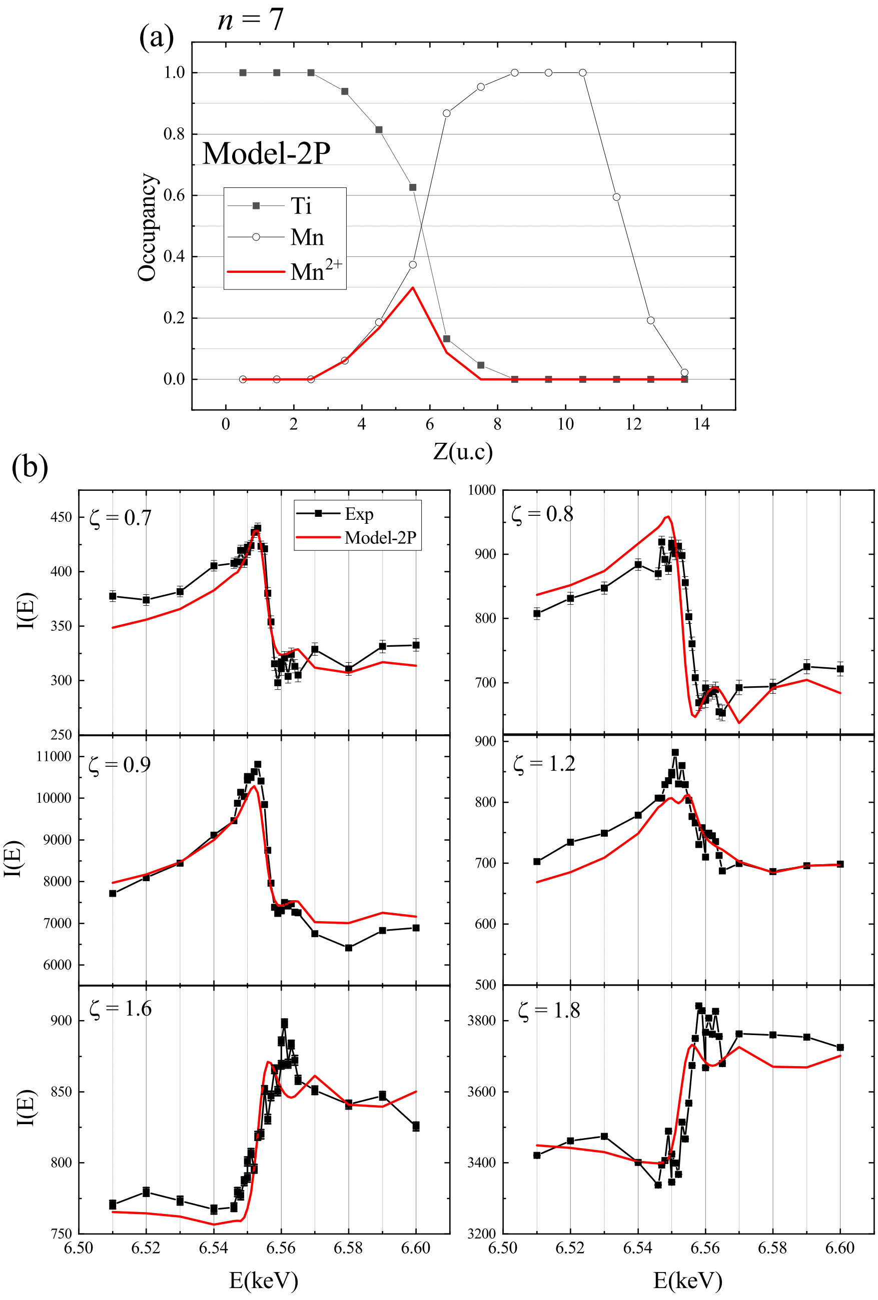

Figure 4.26: The depth dependence of B site atomic occupancy of 'Model-2P' for $(LMO)_7/STO$. (b)The intensity profiles of energy spectra.

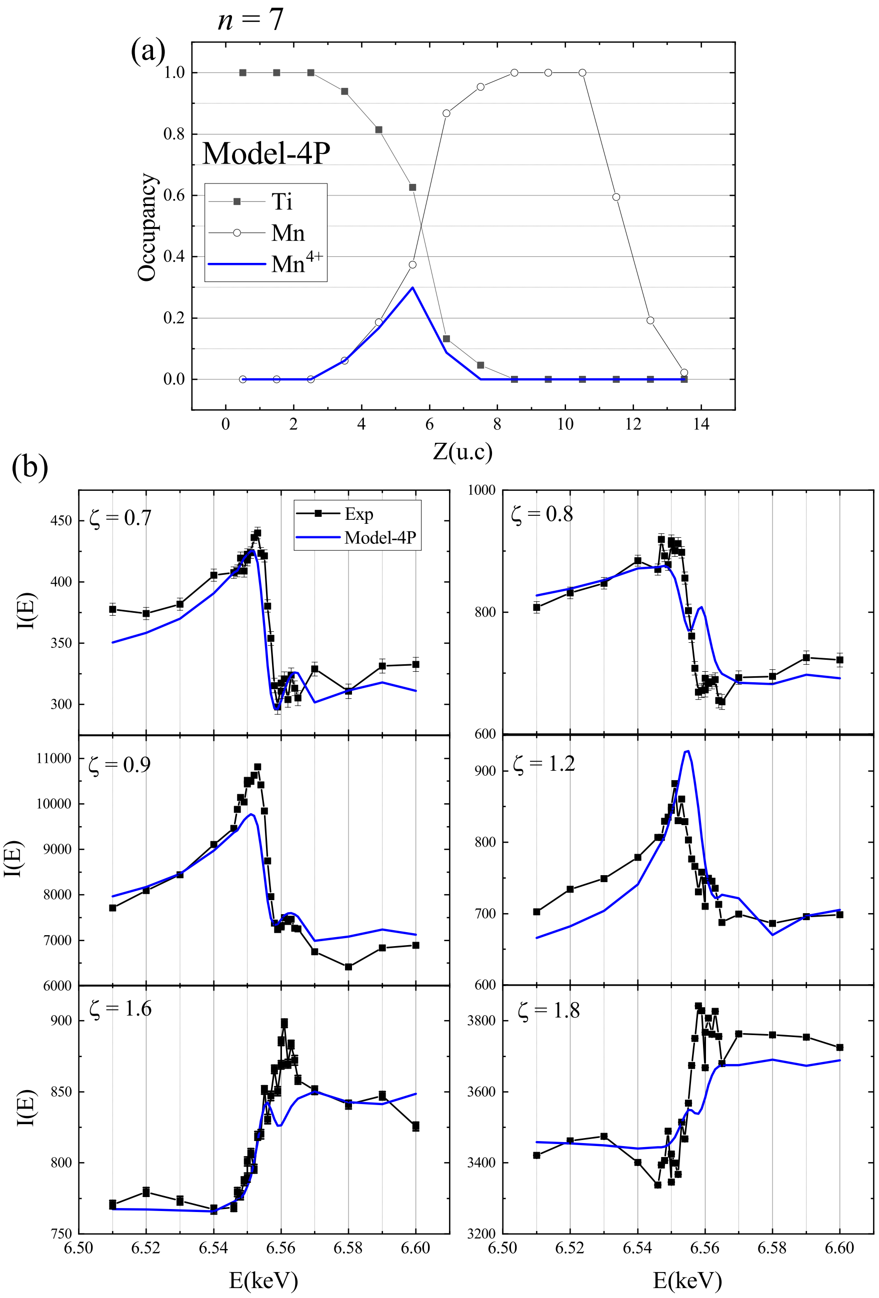

Figure 4.27: (a)The depth dependence of B site atomic occupancy of 'Model-4P' for $(LMO)_7/STO$. (b)The intensity profiles of energy spectra.

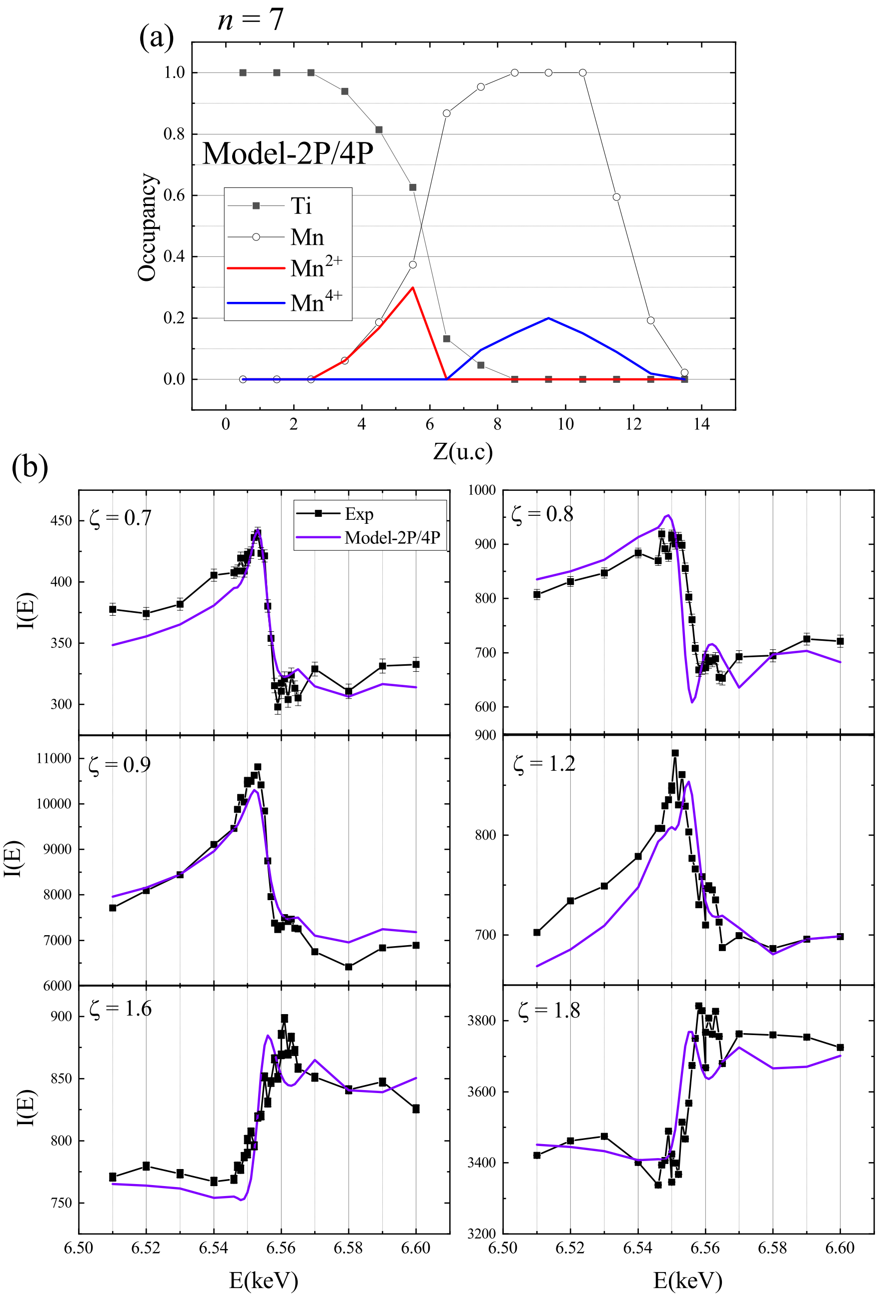

Figure 4.28: (a)The depth dependence of B site atomic occupancy of 'Model-2P/4P' for (LMO)$_7$/STO. (b)The intensity profiles of energy spectra.

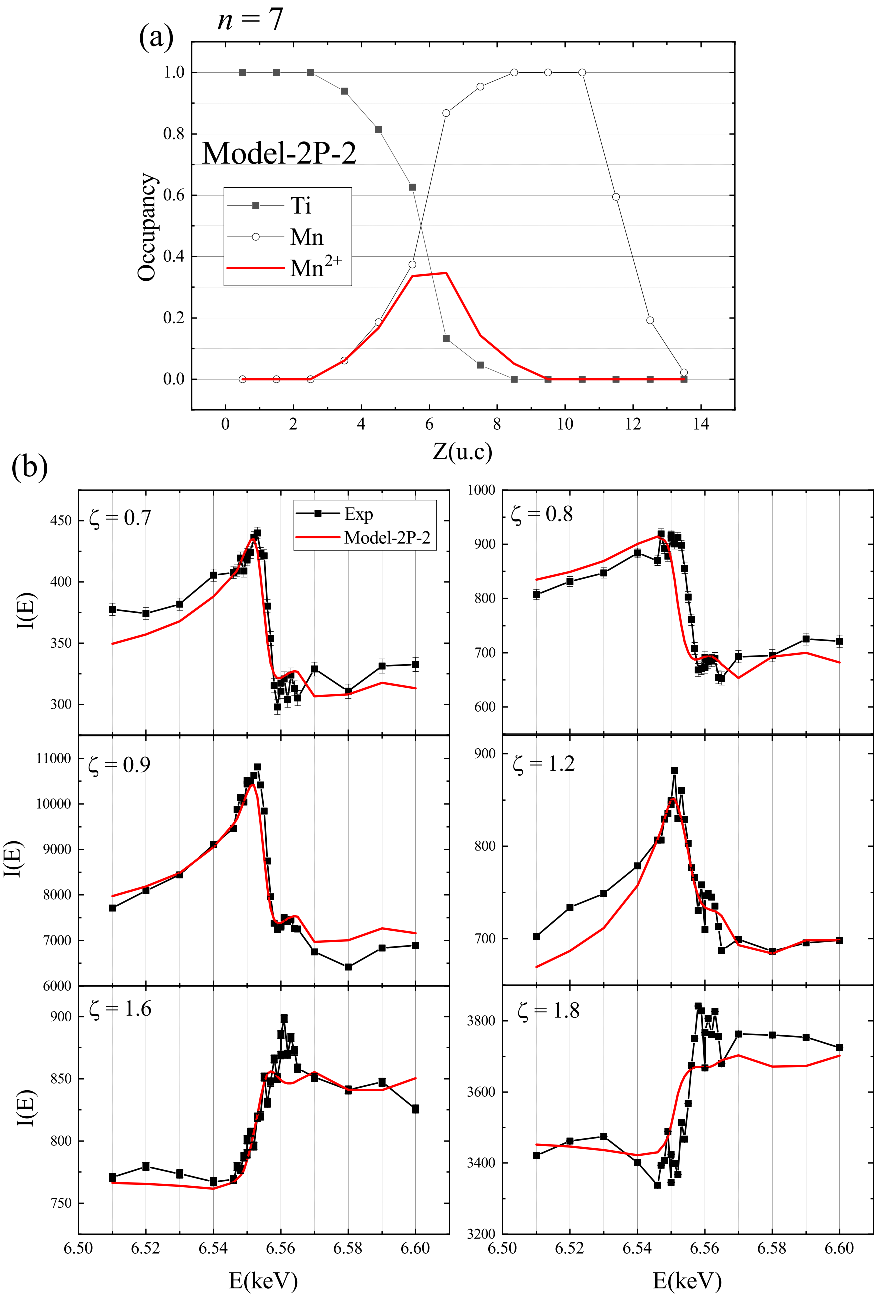

Figure 4.29: (a)The depth dependence of B site atomic occupancy of 'Model-2P-2' for $(LMO)_7/STO$. (b)The intensity profiles of energy spectra.

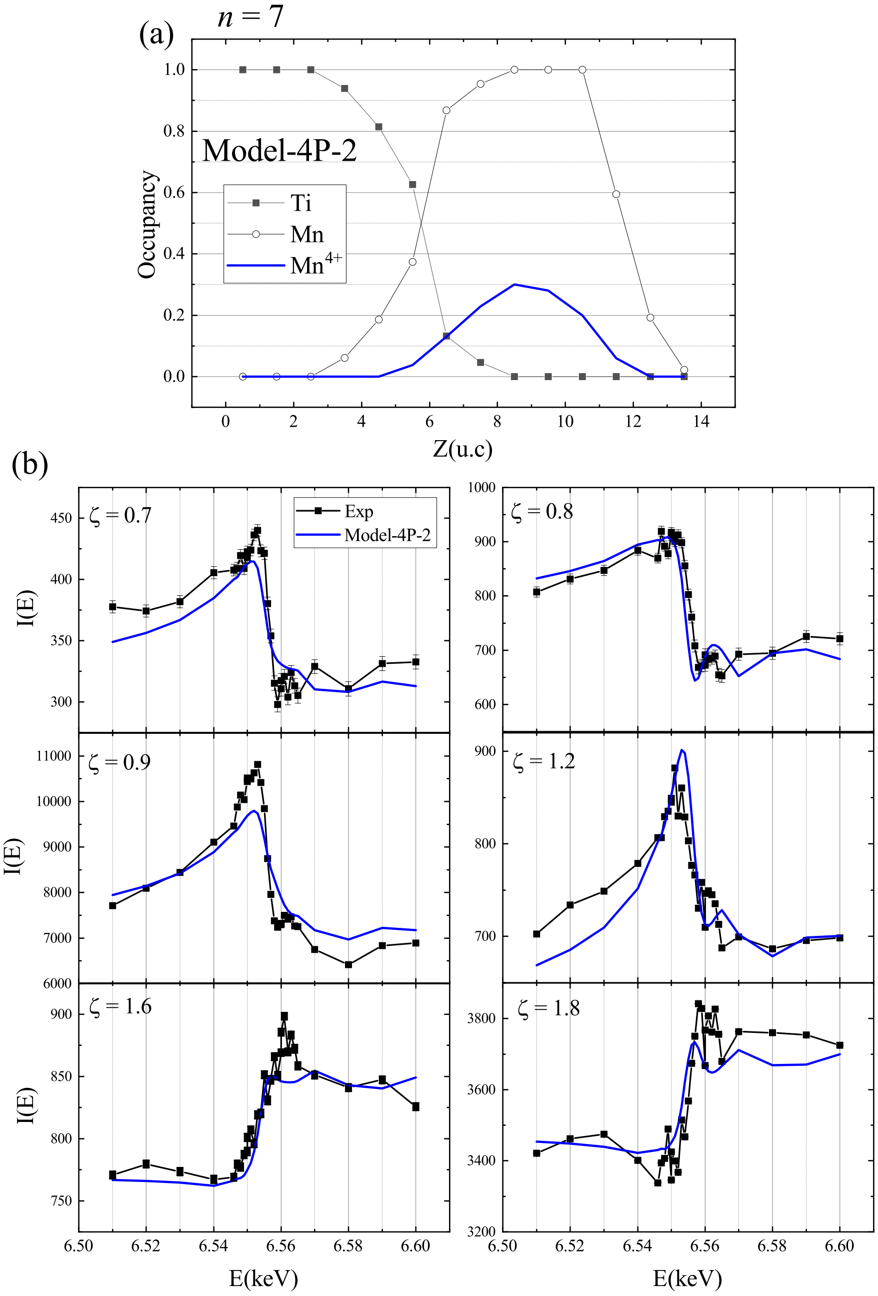

Figure 4.30: (a)The depth dependence of B site atomic occupancy of 'Model-4P-2' for (LMO)$_7$/STO. (b)The intensity profiles of energy spectra.

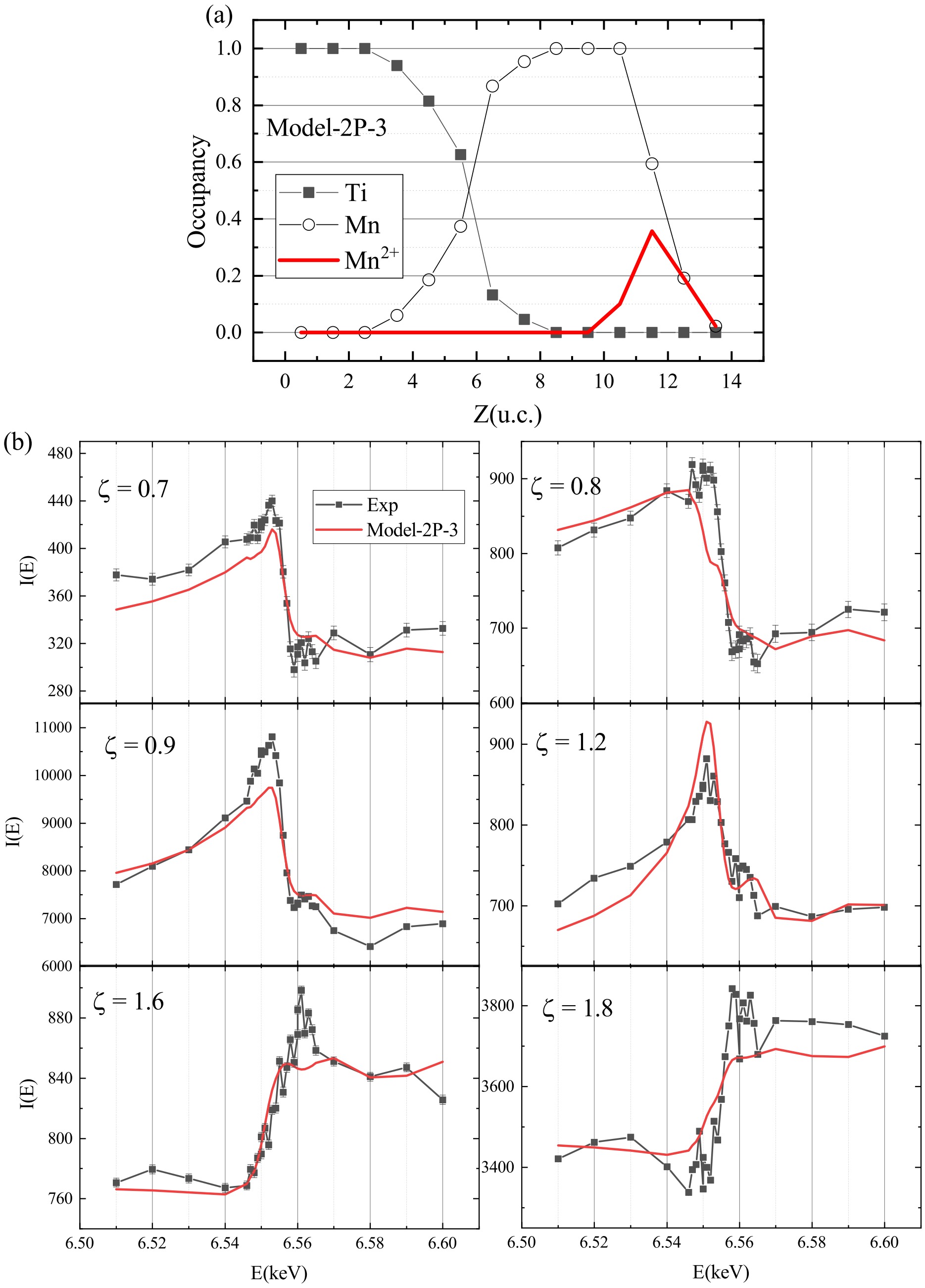

Figure 4.31: (a)The depth dependence of B site atomic occupancy of 'Model-2P-3' for $(LMO)_7/STO$. (b)The intensity profiles of energy spectra.

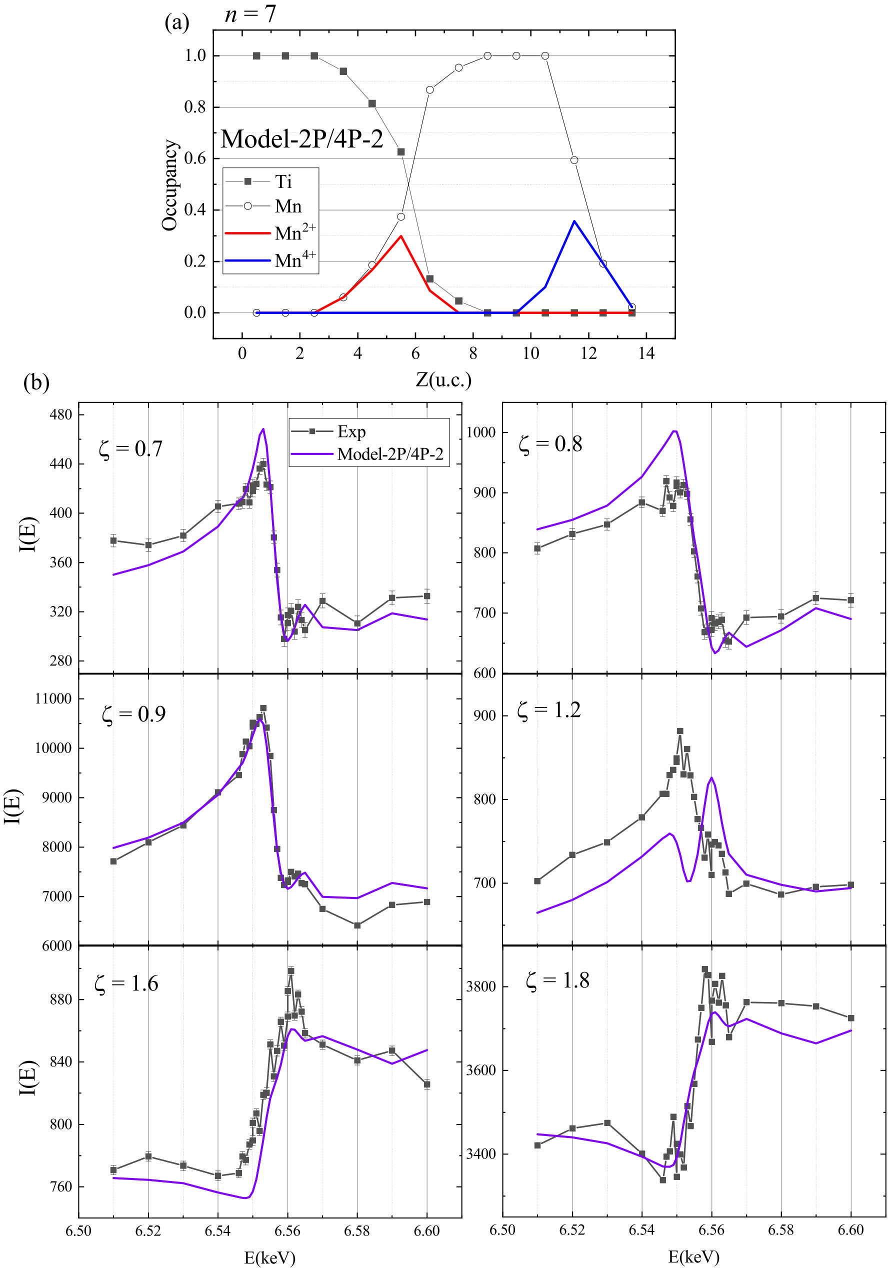

Figure 4.32: (a)The depth dependence of B site atomic occupancy of 'Model-2P/4P-2' for $(LMO)_7/STO$. (b)The intensity profiles of energy spectra.

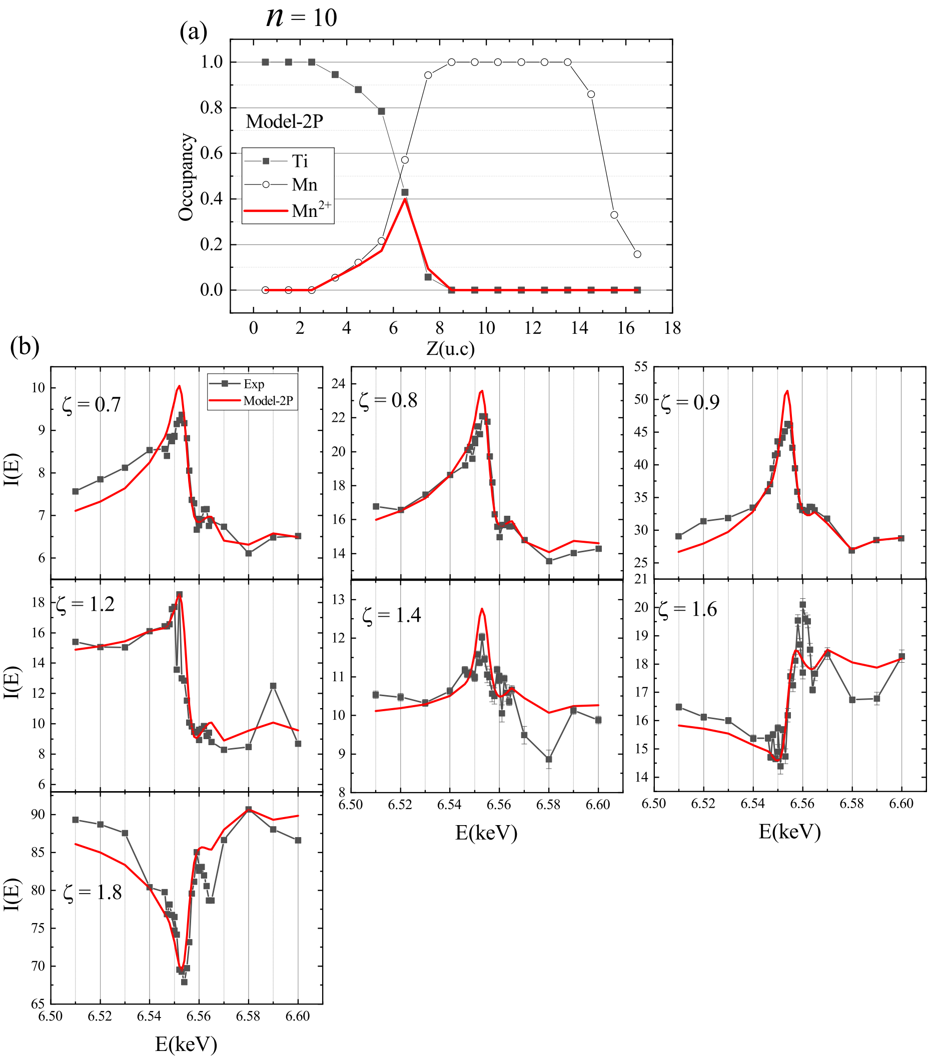

Figure 4.33: The depth dependence of B site atomic occupancy of 'Model-2P' for $(LMO)_{10}/STO$. (b)The intensity profile of energy spectra.

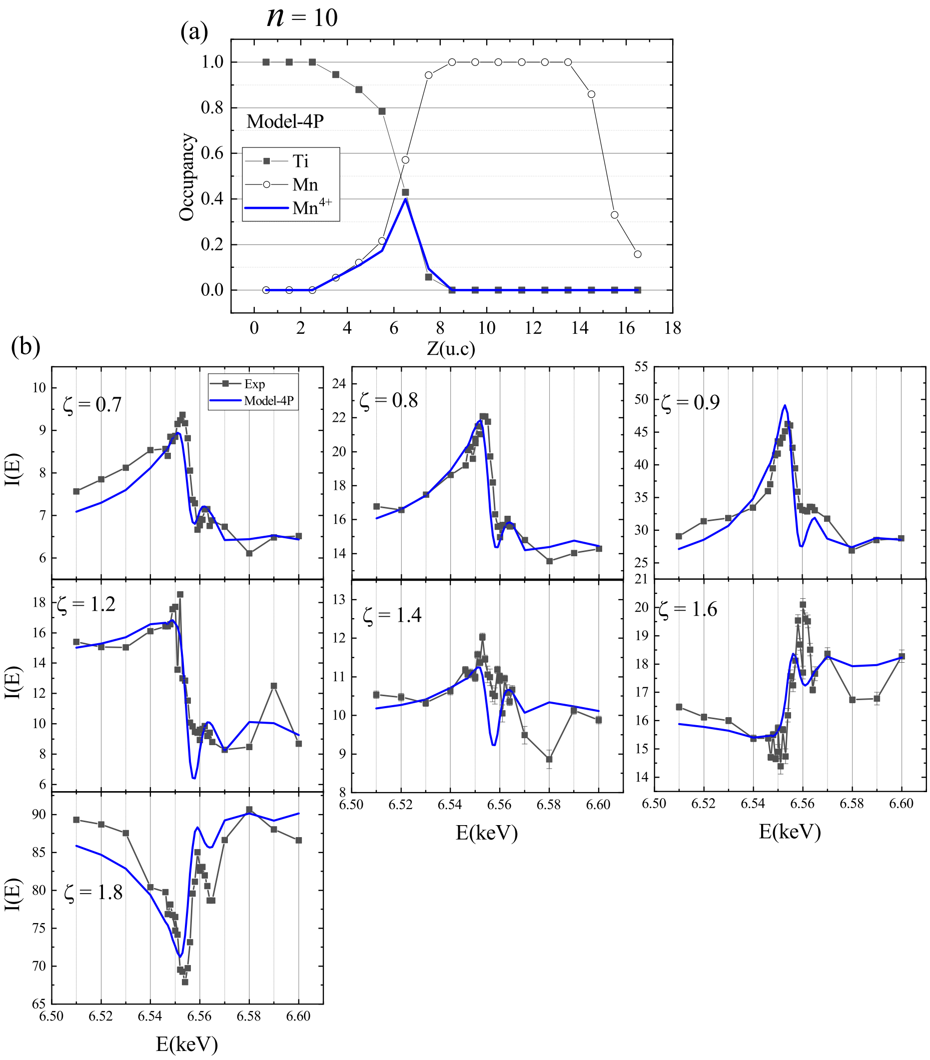

Figure 4.34: (a)The depth dependence of B site atomic occupancy of 'Model-4P' for (LMO)$_{10}$/STO. (b)The intensity profiles of energy spectra.

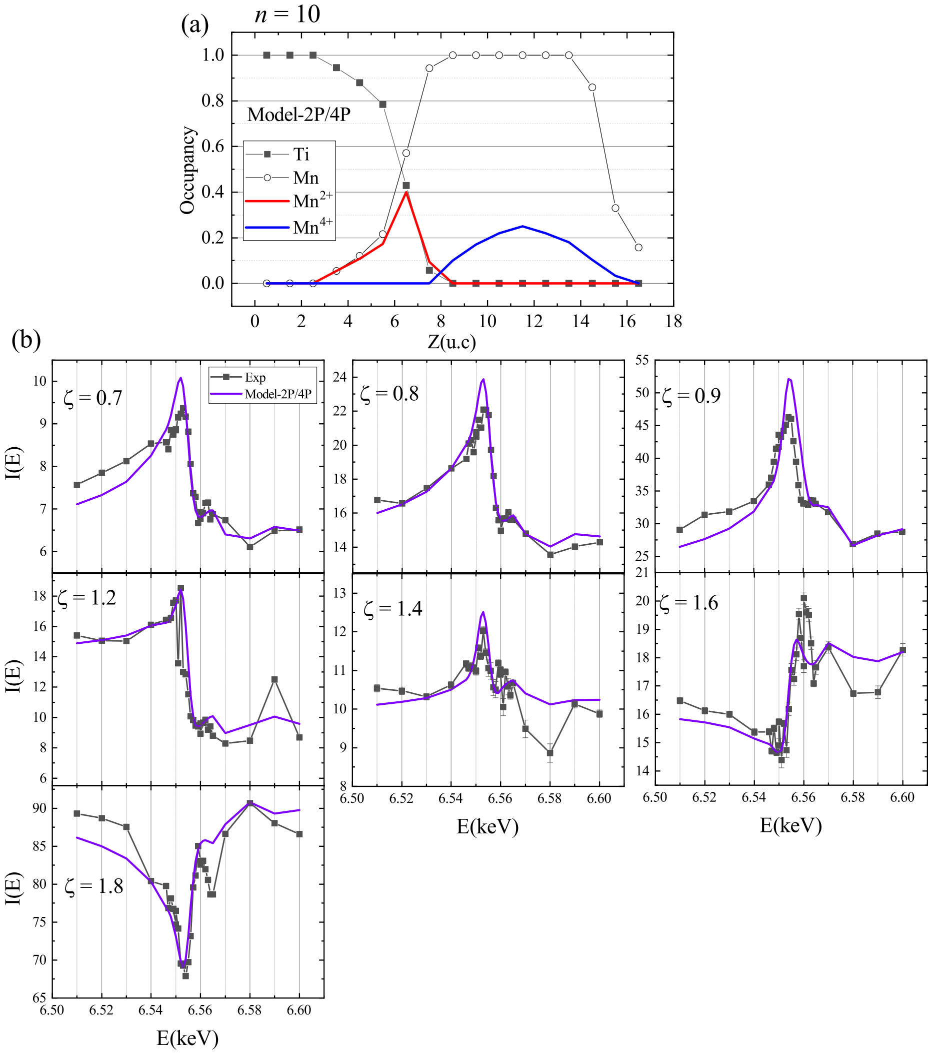

Figure 4.35: (a)The depth dependence of B site atomic occupancy of 'Model-2P/4P' for $(LMO)_{10}/STO$. (b)The intensity profiles of energy spectra.

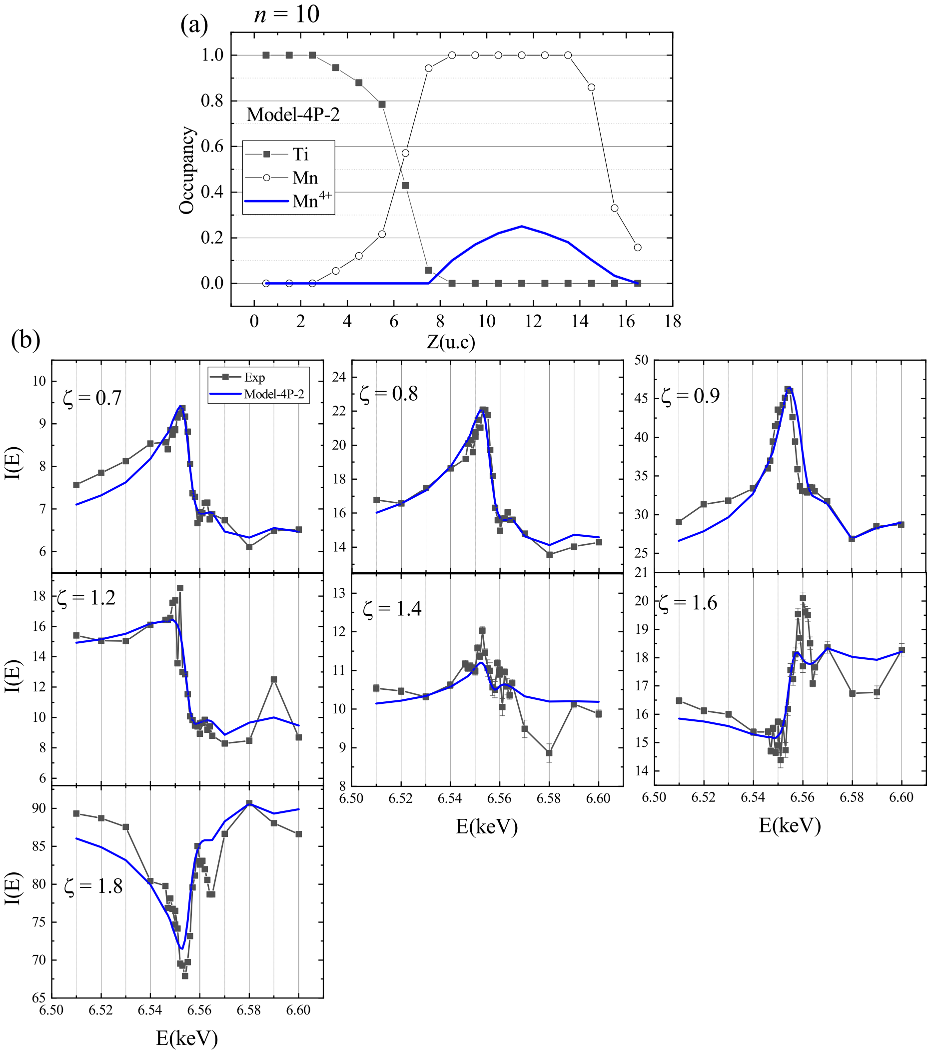

Figure 4.36: (a)The depth dependence of B site atomic occupancy of 'Model-4P-2' for (LMO)$_{10}$/STO. (b)The intensity profiles of energy spectra.

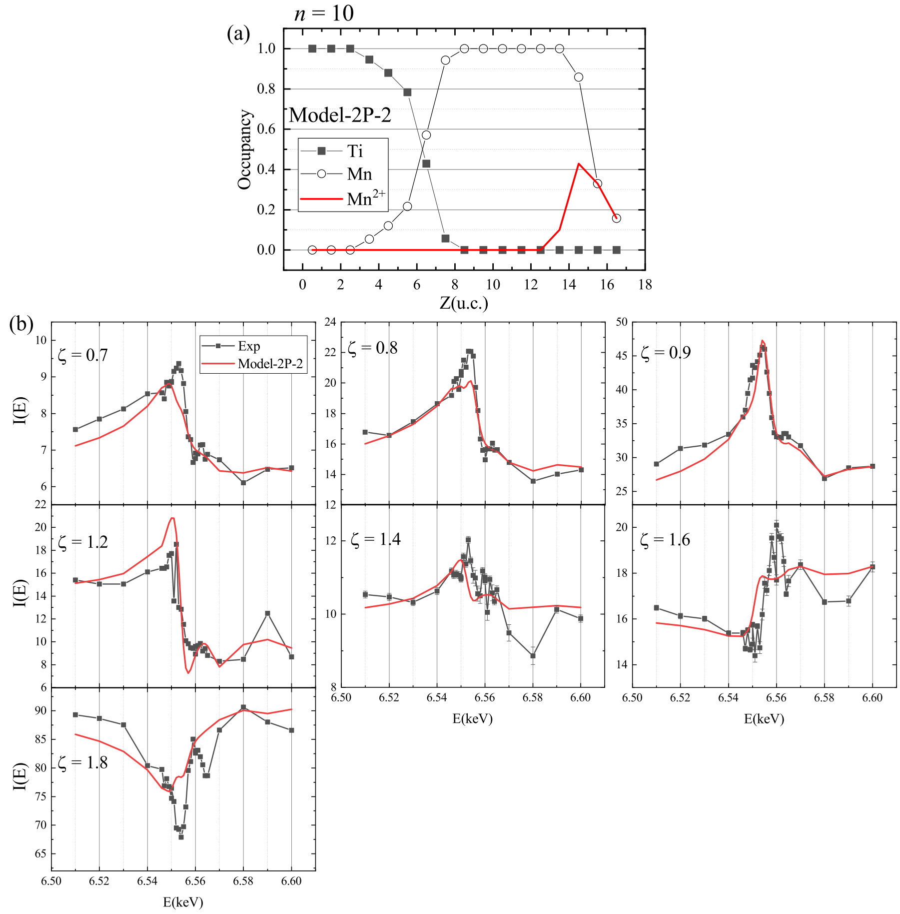

Figure 4.37: (a)The depth dependence of B site atomic occupancy of 'Model-2P-2' for $(LMO)_{10}/STO$. (b)The intensity profiles of energy spectra.

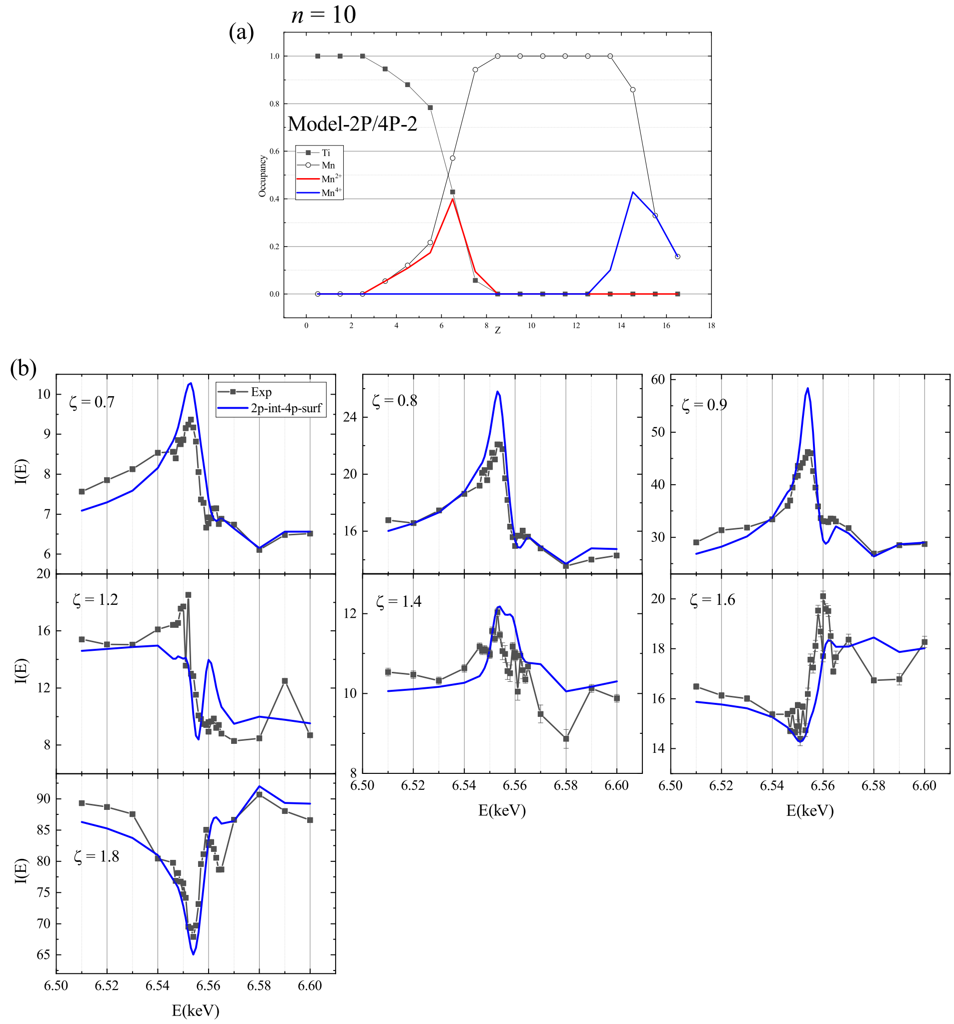

Figure 4.38: (a)The depth dependence of B site atomic occupancy of 'Model-2P/4P-2' for (LMO)$_{10}$/STO. (b)The intensity profiles of energy spectra.

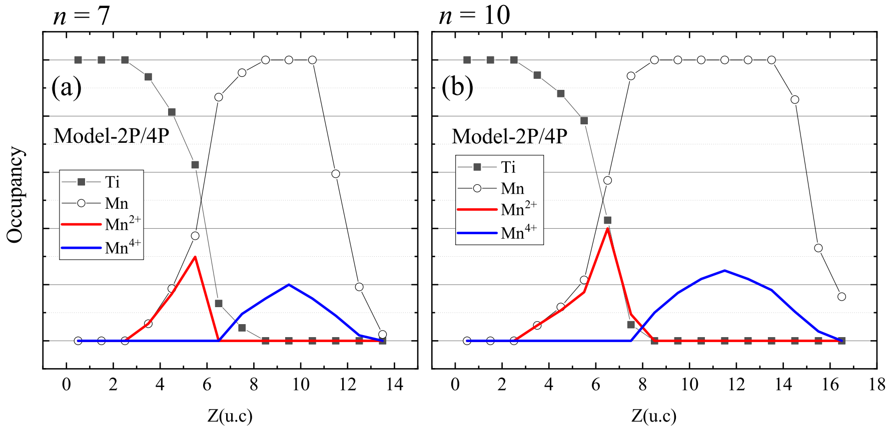

Figure 4.39: The best Mn valence distribution models of (a)$(LMO)_7$/STO and (b)$(LMO)_{10}$/STO.

4.4 Discussion

Thick LMO/STO samples usually exhibit ferromagnetism [103, 112, 120, 121, 123] while the ferromagnetism of less than 5 u.c. thick LMO/STO samples are suppressed[103, 112]. Here, this thickness dependence is discussed from the analysis results of structure and Mn valence distribution.

4.4.1 Structural aspects

Let us discuss the structural aspects of thickness dependence of LMO/STO(Fig. 4.15) A common feature of the structure for all LMO/STO samples is the existence of expanded layer at the top surface LMO layer. The value of c-lattice spacing is comparable to that of AFM samples(3.94 Å ∼). The expanded c-lattice spacing is accompanied with $3z^2 - r^2$ orbital polarization due to JT effect. The stabilized $3z^2 - r^2$ orbital would strengthen the C-type AFM coupling of LMO. The thinner $(LMO)_2$/STO and $(LMO)_4$/STO are composed of such expanded layers, so they do not exhibit the ferromagnetism. Indeed, the expanded region have different δz of La and Mn, suggesting the existence of electric polarization and weakened double exchange interaction. The XLD study in Ref.[137] reports that the $3z^2 - r^2$ orbital are preferable than $x^2 - y^2$ and suggest the lack of surface apical oxygen on the top of MnO_2[137]. Our result of the large c-lattice spacing at the top of LMO layer demonstrate their assumption of surface effect.

The same c-lattice spacing of the 10ML sample at 10K as that of at 300K suggests that large elastic energy is required to alter the cell volume of LMO. An important experimental facts regarding the relationship between epitaxial strain and JT strain in Mn oxide thin films have been reported in Ref[138]. They pointed out that First-order phase transition with clear lattice distortion occurs in only (011) orientated Mn oxides, not in (001). Our (001) oriented LMO films is this elastically hard material.

The remarkable difference of structure between $(LMO)_{2,4}/STO$ and $(LMO)_{7,10}/STO$ samples is shorter c-lattice spacing(3.91 to 3.92Å) of middle layers of $(LMO)_7/STO$ and $(LMO)_{10}/STO$. The reduction of c-lattice spacing is realized by either the reduction of Mn-O-Mn bond angle by the MnO_6 octahedral tilting, shorten Mn-O-Mn bond length by excess oxygen, or volume collapse caused by an orbital disorder[139]. The orbital disorder effect emerging at 750K∼ is not appropriate here. The remaining two possibilities are discussed in the next two sections.

4.4.2 MnO_6 octahedral tilting

Let us examine the MnO_6 octahedral tilting here. Fig. 4.40(a) shows the bulk structure of LMO. The detailed Mn-O-Mn bond length of bulk LMO is reported by J. -S. Zhou and J. B. Goodenough[140]. The bulk LMO has distorted *Pbnm* perovskite including two JT modes, which separate the three different Mn-O bond length as the long and short Mn-O_{II} in (001) plane and Mn-O_{I} extending along c axis. The value of them are Mn-O_{II} = 2.18, 1.91 Å and Mn-O_{I} = 1.96 Å. Here, we assume that these bond lengths have not changed.

First, let us examine the case where c-plane in *Pbnm* is parallel to the surface as shwon in Fig. 4.40(b). The observed c-lattice spacing of thicker LMO is 3.92 Å. This is exactly twice as much as Mn-O_{I}, that is, the MnO_6 octahedron is not tilted. The Mn-O-Mn bond angle is calculated by the in-plane distance of Mn to Mn(=3.905 Å) and bond length of two Mn-O_{II}. In this case, in-plane Mn-O-Mn angle is 145.3°. This value is comparable to $R\mathrm{MnO}_3$ with R = Er or Ho[140]. The band width W is influenced by Mn-O bond length $d_{\mathrm{Mn-O}}$ and Mn-O-Mn bond angle ϕ. According to tight binding model, ϕ dependence of W is given by $W \propto \frac{\cos\omega}{(d_{\mathrm{Mn-O}})^{3.5}}$, where $\omega = (180° - \phi)/2$[141]. This formula indicates that the reduction of the rotation angle narrows the band width, resulting the weaken of double exchange between Mn. The calculated ω angle is not consistent with the larger FM trend in thicker LMO film. The suppression of the magnetization of LMO by reduction of ω angle of MnO_6 is reported in Ref. [115].

In the case of *c*-plane in *Pbnm* perpendicular to the surface as shown in Fig. 4.40(c), the tilt and rotation angle are calculated as 146.8° and 169.9°. The value of Mn-O-Mn angle is still small enough to make LMO FM. As a result, assumption that the decrease in *c*-lattice spacing is due to a decrease in the Mn-O-Mn angle contradicts the tendency of the thicker film having lager magnetism.

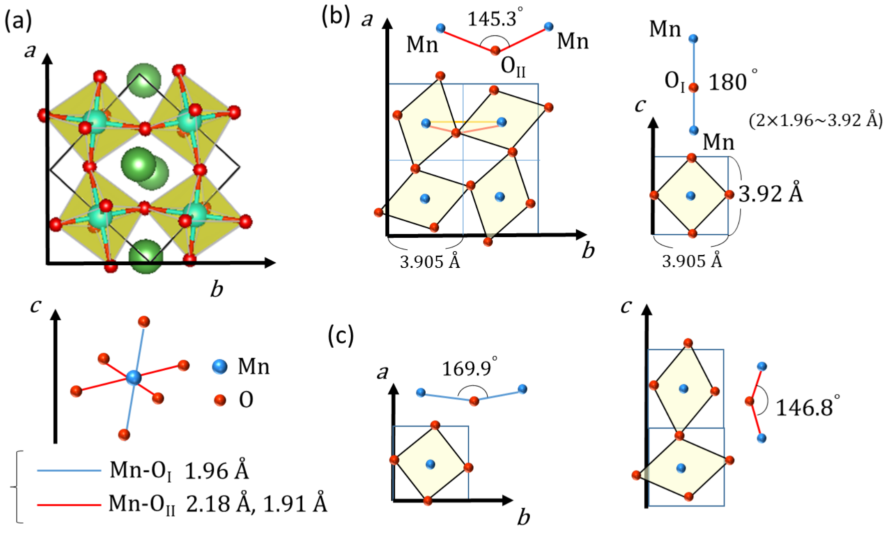

Figure 4.40: (a) Bulk structure of $LaMnO_3$ and three component Mn-O bond length. The rotation and tilt angle of Mn-O-Mn are calculated in the case where *c*-plane in *Pbnm* is (b)parallel and (c) perpendicular to the surface.

4.4.3 Mn valence distribution

The examination of Mn-O-Mn bond angle from our observed structure suggests the decreased *c*-lattice spacing in thicker LMO is originated from not only MnO_6 octahedral tilting but also shorten Mn-O bond length due to introduction of Mn^{4+}. Here, let us discuss the correlation of the lattice and the valence distribution of Mn.

For $(LMO)_4/STO$, the appropriate Mn valence distribution model was not identified from energy spectra. This is due to the lack of a spectrum data in which the signal reflecting the valence distribution appears. Unless the crystal structure is determined, the prediction of effective target points of $\boldsymbol{Q}$ for spectrum measurement should be impossible. Here, we discuss the valence distribution of Mn from the viewpoint of the obtained crystal structure. The excess oxygen introduces Mn^{4+} state and reduces the cell volume of LMO because the values of ionic radii of Mn^{3+} (0.65 Å) is larger than that of Mn^{4+} (0.54 Å). Here, the (La, Ca)MnO_3 system is selected to be the reference[142, 143] because the ionic radii of La and Ca are similar. If we assume that the cell volume is constant with epitaxial strain, we expect 0.58 Å of *c*-lattice spacing reduction by replacing $LaMn^{3+}O_3$ to $LaMn^{4+}O_3$. The difference of *c*-lattice spacing of post annealed sample($c \sim 3.97$ Å) and our analysis result of $(LMO)_4$/STO is $\sim$ 0.03 Å as shown in Fig. 4.15. This value corresponds to 5.2 % concentration of Mn^{4+}. This concentration is comparable to that of AFM phase of $LMO_{3+\delta}$[109].

For $(LMO)_7$/STO and $(LMO)_{10}$/STO, the 'Model-2P/4P', where Mn^{4+} spreads into the middle of LMO is preferred. The smaller *c*-lattice spacing of middle layer at Z = 6 to 8(3.91 to 3.92 Å) than the top of LMO(3.94 to 3.97 Å) shown in Fig. 4.15 accounts for this result. This is consistent with the self-doping effect reported in Ref.[103, 112]. The expected concentration of Mn^{4+} in middle layer LMO of $(LMO)_7$/STO and $(LMO)_{10}$/STO is 8.6 to 10.3 %, comparable to the hole concentration of hole doped FM phase of $LaMnO_{3+\delta}$[109]. The critical film thickness at which this self-dope effect in LMO occurs was 5 to 7 u.c. thick, which is thicker than that of reported value(2 to 5 u.c thick) in Ref.[103, 112]. One possible explanation of the increasing in critical thickness of self-doping is the Nb doping effect of STO substrate. The Fermi level is located just below the conduction band in STO region and modulates the band bending of LMO side. The modulated electronic potential in LMO side reduce the CT electrons in LMO side.

The electron migration not performed from the top surface of LMO to interface is consistent with the result of the depth dependence of *c*-spacing. The expanded surface layer prefers Mn^{3+} state, therefore, CT effect occurred from middle of LMO to LMO/STO interface.

The accumulated Mn^{2+} at the LMO/STO interface should have the lattice expansion of LMO. The 0.65 Å of *c*-lattice spacing expansion by replacing $LaMn^{3+}O_3$ to $LaMn^{2+}O_3$ is expected. However, our $(LMO)_7$/STO and $(LMO)_{10}$/STO samples do not have such a large *c*-lattice spacing. The expected *c*-lattice expansion is 8.7 % from the 0.02 Å larger *c*-spacing at Z = 5 for $(LMO)_7$/STO and Z = 6 for $(LMO)_{10}$/STO than adjacent layers. This is not consistent with the expected models. To provide quantitative verification, the more appropriate value of f' and f'' is required to reproduce those of experimental value.

Models having Mn^{4+} localized at the interface contradicts the results of spectra of $(LMO)_7$/STO and 10 samples. This result rejects some causes on CT across the interface of LMO/STO. Many studies of LMO/STO multilayers argue that (La, Sr)MnO_3 forms at the interface, producing Mn^{4+} and Ti^{3+} [106, 107, 144]. Such CT effect was not observed in the LMO monolayer targeted in this study. According to XPS measurements for LMO/Nb:STO[118], the Ti^{3+} state is not preferable because the unoccupied Ti 3*d* band is located at energetically higher level than Mn 3*d* state. This difference of chemical potential between Ti and Mn could prevents the charge migration from Mn to Ti.

We conclude that the thickness dependent ferromagnetism in LMO films on STO is originated from middle layers with smaller *c*-spacing of LMO in $(LMO)_7$/STO and $(LMO)_{10}$/STO. These middle layers are lost in nonmagnetic $(LMO)_2$/STO and $(LMO)_4$/STO where surface expanded layers are dominant. The smaller *c*-lattice spacing is derived from the excess oxygen in LMO. The larger critical thickness for self doping in LMO than reported value(5 u.c. thick ∼[103, 112]) suggests the Nb doping effect of STO suppress the band bending of LMO due to polar discontinuity.

4.5 Summary of this chapter

The depth dependence of atomic arrangement and Mn valence state were investigated by resonant CTR measurement for n = 2, 4, 7, and 10 u.c. thick LMO samples. Middle layers with small *c*-lattice spacing equal to 3.92Å was observed in only FM sample thicker than 7 u.c., while 4 u.c. thick LMO was composed of only compressively strained thicker layer at the top of LMO, whose value of *c*-lattice spacing is comparable to AFM phase. The results of simulation of resonant CTR data indicates that Mn^{2+} accumulates at the interface and Mn^{4+} spread into middle LMO layer for $(LMO)_7$/STO and $(LMO)_{10}$/STO. This self-doping effect was observed in only $(LMO)_7$/STO and $(LMO)_{10}$/STO. On the other hand, the models in which Mn^{4+} is localized at the interface were rejected for samples with n = 7 and 10. This result supports the self doping driven ferromagnetism, not CT effect from Mn to Ti across the interface.

Chapter 5

Stacking order dependence on the structure of interface between $LaNiO_3$ and $LaMnO_3$

5.1 introduction

The structural study of stacking order dependence of $LaNiO_3$(LNO) and $LaMnO_3$(LMO) multilayer samples is the main topic of this chapter. One of the phenomena that brings about a dramatic change of its transport and magnetic properties is charge transfer(CT) effect. CT effect between tradition metal sites across the interface is mainly caused by polar discontinuity and the difference of chemical potential. The epitaxial interface of $LaNiO_3$ and $LaMnO_3$ has been understood as a ferromagnetic system induced by CT effect between Mn and Ni[91, 145, 146, 147, 148]. Surprisingly, the magnetism is reported to be strongly affected by the stacking order of LMO and LNO[149]. The purpose of this study is to reveal the stacking order effect on structure and valence distribution of Mn ion. To evaluate the stacking order dependence of atomic arrangement and spatial distribution of Mn valence state quantitatively, depth resolved analysis of different valence state was performed by resonant CTR method.

5.1.1 Stacking order dependence of ultrathin films

The effects of the stacking order of thin films sometimes affects the structural properties of the interface. Epitaxial interfaces of strongly correlated oxides are the places where electrons having different states meet each other. The behavior of electrons at there is different from that in the bulk materials because electrons interact with surrounding electrons. In this point of view, the interface between perovskite structure oxide ABO_3 film on top of another perovskite oxide $AB'O_3$ should show the same property with $AB'O_3$ film on top of ABO_3. However, it has been reported that the stacking order does matter for various combination of oxide films. For example, the interface between $LaVO_3$ grown on $SrTiO_3$ (001) surface has larger amount of atomic interdiffusion than $SrTiO_3$ on $LaVO_3$ interface[150]. For $LaVO_3$ grown in the layer-by-layer mode on $SrTiO_3$, Sr segregates to the surface with cation interdiffusion at that interface while $SrTiO_3$ grown on $LaVO_3$, the interface becomes atomically sharp. The asymmetry of the interface structure is presumed to be caused by the difference in the effect of polar discontinuity at the interface depending on the stacking order, but there is no clear arguments.

Such asymmetric interface led by stacking order effects can have a significant effect on interface properties. S. J. May reports the stacking order of superlattice made of antiferromagnetic $SrMnO_3$ and ferromagnetic $LaMnO_3$[151]. The left panels in Fig. 5.1 show the depth dependence of magnetization models reproducing the polarized neutron reflectivity profiles. From the STEM image shown in right, larger magnetization at lower rough interface of $LaMnO_3$ than upper smooth interface indicates a strong dependence on asymmetric roughness of interface.

Another example is the modulation of the exchange bias effect at the $La_xSr_{1-x}MnO_3$-$BiFeO_3$ interface[152]. The change in the roughness of the interface depending on the stacking order affects the *d*-electron correlation across the interface.

5.1.2 The effect of charge transfer across the interface

CT effect is one of the technical approaches to handle the magnetic property in addition to strain and layer sequencing. Let us give the $CaMnO_3/CaRuO_3$ interface as a example[20, 21]. Whereas bulk $CaRuO_3$ and $CaMnO_3$ are paramagnetic metal and G-type antiferromagnetic insulator, the interface of them reveals ferromagnetic. The observed magnetization was $0.85\mu_B$, which was understood as canted spin state, since the fully ferromagnetic Mn moment has $3\mu_B$. To realize the ferromagnetic phase of $CaMnO_3$, a mixture of Mn^{3+} and Mn^{4+} is expected. However, since the atomic layers sequences as $(Ca^{2+}O^{2-})$,$(Ru^{4+}O_2^{2-})$,$(Ca^{2+}O^{2-})$, $(Mn^{4+}O_2^{2-})$..., where all of individual layers has neutral charge, the idea of

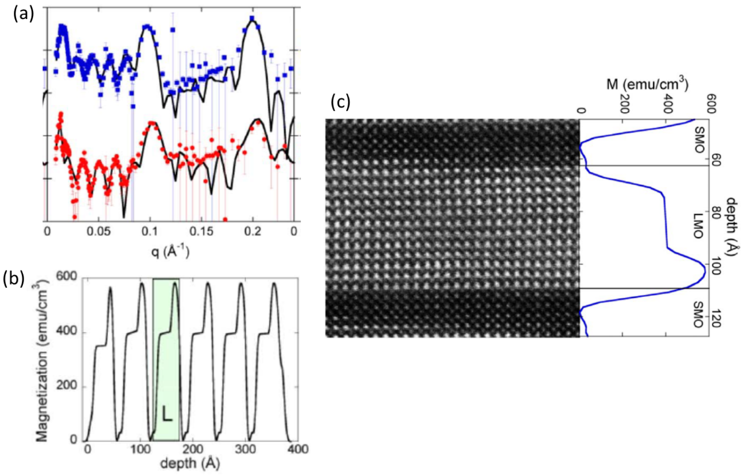

Figure 5.1: Asymmetric atomic interdiffusion at interface of SrMnO$_3$ and LaMnO$_3$ confirmed by (a)Polarized neutron reflectivity and (b)STEM image[151]

CT by polar discontinuity does not arise. The charge leakage of a small number of itinerant electrons across Ohmic contact from CaRuO$_3$ to CaMnO$_3$ is indicated by Density-functional calculations[153] and X-ray resonant magnetic scattering measurements[21]. Magnetic polarized region extended over several unit cells. The exchange bias effect has been observed in the CaMnO$_3$ region where ferromagnetism and antiferromagnetism coexist[154]. Another way to realize interfacial CT effect is modulation doping into A site atom while the B site atom is kept same, for example, LaTiO$_3$/SrTiO$_3$[155] and LaMnO$_3$/SrMnO$_3$[156, 157]. This process causes the nominal electron count on the transition metal to vary across an interface.

5.1.3 Induced ferromagnetism in the interface between LaNiO$_3$ and LaMnO$_3$

In the LNO-LMO superlattice, interfacial ferromagnetism along (001) and (111) axis and exchange-bias(Fig. 5.2) induced in only (111) stacking was reported by M.Gibert[145].

The XAS spectra[146] show the characteristic signal of valence states of Ni($3+ \rightarrow 2+$) and Mn($3+ \rightarrow 4+$) in $[(\mathrm{LNO})_n/(\mathrm{LMO})_2]_m$ superlattice. n dependence of magnetization and the peak signals of Ni^{2+} and Mn^{4+} spectra indicates the charge transfer from Mn to Ni ($\mathrm{Mn}^{3+} + \mathrm{Ni}^{3+} \rightarrow \mathrm{Mn}^{4+} + \mathrm{Ni}^{2+}$). The weak magnetization of Ni is assumed to be from ferromagnetic coupling

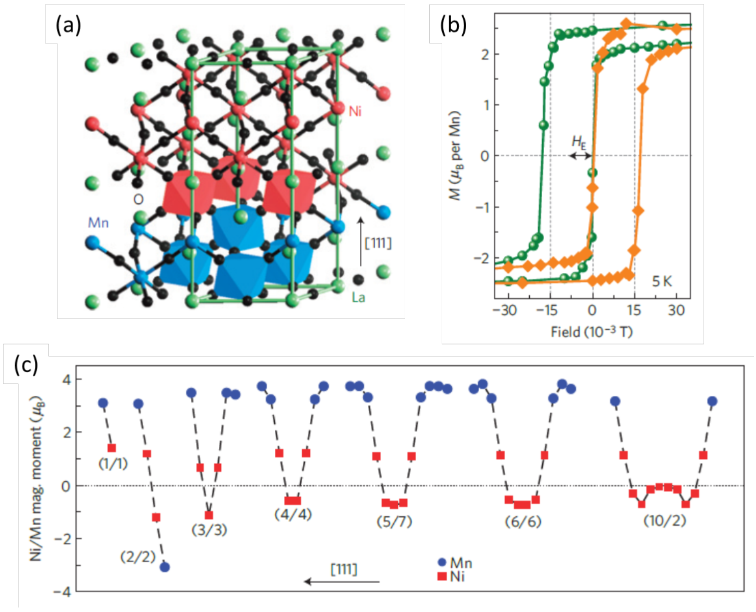

Figure 5.2: Exchange-bias effect in LNO/LMO (111) orientation.[145] (a) Schematic picture of (111) stacking LNO/LMO interface (b)M-H curve (c)Ni/Mn magnetic moment of LNO/LMO with different period of fabrication.

of net magnetization on the Mn and Ni. Through the discussion based on the Kanamori-Goodenough rule in Mn^{4+}-O-Ni^{2+}[158], this charge modulation is assigned to the origin of the induced ferromagnetism. The expected spin

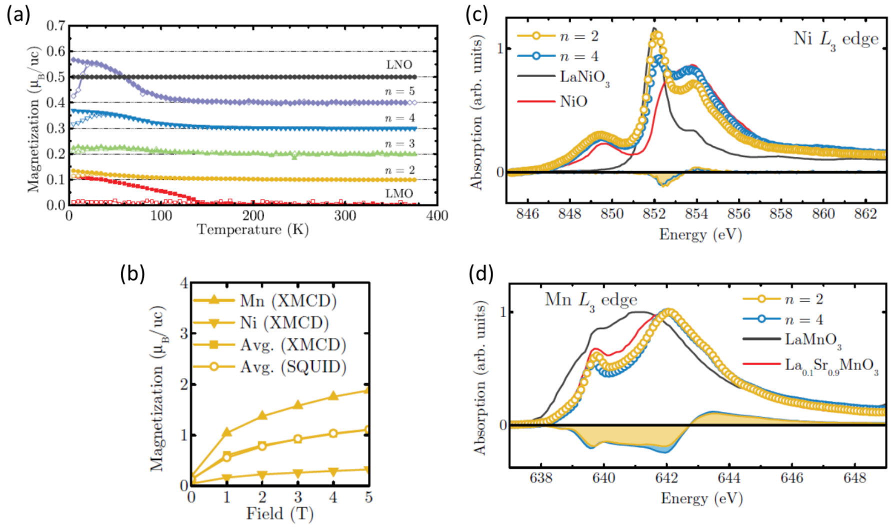

Figure 5.3: [Thickness period n dependence of (a) Magnetization, (b) Magnetization($n = 2$), (c) Mn L_3 edge XAS spectra and (d)Ni L_3 edge spectra of (LNO)$_n$/(LMO)$_2$]$_m$ superlattice on STO substrate[146].

configuration similar to that of La$_2$NiMnO$_6$ corresponds to the atomic coordination in the direction of (111) termination LNO-LMO superlattice. The presence of the exchange bias effect in the (111) and absence in (001) termination are considered qualitatively to be difference of the number of closest sites of Ni and Mn across the interface[145]. A theoretical work reported that the magnitude of FM in different termination was induced by quantum confinement of down spin in LNO region[147]. M. Kitamura reported the asymmetric spatial distribution of different valence state across the LNO-LMO interface[91]. Fig. 5.4 shows the thickness dependence of Ni L and Mn L-edge XAS spectra for LNO(LMO) film on 20 nm thick LMO(LNO). The XAS spectra indicates the different critical thickness of LNO(LMO) film for saturation of another peak derived from Ni^{2+}(Mn^{4+}). The critical thickness 1ML(3ML) for LNO(LMO) film suggests that Mn^{4+} states spread in LMO 3 to 4 times wider than Ni^{2+} localized in only $\sim$1 ML in LNO from interface. Taking into consideration of the results of charge distribution and magnetic moment in Mn and Ni, spin configuration is expected as ferromagnetic state of LMO induced by double exchange mechanism and canted antiferromagnetic state in LNO stabilized under the superexchange between Mn^{4+} and Ni^{2+}[159]. However, this picture of ferromagnetism derived from the charge transfer effect is not a quantitative model of which LMO layer has a significant valence change. A certain level of chemical perturbation always existing around the interface hinders quantitative discrimination of whether the valence distribution extends to the LMO side. For that purpose, accurate interface structure including interface roughness and information on the spatial distribution of valence are required.

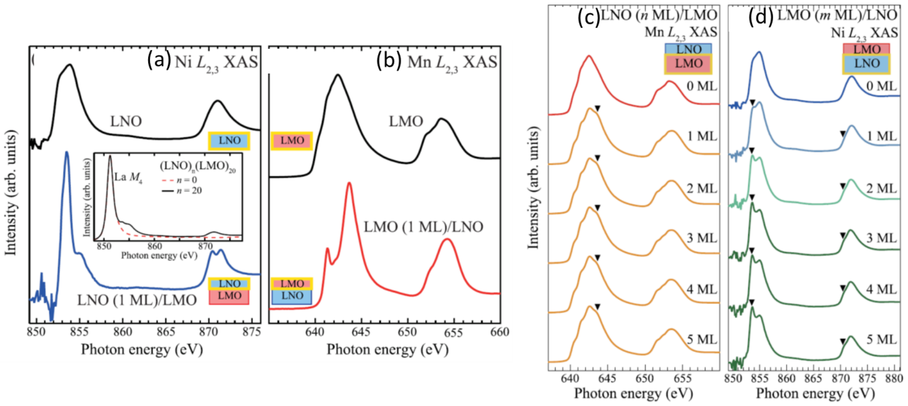

Figure 5.4: (a)Ni and (b)Mn L edge XAS spectra for LNO/LMO and LMO/LNO. (c, d) Thickness dependence of Mn(Ni) L-edge spectra for LNO(LMO) thin film on 20 u.c.LMO(LNO).[91]

The stacking order effect was reported for LNO and LMO interface[149]. LNO on LMO is reported to have much larger magnetization than LMO on LNO. According to Gibert and coworkers[149], LNO on LMO has 4 times larger electric resistance and 7 times larger magnetization than those of LMO on LNO(Fig. 5.5 (a) and (b)). Their soft X-ray reflectivity measurements revealed that the magnetization is nearly homogeneously distributed in the LMO layer within the range of 5 u.c. from the LNO/LMO interface(Fig. 5.5 (c-f)). The different magnetic property was attributed to the interfacial intermixing. The interface in NMT is rougher than that in MNT. They also reported larger electron migration from Mn to Ni in the rougher interface based on the electron energy loss spectroscopy (EELS), while some Mn^{2+} generated by the beam damage was also found. Extensive studies of bulk manganites show that the magnetism of the Mn oxides can be controlled by the hole concentration and the band width[108]. The difference in magnetism found at NMT and MNT interfaces suggest that the difference in hole concentration or Mn-O-Mn angle dominates the band width in LMO[149].

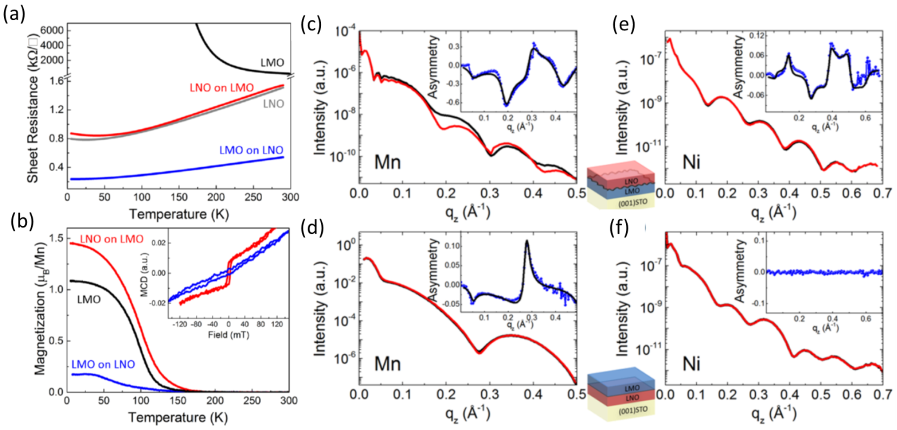

Figure 5.5: (a)Sheet resistance (b)Magnetization per Mn of 10 + 10 u.c. thick LMO on LNO and LNO on LMO. (c-f)Soft X-ray reflectivity measurements[149].

5.2 Motivation

The mechanisms of induced magnetism in oxide materials through the interfacial contacts is roughly summarized to superexchange of B site atoms across the interface, charge transfer and epitaxial strain. In particular, the observation of existence and the spatial distribution of Mn^{4+} state in the LMO region is the key to distinguish what the trigger of FM is dominant. For example, if interfacial charge transfer is the main source, Mn^{4+} is expected to be concentrated on the Mn-Ni interface. If excess oxygen is present homogeneously in LMO, Mn^{4+} also homogeneously exists throughout the LMO region.

We have investigated the interfacial structure of $LaNiO_3$ on $LaMnO_3$ and of $LaMnO_3$ on $LaNiO_3$ bilayers grown on top of $SrTiO_3$ (001) surfaces by CTR scattering method. In addition, we also measured Mn K-edge energy spectra of CTR scattering in order to know the spatial arrangement of Mn^{4+} ions. In this study, we verify the lattice distortion and Mn^{4+} distribution by using non-resonant and resonant surface X-ray diffraction techniques. Regarding the roughness of the interface, which is supposed to be influenced by the stacking order of LNO and LMO, the quantitative difference can be clarified by the element-selective analysis by the resonant CTR method. We shall refer to them as NMT and MNT, respectively.

5.3 Experiments and analysis

5.3.1 Experimental conditions

Epitaxial bilayers LNO/LMO(NMT) and LMO/LNO(MNT) were provided by prof. H. Kumigashira, Prof. K. Horiba and Dr. M. Kitamura. Digitally controlled bilayer structures were fabricated onto atomically flat TiO_2-terminated Nb:$SrTiO_3$ (STO) (001) substrates in a laser molecular-beam epitaxy chamber connected to a photoelectron spectroscopic system at beamline BL-2A MUSASHI of the Photon Factory, KEK. A Nd-doped yttrium-aluminum-garnet laser in the frequency-triplet mode ($\lambda = 355$ nm) at a repetition rate of 1 Hz was used for ablation. Sintered LNO and LMO pellets were used as the targets. Before the film growth, the Nb:STO substrates were annealed at 1050°C under an oxygen pressure of 1×10^{-7} Torr to obtain atomically flat and chemically clean surfaces. During LNO and LMO depositions, the substrate was kept at temperatures of 500°C and 600°C, respectively, and the oxygen pressure was maintained at 1×10^{-3} Torr. The thicknesses of the LNO and LMO layers were precisely controlled by monitoring the intensity oscillation of the specular spot with reflection high-energy electron diffraction during the growth. The heterostructures were subsequently annealed at 400°C for 45 min under an atmospheric pressure of oxygen to fill residual oxygen vacancies.

The CTR scattering measurements were performed with the four circle diffractometers installed at BL-3A, Photon Factory, KEK. Scattered X-ray intensity was measured by a two dimensional pixel array detector XPAD-S70(imXpad). Samples were put in a 10^{-5} torr vacuum chamber to protect them from radiation damage, and all the measurements were performed at room temperature. Using 12 keV X-ray, a non-resonant condition, $hk\zeta$ rods along (h,k) = (0,0), (0,1), (0,2), (1,1), and (1,2) were measured. The range of measured ζ was 0.5 to 4.2 except for the substrate Bragg points. Additionally, 00ζ profiles were measured using several X-ray energies E close to Mn and Ni K-absorption edges to discriminate B-site elements. In order to study the spatial distribution of Mn^{4+}, energy spectra around the Mn K-edge were measured for several scattering vectors along the 00ζ line.

Intensity profiles along $hk\zeta$ rods measured in both non-resonant and resonant conditions were simultaneously analyzed by exchange Monte-Carlo sampling software. In our analysis, the in-plane atomic positions were fixed to the simple cubic $SrTiO_3$ structure. Other parameters, i.e., atomic displacement perpendicular to the surface direction (δz) with respect to the substrate lattice, atomic occupancy (occ), and isotropic atomic displacement parameters (B) were refined. The total atomic occupancy for each site was fixed to unity except for the surface region. Total number of structure parameter was approximately 90 for NMT and MNT. The parameter uncertainty was estimated by the MC sampling with the effective number of observation.

The anomalous scattering factors f' and f'' as functions of E for Mn^{3+} were calculated by FDMNES[160] using bulk $LaMnO_3$ structure[161]. Those for Mn^{4+} were generated by +4 eV of chemical shift from those for Mn^{3+}[126].

The analysis procedure was the same as that performed in chapter 4. Here, The analysis was also performed with the Bayesian inference with assuming that the magnitude of the noise is 10 % of the intensity. The error bars of the Mn^{4+} concentration are estimated by the MC sampling, while the effective number of observation is assumed to be the same with the number of data points.

5.3.2 Analysis and results

Non-resonant and resonant CTR profiles for MNT and NMT films are presented in Fig. 5.6. Open symbols show the experimental results, and the solid curves show the calculated ones. The $R(\equiv \sum_{\zeta,E} |(|F_{\mathrm{expt}}| - |F_{\mathrm{calc}}|)|/|F_{\mathrm{expt}}|)$ values, where F_{expt} and F_{calc} denote the square root of the measured and calculated intensity, are 0.11 for MNT and 0.10 for NMT. Refined $\mathbf{\Theta}$ (δz, occ, and B) for each site, are shown in Fig. 5.7 as functions of depth. Panel (b) shows the depth profile of the c-lattice spacing. The c-lattice spacing for NMT (MNT) were 3.827 ± 0.008 Å(3.803 ± 0.009 Å) in the LNO region, and $3.938\pm$ 0.007 Å (3.91 ± 0.01Å) in the LMO region.

Panel (c) shows the depth profile of atomic occupancy. Ref.[149] reports larger Mn-Ni interdiffusion in LNO on LMO interfaces than LMO on LNO interfaces. Focusing on the atomic occupancy around the interfaces, one can evaluate the degree of atomic interdiffusion. Here, We define a parameter D that expresses the degree of interdiffusion: $D = \sum[0.5^2-(\mathrm{occ}-0.5)^2]$ and the summation is taken over all sites. When we want to evaluate the sharpness of Ni-Mn interface in NMT sample, the sum is taken over Ni sites for $8 \leq \mathrm{Z} \leq 14$. The value $0.5^2 - (\mathrm{occ} - 0.5)^2$ is zero when occ = 1 or 0. The value of D is increased when the degree of interdiffusion is intense. Our results shows D(MNT, Mn-Ni) = 0.40, D(MNT, Ni-Ti) = 0.40, D(MNT, La-Sr) = 0.41, D(NMT, Mn-Ni) = 0.56, D(NMT, Mn-Ti) = 0.46, and D(NMT, La-Sr) = 0.53. Slightly larger value of D for NMT than MNT indicates a little rougher interface is constructed in NMT than MNT, however, the

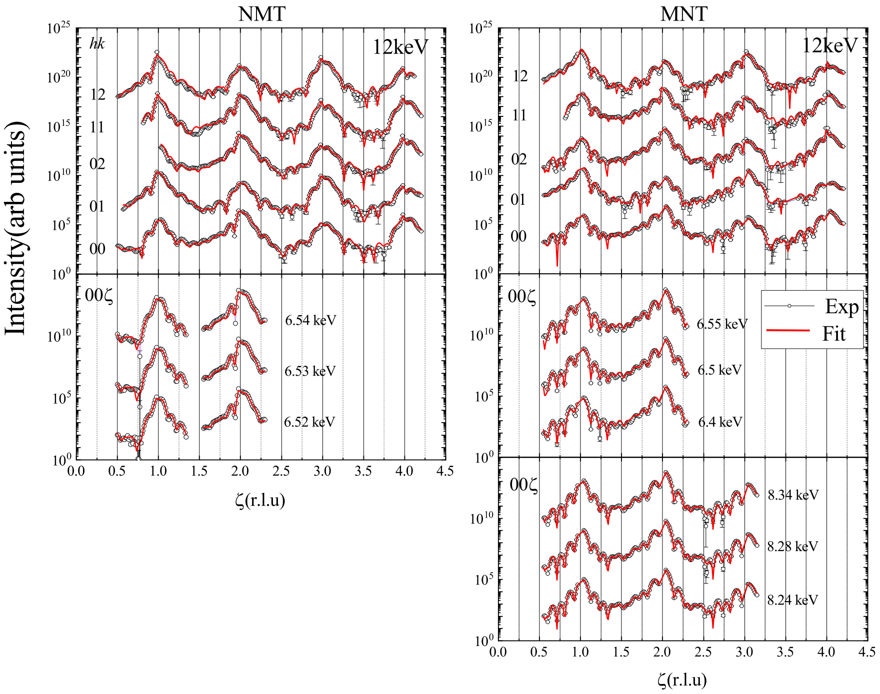

Figure 5.6: CTR scattering profiles along the $hk\zeta$ rods for NMT(left) and MNT(right). The middle and bottom panels show the 00ζ rods in resonant condition close to Mn and Ni K-absorption edge. Open symbols show the experimental results, and the solid curves show the calculated intensity derived from the refined structure. The error bars show the statistical error

difference is not significant. This result is different from the results of 10 + 10 u.c. thick NMT and MNT in Ref.[149]. The film formation method in Ref.[149] is sputtering, which is different from our PLD film formation.

Panel (d) shows the depth profile of B. For NMT sample, B increases as Z increases. Such Z-dependence of B is caused by the in-plane inhomogeneity of the c-lattice spacing. The B values for A-site ions are larger than those for B-sites. In the LNO layer in NMT sample, the same value of B for La and Ni is observed. For MNT sample, large B value for the A-site ion was observed around the interface between STO substrate and LNO layer, where characteristic large c-lattice expansion is observed. Away from the interface, the magnitude of the B is decreased, and the value for A-site ions is very close to that for B-site ions.

The refined Mn^{4+} distribution for NMT an MNT are presented in Fig. 5.8(a) and (b). The high concentration of Mn^{4+} at Mn/Ni interface was observed for NMT while Mn^{4+} is homogeneously distributed in LMO for MNT. Energy spectra around the Mn K-absorption edge measured at several points on 00ζ rod are shown in Figures 5.8(c) and (d). The total amount of electron transfer from Ni to Mn in NMT (MNT) is 0.8 ± 0.3 (0.50 ± 0.2) as shown in Fig. 5.8(e). Total number of Mn layers for NMT and MNT are 4.4 and 4.2, and thus the average hole concentrations of Mn site in the two samples are 18% and 12%, respectively. In pure LMO region of NMT(Z = 8 to 10) and MNT(Z = 13 to 15), the concentration of Mn^{4+} is $\sim$5% and 10%.

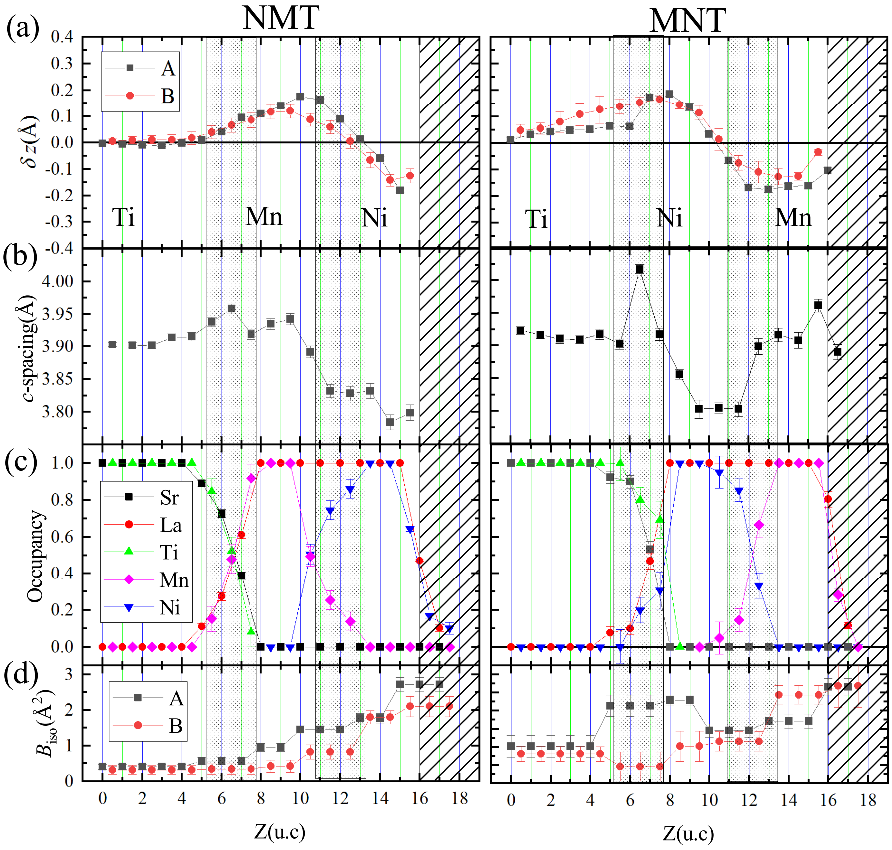

Figure 5.7: (a)δz of A-site and B-site, (b) c-lattice spacing defined by the A-site distance, (c)atomic occupancy of A-site and B-site atoms, and (d)B parameters as a function of depth.

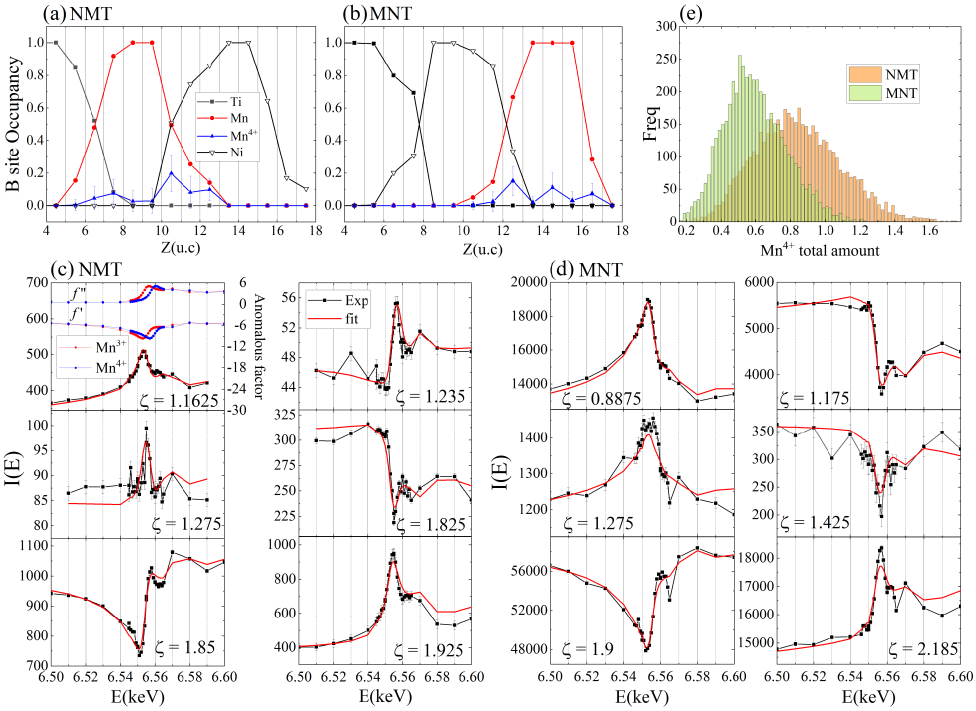

Figure 5.8: (a) Mn^{4+} occupancy as a function of depth for NMT. (b) That for MNT. (c) The energy spectra of scattered X-ray intensity around the Mn K-absorption edge measured at several points on 00ζ rod for NMT. Black plots show the experimental results and red solid lines show the calculated intensity. Anomalous scattering factors f' and f'' for Mn^{3+} and Mn^{4+} used for the analysis are also shown in the panel for $\zeta = 1.1625$. (d) That for MNT. (e) Probability density of total amount of Mn^{4+} derived from the energy spectra.

5.4 Discussion

5.4.1 Interfacial structure of NMT and MNT

Most of LMO films grown on STO show ferromagnetism, which is different from the bulk LMO's canted magnetism. Here, the *c*-lattice spacing of LMO are referred from the reported value in Ref. [123] again. (The *c*-lattice spacing of the as grown and annealed samples were 3.912 Å and 3.973 Å, respectively.) The *c*-lattice spacing of LMO in our NMT and MNT samples are 3.94 Å and 3.91 Å, which are very different from reported value for oxygen reducing annealed LMO but rather close to the value for as grown LMO films. The *c*-lattice spacing value of NMT is close to surface expanded LMO layer of LMO single film on STO and that of MNT is close to middle ferromagnetic layers in LMO of LMO/STO as shown in chapter 4.

Characteristic large *c*-lattice expansion seen in the STO-LNO interface of MNT sample ($Z \sim 7$) can be interpreted as follows. One possible interpretation is the formation of $LaTiO_3$. We find $LaTiO_3$ formation at the STO/LNO interface in MNT sample. As can be seen in Fig. 5.7(b), the LNO/STO interface has nearly 1 monolayer (ML) of $LaTiO_3$. The cell volume of $LaTiO_3$ is 62.596 Å^3. The $LaTiO_3$ layer has large *c*-lattice spacing as shown in panel (b), reflecting its large cell volume[162]. Another possibility is the introduction of oxygen vacancy. Our study on LNO/STO interface in chapter 3 shows that LNO on STO(001) is easy to have oxygen vacancy that results in lattice expansion.

Local electric polarization is also observed in the depth profile of δz presented in Fig. 5.7(a). The electric polarization in perovskite oxides is mainly caused by Slater mode and Last mode atomic displacements, and both of them involve relative displacement of A-site and B-site ions. LNO regions in both samples show little relative displacement of A- and B- site ions, meaning that there is no polarization. Since LNO is metallic, no polarization is as expected.

5.4.2 Atomic displacement parameters

For NMT sample, the larger B values of La ions than those of Mn were observed. This indicates that the $GdFeO_3$-type buckling remains in LMO region. Since STO has no octahedral buckling, the LMO layer in NMT sample should have suppressed $GdFeO_3$-type octahedral rotation. However, this mode is not completely suppressed in LMO region. In the LNO layer in NMT sample, the magnitude of $GdFeO_3$-type octahedral rotation is suppressed. The same value to B in La and Ni indicates the rhombohedral symmetry of LNO, where La site exhibits no atomic displacement from pseudo cubic lattice points.

For MNT sample, large B value for the A-site ion was observed around the STO/LNO interface. This is not consistent with the rhombohedral structure of LNO bulk. This is considered as the structural disorder of $LaTiO_3$ formation or oxygen defects, resulting in large c-lattice expansion at Z = 6. Away from the interface, the magnitude of the B is decreased with Z. The value of B of La is very close to that of Mn. This is a characteristic of the rhombohedral perovskites. In this case, LMO grows on top of LNO and has the same mode of octahedral buckling with LNO. The change of symmetry from $Pbnm$ to $R\bar{3}c$ implies the Mn^{4+} introduction reported in Mn perovskites oxides[109].

5.4.3 Valence distribution of NMT and MNT

Let us examine the Mn valence arrangement from structural point of view. The lattice spacing of LNO thick film on STO is reported to be 3.80 Å [80, 85], which is the same as the present values of $LaNiO_3$ thin flims in Chapter 3. At the LMO/STO interface, Mn^{2+} was reported[112]. First, we examine the possibility of Mn^{2+} formation in our samples. We estimate the lattice expansion caused by the electron accumulation at Mn site. The (La, Ca)MnO_3 system is selected to be the reference[142, 143] as in chapter 4. We expect 0.65 Å of c-lattice spacing expansion by reducing $LaMn^{3+}O_3$ to $LaMn^{2+}O_3$. Fig. 5.7 (b) clearly shows that there is no such a large lattice expansion within the LMO region. Therefore, our bilayer samples do not have a noticeable amount of Mn^{2+}.

At the interface where the Mn and Ni are mixed, atomic displacement itself is insufficient to derive the valence. The Mn^{4+} distribution derived from the energy spectra is therefore needed. Fig. 5.8(a) and (b) show that the Mn^{4+} are concentrated at the LMO/LNO interface in NMT sample, and the leakage of inside to the pure LMO layer is small. Since hole doped LMO is ferromagnetic, the Mn^{4+} rich interface region should be ferromagnetic. The concentrated Mn^{4+} in the interface is a natural consequence of a large number of in-plane Mn-O-Ni contact. The trend of Mn^{4+} distribution not concentrated in the interface but broadened into entire LMO in MNT sample does not straightforwardly deal with the charge migration of Mn-O-Ni contacts. This stacking order dependence of Mn valence distribution is not mentioned in Ref.[91, 159], which pointed out the asymmetric charge distribution across the interface. A qualitative explanation is the influence of the electrostatic potential inside the LMO/LNO due to polar discontinuity between STO substrate and MNT and NMT double layer. In an MNT sample in which electrons move to the surface side, the migrant electrons move in a direction that further enhance the electronic potential in the film. The opposite direction of electron migration is expected in NMT. Therefore, the larger amount of electron transfer in NMT than MNT is expected.

5.4.4 The relationship between structure and Mn valence distribution

Here, the relationship between the structure and Mn valence distribution is discussed. The hole concentrations of Mn site in the pure LMO region of NMT and MNT samples are approximately ∼5 % and 10 %. The more than 5% larger content of Mn^{4+} makes LMO *c*-lattice smaller by 0.026 Å ∼ as discussed in chapter 4. This is consistent with the larger *c*-lattice spacing of LMO in NMT than MNT, and approximately the same as the value of the difference of *c*-lattice spacing of LMO(0.03 Å) between NMT and MNT. Remaining quantity may be derived from disappearance of Jahn-Teller distortion in MNT and different propagation of MnO_6 tilting. The c/a value for MNT is 1.001, which is quite close to unity. This means LMO in MNT is not JT active. The same B value for La and Mn in MNT supports the rhombohedral phase with hole doped $LaMnO_{3+\delta}$[109].

LMO in MNT directly connects to LNO on STO whose Ni-O-Ni angle is 159.9°[80] while those in NMT connects to STO with no BO_6 tilting. Therefore, the MnO_6 tilting of NMT is expected to be modulated to smaller value than MNT as a result of satisfying octahedral connectivity. The larger B values for La than those for Mn observed in LMO region for NMT could be derived from enhanced MnO_6 rotation angle along c axis under compressive strain. However, detailed value of titling and rotation angle cannot be evaluated from our results. To separate the effect of the in-plane displacement and B to the CTR scattering, the more high angle scattering data($\zeta \sim 8$ for perovskites) is required. Data acquisition of high angle scattering data can not achieved by the experimental condition at PF BL-3A.

A large polarization is found at the interface between LMO and LNO in NMT sample and at the LMO region in MNT sample as mentioned above. The polarization in two samples show opposite direction. The direction is affected by the Coulomb interaction between B site atoms and their ionic radii. The relative displacement of Mn, Ni toward substrate in NMT requires smaller and larger ionic radii of Mn and Ni. This is consistent with the charge migration from Mn to Ni. The opposite direction of polarization in MNT is also consistent with the relationship between charge migration and stacking order of LNO and LMO.

We suggest that the different mechanism of FM character in NMT and MNT. For NMT, superexchange between the accumulated Mn^{4+} and Ni^{2+} is the main factor of ferromagnetism. For MNT, the homogeneous Mn^{4+} distribution strengthen double exchange driven ferromagnetism.

5.5 Summary of this chapter

The stacking order of structure and valence distribution of Mn in 5 + 5 u.c. thick $LaNiO_3/LaMnO_3$ and $LaMnO_3/LaNiO_3$ double layer on $SrTiO_3$ substrate were studied. The *c*-lattice spacing in LNO is the same as the value of metallic phase while that for LMO region suggests ferromagnetism. In addition, the larger *c*-spacing of LMO in NMT than MNT was observed. The valence distribution of Mn^{4+} is also different. The Mn^{4+} states concentrates in only Ni/Mn interface in NMT while homogeneous distribution of Mn^{4+} in LMO region is observed for MNT. This trend is consistent with the 0.03 Å larger *c*-lattice spacing of LMO region in NMT than NMT. The asymmetric atomic intermixing in Mn/Ni interface by stacking order of LNO and LMO is not remarkable, which suggests the cation interdiffusion is not affected by the stacking order.

Chapter 6

Conclusions and perspective

This dissertation approaches the interfacial physics of strongly correlated oxide thin films from microscopic structural point of view. The epitaxial interfaces of perovskite oxides exhibit the a variety of properties due to complicated electronic phase of *d* electrons and their correlation across the interface. The elucidation and control of interface physical properties are expected to result in the control of Mott carriers, which surpasses conventional devices by carrier doping. These interfaces provide a fertile ground for creating novel states , however, microscopic understanding of the electronic state of the interface has not been reached. Almost the all discussion on the properties has been based on the electron correlation without understanding the spatially inhomogeneous surroundings of electrons. In order to utilize or manipulate their functionalities, verifying the state of the interface and clarifying the mechanism of properties buried in the interface are necessary.

The research project of this dissertation is based on two subjects. The first is the development of analysis method of surface/interface region. The second is the pursuit for the mechanism of properties in interface, which cannot be realized in the bulk counterpart.

Chapter 1 provides the background of this study. Some examples of previous studies which pursuit or utilize the high potential of the transition metal oxide interface demonstrated by recent atomic-scale synthesis of oxide heterostructures were introduced.Then, we focused on the crystal truncation rod(CTR) scattering method, one of the structural observation technique to reveal the structure in the depth direction with high spatial resolution(subÅ) of structural information. We mentioned the utility and problems of surface X-ray diffraction technique and then, the lack of effective analysis methods of CTR scattering data was raised as a fundamental issue in this dissertation.

In chapter 2, developed analysis technique based on Bayesian inference of CTR data was introduced. We have two difficulties in the direct space method. One is the lack of efficient algorithm to search global minimum of the complex model composed of 10 to 100 of structural parameters. The second is the lack of qualitative technique to evaluate the precision and accuracy of refined parameters. The developed Bayesian inference combined with Monte-Carlo technique enables us to obtain the parameters as probability distribution within a realistic time scale (2 to 3 days per one sample). The performance of software is demonstrated by applying it to a virtual measurement data for a structural model of $LaAlO_3$ thin film on $SrTiO_3$ substrate. After that, we have shown that it is applicable to actual experimental data. Finally, as an example of practical application, we demonstrated the data analysis for the differential measurement data to conduct external electric field switching effect to the polarized structure of $LaAlO_3/SrTiO_3$ interface.

In chapters 3 to 5, the origin of the unique physical properties was discussed from the interface structure of the interface between Ni and Mn oxides using the analysis software shown in chapter 2.

The thickness dependent transport properties of $LaNiO_3$ thin films(1 to 5 unit-cell thick) on (001) surface of $SrTiO_3$(LNO/STO) and $LaAlO_3$(LNO/LAO) were investigated by structural aspects in chapter 3. Samples on both substrates exhibit the metal insulator transition when the thickness is less than 3 u.c. thick. The behavior of density of state observed by the photo emission spectra suggests the different mechanism of MIT for LNO/STO and LNO/LAO. In case of LNO/STO, we found a characteristic expansion of *c*-lattice(3.90 Å) spacing in early stage of LNO growth. This large *c*-lattice indicates the oxygen vacancy formation around the interface. The X-ray absorption spectra showing the existence of Ni^{2+} supports this oxygen-vacancy driven MIT mechanism. For LNO/LAO, we confirmed no clear thickness dependence of LNO cell volume. The structural feature we have discovered is a large structural disorder in about two layers of the surface. Such a disordered structure promotes insulating property of LNO's Anderson localization. A metallic layer with little structural disorder remains in the thicker metallic samples between the surface and interface while thinner films are composed of these disordered layers.

In chapter 4, the thickness dependence of the structure of $LaMnO_3$(LMO) thin films on (001) surface of $SrTiO_3$ substrate, whose magnetization is basically debated on the charge transfer effect between transition metal sites, was investigated. To extract the Mn valence distribution of LMO due to charge transfer effects, we observed resonant CTR data near the Mn *K*-edge CTR in addition to off-resonant condition data of 2, 4, 7 and 10 u.c thick LMO/STO samples. The observed *c*-lattice spacing was

3.92 Å and 3.94 Å ∼ in middle laters and surface region for LMO samples. The results of the energy spectra of CTR signal revealed no outstanding charge transfer occur in 4 u.c. sample. In case of thicker ferromagnetic samples, a certain amount of Mn^{4+} is introduced in the center of LMO. In addition, the sharp peaks in energy spectra derived from Mn^{2+} concentrated at LMO/STO interface were observed for 7 and 10 u.c. thick samples. This result is consistent with the self doping mechanism of LMO/STO.

In chapter 5, the structure of 5+5 u.c. thick of $LaNiO_3$/$LaMnO_3$(NMT) and $LaMnO_3$/$LaNiO_3$(MNT) double layer on $SrTiO_3$ substrate were investigated. The resonant CTR data were analyzed to determine the valence distribution of Mn ion. In addition, the reported stacking order dependence of ferromagnetism derived from the chemical perturbation was examined. We found several stacking order dependence of structure and Mn valence distribution. The c-lattice spacing of LNO region in NMT and MNT is 3.8Å. This is the same value as metallic state of LNO on STO substrate. However, the different values of c in LMO region were observed, 3.94Å for NMT and 3.91 Å for MNT. The clear difference of spatial distribution of Mn^{4+} was also observed. The Mn^{4+} state is concentrated in Mn/Ni interface for NMT while Mn^{4+} is homogeneously distributed in entire LMO region for MNT. This trend is consistent with the larger c-lattice spacing of LMO in NMT than MNT because of smaller ionic radii of Mn^{4+} than Mn^{3+}. This result suggests that the origin of ferromagnetism of the multilayer film in which two kinds of stacking order are different. For NMT sample, the ferromagnetism is derived from concentrated Mn^{4+} suggesting the results of large charge transfer across the interface. The ferromagnetic Mn^{4+}-Ni^{2+} superexchange is expected around the interface. MNT sample shows no remarkable charge transfer but has a uniform hole concentration throughout LMO region, which strengthen the double exchange interaction.

In this dissertation, following subjects are accomplished as general application or quantum study of 2 dimensional electronic state of strongly correlated materials.

The high precised structural analysis of surface/interface structure was achieved by Bayesian inference of CTR scattering data. MC software solves the difficulties of parameter optimization and validates appropriate structural models quantitatively. Semi-automatic and high-speed analysis enables systematic investigation of the interface as the studies for the bulk. The spatial resolution of 0.02 Å for atomic position, application for in-situ measurements, and temperature variation are features that cannot be realized by other methods.

We focused on the perovskite oxide interface and showed the utility of developed analysis technique for structural matter physics of the interface. For example, we successfully explained the origin of insulating properties due to the difference in the substrate in LNO from structural information. In this way, we have completed the fundamental approach for structural-based physics on the interface as in case of the bulk research. This method is expected to make a great contribution to researches on phenomena peculiar to the interface of any materials because of its versatility of target materials. Future prospects are to apply this method to various materials such as solid/liquid interfaces, and in-situ measurements.

The problem with the developed analysis method is the difficulty in identifying the position of light elements such as oxygen. This is a disadvantage in the characteristic of X-ray. This problem can be solved by the development of coherent light sources and collaboration with first-principles calculations. The development of a coherent X-ray light source enables us to visualize in-plane structural roughness as an in-plane distribution of structural domains or step-terrace surface. Our developed software demonstrates the in-plane averaged structural model construction structure using the atomic occupancy. If the in-plane structural disorder can be visualized specifically without expression by atomic occupancy, the position of oxygen atoms can be optimized by first-principles calculations from the obtained lattice.

Recent developments in surface x-ray diffraction include the elucidation of the static structure of complex surfaces/interfaces and time-resolved measurements of materials with simple surface structures. This study is proposed as an effective tool for the former. The latter includes the X-ray photon correlation spectroscopy analysis of CTR scattering intensity using coherent light source[163], a method using a high-energy x-ray[164, 165], and a method using a multi-wavelength light source and a special equipment[166]. For example, the time resolved measurements of crystal growth of thin films[167] provides more suitable conditions for film fabrication. The data accumulation of optimized film fabrication conditions enables a prediction of crystal growth pattern by machine learning and builds more stable interfacial structures, which has already developed for X-ray diffraction data of bulk crystals. The static structure obtained from our analysis method is a useful starting point of the research of time evolution of the structure.

Bibliography

[1] H. Y. Hwang, Y. Iwasa, M. Kawasaki, B. Keimer, N. Nagaosa, and Y. Tokura. Nat. Mater., **11**, 103–113 (2012).

[2] A. Bhattacharya and S. J. May. Annu. Rev. Mater. Res, **44**, 65–90 (2014).

[3] Y. Tokura and N. Nagaosa. Science, **288**, 462–468 (2000).

[4] E. Dagotto. Science, **309**, 257–262 (2005).

[5] J. W. Freeland, K. E. Gray, L. Ozyuzer, P. Berghuis, E. Badica, J. Kavich, H. Zheng, and J. F. Mitchell. Nat. Mater., **4**, 62–67 (2005).

[6] M. Salluzzo, S. Gariglio, X. Torrelles, Z. Ristic, R. Di Capua, J. Drnec, M. M. Sala, G. Ghiringhelli, R. Felici, and N. B. Brookes. Adv. Mater., **25**, 2333–2338 (2013).

[7] J. Chakhalian, J. W. Freeland, A. J. Millis, C. Panagopoulos, and J. M. Rondinelli. Rev. Mod. Phys., **86**, 1189–1202 (2014).

[8] K. Yoshimatsu, K. Horiba, H. Kumigashira, T. Yoshida, A. Fujimori, and M. Oshima. Science, **333**, 319–322 (2011).

[9] K. J. Choi, M. Biegalski, Y. L. Li, A. Sharan, J. Schubert, R. Uecker, P. Reiche, Y. B. Chen, X. Q. Pan, V. Gopalan, L.-Q. Chen, D. G. Schlom, and C. B. Eom. Science, **306**, 1005–1009 (2004).

[10] Y. Konishi, Z. Fang, M. Izumi, T. Manako, M. Kasai, H. Kuwahara, M. Kawasaki, K. Terakura, and Y. Tokura. J. Phys. Soc. Jpn., **68**, 3790–3793 (1999).

[11] J. M. Rondinelli and N. A. Spaldin. Phys. Rev. B, **79**, 054409 (2009).

[12] J. H. Lee, L. Fang, E. Vlahos, X. Ke, Y. W. Jung, L. F. Kourkoutis, J.-W. Kim, P. J. Ryan, T. Heeg, M. Roeckerath, V. Goian,

M. Bernhagen, R. Uecker, P. C. Hammel, K. M. Rabe, S. Kamba, J. Schubert, J. W. Freeland, D. A. Muller, C. J. Fennie, P. Schiffer, V. Gopalan, E. Johnston-Halperin, and D. G. Schlom. Nature, **466**, 954–958 (2010).

[13] J. W. Seo, W. Prellier, P. Padhan, P. Boullay, J.-Y. Kim, H. Lee, C. D. Batista, I. Martin, E. E. M. Chia, T. Wu, B.-G. Cho, and C. Panagopoulos. Phys. Rev. Lett., **105**, 167206 (2010).

[14] A. Ohtomo and H. Y. Hwang. Nature, **427**, 423–426 (2004).

[15] N. Nakagawa, H. Y. Hwang, and D. A. Muller. Nat. Mater., **5**, 204 (2006).

[16] T. Yajima, Y. Hikita, M. Minohara, C. Bell, J. A. Mundy, L. F. Kourkoutis, D. A. Muller, H. Kumigashira, M. Oshima, and H. Y. Hwang. Nat. Commun., **6**, 6759 (2015).

[17] J. M. Rondinelli, S. J. May, and J. W. Freeland. MRS Bull., **37**, 261–270 (2012).

[18] D. Kan, R. Aso, R. Sato, M. Haruta, H. Kurata, and Y. Shimakawa. Nat. Mater., **15**, 432 (2016).

[19] S. J. May, T. S. Santos, and A. Bhattacharya. Phys. Rev. B, **79**, 115127 (2009).

[20] K. S. Takahashi, M. Kawasaki, and Y. Tokura. Appl. Phys. Lett., **79**, 1324–1326 (2001).

[21] J. W. Freeland, J. Chakhalian, A. V. Boris, J.-M. Tonnerre, J. J. Kavich, P. Yordanov, S. Grenier, P. Zschack, E. Karapetrova, P. Popovich, H. N. Lee, and B. Keimer. Phys. Rev. B, **81**, 094414 (2010).

[22] D. D. Fong, C. Cionca, Y. Yacoby, G. B. Stephenson, J. A. Eastman, P. H. Fuoss, S. K. Streiffer, C. Thompson, R. Clarke, R. Pindak, and E. A. Stern. Phys. Rev. B, **71**, 144112 (2005).

[23] P. R. Willmott, S. A. Pauli, R. Herger, C. M. Schlepütz, D. Martoccia, B. D. Patterson, B. Delley, R. Clarke, D. Kumah, C. Cionca, and Y. Yacoby. Phys. Rev. Lett., **99**, 155502 (2007).

[24] P. Perna, D. Maccariello, M. Radovic, U. S. d. Uccio, I. Pallecchi, M. Codda, D. MarrH, C. Cantoni, J. Gazquez, M. Varela, S. J. Pennycook, and F. M. Granozio. Appl. Phys. Lett., **97**, 152111 (2010).

[25] C. Cantoni, J. Gazquez, F. Miletto Granozio, M. P. Oxley, M. Varela, A. R. Lupini, S. J. Pennycook, C. Aruta, U. S. d. Uccio, P. Perna, and D. Maccariello. Adv. Mater., **24**, 3952–3957 (2012).

[26] S. R. Andrews and R. A. Cowley. J. Phys. C: Solid state Phys., **18**, 6427–6439 (1985).

[27] I. K. Robinson. Phys. Rev. B, **33**, 3830–3836 (1986).

[28] R. Feidenhans. Surf. Sci. Rep., **10**, 105 – 188 (1989).

[29] Y. Wakabayashi, T. Shirasawa, W. Voegeli, and T. Takahashi. J. Phys. Soc. Jpn., **87**, 061010 (2018).

[30] R. Yamamoto, C. Bell, Y. Hikita, H. Y. Hwang, H. Nakamura, T. Kimura, and Y. Wakabayashi. Phys. Rev. Lett., **107**, 036104 (2011).

[31] C. M. Schlepütz, R. Herger, P. R. Willmott, B. D. Patterson, O. Bunk, C. Brönnimann, B. Henrich, G. Hülsen, and E. F. Eikenberry. Act. Cryst. A, **61**, 418–425 (2005).

[32] J. R. Fienup. Opt. Lett., **3**, 27–29 (1978).

[33] J. R. Fienup. Appl. Opt., **21**, 2758–2769 (1982).

[34] V. Elser. J. Opt. Soc. Am. A, **20**, 40–55 (2003).

[35] M. Bj*ö*rck, C. M. Schlep*ü*tz, S. A. Pauli, D. Martoccia, R. Herger, and P. R. Willmott. J. Phys. Condens. Matter., **20**, 445006 (2008).

[36] T. Takahashi, K. Sumitani, and S. Kusano. Surf. Sci., **493**, 36 – 41 (2001).

[37] Y. Yacoby, M. Sowwan, E. Stern, J. O. Cross, D. Brewe, R. Pindak, J. Pitney, E. M. Dufresne, and R. Clarke. Nature Mat., **1**, 99–101 (2002).

[38] M. Sowwan, Y. Yacoby, J. Pitney, R. MacHarrie, M. Hong, J. Cross, D. A. Walko, R. Clarke, R. Pindak, and E. A. Stern. Phys. Rev. B, **66**, 205311 (2002).

[39] Y. Wakabayashi, M. Nakamura, K. Sasaki, T. Maeda, Y. Kishi, H. Ishii, N. Kobayashi, S. Yanagisawa, Y. Shimo, and Y. Kubozono. J. Am. Chem. Soc., **140**, 14046–14049 (2018).

[40] E. Cohen, S. Yochelis, O. Westreich, S. Shusterman, D. P. Kumah, R. Clarke, Y. Yacoby, and Y. Paltiel. Appl. Phys. Lett., **98**, 243115 (2011).

[41] E. Vlieg. J. Appl. Cryst., **33**, 401–405 (2000).

[42] V. Vonk. J. Appl. Cryst., **44**, 1217–1221 (2011).

[43] W. H. Press, S. A. Teukolsky, W. T. Vetterling, and B. P. Flannery. Numerical recipes in C : the art of scientific computing, pages 436–447 (1988).

[44] E. Landree, C. Collazo-Davila, and L. D. Marks. Acta Crystallographica Section B, **53**, 916–922 (1997).

[45] M. Björck and G. Andersson. J. Appl. Cryst., **40**, 1174–1178 (2007).

[46] M. Björck. J. Appl. Cryst., **44**, 1198–1204 (2011).

[47] W. v. d. Linden, V. Dose, and U. v. Toussaint. *Bayesian Probability Theory: Applications in the Physical Sciences.* Cambridge University Press, New York, NY, USA, (2014).

[48] A. Gelman, J. B. Carlin, H. S. Stern, and D. B. Rubin. *Bayesian Data Analysis.* Chapman and Hall/CRC, 2nd ed. edition, (2004).

[49] H. Szu and R. Hartley. Phys. Lett. A, **122**, 157 – 162 (1987).

[50] R. L. McGreevy and L. Pusztai. Mole. Simu., **1**, 359–367 (1988).

[51] M. D'Alessandro and F. Cilloco. Phys. Rev. E, **82**, 021128 (2010).

[52] M. D'Alessandro. Phys. Rev. E, **84**, 041130 (2011).

[53] S. Ikeda and H. Kono. Opt. Express, **20**, 3375–3387 (2012).

[54] M. Hoshino, Y. Nakanishi-Ohno, and D. Hashizume. Sci. Rep., **9**, 11886 (2019).

[55] N. Metropolis, A. W. Rosenbluth, M. N. Rosenbluth, A. H. Teller, and E. Teller. J. Chem. Phys., **21**, 1087–1092 (1953).

[56] B. Efron. Biometrika, **68**, 589–599 (1981).

[57] H. Zhou, R. Pindak, R. Clarke, D. M. Steinberg, and Y. Yacoby. J. Phys. D: Appl. Phys., **45**, 195302 (2012).

[58] A. D. Caviglia, S. Gariglio, N. Reyren, D. Jaccard, T. Schneider, M. Gabay, S. Thiel, G. Hammerl, J. Mannhart, and J.-M. Triscone. Nature, **456**, 624–627 (2008).

[59] C. Bell, S. Harashima, Y. Kozuka, M. Kim, B. G. Kim, Y. Hikita, and H. Y. Hwang. Phys. Rev. Lett., **103**, 226802 (2009).

[60] M. Minohara, Y. Hikita, C. Bell, H. Inoue, M. Hosoda, H. K. Sato, H. Kumigashira, M. Oshima, E. Ikenaga, and H. Y. Hwang. Sci. Rep., **7**, 9516 (2017).

[61] R. Yamamoto, H. Morisaki, O. Sakata, H. Shimotani, H. Yuan, Y. Iwasa, T. Kimura, and Y. Wakabayashi. Appl. Phys. Lett., **101**, 053122 (2012).

[62] R. V. Wang, D. D. Fong, F. Jiang, M. J. Highland, P. H. Fuoss, C. Thompson, A. M. Kolpak, J. A. Eastman, S. K. Streiffer, A. M. Rappe, and G. B. Stephenson. Phys. Rev. Lett., **102**, 047601 (2009).

[63] K. Nagai, M. Anada, Y. Nakanishi-Ohno, M, Okada, Y, Wakabayashi. J. Appl. Cryst., accepted, (2019).

[64] S. Sasaki. KEK Report 88-14, (1989).

[65] J. c. v. Chaloupka and G. Khaliullin. Phys. Rev. Lett., **100**, 016404 (2008).

[66] A. S. Disa, F. J. Walker, S. Ismail-Beigi, and C. H. Ahn. APL Mater., **3**, 062303 (2015).

[67] S. Middey, J. Chakhalian, P. Mahadevan, J. Freeland, A. Millis, and D. Sarma. Annu. Rev. Mater. Res., **46**, 305–334 (2016).

[68] M. L. Medarde. J. Phys. Condens. Matter., **9**, 1679–1707 (1997).

[69] J. A. Alonso, J. L. García-Muñoz, M. T. Fernández-Díaz, M. A. G. Aranda, M. J. Martínez-Lope, and M. T. Casais. Phys. Rev. Lett., **82**, 3871–3874 (1999).

[70] J.-S. Zhou and J. B. Goodenough. Phys. Rev. B, **69**, 153105 (2004).

[71] J. Chakhalian, J. M. Rondinelli, J. Liu, B. A. Gray, M. Kareev, E. J. Moon, N. Prasai, J. L. Cohn, M. Varela, I. C. Tung, M. J. Bedzyk, S. G. Altendorf, F. Strigari, B. Dabrowski, L. H. Tjeng, P. J. Ryan, and J. W. Freeland. Phys. Rev. Lett., **107**, 116805 (2011).

[72] E. Benckiser, M. W. Haverkort, S. BrDuan ck, E. Goering, S. Macke, A. FraDan Tan, X. Yang, O. K. Andersen, G. Cristiani, H.-U. Habermeier, A. V. Boris, I. Zegkinoglou, P. Wochner, H.-J. Kim, V. Hinkov, and B. Keimer. Nat. Mater., **10**, 189–193 (2011).

[73] H. Chen, D. P. Kumah, A. S. Disa, F. J. Walker, C. H. Ahn, and S. Ismail-Beigi. Phys. Rev. Lett., **110**, 186402 (2013).

[74] E. Sakai, M. Tamamitsu, K. Yoshimatsu, , K. Horiba, M. Oshima, and H. Kumigashira. Photon Factory Act. Rep., **29**, 149 (2012).

[75] E. Sakai, M. Tamamitsu, K. Yoshimatsu, S. Okamoto, K. Horiba, M. Oshima, and H. Kumigashira. Phys. Rev. B, **87**, 075132 (2013).

[76] P. D. C. King, H. I. Wei, Y. F. Nie, M. Uchida, C. Adamo, S. Zhu, X. He, I. Bozovic, D. G. Schlom, and K. M. Shen. Nat. nanotech., **9**, 443 (2014).

[77] A. M. Kaiser, A. X. Gray, G. Conti, J. Son, A. Greer, A. Perona, A. Rattanachata, A. Y. Saw, A. Bostwick, S. Yang, S.-H. Yang, E. M. Gullikson, J. B. Kortright, S. Stemmer, and C. S. Fadley. Phys. Rev. Lett., **107**, 116402 (2011).

[78] I.-C. Tung, G. Luo, J. H. Lee, S. H. Chang, J. Moyer, H. Hong, M. J. Bedzyk, H. Zhou, D. Morgan, D. D. Fong, and J. W. Freeland. Phys. Rev. Mater., **1**, 053404 (2017).

[79] L. Qiao and X. Bi. Europhys. Lett., **93**, 57002 (2011).

[80] S. J. May, J.-W. Kim, J. M. Rondinelli, E. Karapetrova, N. A. Spaldin, A. Bhattacharya, and P. J. Ryan. Phys. Rev. B, **82**, 014110 (2010).

[81] J. Liu, S. Okamoto, M. v. Veenendaal, M. Kareev, B. Gray, P. Ryan, J. W. Freeland, and J. Chakhalian. Phys. Rev. B, **83**, 161102 (2011).

[82] D. C. Licciardello and D. J. Thouless. Phys. Rev. Lett., **35**, 1475–1478 (1975).

[83] R. Scherwitzl, S. Gariglio, M. Gabay, P. Zubko, M. Gibert, and J.-M. Triscone. Phys. Rev. Lett., **106**, 246403 (2011).

[84] W. Brenig, G. H. Döhler, and H. Heyszenau. The Philosophical Magazine: J. Theo. Exp. and Appl. Phys., **27**, 1093–1103 (1973).

[85] F. Sánchez, C. Ferrater, C. Guerrero, M. García-Cuenca, and M. Varela. Appl. Phys. A, **71**, 59–64 (2000).

[86] D. P. Kumah, A. Malashevich, A. S. Disa, D. A. Arena, F. J. Walker, S. Ismail-Beigi, and C. H. Ahn. Phys. Rev. Appl., **2**, 054004 (2014).

[87] D. P. Kumah, A. S. Disa, J. H. Ngai, H. Chen, A. Malashevich, J. W. Reiner, S. Ismail-Beigi, F. J. Walker, and C. H. Ahn. Adv. Mater., **26**, 1935–1940 (2014).

[88] J. Hwang, J. Son, J. Y. Zhang, A. Janotti, C. G. V. d. Walle, and S. Stemmer. Phys. Rev. B, **87**, 060101 (2013).

[89] R. J. Francis, S. C. Moss, and A. J. Jacobson. Phys. Rev. B, **64**, 235425 (2001).

[90] Y. Wakabayashi, H. Maeda, T. Kimura, O. Sakata, E. Sakai, and H. Kumigashira. e-J. Surf. Sci. Nanotech., **14**, 14–16 (2016).

[91] M. Kitamura, K. Horiba, M. Kobayashi, E. Sakai, M. Minohara, T. Mitsuhashi, A. Fujimori, T. Nagai, H. Fujioka, and H. Kumigashira. Appl. Phys. Lett., **108**, 111603 (2016).

[92] J. C. Rojas Sánchez, B. Nelson-Cheeseman, M. Granada, E. Arenholz, and L. B. Steren. Phys. Rev. B, **85**, 094427 (2012).

[93] H. K. Yoo, Y. J. Chang, L. Moreschini, H.-D. Kim, C. H. Sohn, S. Sinn, J. S. Oh, C.-T. Kuo, A. Bostwick, E. Rotenberg, and T. W. Noh. Appl. Phys. Lett., **106**, 121601 (2015).

[94] M. Kawai, S. Inoue, M. Mizumaki, N. Kawamura, N. Ichikawa, and Y. Shimakawa. Appl. Phys. Lett., **94**, 082102 (2009).

[95] J. P. Ruf, P. D. C. King, V. B. Nascimento, D. G. Schlom, and K. M. Shen. Phys. Rev. B, **95**, 115418 (2017).

[96] D. Sarma. J. of Solid State Chem., **88**, 45 – 52 (1990).

[97] J. A. Alonso, M. J. Martínez-Lope, M. T. Casais, J. L. García-Muñoz, and M. T. Fernández-Díaz. Phys. Rev. B, **61**, 1756–1763 (2000).

[98] M. Medarde, M. T. Fernández-Díaz, and P. Lacorre. Phys. Rev. B, **78**, 212101 (2008).

[99] K. Rajeev, G. Shivashankar, and A. Raychaudhuri. Solid State Commun., **79**, 591 – 595 (1991).

[100] Y. Kumar, R. J. Choudhary, A. P. Singh, G. Anjum, and R. Kumar. J. Appl. Phys., **108**, 083706 (2010).

[101] J. Fowlie, C. l. Lichtensteiger, M. Gibert, H. Meley, P. Willmott, and J.-M. Triscone. Nano Lett., **19**, 4188–4194 (2019).

[102] J. L. García-Muñoz, J. Rodríguez-Carvajal, P. Lacorre, and J. B. Torrance. Phys. Rev. B, **46**, 4414–4425 (1992).

[103] X. R. Wang, C. J. Li, W. M. Lü, T. R. Paudel, D. P. Leusink, M. Hoek, N. Poccia, A. Vailionis, T. Venkatesan, J. M. D. Coey, E. Y. Tsymbal, Ariando, and H. Hilgenkamp. Science, **349**, 716–719 (2015).

[104] X. Zhai, C. S. Mohapatra, A. B. Shah, J.-M. Zuo, and J. N. Eckstein. J. Appl. Phys., **113**, 173913 (2013).

[105] W. S. Choi, D. W. Jeong, S. S. A. Seo, Y. S. Lee, T. H. Kim, S. Y. Jang, H. N. Lee, and K. Myung-Whun. Phys. Rev. B, **83**, 195113 (2011).

[106] J. Garcia-Barriocanal, F. Y. Bruno, A. Rivera-Calzada, Z. Sefrioui, N. M. Nemes, M. Garcia-Hernández, J. Rubio-Zuazo, G. R. Castro, M. Varela, S. J. Pennycook, C. Leon, and J. Santamaria. Adv. Mater., **22**, 627–632 (2010).

[107] J. Garcia-Barriocanal, J. C. Cezar, F. Y. Bruno, P. Thakur, N. B. Brookes, C. Utfeld, A. Rivera-Calzada, S. R. Giblin, J. W. Taylor, J. A. Duffy, S. B. Dugdale, T. Nakamura, K. Kodama, C. Leon, S. Okamoto, and J. Santamaria. Nat. Commun., **1**, 82 (2010).

[108] M. Imada, A. Fujimori, and Y. Tokura. Rev. Mod. Phys., **70**, 1039–1263 (1998).

[109] J. Töpfer and J. Goodenough. J. Solid State Chem., **130**, 117 – 128 (1997).

[110] J. M. D. Coey, M. Viret, and S. v. Molnr. Adv. Phys., **48**, 167–293 (1999).

[111] A. Urushibara, Y. Moritomo, T. Arima, A. Asamitsu, G. Kido, and Y. Tokura. Phys. Rev. B, **51**, 14103–14109 (1995).

[112] Z. Chen, Z. Chen, Z. Q. Liu, M. E. Holtz, C. J. Li, X. R. Wang, W. M. Lü, M. Motapothula, L. S. Fan, J. A. Turcaud, L. R. Dedon, C. Frederick, R. J. Xu, R. Gao, A. T. N'Diaye, E. Arenholz, J. A. Mundy, T. Venkatesan, D. A. Muller, L.-W. Wang, J. Liu, and L. W. Martin. Phys. Rev. Lett., **119**, 156801 (2017).

[113] J. A. Mundy, Y. Hikita, T. Hidaka, T. Yajima, T. Higuchi, H. Y. Hwang, D. A. Muller, and L. F. Kourkoutis. Nat. Commun., **5**, 3464 (2014).

[114] X. Hong, A. Posadas, and C. H. Ahn. Appl. Phys. Lett., **86**, 142501 (2005).

[115] X. Zhai, L. Cheng, Y. Liu, C. M. Schlepütz, S. Dong, H. Li, X. Zhang, S. Chu, L. Zheng, J. Zhang, A. Zhao, H. Hong, A. Bhattacharya, J. N. Eckstein, and C. Zeng. Nat. Commun., **5**, 4283 (2014).

[116] J. Fujioka, M. Nakamura, M. Kawasaki, and Y. Tokura. J. Appl. Phys., **111**, 016107 (2012).

[117] M. Nakamura, A. Sawa, J. Fujioka, M. Kawasaki, and Y. Tokura. Phys. Rev. B, **82**, 201101 (2010).

[118] M. Kitamura, M. Kobayashi, E. Sakai, R. Takahashi, M. Lippmaa, K. Horiba, H. Fujioka, and H. Kumigashira. Appl. Phys. Lett., **106**, 061605 (2015).

[119] H. S. Kim and H. M. Christen. J. Phys. Condens. Matter., **22**, 146007 (2010).

[120] W. S. Choi, D. Jeong, S. Jang, Z. Marton, S. Seo, H. Lee, and Y. Lee. J. Korean. Phys. Soc., **58**, 569–574 (2011).

[121] J. Roqueta, A. Pomar, L. Balcells, C. Frontera, S. Valencia, R. Abrudan, B. Bozzo, Z. Konstantinović, J. Santiso, and B. Martínez. Cryst. Growth Des., **15**, 5332–5337 (2015).

[122] I. V. Borisenko, M. A. Karpov, and G. A. Ovsyannikov. Tech. Phys. Lett, **39**, 1027–1030 (2013).

[123] W. S. Choi, Z. Marton, S. Y. Jang, S. J. Moon, B. C. Jeon, J. H. Shin, S. S. A. Seo, T. W. Noh, K. Myung-Whun, H. N. Lee, and Y. S. Lee. J. Phys. D: Appl. Phys., **42**, 165401 (2009).

[124] Y. Murakami, J. P. Hill, D. Gibbs, M. Blume, I. Koyama, M. Tanaka, H. Kawata, T. Arima, Y. Tokura, K. Hirota, and Y. Endoh. Phys. Rev. Lett., **81**, 582–585 (1998).

[125] K. Nakamura, T. Arima, A. Nakazawa, Y. Wakabayashi, and Y. Murakami. Phys. Rev. B, **60**, 2425–2428 (1999).

[126] H. Nakao, J. Nishimura, Y. Murakami, A. Ohtomo, T. Fukumura, M. Kawasaki, T. Koida, Y. Wakabayashi, and H. Sawa. J. Phys. Soc. Jpn., **78**, 024602 (2009).

[127] E. D. Specht and F. J. Walker. Phys. Rev. B, **47**, 13743–13751 (1993).

[128] E. Perret, C. Park, D. D. Fong, K.-C. Chang, B. J. Ingram, J. A. Eastman, P. M. Baldo, and P. H. Fuoss. J. Appl. Cryst., **46**, 76–87 (2013).

[129] Y. S. Chu, H. You, J. A. Tanzer, T. E. Lister, and Z. Nagy. Phys. Rev. Lett., **83**, 552–555 (1999).

[130] F. J. Walker, E. D. Specht, and R. A. McKee. Phys. Rev. Lett., **67**, 2818–2821 (1991).

[131] M. Takahashi and J. Mizuki. Phys. Rev. Lett., **96**, 055506 (2006).

[132] M. An, Y. Weng, H. Zhang, J.-J. Zhang, Y. Zhang, and S. Dong. Phys. Rev. B, **96**, 235112 (2017).

[133] H. M. Liu, C. Y. Ma, P. X. Zhou, S. Dong, and J.-M. Liu. J. Appl. Phys., **113**, 17D902 (2013).

[134] Y. Joly, O. Bunău, J. E. Lorenzo, R. M. Galéra, S. Grenier, and B. Thompson. J. Phys. Conf. Ser., **190**, 012007 (2009).

[135] J. A. BEARDEN and A. F. BURR. Rev. Mod. Phys., **39**, 125–142 (1967).

[136] G. Subías, J. García, M. G. Proietti, and J. Blasco. Phys. Rev. B, **56**, 8183–8191 (1997).

[137] J. J. Peng, C. Song, F. Li, Y. D. Gu, G. Y. Wang, and F. Pan. Phys. Rev. B, **94**, 214404 (2016).

[138] Y. Wakabayashi, D. Bizen, Y. Kubo, H. Nakao, Y. Murakami, M. Nakamura, Y. Ogimoto, K. Miyano, and H. Sawa. J. Phys. Soc. Jpn., **77**, 014712 (2008).

[139] T. Chatterji, F. m. c. Fauth, B. Ouladdiaf, P. Mandal, and B. Ghosh. Phys. Rev. B, **68**, 052406 (2003).

[140] J.-S. Zhou and J. B. Goodenough. Phys. Rev. Lett., **96**, 247202 (2006).

[141] M. Medarde, J. Mesot, P. Lacorre, S. Rosenkranz, P. Fischer, and K. Gobrecht. Phys. Rev. B, **52**, 9248–9258 (1995).

[142] S. J. Hibble, S. P. Cooper, A. C. Hannon, I. D. Fawcett, and M. Greenblatt. J. Phys. Condens. Matter., **11**, 9221–9238 (1999).

[143] R. Ganguly, V. Siruguri, I. K. Gopalakrishnan, and J. V. Yakhmi. J. Phys. Condens. Matter., **12**, 1683–1689 (2000).

[144] A. B. Shah, Q. M. Ramasse, X. Zhai, J. G. Wen, S. J. May, I. Petrov, A. Bhattacharya, P. Abbamonte, J. N. Eckstein, and J.-M. Zuo. Adv. Mater., **22**, 1156–1160 (2010).

[145] M. Gibert, P. Zubko, R. Scherwitzl, J. t. aiguez, and J.-M. Triscone. Nat. Mater., **11**, 195–198 (2012).

[146] J. Hoffman, I. C. Tung, B. B. Nelson-Cheeseman, M. Liu, J. W. Freeland, and A. Bhattacharya. Phys. Rev. B, **88**, 144411 (2013).

[147] S. Dong and E. Dagotto. Phys. Rev. B, **87**, 195116 (2013).

[148] H. Wei, J. L. Barzola-Quiquia, C. Yang, C. Patzig, T. HUche, P. Esquinazi, M. Grundmann, and M. Lorenz. Appl. Phys. Lett., **110**, 102403 (2017).

[149] M. Gibert, M. Viret, A. Torres-Pardo, C. Piamonteze, P. Zubko, N. Jaouen, J.-M. Tonnerre, A. Mougin, J. Fowlie, S. Catalano, A. Gloter, O. StHphan, and J.-M. Triscone. Nano Lett., **15**, 7355–7361 (2015).

[150] L. F. Kourkoutis, D. A. Muller, Y. Hotta, and H. Y. Hwang. Appl. Phys. Lett., **91**, 163101 (2007).

[151] S. J. May, A. B. Shah, S. G. E. t. Velthuis, M. R. Fitzsimmons, J. M. Zuo, X. Zhai, J. N. Eckstein, S. D. Bader, and A. Bhattacharya. Phys. Rev. B, **77**, 174409 (2008).

[152] M. Vafaee, S. Finizio, H. Deniz, D. Hesse, H. Zabel, G. Jakob, and M. Klui. Appl. Phys. Lett., **108**, 072401 (2016).

[153] B. R. K. Nanda, S. Satpathy, and M. S. Springborg. Phys. Rev. Lett., **98**, 216804 (2007).

[154] C. He, A. J. Grutter, M. Gu, N. D. Browning, Y. Takamura, B. J. Kirby, J. A. Borchers, J. W. Kim, M. R. Fitzsimmons, X. Zhai, V. V.

Mehta, F. J. Wong, and Y. Suzuki. Phys. Rev. Lett., **109**, 197202 (2012).

[155] A. Ohtomo, D. A. Muller, J. L. Grazul, and H. Y. Hwang. Nature, **419**, 378–380 (2002).

[156] T. Koida, M. Lippmaa, T. Fukumura, K. Itaka, Y. Matsumoto, M. Kawasaki, and H. Koinuma. Phys. Rev. B, **66**, 144418 (2002).

[157] A. Bhattacharya, S. J. May, S. G. E. t. Velthuis, M. Warusawithana, X. Zhai, B. Jiang, J.-M. Zuo, M. R. Fitzsimmons, S. D. Bader, and J. N. Eckstein. Phys. Rev. Lett., **100**, 257203 (2008).

[158] M. Kitamura, I. Ohkubo, M. Matsunami, K. Horiba, H. Kumigashira, Y. Matsumoto, H. Koinuma, and M. Oshima. Appl. Phys. Lett., **94**, 262503 (2009).

[159] M. Kitamura, M. Kobayashi, E. Sakai, M. Minohara, R. Yukawa, D. Shiga, K. Amemiya, Y. Nonaka, G. Shibata, A. Fujimori, H. Fujioka, K. Horiba, and H. Kumigashira. Phys. Rev. B, **100**, 245132 (2019).

[160] O. Bunău and Y. Joly. J. Phys. Condens. Matter., **21**, 345501 (2009).

[161] J. Rodríguez-Carvajal, M. Hennion, F. Moussa, A. H. Moudden, L. Pinsard, and A. Revcolevschi. Phys. Rev. B, **57**, R3189–R3192 (1998).

[162] S. Okamoto, A. J. Millis, and N. A. Spaldin. Phys. Rev. Lett., **97**, 056802 (2006).

[163] M. S. Pierce, K. C. Chang, D. Hennessy, V. Komanicky, M. Sprung, A. Sandy, and H. You. Phys. Rev. Lett., **103**, 165501 (2009).

[164] J. Gustafson, M. Shipilin, C. Zhang, A. Stierle, U. Hejral, U. Ruett, O. Gutowski, P.-A. Carlsson, M. Skoglundh, and E. Lundgren. Science, **343**, 758–761 (2014).

[165] H. Fujii, Y. Wakabayashi, and T. Doi. J. Electrochem. Soc., **166**, E212–E216 (2019).

[166] T. Shirasawa, T. Masuda, W. Voegeli, E. Arakawa, C. Kamezawa, T. Takahashi, K. Uosaki, and T. Matsushita. J. Phys. Chem. C, **121**, 24726–24732 (2017).

[167] G. Ju, D. Xu, M. J. Highland, C. Thompson, H. Zhou, J. A. Eastman, P. H. Fuoss, P. Zapol, H. Kim, and G. B. Stephenson. Nat. Phys., **15**, 589–594 (2019).

Appendix A

Format of input files for MC software

Input text files for MC software(Replica exchange ver.) are needed to be written as follows.

(a)Bulk structure file

1st line: $a \quad b \quad c \quad \alpha \quad \beta \quad \gamma$
2nd ∼: N site-index x y z B occ
$\vdots$

1st line: The lattice constants of bulk structure
2nd ∼: Atomic number, the index number of atoms in the same site, fractional atomic position x, y, z, atomic displacement parameter, atomic occupancy

(b)Film structural parameters file

1st line: Intensity-scale Noise-scale Noise-value Bulk-B
2nd : Introduction of the format of 3rd∼ lines
3rd∼: Atom-index N x y z B toccf foccf foccf-2 fitting-switch x-index x-param x-ratio$\cdots$ x-MIN x-MAX $\cdots$

•Atom-index: The index number of atoms. The start number is 0.

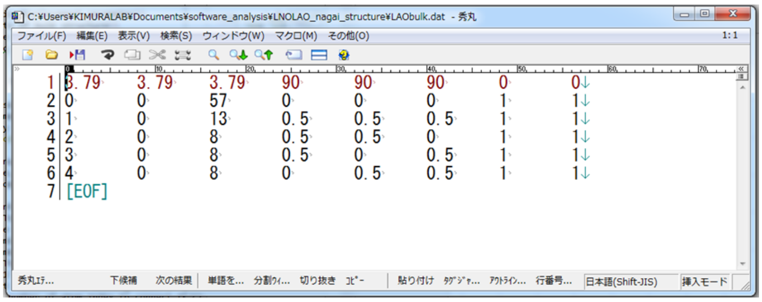

C:¥Users¥KIMURALAB¥Documents¥software_analysis¥LNOLAO_nagai_structure¥LAObulk.dat - 秀丸

```
3.79	3.79	3.79	90	90	90	0	0
0	0	57	0	0	0	1	1
1	0	13	0.5	0.5	0.5	1	1
2	0	8	0.5	0.5	0	1	1
3	0	8	0.5	0	0.5	1	1
4	0	8	0	0.5	0.5	1	1
[EOF]
```

Figure A.1: Example of Bulk structure file. (pseudo cubic LaAlO$_3$(001) substrate)

•N: Atom number (Example, the value of N for Oxygen is 8.)
·x, y, z: Fractional atomic position. The interface position is z = 0 and positive number is the direction to the surface side.
•*B*: Atomic displacement parameter
•toccf, foccf, foccf2: Total atomic occupancy, fractional atomic occupancy, fractional atomic occupancy of different valence state of the same atom. Atomic occupancy is calculated by toccf × foccf × foccf2. foccf is utilized for the atomic interdiffusion. foccf2 is utilized for the fraction of different valence state in this
•fitting-switch: The number to refine the parameters written in the same line. Please enter the number composed of 0(off) or 1(on). The number of each digit corresponds to the each parameters from the left number. For example, if you write ‘1111111’, all parameters(x ∼ foccf-2) of the atom written in this line are refined. If you would like to refine only z and *B*, please write ‘11000’, not ‘0011000’. The leading numbers ‘00’ correspond to x and y must be omitted.
•x-index: The number of atom index to connect the parameter of an atom in this line.
•x-param: The number of ‘parameter number’ to connect the parameter of an atom in this line. The parameter numbers are x: 0, y: 1, z: 2, *B*: 3, toccf: 4, foccf: 5, foccf-2: 6.
•x-ratio: The magnification of the value of MC step of the parameter to that of the target parameter. For example, if you want to move x
•x-MAX, x-MIN: The maximum and minimum value of the parameter. The MC step to the out side of [x-MIN, x-MAX] is prohibited.

Please write x-ratio, x-param, x-ratio and x-Max, x-Min for all parameters.

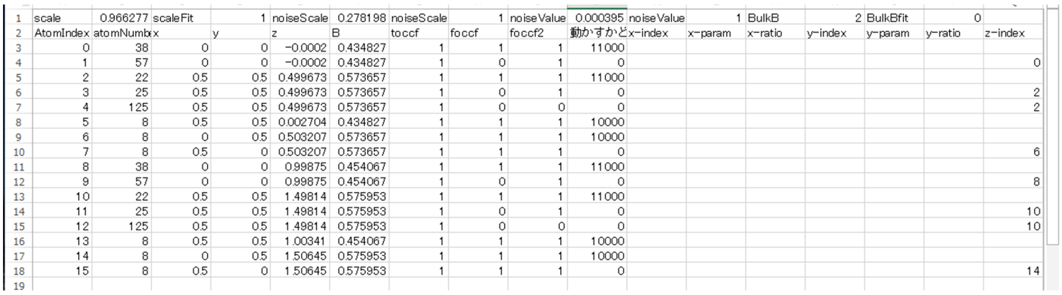

1	scale	0.966277	scaleFit	1	noiseScale	0.278198	noiseScale	1	noiseValue	0.000395	noiseValue	1	BulkB	2	BulkBfit	0	
2	AtomIndex	atomNumb	x	y	z	B	toccf	foccf	foccf2	動かすかど	x−index	x−param	x−ratio	y−index	y−param	y−ratio	z−index
3	0	38	0	0	−0.0002	0.434827	1	1	1	11000							
4	1	57	0	0	−0.0002	0.434827	1	0	1	0							0
5	2	22	0.5	0.5	0.499673	0.573657	1	1	1	11000							
6	3	25	0.5	0.5	0.499673	0.573657	1	0	1	0							2
7	4	125	0.5	0.5	0.499673	0.573657	1	0	0	0							2
8	5	8	0.5	0.5	0.002704	0.434827	1	1	1	10000							
9	6	8	0	0.5	0.503207	0.573657	1	1	1	10000							
10	7	8	0.5	0	0.503207	0.573657	1	1	1	0							6
11	8	38	0	0	0.99875	0.454067	1	1	1	11000							
12	9	57	0	0	0.99875	0.454067	1	0	1	0							8
13	10	22	0.5	0.5	1.49814	0.575953	1	1	1	11000							
14	11	25	0.5	0.5	1.49814	0.575953	1	0	1	0							10
15	12	125	0.5	0.5	1.49814	0.575953	1	0	0	0							10
16	13	8	0.5	0.5	1.00341	0.454067	1	1	1	10000							
17	14	8	0	0.5	1.50645	0.575953	1	1	1	10000							
18	15	8	0.5	0	1.50645	0.575953	1	1	1	0							14
19																	

Figure A.2: Film structural parameters file. 2 unit-cell thick $LaMnO_3$ (Part 1)

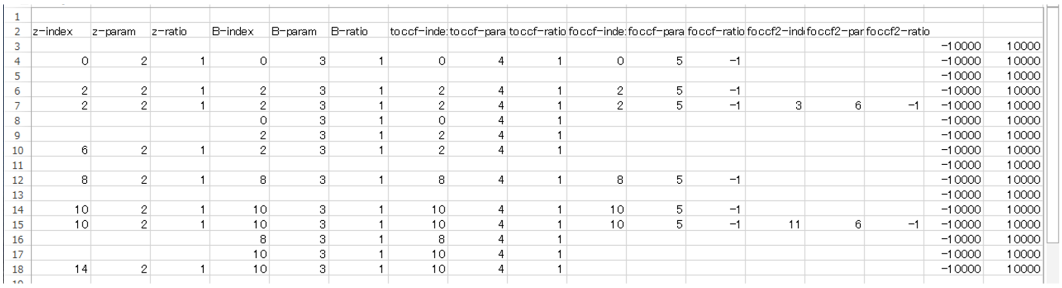

1																	
2	z−index	z−param	z−ratio	B−index	B−param	B−ratio	toccf−inde:	toccf−para	toccf−ratio	foccf−inde:	foccf−para	foccf−ratio	foccf2−ind	foccf2−par	foccf2−ratio		
3																−10000	10000
4	0	2	1	0	3	1	0	4	1	0	5	−1				−10000	10000
5																−10000	10000
6	2	2	1	2	3	1	2	4	1	2	5	−1				−10000	10000
7	2	2	1	2	3	1	2	4	1	2	5	−1	3	6	−1	−10000	10000
8				0	3	1	0	4	1							−10000	10000
9				2	3	1	2	4	1							−10000	10000
10	6	2	1	2	3	1	2	4	1							−10000	10000
11																−10000	10000
12	8	2	1	8	3	1	8	4	1	8	5	−1				−10000	10000
13																−10000	10000
14	10	2	1	10	3	1	10	4	1	10	5	−1				−10000	10000
15	10	2	1	10	3	1	10	4	1	10	5	−1	11	6	−1	−10000	10000
16				8	3	1	8	4	1							−10000	10000
17				10	3	1	10	4	1							−10000	10000
18	14	2	1	10	3	1	10	4	1							−10000	10000

Figure A.3: Film structural parameters file. 2 unit-cell thick $LaMnO_3$ (Part 2)

(c)Intensity data file

h k l I_{exp} I_{calc} I_{stat} anomalous-num relative-intensity-scale-index relative-intensity-scale-value Energy

⋮

- h, k, l: The value of $\boldsymbol{Q} = h, k, l$
- I_{exp}: Experimental value of intensity at h, k, l.
- I_{calc}: the calculated value of the intensity from the model. Input value of I_{calc} has no effects on the calculation.
- I_{stat}: The value of statistical noise.

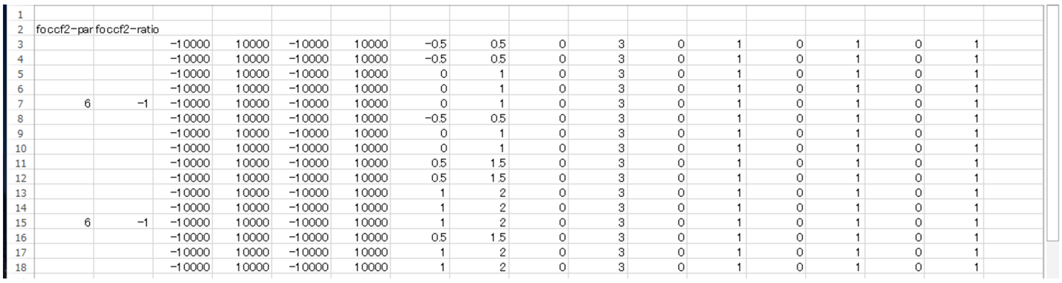

1																
2	foccf2-par	foccf2-ratio														
3			−10000	10000	−10000	10000	−0.5	0.5	0	3	0	1	0	1	0	1
4			−10000	10000	−10000	10000	−0.5	0.5	0	3	0	1	0	1	0	1
5			−10000	10000	−10000	10000	0	1	0	3	0	1	0	1	0	1
6			−10000	10000	−10000	10000	0	1	0	3	0	1	0	1	0	1
7	6	−1	−10000	10000	−10000	10000	0	1	0	3	0	1	0	1	0	1
8			−10000	10000	−10000	10000	−0.5	0.5	0	3	0	1	0	1	0	1
9			−10000	10000	−10000	10000	0	1	0	3	0	1	0	1	0	1
10			−10000	10000	−10000	10000	0	1	0	3	0	1	0	1	0	1
11			−10000	10000	−10000	10000	0.5	1.5	0	3	0	1	0	1	0	1
12			−10000	10000	−10000	10000	0.5	1.5	0	3	0	1	0	1	0	1
13			−10000	10000	−10000	10000	1	2	0	3	0	1	0	1	0	1
14			−10000	10000	−10000	10000	1	2	0	3	0	1	0	1	0	1
15	6	−1	−10000	10000	−10000	10000	1	2	0	3	0	1	0	1	0	1
16			−10000	10000	−10000	10000	0.5	1.5	0	3	0	1	0	1	0	1
17			−10000	10000	−10000	10000	1	2	0	3	0	1	0	1	0	1
18			−10000	10000	−10000	10000	1	2	0	3	0	1	0	1	0	1

Figure A.4: Film structural parameters file. 2 unit-cell thick $LaMnO_3$ (Part 3)

- anomalous-num: ‘Anomalous number’ same as the anomalous scattering factor file.
- relative-intensity-scale-index: The index of the intensity with different value of scale factor.
- relative-intensity-scale-value: The relative value of the intensity scale to that with relative-intensity-scale-index = 0. The value of ‘relative-intensity-scale-value’ with relative-intensity-scale-index = 1∼ is the scale parameter of MC calculation. The value of ‘relative-intensity-scale-value’ with relative-intensity-scale-index = 0 is fixed.

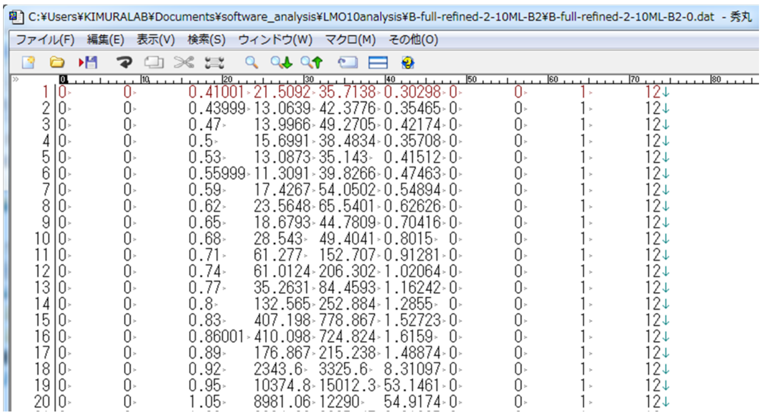

```
0	0	0.41001	21.5092	35.7138	0.30298	0	0	1	12
0	0	0.43999	13.0639	42.3776	0.35465	0	0	1	12
0	0	0.47	13.9966	49.2705	0.42174	0	0	1	12
0	0	0.5	15.6991	38.4834	0.35708	0	0	1	12
0	0	0.53	13.0873	35.143	0.41512	0	0	1	12
0	0	0.55999	11.3091	39.8266	0.47463	0	0	1	12
0	0	0.59	17.4267	54.0502	0.54894	0	0	1	12
0	0	0.62	23.5648	65.5401	0.62626	0	0	1	12
0	0	0.65	18.6793	44.7809	0.70416	0	0	1	12
0	0	0.68	28.543	49.4041	0.8015	0	0	1	12
0	0	0.71	61.277	152.707	0.91281	0	0	1	12
0	0	0.74	61.0124	206.302	1.02064	0	0	1	12
0	0	0.77	35.2631	84.4593	1.16242	0	0	1	12
0	0	0.8	132.565	252.884	1.2855	0	0	1	12
0	0	0.83	407.198	778.867	1.52723	0	0	1	12
0	0	0.86001	410.098	724.824	1.6159	0	0	1	12
0	0	0.89	176.867	215.238	1.48874	0	0	1	12
0	0	0.92	2343.6	3325.6	8.31097	0	0	1	12
0	0	0.95	10374.8	15012.3	53.1461	0	0	1	12
0	0	1.05	8981.06	12290	54.9174	0	0	1	12
```

Figure A.5: Example of Intensity data file.

(d)Anomalous scattering factor file

N f' f''

⋮

Please write atomic number N, the value of $f'(E)$ and $f''(E)$. You need to create one anomalous scattering factor file per energy E. The file name corresponding to anomalous-num = 0 is ‘anomalous.dat’, and those of files after anomalous-num = 1 $\sim$ are anomalous1.dat, anomalous2.dat, ...

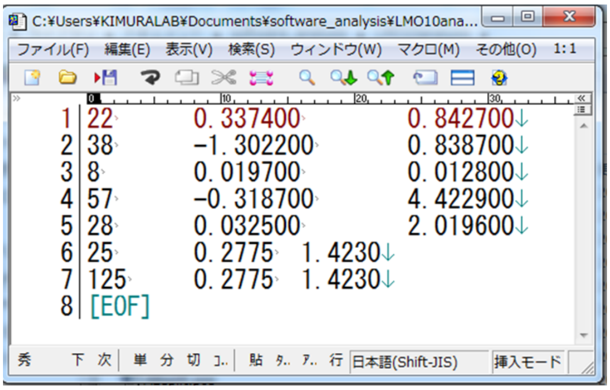

```
22	0.337400		0.842700
38	-1.302200		0.838700
8	0.019700		0.012800
57	-0.318700		4.422900
28	0.032500		2.019600
25	0.2775	1.4230
125	0.2775	1.4230
[EOF]
```

Figure A.6: Example of Anomalous scattering factor file.

All numbers written in these files are necessary to be separated by tab character. Please put these files into the current directory for analysis with .exe file. To execute this software, please write the bellow command on command line as

”Software-name(.exe) Bulk-structure-filename Intensity-filename Initial-structural-parameters-filename output-filename The-highest-inverse-temperature The-lowest-inverse-temperature Iteration-number”

Total number of arguments is 8. Please add extension of input filenames except for output-filename. The number of replicas and the frequency of exchanging replicas are controlled in source code.

After MC calculation, a folder named as the ‘outputfile’ will be created. The following files will be created in that folder.

(a)output-filename.log

The values of the cost function per 100 MC steps of all replicas are recorded. Parameters convergence is judged by whether the value of cost function is stable or not.

(b)output-filename-n.pos
(c)output-filename-n.dat

(b)Film structure file and (c)Intensity file of the final result(one sample) of MC calculation for each replica n. These files have the same format as the input files, so they can be used as initial values for the next MC calculation.

(d)output-filename-n.par

A file that records the transitions of all optimized parameter values. The posterior probability distribution of parameters is generated from this file.

Acknowledgements

I would like to express my sincerest gratitude to Prof. Wakabayashi for his dedicated supports. He taught me not only the knowledge of physics but also experiments and analysis technique of X-ray diffraction. He provided guidance of approaching for the study of material science.

Prof. Y. Suzuki supported my PhD course research during my commission for research supervision in Tohoku University. He was engaged in the judge of my PhD course dissertation. I would like to give him warmest expressions of appreciation for his supports.

This research has been accomplished by the great contributions of many collaborators. I would like to appreciate the following people: Prof. M. Okada and Dr. Y. Nakanishi-Ohno (introduction and discussion of data analysis by information science), Prof. H. Kumigashira, Prof. K. Horiba, Dr. E. Sakai and Dr. M. Kitamura(sample preparation of perovskite oxide thin films and discussion about the properties of them), Prof. Y. Morikawa and Dr. H. D. Nguyen(discussion about $\mathrm{LaNiO_3}$ thin films based on *ab* initio calculation), Prof. H. Nakao (KEK) and Dr. H. Tajiri(JASRI) (support for experiments at the synchrotron radiation facility), Prof. T. Kimura, Dr. K. Kimura and Dr. H. Ueda, Dr. H. Zhou(experiments and analysis in Argonne national laboratory).

Also I thank all members and secretaries(Ms. Inoue, Ms. Wada and Ms. Kurashige) of Kimura and Wakabayashi laboratory. In particular, Mr. Fujii supported my experiments and analysis with his advanced experimental techniques and extensive my knowledge of X-ray diffraction. Mr. Nagai has improved my analysis software to make it better and more practical. He joined my experiments and provided me with dedicated support. Our quick CTR measurement was realized by 2 dimensional detector installed by Mr. Kowa. I would like to give them the utmost respect.

Finally, I would like to express my great thanks to my family for supporting me in my life for many years.

The synchrotron radiation experiments at the Photon Factory were performed with the approval of the Photon Factory Program Advisory Committee (Proposals No. 2012G091, No. 2013S2-002, No. 2015S2-005, No. 2015S2-009 and No. 2018G533).

The synchrotron radiation experiments at the BL13XU of SPring-8 were performed with the approval of the NIMS Nanotechnology Platform (Proposal No. 2012B4901, No. 2013A4901 and No. 2019A1113).

Publication List

Original papers

M.Anada, Y. Nakanishi-Ohno, M. Okada, T. Kimura and Y. Wakabayashi, ”Bayesian inference of metal oxide ultrathin film structure based on crystal truncation rod measurements” J. Appl. Cryst. **50**, 1611-1616 (2017).

M.Anada, K. Kowa, H. Maeda, E. Sakai, M. Kitamura, H. Kumigashira, O. Sakata, Y. Nakanishi-Ohno, M. Okada, T. Kimura and Y. Wakabayashi, ”Spatial coherence of the insulating phase in quasi-two-dimensional LaNiO$_3$ films” Phys. Rev. B, **98**, 014105-1-8 (2018).

D. Kan, **M.Anada**, Y. Wakabayashi, H. Tajiri, and Y. Shimakawa, ”Oxygen octahedral distortions in compressively strained SrRuO$_3$ epitaxial thin films” J. Appl. Phys. **123**, 235303-1-5 (2018).

Y. Heo, D. Kan, **M.Anada**, Y. Wakabayashi, H. Tajiri, and Y. Shimakawa, ”Correlations between oxygen octahedral distortions and magnetic and transport properties in strained La$_{0.5}$Sr$_{0.5}$CoO$_3$ thin films” Phys. Rev. B **99**, 174420 (2019).

K. Nagai, **M.Anada**, Y. Nakanishi-Ohno, M, Okada, and Y, Wakabayash, ”Robust surface structure analysis with a reliable error estimation by the exchange Monte Carlo method”, J. Appl. Cryst. accepted (2020).

International conferences

M.Anada, Y. Nakanishi-Ohno, M. Okada, T. Kimura, and Y. Wakabayashi, ”Reverse Monte-Carlo analysis of CTR data from perovskite-type oxide thin films”, 14th International Conference on Surface X-ray and Neutron Scattering (SXNS14), New York, USA (2016).

M.Anada, Y. Nakanishi-Ohno, M. Okada, T. Kimura and Y. Wakabayashi, "X-ray structure analysis software for perovskite-type oxide thin films", International Workshop on Oxide Electronics, Chicago, USA (2017).

M.Anada, K. Kowa, Y. Maeda, M. Kitamura, E. Sakai, H. Kumigashira, O. Sakata, Y. Nakanishi-Ohno, M. Okada and Y. Wakabayashi, "Structural elucidation of two different insulating states of $LaNiO_3$ ultrathin films", 15th International Conference on Surface X-ray and Neutron Scattering, Pohang, Korea (2018).